Project No. 12-3582

Experimentally Validated Numerical Models of Non-Isothermal Turbulent Mixing in High Temperature Reactors

Reactor Concepts Research Development and Demonstration (RCRD&D)

Mark Kimber
University of Pittsburgh

Steven Reeves, Federal POC
Carl Stoots, Technical POC

NEUP Nuclear Energy University Programs
U.S. Department of Energy

FINAL REPORT

Experimentally Validated Numerical Models of Non-Isothermal Turbulent Mixing in High Temperature Reactors

(NEUP 12-3582)

Recipient: University of Pittsburgh
Of The Commonwealth System
of High Education
116 Atwood Street, Suite 201
Pittsburgh, PA 15260

Principal Investigator: Mark L. Kimber, 979-458-3952, mark.kimber@tamu.edu

Co-PIs: John C. Brigham, brigham@pitt.edu

Anirban Jana, anirban@psc.edu

Executive Summary

In the Very High Temperature Reactor (VHTR), the non-uniform heat generation and flow maldistribution of coolant in the core generates conditions leading into the lower plenum with many jets at different temperatures and velocities. The hope is that the combined flow becomes fully mixed in a short distance so that the fluctuating temperatures in the mixing region do not cause unwanted thermal stresses in the supporting structures. These cyclic thermal stresses can cause degradation of the wall microstructure including crack initiation and growth, ultimately leading to the fatigue failure in the lower plenum, and can be accelerated by the high temperature environment in the VHTR. The focus of this project was to provide experimental data for future validation of computational efforts aimed at capturing the turbulent mixing in the lower plenum. Computational fluid dynamics (CFD) is also used as part of this effort to assess the requirements to model fundamental flows with application to the lower plenum as well at the applied flow conditions that mimic the experimental facilities. These efforts will lay the groundwork for future incorporation of stress analysis as well as fatigue and failure studies for multiple VHTR components. An additional emphasis is placed on reduced order models (ROM) using canonical flows, which will help to balance computational expense and accuracy and enable future work in uncertainty quantification.

The flow in the lower plenum is extremely complex with hundreds of cooling jets entering and then being forced to change directions by 90° while navigating through an array of cylindrical support posts. Generating experimental data for such a complicated flow is difficult, not to mention that the computational requirements to generate an adequate temporal and spatial sampling is extremely expensive and time consuming. Therefore, the ultimate focus of this research is a “unit cell” which consists of six jets in the presence of a crossflow, and seven cylindrical support posts. It is scaled to achieve similar ranges of key dimensionless numbers. This serves to mimic flow conditions in different regions of the lower plenum by adjusting velocities, temperatures, and orientations, and represents a compromise between the complexity inside the full-scale application and the ideal conditions of a more fundamental study.

In addition to the unit cell experiments and simulations, the complex flows in the VHTR lower plenum are broken down into a number of simplified (in some cases even fundamental) flows, two of which are turbulent jets and flow past cylinders. Each of these are studied, computationally and experimentally for isothermal and non-isothermal conditions. Flows where trusted experimental data is available in the literature (e.g., turbulent free jet), additional experiments are not needed. The result of these efforts is a database of experimental data and multiple computational studies, which provide an outlook to the requirements, needed to capture turbulent mixing flow physics The ROM results provide assessments for appropriate resource-light models that balance accuracy with reduced computational burdens.

Table of Contents

Executive Summary i

Table of Contents iii

List of Figures vi

List of Tables xviii

1 Background and Motivation 1

2 Experimental Studies 3

2.1 Background and Literature Review 3

2.1.1 Thermal Striping and Triple Jet Studies 3

2.2 Experimental Facility Design 8

2.2.1 Flow Skid Design 8

2.2.2 Unit Cell Experimental Design 20

2.3 Characterization of Jet Flow Behavior 33

2.3.1 Experimental Approach 33

2.3.2 Velocity Contours and Turbulence Quantification 48

2.3.3 Quantification of Jet Profile 50

2.4 Measurements in a Parallel Triple-Jet 56

2.4.1 Error Assessment of Triple-Jet Measurements 57

2.4.2 Analysis of Triple-Jet Profiles 64

2.4.3 Trends in the Triple-Jet 70

2.5 Non-Isothermal Triple Jet Near Solid Wall 76

2.5.1 Experimental Parameters 77

2.5.2 Experimental Methods 79

2.5.3 Experimental Results – Temperature Contours 80

2.5.4 Experimental Results – Jet-Induced Temperature Peaks 82

2.6 Unit Cell Experiments 86

2.6.1 Boundary Conditions – Jet Inlet 95

2.6.2 Boundary Conditions – Crossflow 100

2.6.3 Experimental Results 103

3 Computational Studies 116

3.1 RANS Model of VHTR Lower Plenum 117

3.2 RANS Simulations of Isothermal Turbulent Round Jets 126

3.2.1 Computational Model 127

3.2.2 Results and Discussion 129

3.3 Large Eddy Simulations of Isothermal Turbulent Round Jets 131

3.3.1 Computational Model 132

3.3.2 Results and Discussion 140

3.4 Non-Isothermal Turbulent Round Jets 160

3.5 Flow Past a Circular Cylinder 171

3.5.1 Isothermal Flow Over a Cylinder 171

3.5.2 Non-Isothermal Flow Over a Cylinder 180

3.6 Large Eddy Simulations of Unit Cell 185

3.6.1 Temperature and Velocity Specification 186

3.6.2 Mesh Configuration 188

3.6.3 LES Specification 190

3.6.4 Results and Discussion 191

3.7 Unit Cell Simulations vs. Experimental Data 213

3.7.1 Case I 213

3.7.2 Case II 223

3.7.3 Case III 230

4 Reduced-Order Modeling 240

4.1.1 Proper Orthogonal Decomposition 240

4.1.2 Galerkin-Projection for Incompressible Navier-Stokes 242

4.1.3 Application to Flow Around a Circular Cylinder 244

4.1.4 Accuracy of Reduced Order Model 246

4.2 Reduced-Order Modeling of Compressible Turbulent Flows 251

4.2.1 POD Galerkin Projection ROM for Compressible Navier-Stokes 252

4.2.2 Application to Flow Around a Circular Cylinder 254

4.2.3 Regression-Based Reduced-Order Modeling 257

5 Bibliography 260

List of Figures

Figure 2-1: Illustration of a round parallel triple-jet showing the mixing and development downstream... 5

Figure 2-2. Schematic of the experimental test section with honeycomb flow conditioners pictured..... 10

Figure 2-3. Triple-jet experimental test section 12

Figure 2-4. (a) Plot of predicted system curve with the manufacturer supplied blower curves (b) Experimentally measured system curves and blower curve 16

Figure 2-5. Percent uncertainty of mass flow rate and individual uncertainty components 19

Figure 2-6. Half-model of the VHTR lower plenum with jets (colored) and posts (grey) [21]..... 21

Figure 2-7. Matched index of refraction facility test section at INL [26]..... 21

Figure 2-8. Experimental unit cell for studying the lower plenum of the VHTR 23

Figure 2-9. Isometric view of the test section with key design components highlighted 25

Figure 2-10. Thermocouple/Support post assembly with thermocouples shown 26

Figure 2-11. Cross flow wind tunnel design 27

Figure 2-12. (a) Array of six jets located above test section (b) transparent jet revealing internal honeycomb insert..... 29

Figure 2-13: Transparent circular top plate with post configuration 30

Figure 2-14: Stepper motor coupled to center post via a shaft 31

Figure 2-15. Ice point facility 32

Figure 2-16. Illustration of experimental facility for studies for single round..... 34

Figure 2-17. Qualitative velocity contours at $\boldsymbol{x/Djet}$ = 0.33 for (a) straight pipe, (b) coarse honeycomb, and (c) refined honeycomb. The geometric extent of the round jet is depicted by a dashed line..... 35

Figure 2-18. (a) Coarse honeycomb (b) refined honeycomb (c) ceramic honeycomb (shown in pipe coupling) 36

Figure 2-19. Calibration velocity versus CTA voltage corrected for temperature..... 38

Figure 2-20. Comparison of calibration and predicted velocities 39

Figure 2-21. CTA calibration curves for heated flows 40

Figure 2-22. Temperature dependency of $\boldsymbol{a}$ and with curve fits shown 42

Figure 2-23. Curve fit velocity versus calibration velocity for all tested data 43

Figure 2-24. CTA and CCA two-wire probe 44

Figure 2-25. (a) Velocity magnitude with simultaneous temperature correction [m s^{-1}] (b) Velocity mangitude with collocated temperature correction [m s^{-1}] (c) Temperature [°C]. For each contour, the circular jet geometry is included for reference (solid black line, $\boldsymbol{Djet}$ = 0.875 in (22.23 mm)). $\mathbf{Re}\boldsymbol{jet}$ = 1.06 × 10^4 46

Figure 2-26. Error [m s^{-1}] between different velocity correction methods. The circular jet geometry is included for reference (solid black line, $\boldsymbol{Djet}$ = 0.875 in (22.23 mm)). $\mathbf{Re}\boldsymbol{jet}$ = 1.06 × 10^4..... 47

Figure 2-27. Triple-jet velocity magnitude for $\boldsymbol{R}$ = ½; $\boldsymbol{\Delta T}$ = 60 °C (a) Velocity magnitude using simultaneous temperature correction (b) Velocity magnitude using collocated temperature correction. 48

Figure 2-28. Contours at $\boldsymbol{x}/\boldsymbol{Djet}$ = 0.09. (a) Simultaneously corrected velocity magnitude (m s^{-1}), (b) turbulent kinetic energy (m^2 s^{-2}), and (c) percent turbulence intensity. For each contour, the circular jet geometry is included for reference (solid black line, $\boldsymbol{Djet}$ = 22.23 mm). $\mathbf{Re}\boldsymbol{jet}$ = 1.06x10^4.. 50

Figure 2-29. Surface plots of single jet contours. (a) Turbulent kinetic energy [m^2 s^{-2}] (b) Percent turbulent intensity..... 50

Figure 2-30. Schematic of line traces used to analyze single jet 52

Figure 2-31. Normalized velocity contours "folded" on each other with curve over 90% $\boldsymbol{Djet}$ for $\boldsymbol{x}/\boldsymbol{Djet}$ = 0.09 for $\mathbf{Re}\boldsymbol{jet}$ = 10.6 × 10^3, $\boldsymbol{U0}$ = 13.78 m s^{-1} 52

Figure 2-32. Temperature contours "folded" on each other with curve over 90% $\boldsymbol{Djet}$ for $\boldsymbol{x}/\boldsymbol{Djet}$ = 0.09 for $\mathbf{Re}\boldsymbol{jet}$ = 10.6 × 10^3, $\boldsymbol{U0}$ = 13.78 m s^{-1} 55

Figure 2-33. Case H1: $\boldsymbol{R}$ = ½, $\boldsymbol{\Delta T}$ = 44.4 °C, $\boldsymbol{S}/\boldsymbol{Djet}$ = 1.41 measured at $\boldsymbol{x}/\boldsymbol{Djet}$ = 0.09 (a) profiles of velocity magnitude [m s^{-1}], and (b) temperature profiles [°C]..... 60

Figure 2-34. Case H4: $\boldsymbol{R}$ = ½, $\boldsymbol{\Delta T}$ = 44.4 °C, $\boldsymbol{S/Djet}$ = 3 measured at $\boldsymbol{x/Djet}$ = 0.09 (a) profiles of velocity magnitude [m s^{-1}], and (b) temperature profiles [°C]..... 61

Figure 2-35. Case H5: $\boldsymbol{R}$ = ½, $\boldsymbol{\Delta T}$ = 11.1 °C, $\boldsymbol{S/Djet}$ = 3 measured at $\boldsymbol{x/Djet}$ = 0.09 (a) profiles of velocity magnitude [m s^{-1}], and (b) temperature profiles [°C]..... 62

Figure 2-36. Difference in temporally congruent and spatially congruent velocity correction methods [m s^{-1}]..... 63

Figure 2-37. Velocity contours [m s^{-1}] for $\boldsymbol{R}$ = ½, $\boldsymbol{\Delta T}$ = 44.4 °C, $\boldsymbol{S/Djet}$ = 1.41 (a) measured at $\boldsymbol{x/Djet}$ = 0.09, (b) measured at $\boldsymbol{x/Djet}$ = 5.09, and (c) measured at $\boldsymbol{x/Djet}$ = 10.09 65

Figure 2-38. Temperature contours [°C] for $\boldsymbol{R}$ = ½, $\boldsymbol{\Delta T}$ = 44.4°C, $\boldsymbol{S/Djet}$ = 1.41 (a) measured at $\boldsymbol{x/Djet}$ = 0.09, (b) measured at $\boldsymbol{x/Djet}$ = 5.09, and (c) measured at $\boldsymbol{x/Djet}$ = 10.09 66

Figure 2-39. Traces for triple-jet study and the averaging applied – □ inner horizontal averages, x outer horizontal averages, o vertical averages, □ inner diagonal averages, x outer diagonal traces. Black circle represents jet. 67

Figure 2-40. Symmetrically averaged inlet profiles the Case H1 measured at $\boldsymbol{x/Djet}$ =0.09. (a) averaged traces for both hot jets; (b) averaged traces for cold jet..... 68

Figure 2-41. Symmetrically averaged inlet profiles the Case H4 measured at $\boldsymbol{x/Djet}$ = 0.09. (a) averaged traces for both hot jets; (b) averaged traces for cold jet..... 69

Figure 2-42. Symmetrically averaged inlet profiles the Case H5 measured at $\boldsymbol{x/Djet}$ = 0.09. (a) averaged traces for both hot jets; (b) averaged traces for cold jet..... 70

Figure 2-43. Effects of temperature on the non-dimensional triple-jet velocity profile for different downstream distances (a) measured at $\boldsymbol{x/Djet}$ = 0.09; (b) measured at $\boldsymbol{x/Djet}$ = 0.59; (c) measured at $\boldsymbol{x/Djet}$ = 1.09; (d) measured at $\boldsymbol{x/Djet}$ = 4.09; (e) measured at $\boldsymbol{x/Djet}$ = 6.09..... 73

Figure 2-44. Effect of temperature difference on the non-dimensional triple-jet temperature profiles at different downstream distances (a) measured at $\boldsymbol{x/Djet}$ = 0.09; (b) measured at $\boldsymbol{x/Djet}$ = 0.59; (c) measured at $\boldsymbol{x/Djet}$ = 1.09; (d) measured at $\boldsymbol{x/Djet}$ = 4.09; (e) measured at $\boldsymbol{x/Djet}$ = 6.09..... 74

Figure 2-45. Differences related to velocity ratio for triple-jet velocity profiles at different downstream distances (a) measured at $\boldsymbol{x/Djet}$ = 0.09; (b) measured at $\boldsymbol{x/Djet}$ = 0.59; (c) measured at $\boldsymbol{x/Djet}$ = 1.09; (d) measured at $\boldsymbol{x/Djet}$ = 4.09; (e) measured at $\boldsymbol{x/Djet}$ = 6.09 75

Figure 2-46. Isometric view of triple jet near solid parallel wall 77

Figure 2-47. Top view of triple jet test section with confining wall 78

Figure 2-48. Front view of test section and IR viewports 79

Figure 2-49. Contours of triple jet-induced temperature fields across parallel wall. Approximate size of each image is 13.4 cm x 17.1 cm 82

Figure 2-50. (a) Case 1, Port 1 temperature field with imposed line traces (b) Case 1, Port 1 polycarbonate plate surface temperatures 83

Figure 2-51. Temperature line profiles for (a) Case 1, (b) Case 2, and (c) Case 3 84

Figure 2-52. Peak temperature location for each line trace shown in Figure 2-51. 85

Figure 2-53. Unit cell test section (a) isometric view, (b) top view, (c) front view, and (d) side view 87

Figure 2-54. Top view of unit cell test section depicting (a) inline cylinder array and (b) staggered post array. Cross flow is in $+\boldsymbol{x}$-direction and jets are flowing in the $+\boldsymbol{z}$-direction (into page). 88

Figure 2-55. Basic PIV arrangement utilized for experimental testing 90

Figure 2-56. Example of image subtraction feature using the case 2 post G optical configuration (a) raw image and (b) after image subtraction filter 93

Figure 2-57. Visualization of non-isothermal jet configuration for each of the proposed test cases. Note: coordinate system in (a) is consistent for each figure, jet flows are into the page ($+\boldsymbol{z}$-direction), and cross flow is in $+\boldsymbol{x}$ direction 95

Figure 2-58. Three jet manifold configuration for jet inlet testing 97

Figure 2-59. Convergence of case 1 jet 6 inlet velocity statistics (a) mean velocities, (b) standard deviation of velocities, (c) second order moments, and (d) third order moments 98

Figure 2-60. Case 1 'hot' manifold (a) velocity contour and (b) inlet velocity profile and case 2 'hot' manifold (c) velocity contour and (d) inlet velocity profile 99

Figure 2-61. Convergence of case 1 cross flow velocity statistics (a) mean velocities (b) standard deviation of velocities (c) second order moments and (d) third order moments 101

Figure 2-62. Cross flow inlet velocity trace for each case 102

Figure 2-63. Areas of interest for the (a) staggered and (b) in-line post configurations 106

Figure 2-64. Contours of ensemble averaged and standard deviation of velocity components for (a-d) case 1, (e-h) case 2, and (i-l) case 3 109

Figure 2-65. Case 1 mean velocity components along $\boldsymbol{x/Lts}$ = -0.03 109

Figure 2-66. Case 1 Reynolds stress components along $\boldsymbol{x/Lts}$ = -0.03 110

Figure 2-67. Case 2 mean velocity components along $\boldsymbol{x/Lts}$ = -0.0 111

Figure 2-68. Case 2 Reynolds stresses along $\boldsymbol{x/Lts}$ = -0.0 112

Figure 2-69. Case 3 mean velocity components along $\boldsymbol{x/Lts}$ = -0.03 113

Figure 2-70. Case 3 Reynolds stress components along $\boldsymbol{x/Lts}$ = -0.03 114

Figure 3-1. CFD Model of the lower plenum geometry 118

Figure 3-2. Snapshot of the mesh at the top surface using ParaView 118

Figure 3-3. (a) The simulated temperature at the surface of the lower plenum; and (b) at locations A, B and C (from left to right) 123

Figure 3-4. Simulated helium temperatures at the different cross-sections where measurements are of interest in the non-isothermal prototype model 124

Figure 3-5. Simulated veloctity magnitudes at the different cross-sections where measurements are of interest in the non-isothermal prototype model 125

Figure 3-6. Schematic of the RANS simulation domain mimicking HCG experiments [50] 127

Figure 3-7. Centerline velocity for RANS models of turbulent jet 130

Figure 3-8. Velocity profiles at X=70*D* for different enclosure sizes 131

Figure 3-9. Comparison of the size of the LES simulation domain ($\boldsymbol{R}$ = 55$\boldsymbol{D}$/2) and HCG experimental domain ($\boldsymbol{R}$ = 96$\boldsymbol{D}$). The wedge geometry shown for the experimental domain is the axisymmetric domain (b) Views of the mesh near the inlet and at the side walls for the LES model 133

Figure 3-10. Mesh spacing in radial and axial direction. The grid is symmetric with respect to the jet axis 135

Figure 3-11. (a) Comparison of mean centerline time averaged velocities for different LES models ($|\boldsymbol{UC}|$ - centerline velocity magnitude; $\boldsymbol{Uinlet}$ – average velocity at inlet); (b) The effect of inlet fluctuations on the simulated potential core length 136

Figure 3-12. Computational model of the double upstream contraction used in the experiments of HCG 138

Figure 3-13. Contours of vorticity magnitude near the nozzle exit at different time instances 139

Figure 3-14. Contours of vorticity magnitude at the nozzle exit for the LES domain at different time instances 141

Figure 3-15. Effect of time-averaging on (a) the centerline velocity magnitude ($|\boldsymbol{UC}|$) and (b) inverse centerline velocity for the LES simulation. Data in the initial 3.5 × 10^2 residence times is not considered in the time-averaging. 142

Figure 3-16. Comparison of axial stress profiles at $\boldsymbol{x}$ = 70$\boldsymbol{D}$ for different time average interval (a) without azimuthal averaging and (b) with azimuthal averaging. (FHW: flying hot wire measurements; LDA: laser Doppler anemometer measurements) 143

Figure 3-17. Comparison of axial component of turbulent kinetic energy at $\boldsymbol{x}$ = 70$\boldsymbol{D}$ 144

Figure 3-18. Comparison of radial component of turbulent kinetic energy at $\boldsymbol{x}$ = 70$\boldsymbol{D}$ 145

Figure 3-19. Comparison of azimuthal component of turbulent kinetic energy at $\boldsymbol{x}$ = 70$\boldsymbol{D}$ 146

Figure 3-20. Comparison of turbulence shear stress at $\boldsymbol{x}$ = 70$\boldsymbol{D}$ 146

Figure 3-21. Normalized axial velocity profiles at different axial locations 147

Figure 3-22. Normalized axial stress profiles at different axial locations 147

Figure 3-23. Comparison of axial flux of $\boldsymbol{uu}$ 149

Figure 3-24. Comparison of axial flux of $\boldsymbol{uv}$ 149

Figure 3-25. Comparison of axial flux of $\boldsymbol{ww}$ 150

Figure 3-26. Comparison of radial flux of $\boldsymbol{uv}$ 151

Figure 3-27. Comparison of radial flux of $\boldsymbol{vv}$ 151

Figure 3-28. Comparison of radial flux of $\boldsymbol{ww}$ 152

Figure 3-29. Turbulent kinetic energy budget in self-similar region, quantities are normalized by $\boldsymbol{Uc3}$. Grey lines corresponding to LES data of B&B 153

Figure 3-30. Balance of $\boldsymbol{uu}$ in self-similar region, quantities are normalized by $\boldsymbol{Uc3}$. Grey lines corresponding to LES data of B&B 154

Figure 3-31. Balance of $\boldsymbol{vv}$ in self-similar region, quantities are normalized by $\boldsymbol{Uc3}$. Grey lines corresponding to LES data of B&B 155

Figure 3-32. Balance of $\boldsymbol{ww}$ in self-similar region, quantities are normalized by $\boldsymbol{Uc3}$. Grey lines corresponding to LES data of B&B 155

Figure 3-33. Balance of $\boldsymbol{uv}$ in self-similar region, quantities are normalized by $\boldsymbol{Uc3}$. Grey lines corresponding to LES data of B&B 157

Figure 3-34. Comparison of mean convection (advection) and production of turbulent kinetic energy budget in self-similar region, quantities are normalized by $\boldsymbol{Uc3}$ 158

Figure 3-35. Comparison of turbulence diffusion and pressure diffusion of turbulent kinetic energy budget in self-similar region, quantities are normalized by $\boldsymbol{Uc3}$ 159

Figure 3-36. Mesh spacing in radial and axial direction. The grid is symmetric in respect to the jet axis163

Figure 3-37. Computational model of the upstream contraction used in the experiments of Mi et al. [47] 164

Figure 3-38. Centerline normalized inverse temperature 165

Figure 3-39. Streamwise versions of the normalized temperature mean 166

Figure 3-40. Streamwise versions of scalar half-radius 167

Figure 3-41. Radial profile of normalized mean temperature at several locations 167

Figure 3-42. Streamwise variation of the temperature RMS along the jet centerline 168

Figure 3-43. Streamwise variation of the temperature RMS over centerline along the jet centerline 169

Figure 3-44. Radial profiles of the normalized temperature RMS over centerline 170

Figure 3-45. (a) The computational domain; and (b) Mesh near the surface of the cylinder 172

Figure 3-46. Contours of vorticity magnitude at different time instances during a single vortex shedding cycle 173

Figure 3-47. Comparison of mean stream-wise velocity in the wake centerline for isothermal flow over a circular cylinder at **Re** = 3900. $\boldsymbol{x}$ = D/2 is the surface of the cylinder. 175

Figure 3-48. Comparison of mean stream-wise velocity at different locations in the wake of a circular cylinder at Re = 3900 175

Figure 3-49. Mean transverse velocity at different locations in the wake of a circular cylinder at **Re** = 3900 177

Figure 3-50. Stream-wise velocity fluctuations at different locations in the wake of a circular cylinder at **Re** = 3900 178

Figure 3-51. Transverse velocity fluctuations at different locations in the wake of a circular cylinder at **Re** = 3900 179

Figure 3-52. Contours of instantaneous vorticity magnitude in the near-wake for different Reynolds numbers 181

Figure 3-53. Contours of instantaneous temperature in the near-wake for different Reynolds numbers . 181

Figure 3-54. Time-averaged and RMS Nusselt number distributions around a circular cylinder for Reynolds number of 3000, 5900, and 7400. 183

Figure 3-55. Time-histories of the instantaneous RMS Nusselt number for **Re** = 5900. 184

Figure 3-56. Computational unit cell domain for LES studying of lower plenum of the VHTR a) unit cells A and C, and b) unit cell B 186

Figure 3-57. Jets and posts identification and jet temperature specifications for each case 187

Figure 3-58. Unit cell mesh configuration 189

Figure 3-59. Jet penetration for each case..... 192

Figure 3-60. Flattened time-averaged temperature distribution on posts for case A. The vertical axis for all plots is the z-direction with z = 0 (jet inlets) at the top. 193

Figure 3-61. The time-averaged temperature of posts for different height locations - case A 195

Figure 3-62. The time-averaged square of temperature fluctuations of posts for different height locations - case A..... 195

Figure 3-63. Stream tracer of jet NW for case A 197

Figure 3-64. Stream tracer of jet SW and S for case A (the colorbar in Figure 3-63 also applied here). 197

Figure 3-65. Flattened posts temperature distributions for case B. The vertical axis for all plots is the z-direction with z = 0 (jet inlets) at the top. 199

Figure 3-66. The time-averaged temperature of posts for different height locations - case B..... 200

Figure 3-67. The time-averaged square of temperature fluctuations of posts for different height locations - case B 200

Figure 3-68. Flattened posts temperature distributions for case C. The vertical axis for all plots is the z-direction with z = 0 (jet inlets) at the top. 202

Figure 3-69. The time-averaged temperature of posts for different height locations - case C..... 204

Figure 3-70. The time-averaged square of temperature fluctuations of posts for different height locations - Case C 204

Figure 3-71. The time-averaged velocities (m/s) near posts at different heights for case A: crossflow direction (top row) and transverse direction (bottom row) 206

Figure 3-72. The time-averaged velocities (m/s) near posts at different heights for case B: crossflow direction (top row) and transverse direction (bottom row) 207

Figure 3-73. Time-averaged crossflow direction of velocity (m/s) at *L/2* for case B. 208

Figure 3-74. Time-averaged crossflow direction of velocity (m/s) at *L/2* for case B without Jets. 208

Figure 3-75. Time averaged crossflow direction of velocity (m/s) at *L/2* for case A. 208

Figure 3-76. Time-averaged crossflow direction of velocity (m/s) at *L/2* for case A without Jets..... 209

Figure 3-77. Time-averaged velocities (m/s) near posts at different heights for case C: crossflow direction (top row) and transverse direction (bottom row) 209

Figure 3-78. Time-averaged crossflow direction of velocity (m/s) at *L/2* for case C. 210

Figure 3-79. Time-averaged crossflow direction of velocity (m/s) at *L/2* for case C without Jets..... 210

Figure 3-80. Schematic representation of flow recirculation in case C (background contour is instantaneous temperature). 211

Figure 3-81. Unit cell I showing the three line traces of interest for further analysis. Dimensions shown in the figure are meters. The z direction is into the page. 214

Figure 3-82. Velocities (m/s) along line G at z/H = 0.50 for unit cell I. Unit for y is meters. For reference, the crossflow velocity is 12.53 m/s. 215

Figure 3-83. Velocities (m/s) along line G at z/H = 0.75 for unit cell I. Unit for y is meters. For reference, the crossflow velocity is 12.53 m/s. 216

Figure 3-84. Reynold stresses (m^2/s^2) along line G at z/H = 0.50 for unit cell I. Unit for y is meters. For reference, the crossflow velocity is 12.53 m/s. 217

Figure 3-85. Reynold stresses (m^2/s^2) along line G at z/H = 0.75 for unit cell I. Unit for y is meters. For reference, the crossflow velocity is 12.53 m/s. 218

Figure 3-86. Velocities (m/s) along line Ein at z/H = 0.50 for unit cell I. Unit for y is meters. For reference, the crossflow velocity is 12.53 m/s. 219

Figure 3-87. Reynold stresses (m^2/s^2) along line Ein at z/H = 0.50 for unit cell I. Unit for y is meters. For reference, the crossflow velocity is 12.53 m/s 220

Figure 3-88. Velocities (m/s) along line Eout at z/H = 0.50 for unit cell I. Unit for y is meters. For reference, the crossflow velocity is 12.53 m/s. 221

Figure 3-89. Reynold stresses (m^2/s^2) along line Eout at z/H = 0.50 for unit cell I. Unit for y is meters. For reference, the crossflow velocity is 12.53 m/s. 222

Figure 3-90. Unit cell II showing the two line traces of interest for further analysis. Dimensions shown in the figure are meters. The z direction is into the page. 223

Figure 3-91. Velocities (m/s) along line G at z/H = 0.50 for unit cell II. Unit for y is meters. For reference, the crossflow velocity is 14.72 m/s. 224

Figure 3-92. Reynold stresses (m^2/s^2) along line G at z/H = 0.50 for unit cell II. Unit for y is meters. For reference, the crossflow velocity is 14.72 m/s. 225

Figure 3-93. Velocities (m/s) along line E at z/H = 0.50 for unit cell II. Unit for y is meters. For reference, the crossflow velocity is 14.72 m/s. 226

Figure 3-94. Velocities (m/s) along line E at z/H = 0.75 for unit cell II. Unit for y is meters. For reference, the crossflow velocity is 14.72 m/s. 227

Figure 3-95. Reynold stresses (m^2/s^2) along line E at z/H = 0.50 for unit cell II. Unit for y is meters. For reference, the crossflow velocity is 14.72 m/s. 228

Figure 3-96. Reynold stresses (m^2/s^2) along line E at z/H = 0.75 for unit cell II. Unit for y is meters. For reference, the crossflow velocity is 14.72 m/s. 229

Figure 3-97. Unit cell III showing the three line traces of interest for further analysis. Dimensions shown in the figure are meters. The z direction is into the page. 230

Figure 3-98. Velocities (m/s) along line G at z/H = 0.50 for unit cell III. Unit for y is meters. For reference, the crossflow velocity is 7.68 m/s. 231

Figure 3-99. Velocities (m/s) along line G at z/H = 0.75 for unit cell III. Unit for y is meters. For reference, the crossflow velocity is 7.68 m/s. 232

Figure 3-100. Reynold stresses (m^2/s^2) along line G at z/H = 0.50 for unit cell III. Unit for y is meters. For reference, the crossflow velocity is 7.68 m/s. 233

Figure 3-101. Reynold stresses (m^2/s^2) along line G at z/H = 0.75 for unit cell III. Unit for y is meters. For reference, the crossflow velocity is 7.68 m/s. 234

Figure 3-102. Velocities (m/s) along line Eout at z/H = 0.50 for unit cell III. Unit for y is meters. For reference, the crossflow velocity is 7.68 m/s. 235

Figure 3-103. Velocities (m/s) along line Eout at z/H = 0.75 for unit cell III. Unit for y is meters. For reference, the crossflow velocity is 7.68 m/s. 236

Figure 3-104. Reynold stresses (m^2/s^2) along line Eout at z/H = 0.50 for unit cell III. Unit for y is meters. For reference, the crossflow velocity is 7.68 m/s. 237

Figure 3-105. Reynold stresses (m^2/s^2) along line Eout at z/H = 0.75 for unit cell III. Unit for y is meters. For reference, the crossflow velocity is 7.68 m/s. 238

Figure 4-1: Schematic of flow around a circular cylinder 244

Figure 4-2: Boundary designations for POD test case 244

Figure 4-3: Schematic of LES computational domain 246

Figure 4-4: $\boldsymbol{x}$-component of the first POD mode obtained from URANS 247

Figure 4-5: $\boldsymbol{x}$-component of the second POD mode obtained from URANS 247

Figure 4-6: $\boldsymbol{x}$-component of the first POD mode obtained from LES 248

Figure 4-7: $\boldsymbol{x}$-component of the second POD mode obtained from LES 248

Figure 4-8: Comparison between the first modal coefficient results of the Galerkin projection approach (LHS figure) and the linear interpolation (regression-based approach) (RHS figure) 249

Figure 4-9: Comparison between the second modal coefficient results of the Galerkin projection approach (LHS figure) and the linear interpolation (regression-based approach) (RHS figure) 250

Figure 4-10: Variation of first two model coefficients of the ROM constructed from LES data 250

Figure 4-11: (a) $\boldsymbol{x}$-component of the first velocity POD mode; (b) $\boldsymbol{y}$-component of the first velocity POD mode; (c) $\boldsymbol{x}$-component of the second velocity POD mode; (d) $\boldsymbol{y}$-component of the second velocity POD mode 255

Figure 4-12: Convergence of the cumulative energy of velocity modes vs. mode number 256

Figure 4-13: Convergence of the cumulative energy of modes vs. mode number 257

List of Tables

Table 2-1. Pipe Lengths and diameters in flow skid 14

Table 2-2. Expansion and contraction ratios 14

Table 2-3. Assumed values and uncertainties 18

Table 2-4. Velocity and temperature calibration experiments 54

Table 2-5. Matrix of cases mapped in horizontal plane 56

Table 2-6. Matrix of cases mapped in vertical plane through jet centerline 57

Table 2-7. Errors in experimental inlet conditions for vertical plane mapping 58

Table 2-8. Errors in experimental inlet conditions for vertical plane mapping 59

Table 2-9. Estimated bulk temperature of flow into test section for each case 72

Table 2-10. Experimental triple jet configurations for parallel plate experiments 78

Table 2-11. Unit cell test section dimensions 89

Table 2-12. High speed camera scale factor calibrations. 91

Table 2-13. PIV recording parameters. 91

Table 2-14. Vector field processing parameters 92

Table 2-15. Experimental test cases for unit cell studies 94

Table 2-16. Repeatability assessment for case with highest absolute jet inlet temperatures (case I) 96

Table 2-18. Cross flow inlet average velocities and uniformity 103

Table 2-19. Outer posts mean temperature measurements for unit cell test cases 104

Table 2-20. Case 1 center post mean temperatures as a function of rotational position 105

Table 2-21. Case 2 center post mean temperatures as a function of rotational position 105

Table 2-22. Case 3 center post mean temperatures as a function of rotational position 106

Table 3-1. Distribution of inlet pipe diameters 119

Table 3-2. The flow condition at the inlets 119

Table 3-3. Reynolds number of flow at the inlets 120

Table 3-4. The boundary conditions for the simulation domain. P refers to the pressure in Pa scaled by density in kg/m^3 128

Table 3-5. Effect of simulation time on turbulent intensity at the nozzle exit 139

Table 3-6. Effect of grid points in span-wise direction ($\boldsymbol{Nz}$) and span-wise length ($\boldsymbol{Lz}$) on simulated Strouhal number ($\mathbf{St}$) and average drag coefficient ($\boldsymbol{CD}$) using LES [58] 171

Table 3-7. Minimum and maximum $\boldsymbol{y}+$ near the cylinder wall during a single vortex shedding cycle. 174

Table 3-8. Jets and Crossflow velocity and temperature specification for each case 188

Table 4-1: POD Modes and Corresponding Eigenvalues Obtained from URANS 249

Table 4-2: POD Modes and Corresponding Eigenvalues Obtained from LES 249

Table 4-3: Prediction of velocity fields using ROM constructed from URANS data 251

Table 4-4: Prediction of velocity fields using ROM constructed from LES data 251

Table 4-5: Eigenvalues corresponding to each of the first five velocity POD modes 255

Table 4-6: Eigenvalues corresponding to each of the first five velocity POD modes 256

Table 4-7: Prediction of new velocity fields based on a regression-based approach for velocity POD modes (M.C. stands for modal coefficient) 258

Table 4-8: Prediction of all dynamical variables based on a regression-based approach (M.C. stands for modal coefficient) 258

1 Background and Motivation

The Very High Temperature Reactor (VHTR) is a next generation nuclear reactor, one of the six concepts originally proposed by the Generation IV International Forum (GIF). Of the handful of advanced reactor designs, the VHTR is likely the closest to realization, and will enable high-efficiency production of electricity and/or hydrogen, as well as process heat. Critical for mission success is the need to address several performance and safety issues related to the thermal hydraulics of the VHTR, identified in a comprehensive report published in 2002 [1]. To overcome each of these roadblocks, the report recommends establishing experimentally validated, computationally tractable CFD models that are able to capture all the relevant physics. In the VHTR, helium is employed as the coolant, and could subsequently be used for high-efficiency production of either electricity or hydrogen. The Helium travels vertically downward through the core picking up heat from the core and then enters the lower plenum much like an array of jets. Due to the non-uniform heat generation in the core, the temperature of these jets directed into the lower plenum can vary significantly. In the current designs for the VHTR lower plenum 272 jets issue into a hexagonal array of 196 posts. In this design, there are 68, 72, and 132 jets with diameters of 83.8 mm, 16.8 mm jets, 144.8 mm. respectively. These jets can vary in both inlet temperature and mass flow rate. The temperatures can vary from 1050 K to 1370 K with velocities ranging from 12 m/s to 150 m/s [2]. Analysis by Rodriguez and El-Genk [3], as well as Bayless [4], suggest temperature differences between two jets in close proximity can be on the order of 300°C, with velocity differences of 50-100 m/s. Once in the lower plenum, the flow of these jets changes directions by 90° and traverses across complex geometric features, including an array of cylindrical support posts. Before the flow becomes fully mixed the temperatures in the flow are fluctuating and can cause hot streaks. If these temperature fluctuations are transmitted to the solid supporting structure nearby, concerns exist regarding structural failure due to thermal fatigue. This phenomenon is known as thermal striping, and represents a significant challenge for the next generation gas cooled nuclear reactors, not just the VHTR. In order to achieve approval for any new reactor design, thermal hydraulic analysis must be performed of the reactor under normal and accident scenarios. Modeling

tools used for this purpose (e.g., TRACE, RELAP) have been vetted by the Nuclear Regulatory Commission (NRC) through rigorous verification and validation (V&V) procedures. Therefore, a certain level of trust is tied to the analysis results themselves. However, this same amount of trust cannot be applied for next generation reactors, whose operating conditions in many cases are outside of the vetted bounds for today's prevalent reactor types. In addition, the fully vetted tools are systems level codes with lower spatial and temporal thermal-hydraulic modeling capabilities, and cannot account for localized phenomena such as thermal striping. Therefore, a significant need exists for a more fundamental understanding of this complicated lower plenum flow, one where modeling tools have also been experimentally validated for turbulent mixing of isothermal and non-isothermal flows. In order to made steps toward this end goal, this project focused providing significant advances on understanding and predicting the flow physics for turbulent mixing. Advances are made from (i) experimental, (ii) computational, and (iii) reduced order modeling (ROM) perspectives. For experiments, high quality data is provided which is pertinent to gas cooled reactors, and can serve a valuable purpose in future validation efforts. The computational work addresses modeling requirements for fundamental and applied flow conditions, and the ROM efforts quantifies the potential of reducing computational cost while maintaining an adequate level of accuracy in capturing the desired physics. The next three sections of this report focus on the experimental, computational, and ROM-based efforts.

2 Experimental Studies

The experimental facilities built as part of this project accommodate round triple jet studies and a scaled portion of the VHTR lower plenum. The same flow motivation skid is used for both of these experiments and is discussed along with the facility design in Section 2.2. This is preceded by a literature review describing the research that lead up to the current work. The remainder of Section 2 includes the experimental results and uncertainty analysis.

2.1 Background and Literature Review

2.1.1 Thermal Striping and Triple Jet Studies

Thermal striping is the process by which temperature fluctuations due to mixing of different temperature fluid flows are transported through the fluid boundary layers at the wall and then into the support structure. It has been observed that, with time, this can cause thermal fatigue. The Sodium Fast-Breeding reactor PHENIX (France) experienced cracking from thermal striping in a mixing tee due to stratified flow from injection [5].

The concept of thermal striping has been explored previously by several authors, however always in specific geometric configurations, with a limited number of operational parameters. Perhaps the most extensively studied flow configuration is stratified flow, specifically in regard to internal pipe flow with a tee branch. A 1993 study by Kim et al [6] investigated thermal stratification, turbulence penetration, and thermal striping where hot flow passed through a mixing tee. The branch of the tee was stagnant and at a lower temperature. Their primary interest was determining the conditions where thermal striping was observed in the stagnant branch. Using two thin film anemometers and dye injection, flow patterns were categorized in the branch piping. Additional attention was given to determining the effects of swirl in the bypass flow. It was found that the turbulence penetration length was independent of the main line velocity. Leakage of the cold-branch line into the main line was found to be minimal under most conditions.

Similar research was carried out by Kimura et al. [7] in 2005. Cold fluid was injected perpendicularly into a heated cross flow. The intent was to determine the effects of having an upstream

elbow in the cross flow, and to better understand turbulent temperature mixing upstream of the injection. The velocity field was visualized using Particle Image Velocimetry (PIV), while the downstream temperature was measured using a movable thermocouple tree. Three different branch flows were classified and investigated based on momentum ratio, corresponding to an impinging branch jet, deflecting jet, and wall jet. Temperature fluctuation and fluctuation intensity were measured for each case. It was found that the elbow significantly increased the temperature fluctuation intensity for all scenarios. Special consideration was given to the wall jet case, where a large fluctuation was witnessed due to the effects of an upstream elbow.

In a 2009 experiment by Kamide et al. [8], the work of Kimura et al. [7] was expanded to include comparisons to numerical results. Experiments were conducted without an upstream elbow and compared to a finite difference thermal hydraulic code. Flow visualization of the wall jet case revealed strong eddy formation just downstream of the branch pipe opening, but not for the case of the deflecting or impinging jets. These eddies had large temperature fluctuations in them, believed to contribute strongly to thermal mixing behavior. Moreover, for the wall jet, a prominent temperature fluctuation frequency was found at a Strouhal number of approximately 0.2. This is similar to Karmen Vortex generation from flow past a cylinder, where a Strouhal number of 0.2 is expected across a wide range of Reynolds numbers. For the conditions in Kamide et al. [8], a Strouhal number of 0.2 corresponds to a prominent frequency of approximately 6 Hz. A prominent temperature fluctuation frequency was not found for the impinging and wall jets.

A Detached Eddy Simulation (DES) code, a hybrid of Reynolds Averaged Navier Stokes (RANS) and Large Eddy Simulation (LES) codes, was used by Nakamura et al. [9] to further investigate thermal striping in a mixing tee. Numerical results of the DES were compared to the WALTON experimental data from the Japan Nuclear Cycle Development Institute (JNCDI). Similar to previous studies by Kimura et al. [7] and Kamide et al. [8], cold water was injected in the branch of the mixing tee. The DES code accurately predicted distributions of temperature fluctuation for both the impinging and deflecting jet. However, the maximum fluctuation intensity in the wall jet case was underestimated by the code. Finally, frequency

distributions of temperature near the pipe walls were in good agreement between the experiment and the DES.

A parallel triple-jet is somewhat of a canonical flow in thermal mixing. A parallel triple-jet, much as the name implies, consists of three jets, whose axes lay in a common plane, an illustration of which is shown in Figure 2-1. Triple-jet investigations have included both round jets and slot jets, normally with the two outer jets sharing a common flow condition, while the center jet is varied. There are numerous variables that can be studied including the velocity ratio between the center jet and the isovelocity outer jets, the temperature difference between the cold center jet and the hot outer jets, and geometric properties of the three-jet array (e.g., spacing between jets). Of particular interest is the manner in which temperature fluctuations in the flow field occur and how they are attenuated within the flow field.

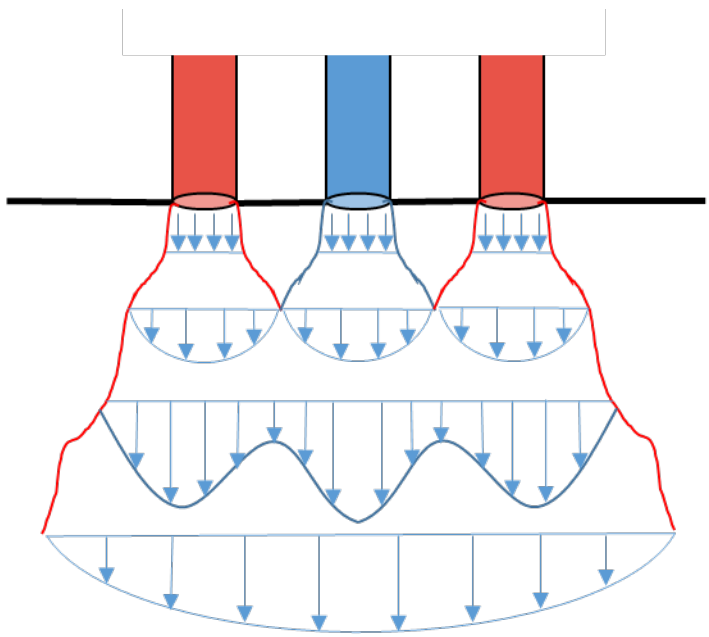

Figure 2-1: Illustration of a round parallel triple-jet showing the mixing and development downstream

Tokuhiro and Kimura [10] investigated the thermal striping phenomenon in vertical parallel triple slot jets, producing a quasi-two dimensional flow. For the experiment, a non-buoyant, cold jet, was situated between two buoyant hot jets. Velocity ratios between the hot and cold jets were varied, as well as temperature differences between the jets. Velocity was measured using ultrasound Doppler velocimetry,

while temperature data was collected using a movable thermocouple tree. Additionally, dye injection was used to visualize the flow fields. Data for the non-isothermal triple-jet was compared to data for a single jet. For the triple-jet, local maximums of the velocity field were observed close to the center of each jet. These distinct peaks decayed along the axial distance, as the fluid approached a well-mixed condition. However, the flow was not symmetric about the center jet, possibly due to measurement error. The velocity fluctuation intensity was calculated along the axial direction for the center of the cold jet. Compared to the single jet, the non-dimensional fluctuation intensity is approximately three times larger for the triple-jet until 9 diameters downstream, denoted as $x/D_{jet} = 9$. Temperature data was collected for the spanwise and axial directions, for both the isovelocity and non-isovelocity conditions. For axial locations near to the jet exit, sharp temperature gradients were observed near the interface of the hot and cold jets. The gradients decreased as axial distance increased, since the fluid temperature was approaching a mixed temperature everywhere in the flow. Additionally, at the interface of the jets, large temperature fluctuations were measured. Moreover, the temperature fluctuation intensity was larger for the isovelocity case than the non-isovelocity case. Axially, the largest temperature fluctuation intensities coincided with the center of the cold jet, at approximately 5 diameters downstream.

Continuing this work using the same experimental setup, Kimura et al. [11] investigated frequency content of the temperature profile for use in turbulence models. The data collected was compared to numerical models based on unsteady Reynolds averaged Navier-Stokes (uRANS), low Reynolds number turbulence stress and heat flux model (LRSFM), and quasi-direct numerical simulation (DNS). The DNS accurately predicted temperature profiles and fluctuation intensities everywhere in the flow, while the LRSFM and uRANS models normally underestimated the fluctuation intensity in the flow, as well as overestimated temperature at some locations. When estimating temperature fluctuations in the flow, only the DNS model accurately predicted the frequency content of the fluid. This work was further expanded by Kimura et al. [12], in 2007. While this body of work was well conducted, the range of the experiments is very limited. For the water experiments, the largest velocity ratio studied between the cold jet and the hot jet was only 1 (i.e., the hot jet was always at a higher velocity). Similarly, the maximum temperature

difference between the hot and cold jet studied was only 40°C. For the VHTR lower plenum, this can be as high as 300°C [3,4].

A 2007 study by Choi and Kim [13] further evaluated turbulence models for thermal striping in a triple-jet. A two-layer model, a shear stress transport model, and an elliptic relaxation model for turbulence were compared to experimental data. From the test, the elliptic relaxation model was the only model capable of predicting the oscillatory behavior of the jets, as well as the time averaged temperature and temperature fluctuation intensity. However, all three models predicted slower downstream mixing than was experimentally measured. It is worth nothing, a Power Spectral Density (PSD) of the temperature time history showed prominent frequencies around 22 Hz and 60 Hz in the planar triple-jet experiment.

Many of the high quality studies mentioned focus on slot jet geometries. For the VHTR lower plenum, round jet studies are more applicable. When reviewing literature for arrays of round jets, three predominant works were found which most closely pertain to the body of work contained in this report. Two sets of analytical work [14,15] attempted to quantify the mixing behavior of twin round jets. Knystautas [14] studied closely spaced circular jets (S/D_{jet} = 1.5, Re_{jet} = 44,000) to determine if sufficiently far downstream the flow field could be treated as two-dimensional. However, detailed measurement of the jet inlet profiles or discussion of flow conditioning was not given. Additionally, no investigation is given into the effects of various flow variables on the flow field observed [14]. Pani and Dash [15] investigated centerline decay rates for the center jet in an array based on the number of round jets in the array (S/D_{jet} = 1.5, 3.0) and as a function of the jet shape. While several analytically derived profiles are presented, there is no investigation into the near field of the jet, the area of most interest for the lower plenum. More in depth experimental work was conducted by Harima et al. looking at mixing processes in twin jets. Investigating three different jet spacings, S/D_{jet} = 2, 4, and 8, the mean flow profiles were presented for $x/D_{jet} > 5$. Work was done to quantify the combining or necking of the jets as well as discussion of the combining of the jets [16]. A more recent study looked at the differences between a row of confluent round jets and a square array. For the row of jets study, the jet spacing was S/D_{jet} = 2.82. PIV and LDA measurements were compared to RANS simulations utilizing both the k-ε turbulence model and an RSM

simulation. Specific care and concern was given to identifying the merging point and combining point of the jet [17]. For current work the merging point is defined as the axial distance where the negative recirculating region between two jets becomes positive. At this location the two jets begin to behave as a single jet. The combining point is defined as the axial location at which the maximum velocity occurs on the symmetry plane between neighboring jets. At this location velocity profiles in the twin jet begin to resemble those for a single jet.

While much work has been conducted investigating thermal striping, several key limitations exist in the previous studies. First, while much has been done investigating slot-jets, studies are scarce for arrays of round jets such as those seen in the lower plenum. Furthermore, the current body of work has only investigated for a limited range of jet Reynolds numbers, velocity ratios, and temperature differences, none of which accurately represent those expected in the VHTR lower plenum. Also missing from the current work is the effect on flow condition, specifically velocity inlet profile and turbulent intensity profiles on the mixing of jets. In order to address these limitations and provide data more application to VHTR lower plenum flows, the current research focuses on round jet configurations where the mixing is examined between neighboring jets. Specifically, a round triple-jet facility is designed and built to quantify the dependence of the mixing parameters on factors including Reynolds number, temperature difference, and jet spacing. These relationships are evaluated from the near field to intermediate downstream locations.

2.2 Experimental Facility Design

2.2.1 Flow Skid Design

In order to improve the current body of work on thermal striping, it was necessary to increase the range of variables considered in previous studies. Investigators at the Idaho National Laboratory (INL) [1, 18 -22] have performed numerous experimental studies aimed at characterizing the turbulence in the VHTR lower plenum. They have built a 6.55:1 scale model of a portion of the lower plenum enabling them to study the isothermal turbulent mixing between multiple jets. This scaled model used a jet diameter of 0.87 in (22.10 mm). In order to take advantage of standard tubing sizes, the present facility utilizes a jet diameter

of 0.875 in (22.2 mm). The goal of the experimental setup was to create three simultaneous flows capable of producing jet Reynolds numbers of at least 25,000. Although the setup can easily accommodate jets of different geometries (e.g., round, square, slot), the focus of the facility was round jets. Additionally, in order to expand upon previous experimental ranges in parallel triple-jet studies [10], the target for the maximum operating temperature of the facility was 150 °C. For a 22.2 mm diameter air jet at a Reynolds number of 25,000 and temperature of 150 °C, the jet velocity was determined to be 18.2 m s^{-1}. Since the facility is to be used for thermal striping investigations, it was determined that the temperature and velocity of each of the three jets should be independently controlled with a maximum ΔT between any two jets of 100 °C. In order to determine a final design, an iterative approach was utilized until agreement was found between the desired specifications and actual hardware specifications. Only the hardware utilized in the final design is considered here.

Shown in Figure 2-2 is a diagram illustrating the design of the experimental flow skid. This closed-loop air handling system is driven by a variable speed blower (Model AT700 with 7.5 HP motor and water cooling), which supplies the flow motivation for all three jets. A portion of the flow from the blower is taken from the main line and fed through a heat exchanger, whose cold side is supplied by the building chilled water lines. This flow channel constitutes the "cold" jet. The remainder of the flow in the main line is then split into two additional lines, each of which is then sent through individually controlled heaters. These two channels of flow constitute the two hot jets. Pressure drop across an orifice plate is used in each of the three flow channels (two hot jets and one cold jet) to monitor the individual flow rates. All the flow entering the test section does so through one of these three jets, each of which has a honeycomb flow straightener upstream of the test section as shown. Exiting the test section is a single line which returns the mixed flow back to the blower. An additional heat exchanger is placed after the test section and before the blower in order to account for any heat gained in the flow from the blower itself. This provides a solution for scenarios where the desired jet temperature is only slightly above ambient conditions, where the heat imparted to the flow by the blower may become significant. Finally, there is a bypass line in parallel with the flow through the blower and system heat exchanger, which can vary between completely closed and

completely open, to accommodate low mass flow rate experiments. Actuated valves for each of three flow channels along with a fourth in the bypass line allow independent control of the flow rate for each jet. A pressure relief valve designed for 20.1 kPa ensures the pressure in the flow loop does not exceed acceptable limits for the blower.

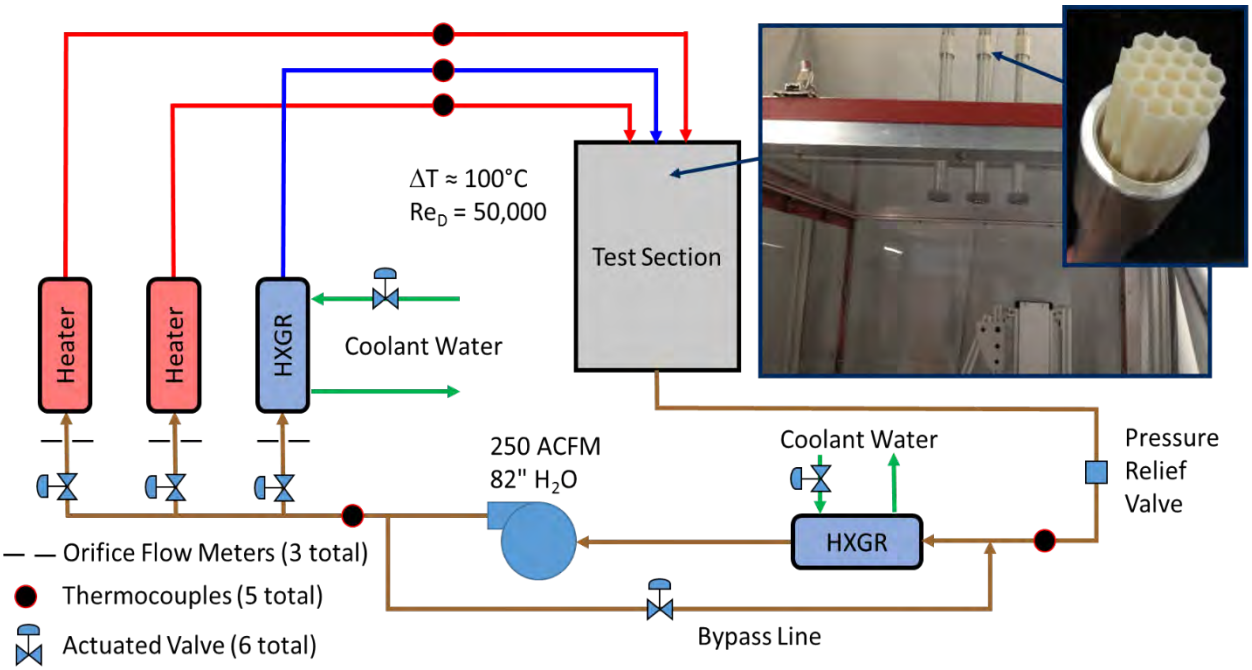

Figure 2-2. Schematic of the experimental test section with honeycomb flow conditioners pictured

The test section is utilized in both single and triple-jet experiments via a removable spacing plate, as shown in Figure 2-3. The test section has dimensions of 813 mm × 813 mm × 1016 mm and is made from a high temperature polycarbonate material, LEXAN®. LEXAN® is optically transparent so that particle image velocimetry (PIV) can be accommodated for full field velocity measurements (although PIV is not considered in this work). The test section was designed such that it had a removable door for easy access to any internal measurement equipment. On this door, special consideration was given for mounting of an Infrared-Viewport (FLIR IRW-4C) for use with IR camera (FLIR SC5000) measurements (not considered in the present work). Internally, an 8020 aluminum extrusion frame is used for supporting any test equipment, as well as the 3-axis, high temperature, linear stages (not shown in the figure) supplied by

Parker Hannifan Inc. The stages can travel 457 mm in the vertical direction, as well 254 mm in both horizontal directions. The setup was sealed using a high temperature rubber gasket. The test section was insulated using 1 in thick high density polystyrene with an R value of 0.241 K m W^{-1}.

Although the designed apparatus is a closed loop system, conservative design principles were implemented by treating all components as once-through. Since the heating elements for the two hot jets and the heat exchanger for the cold jet are fed with the same bulk temperature, their ability to increase or decrease the temperature of the fluid before it reaches the test section is critical in meeting the overall test conditions desired. The upper and lower bounds for the operating temperature are 150 °C (maximum temperature for certain measuring components in test section) and 25 °C (temperature of building chilled water supply), respectively. The maximum desired temperature differential between hot and colds jets is ΔT = 100 °C. For the two hot jet heaters, the air temperature is assumed to increase by up to 80 °C in a single pass. For flow with a Reynolds number of 50,000, this suggests a mass flow rate of 0.0173 kg s^{-1}, the corresponding heating requirements can then easily be found according to the following expression:

$$Q = \dot{m} C_p \Delta T \tag{2-1}$$

where C_p is the heat capacity of the air (1070 J kg^{-1} K^{-1}), evaluated at 150 °C. This results in 2.9 kW required for each hot jet. As a result, two inline 3 kW, screw plug, immersion heaters (custom manufactured by Wattco) are used. These heaters are 30 in long, with a 0.403 in diameter sheath and a power density of 2.17 × 10^4 W m^{-2}. The accuracy of the supplied control system is 0.1% of the user desired temperature.

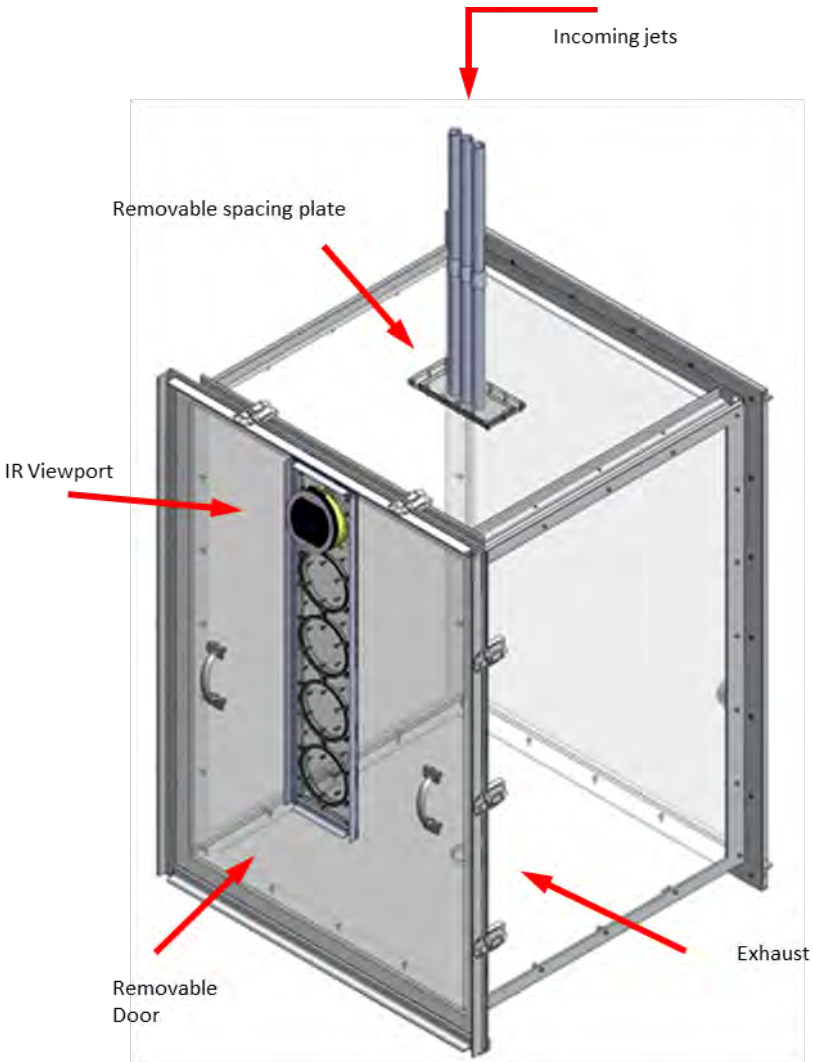

Figure 2-3. Triple-jet experimental test section

The next component sourced was the heat exchanger for the cold jet. Here, in order to provide a conservative analysis, it was assumed that it should be able to create the desired temperature difference of 100 °C without the aid of the hot jet heaters. It was assumed the exhaust temperature of the test section was equal to that of the hottest jet (150 °C) and that no heat losses occur through the piping network leading up to entrance of the cold jet heat exchanger. The mass flow rate is the same as that considered during the hot jet analysis (0.0173 kg s^{-1}), and therefore dictates a heat removal of 3.69 kW (found using Eq. (2-1)). For the water side of the heat exchanger, the inlet temperature was assumed to be 25°C (chilled water supply

temperature) and outlet coolant temperature of 35°C to insure that in case of an accident, the risk of being burned due to high fluid temperatures is minimal or non-existent. A shell and tube type heat exchanger (Southwest Thermal BOSCO AB1008-98500) can provide 4.19 kW of heat removal, well over the performance needed. The surface area on the tube side of the heat exchanger is 2.19 m^2.

A second heat exchanger (Southwest Thermal BOSCO AB705-98500) is used to cool the exhaust flow from the test section in order to remove any heat that may be imparted by the blower during continual operation. The maximum temperature difference for this heat exchanger was specified at 40 °C with the total mass flow rate for the air including the two hot jet channels and single cold jet channel (total of 0.0519 kg s^{-1}). Calculating the heat removed, according to Eq. (2-1), the total heat removed is 0.9 kW.

The final component sourced was the blower. The blower is the most important parameter for determining the flow rate, and subsequently the jet velocities, possible in the system. In order to determine the possible flow rates, a thorough estimation of the system pressure drop is necessary. However, before pressure drop can be accurately determined, the final piping configuration, which depends on the specific blower chosen, is needed. Here, the equations utilized when calculating the pressure drop are stepped through. This pressure drop, along with the pump curve of the blower, was then used to calculate actual operating ranges. For the present study, only flow in a single jet, with the bypass completely closed, was considered.

Shown in Table 2-1 are the various diameters of pipe used in the flow skid. First, the primary pressure losses due to pipe length (ΔP) were calculated according to Eq. (2-2), where f is the friction factor, L is the length of the pipe, D is the pipe diameter, and $\boldsymbol{U}$ is the average velocity in the pipe. The friction factor, f, was iteratively calculated using the Colebrook Equation (see Eq. (2-3)), which depends on the Reynolds number of the pipe, Re_{pipe}, and the surface roughness of the pipe, e (which is taken to be 0.045 mm).

$$\Delta P_{pipe} = f \rho \frac{L}{D} \frac{\langle |\mathbf{U}| \rangle^2}{2} \tag{2-2}$$

$$\frac{1}{\sqrt{f}} = -2\ln\left(\frac{e/D}{3.7} + \frac{2.51}{Re_{pipe}\sqrt{f}}\right) \tag{2-3}$$

Table 2-1. Pipe Lengths and diameters in flow skid

Diameter (in)	0.75	1	1	3	4
Length (in)	0	72	28	12	8

Similarly, the minor pressure losses, due to expansion and contraction between pipes of different sizes, were calculated. The minor losses ($\Delta P_{\exp}$) were calculated according to Eq. (2-4), where the small and large diameters are d and D, respectively [23]. The average velocity is always calculated in the smaller pipe diameter, regardless of whether the change in pipe diameter is an expansion or contraction. Shown in Table 2-2 is the expansion/contraction ratio, $d{:}D$, and the number of each expansion/contraction in the current piping configuration being analyzed.

$$\Delta P_{exp} = \frac{1}{2}\left[1 - \left(\frac{d}{D}\right)^2\right]\frac{\rho\langle|\mathbf{U}|\rangle^2}{2} \tag{2-4}$$

Table 2-2. Expansion and contraction ratios

$d{:}D$ (in:in)	Number
0.75:2	1
1:2	6
1:3	2
2:3	1
0.75:36	2

Finally, it was assumed the pressure drop across the system heat exchanger and the heater was 0.2 psi (1.4 kPa), as per manufacturer specifications. Although in reality, the actual pressure drop across the air side of the heat exchanger is dependent on the flow rate, this data was not available to include in the present analysis. This assumption causes the predicted system curve to have a non-zero pressure, even when the

flow rate is set at zero. The blower selected is a Paxton AT700 centrifugal air blower. It is capable of producing 280 CFM (0.118 m^3 s^{-1}), at 3.035 psi (20.9 kPa). The blower is powered by a 7.5 HP Emerson Technologies motor, controlled by a GS2-27P5 variable frequency drive (Automation Direct). In order to calculate the achievable operating conditions, the blower curve must be analyzed in conjunction with the system curve. A family of blower curves supplied by the manufacturer is shown in Figure 2-4(a), along with the predicted system curve. As previously noted, the system curve intercepts the pressure axis at approximately 1.4 kPa (due to the constant pressure drop assumed for the heat exchanger). The pre-supplied specifications for the blower curves did not provide data below a certain flow rate, denoted by the vertical black line at approximately 0.052 kg s^{-1}. To the left of this line, a constant pressure drop is assumed.

In order to determine the accuracy of the predicted system curves, and validate the assumption in regard to the blower behavior at low flow rates, experimental measurements were taken. Only a single jet (cold jet channel) was used in an isothermal configuration (water side of heat exchanger was not operating). These experiments focused on acquiring portions of both the blower curves and system curves. The results are shown in Figure 2-4(b). The pressure drop across the blower was measured with a 0 – 2 psi (0 – 13.8 kPa) linear pressure transducer with an output current of 4 – 20 mA. The experiments were limited in that the pressure needed to remain below 2 psi to protect the transducer used. The mass flow rate through the system was measured by quantifying the pressure drop across the orifice plate using a linear pressure transducer (0 – 1 psi (6.9 kPa) with 4 – 20 mA output). The system curve was collected by completely opening the control valve of the jet and increasing the horsepower to the blower. The blower curves were acquired by keeping the horsepower to the blower constant and adjusting the control valve of the jet, to increase system pressure drop. Five unique horsepower settings were considered, thereby generating 5 blower curves. Note that collecting data in this manner precludes characterizing the blower performance beyond the operating point (intersection of blower and system curves). Therefore, blower curve data was only captured to the left of the system curve. The assumption of constant pressure in this region seems to be validated. The predicted system curve is also included in Figure 2-4(b) for direct comparison with the experimental curve. Worth noting is that the pressure is under-predicted for reasonably high flow rates.

This is likely due to the fact that head losses for the entire piping network are not known with an extremely high level of confidence.

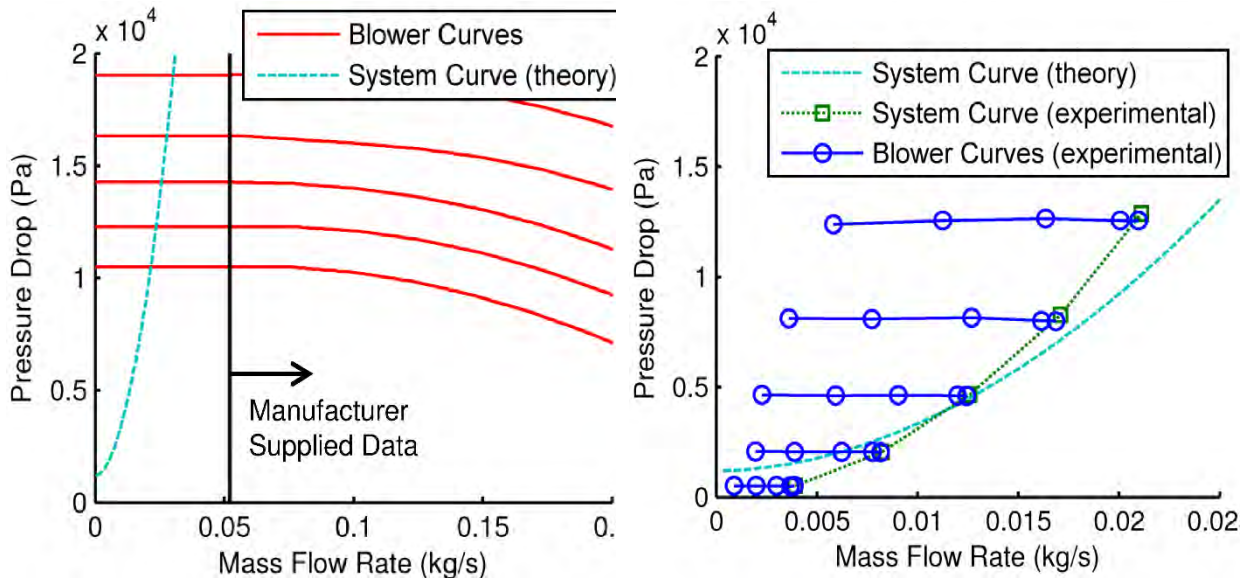

Figure 2-4. (a) Plot of predicted system curve with the manufacturer supplied blower curves (b) Experimentally measured system curves and blower curve

One important function considered in the design of the experimental setup was the ability to control the flow rate, and thereby be able to dial in a specific jet Reynolds number. The ability to do this is closely tied to the uncertainty of the mass flow rate. As previously discussed, the mass flow rate is determined from the differential pressure drop across an orifice plate. The mass flow rate of an compressible fluid, traveling through an orifice plate, can be calculated according to Eq.(2-5), where the isentropic expansion factor (Y) is defined in Eq. (2-6), where C_D is the discharge coefficient for the selected orifice plate, D_o is the orifice plate diameter, D_{pipe} is the internal diameter of the 2 in (50.8 mm) NPT piping leading to the orifice plate, T_o is the temperature at the inlet of the orifice, P_o is the absolute pressure at the orifice inlet, ΔP is the pressure drop across the orifice, and γ is the specific heat ratio.

$$\dot{m} = \sqrt{\frac{RT_oZ}{P_o}}\,\frac{D_o^2\pi}{4}\,\frac{C_D}{\sqrt{1-\frac{D_o^4}{D_{pipe}^4}}}\sqrt{\Delta P}\,Y \tag{2-5}$$

$$Y = \sqrt{\left(\frac{P_o-\Delta P}{P_o}\right)^{2/\gamma}\left(\frac{\gamma}{\gamma-1}\right)\left(\frac{1-\left(\frac{P_o-\Delta P}{P_o}\right)^{\frac{\gamma-1}{\gamma}}}{1-\left(\frac{P_o-\Delta P}{P_o}\right)}\right)\left(\frac{1-\frac{D_o^4}{D_{pipe}^4}}{1-\frac{D_o^4}{D_{pipe}^4}\left(\frac{P_o-\Delta P}{P_o}\right)}\right)} \tag{2-6}$$

Shown in Table 2-3 are the assumed values for each parameter, as well as their respective uncertainties. Using these values, the uncertainty of the actual mass flow measurement was calculated using standard propagation of uncertainty analysis [23]. Accordingly, in order to maintain an average jet velocity of 15 m s^{-1} at 27 °C, corresponding to a jet Reynolds number of 20.6×10^3, the mass flow rate is 6.437×10^{-3} kg s^{-1}, and the pressure drop across the orifice plate is 0.024 psi. This corresponds to an uncertainty in mass flow rate of 0.305%. Similar calculations were carried out assuming the gas was incompressible, meaning that the isentropic expansion factor was equal to a value of 1. Assuming the gas was incompressible, the uncertainty in the mass flow rate is 4.5×10^{-4} % different from that when the isentropic expansion factor was solved for. Since this change is three orders of magnitude less than the calculated uncertainty, the incompressible flow assumption is applied to reduce the complexity of uncertainty calculation. For the extreme case, where the Reynolds number is 25×10^3, corresponding to an average jet velocity of 18.25 m s^{-1} and a mass flow rate of 7.831×10^{-3} kg s^{-1} at a temperature of 27 °C, and a pressure drop across the orifice of 0.036 psi, the uncertainty for the compressible mass flow rate was 0.273 %.

Table 2-3. Assumed values and uncertainties

	Value	Uncertainty
D_o (in)	1.0231	0.001
D_{pipe} (in)	2.067	0.001
T_o (K)	293.15	0.1
P_o (psi)	17	0.025
ΔP (psi)	0.036	$9 \cdot 10^{-5}$
γ (1)	1.389	0.01

Shown in Figure 2-5 is a plot of the total uncertainty of the mass flow rate, as well as for each of the terms necessary in calculating the total uncertainty. As shown, the most significant contribution to the overall uncertainty in mass flow rate comes from the uncertainty associated with measuring the pressure drop across the orifice plate. Since the uncertainty in this pressure measurement is a constant value, its influence on the overall uncertainty diminishes as the flow rate increases. At sufficiently high flow rates, the overall uncertainty becomes nearly constant (approximately 0.27 %). For these calculations the orifice pressure drop transducers were a 0 – 0.249 kPa high accuracy (± 0.25% FS) Setra Model 2461 pressure transducer with 4 – 20 mA output. These pressure transducers are used in the remainder of this work.

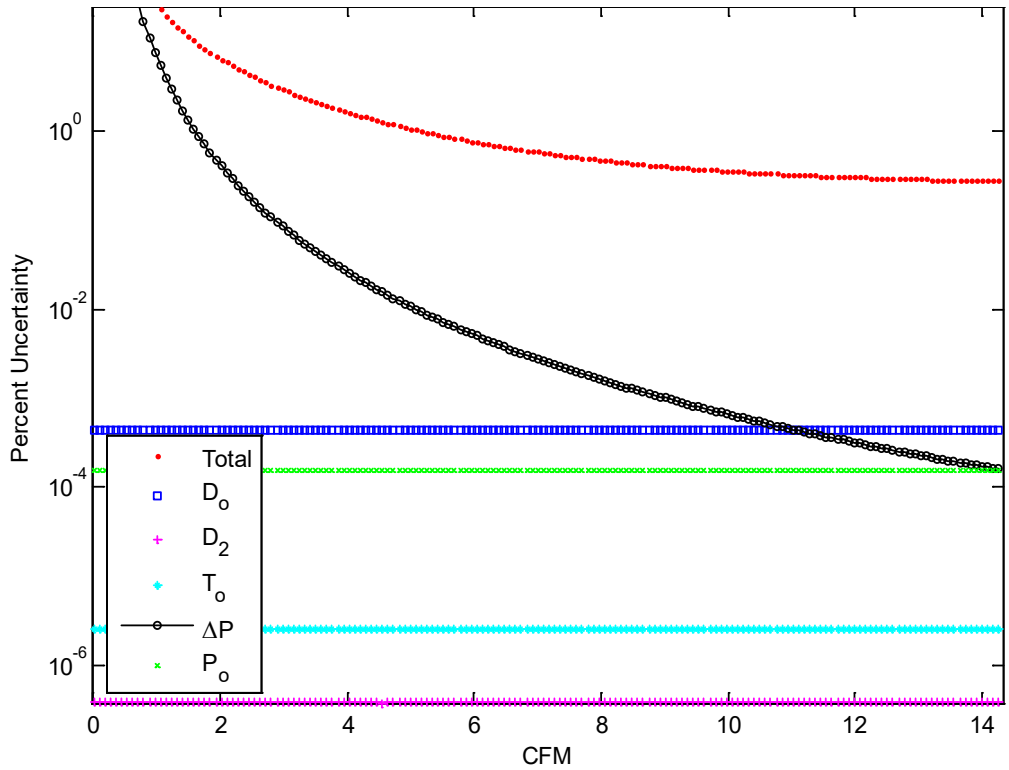

Figure 2-5. Percent uncertainty of mass flow rate and individual uncertainty components

The mass flow rate is measured utilizing an orifice flow plate and controlled via electronically actuated valves, Belimo model AFB-24-SR, with 2 – 10 V input. The valves were controlled utilizing a Koyo DirecLogic 06 PLC (D0-06DD2) with signal I/O utilizing three unique DAQ cards (F0-04AD-1, F0-08ADH-1, F0-08DAH-1). In order to implement real time control of the mass flow rate, the pressure drop across the orifice plate was gathered and used in Eq.(2-5). In Eq. (2-5), the isentropic expansion factor Y is replaced with the empirical value Y_{exp}, as shown in Eq. (2-7). Note that the discharge coefficient C_d is found from interpolation of experimental data and is performed utilizing a table look up based on β and the orifice Reynolds number. During all calculations, geometric parameters such as orifice diameter are corrected to account for thermal expansion due to the increased temperature. For a more detailed explanation of the calculation of

flow rate across an orifice plate, including explanation for the empirical fit of the isentropic expansion factor and the discharge coefficient, see [24].

$$Y_{\exp} = 1 - \frac{0.41 + 0.35\beta^4}{\gamma} \frac{\Delta P_o}{P_o} \tag{2-7}$$

2.2.2 Unit Cell Experimental Design

Design modifications were made in order to also evaluate physics more closely tied to the actual VHTR lower plenum. This is done by designing a unit cell test section, one that represents a portion of the lower plenum, complete with support posts. A half model of the lower plenum [21] is shown in Figure 2-6. As previously noted, the jets and posts combine to create a complex flow field that is a combination of many canonical problems, including impinging jets, jet arrays, jets issuing into cross flow, and flow past tube bundles. Several studies have been conducted which specifically investigated turbulent mixing and thermal striping in the lower plenum of the VHTR. However, for all these studies, the typical experimental domain is that originally designed by INL and used in their matched index of refraction (MIR) facility [21-22, 25], shown in Figure 2-7 [26]. This facility was designed based on an in-depth scaling analysis, and therefore generates conditions in the same range of key dimensionless parameters when compared to the full scale VHTR design. In the years that followed its construction, this facility became somewhat of a canonical VHTR-related configuration, with multiple research groups performing relevant experimental and computational studies. The MIR facility is achieved with mineral oil as its working fluid, kept within a reasonably tight temperature window in order to maintain the transparent fluid-solid interfaces between it and the solid quartz material. As a result, non-isothermal studies are precluded. In addition, the model is meant to mimic a slice of the lower plenum near the line of symmetry in Figure 2-6, and therefore cannot be used to investigate interactions between more than two neighboring jets. Additional scaling studies have been conducted by Oregon State University [27] and Texas A & M University [2], both of which were considered when designing the lower plenum model for use in conjunction with the present facility investigated in the present body of work.

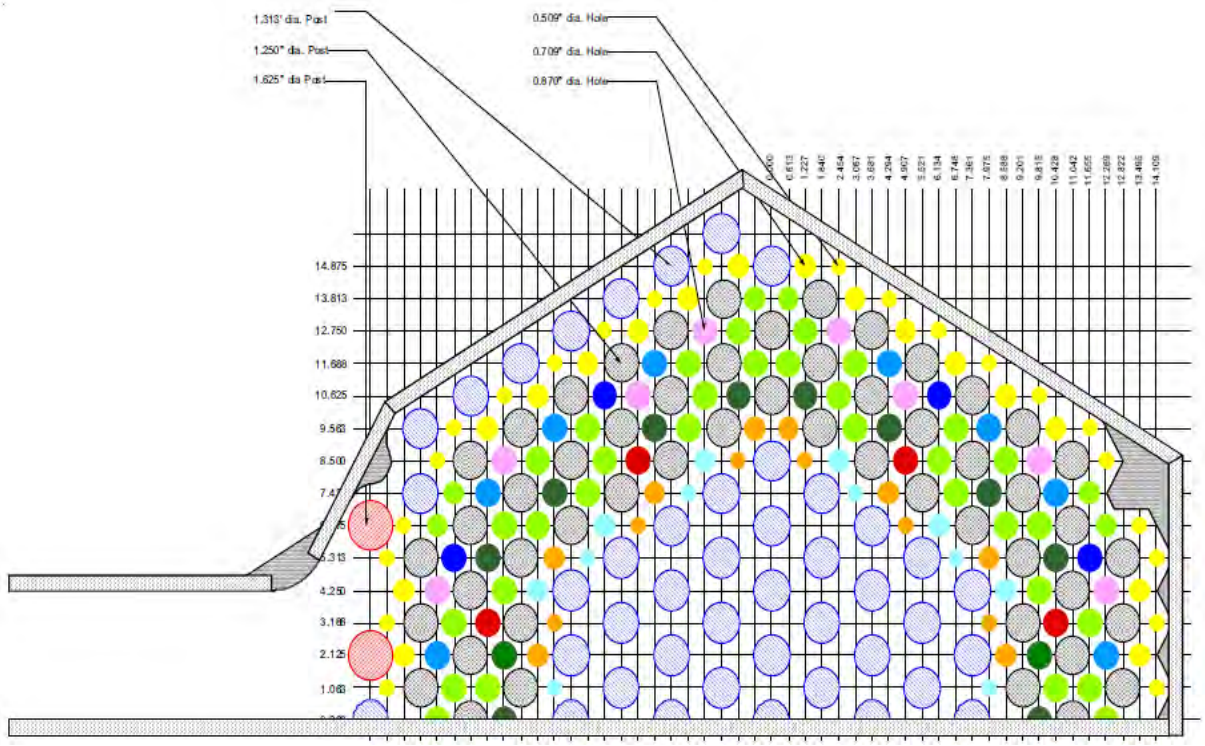

Figure 2-6. Half-model of the VHTR lower plenum with jets (colored) and posts (grey) [21]

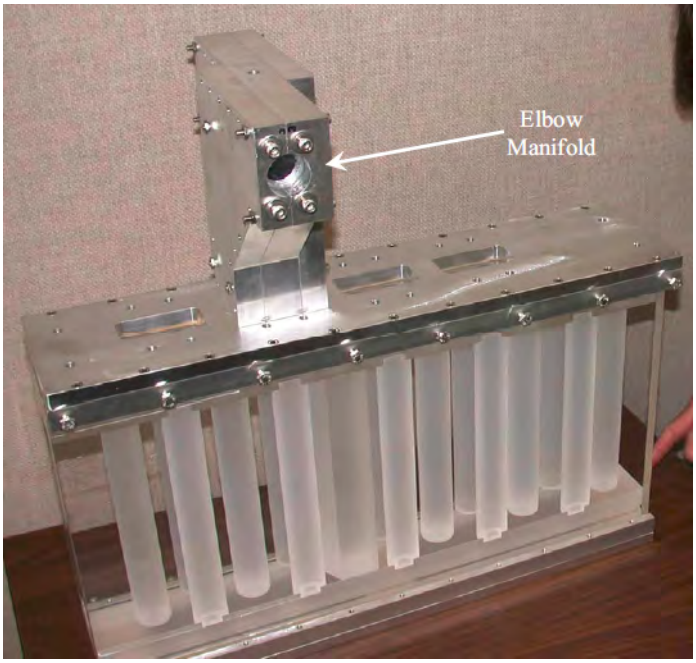

Figure 2-7. Matched index of refraction facility test section at INL [26]

In order to expand upon current studies related to isothermal and non-isothermal flows in the lower plenum, an experimental facility is designed to enable high-quality data collection for future validation studies. A repeating flow configuration, referred to as the unit cell is the focus of this experimental facility, and consists of six jets arranged in a hexagonal pattern whose flow enters the test section with the dominant flow direction along the length of the seven cylindrical support posts. This flow is then met by an orthogonal crossflow. This is illustrated in Figure 2-8, and focuses on three unique configurations of the flow in the half model of the VHTR lower plenum labeled Case A, B, and C. By adjusting the velocities and temperatures of the six jets and the strength and temperature of the crossflow, different regions of the lower plenum can be experimentally simulated. Each of the cases have unique flow features that are considered during the design. Case C represents a unit cell far away from the outlet of the lower plenum. For this case, the cross flow velocity and temperature are very low. Assuming Gaussian shaped temperature and/or velocity profiles in the radial direction, one could assume two unique jet temperatures and flow rates (designated by the numbers 1 and 2 shown on the jets). Geometrically, Case C is similar to Case A as both represent flow across a staggered tube bundle. However, in Case A, which is near the outlet, the cross flow velocity and temperature are much larger than in Case C. Case B then represents a unit cell near the periphery of the lower plenum. In this case, there is a low cross flow velocity and temperature; however, the orientation with respect to the cross flow is more closely represented by that of an inline tube bundle. For this case, three unique jet temperatures would exist, as depicted by the numbers 1, 2, and 3.

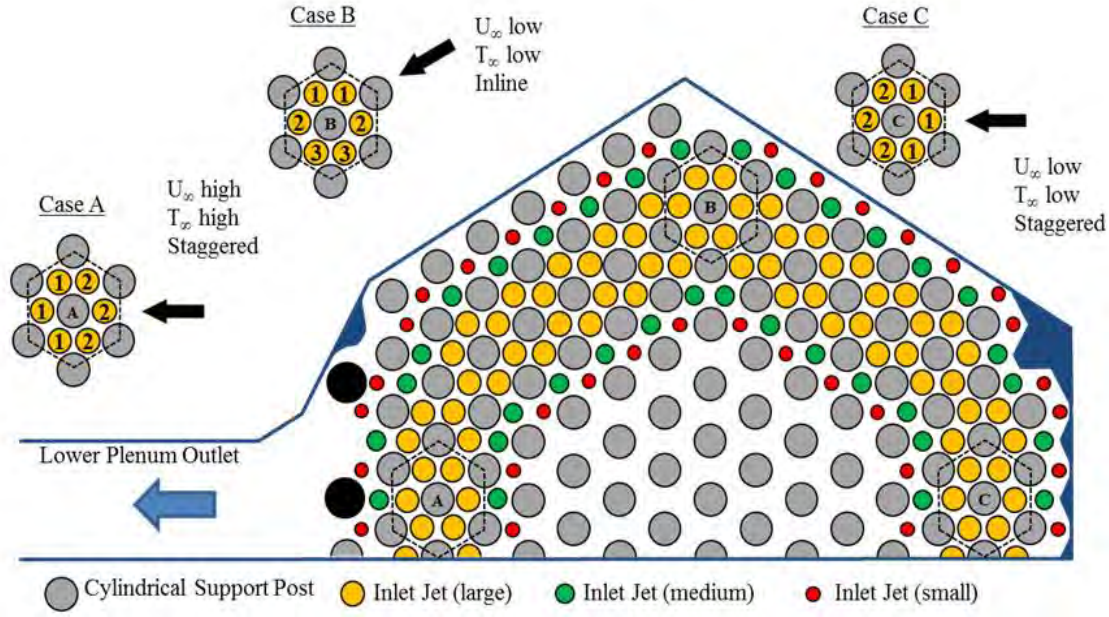

Figure 2-8. Experimental unit cell for studying the lower plenum of the VHTR

Before examining the three unit cell cases detailed in Figure 2-8, the extensive VHTR lower plenum scaling studies conducted by INL [18-21, 28] were reviewed. As explained by Condie et al. [21], based on expected Richardson numbers, it is reasonable to assume that during full power operation the jets in the lower plenum are momentum-driven with negligible buoyancy effects. Based on the preliminary simulations conducted by Mazumdar et al. [29], scaling of the lower plenum was further investigated. In the lower plenum, jet Reynolds numbers vary from 10^3 to 10^5, while the transverse Reynolds number, calculated based on the cross flow velocity and jet diameter, can be as large as 51,000 assuming a maximum crossflow velocity of 70 m s^{-1}. In areas with large transverse velocities (~ 50 m s^{-1}) the transverse velocity ratio ($R = V_{jet}/V_{trans}$) can be less than one-half. For locations with minimal transverse flow near the edges of the plenum, transverse velocity ratio can be very large (~ 70 based on a maximum jet velocity of 148 m s^{-1} [29]). However, typical of the majority of the jets in the lower plenum is a transverse velocity ratio between 0.5 – 5. Similarly, in the lower plenum, post Reynolds numbers reach 70,000 with shedding

frequencies of approximately 60 Hz, based on a Strouhal number of 0.2. For a detailed description of non-dimensionalization and scaling in fluid flows, refer to [30].

Design of the facility is achieved using standard scaling requirements for matching many non-dimensional parameters in the VHTR lower plenum including jet Reynolds number, post Reynolds number and vortex shedding frequency, transverse Reynolds number, and plenum Reynolds number, as well as maintaining geometric similarity. The MIR facility designed at INL to study turbulent mixing in the VHTR lower plenum utilized a 6.55:1 scale model [2-4, 19-20, 28], which resulted in a jet diameter of 22.10 mm. For the current work, a scaling of 6.598:1 was selected such that standard tubing sizes 22.23 mm (0.875 in) could be used. Based on this same scaling, the post diameter was 31.75 mm, with a length of 217.49 mm, which also represents the scaled plenum height.

Utilizing the previously designed flow motivation skid, the maximum achievable Reynolds number in a single experimental jet is approximately 25,000, while the maximum achievable jet Reynolds number when all six jets are run at equal flow rates, is approximately 12,500. In order to motivate the cross flow, an axial fan capable of producing transverse velocity ratios of 0.25 – 1.0, which is inside the typical range experienced in the lower plenum. The axial fan, which will be described in further detail later, can motivate nearly 7,500 cfm of air in the setup, yielding a maximum Reynolds number based on the test section's hydraulic diameter of approximately 1.32×10^6. The maximum achievable post Reynolds number in the facility is approximately 70,000 based on the post diameter and crossflow velocity. The post vortex shedding frequency would be expected at 220 Hz for a Strouhal number of 0.2. The maximum temperature difference in the unit cell experiment is the same as the maximum producible in the flow skid (i.e., ΔT = 100 K).

After addressing desired flow requirements for scaling of the experiment, concern was given to what temperature and velocity measurements were both possible and desired. PIV measurements were determined to be a sufficient method of capturing the velocity fields. Ethylene Glycol, Bis(2-ethylhexyl sebacate), was chosen as the seeder particle for this application. The TSI Six-Jet Atomizer 9306 was used as the dispersion method for the seeding material and enabled fully seeded flow within 5-10 seconds. Data

capture commenced within the next 5-10 seconds after the seeding conditions were met. The average particle size is 0.65 μm with 95% of the particles between 0.5 and 1.5 μm. The insertion point for the atomizer is located upstream of the fan. To ensure a mass balance in the system, an exit is also cut out of the ducting which then reconnects to the flow motivation skid.

A CAD model of the unit cell design is shown in Figure 2-9. There are several key features apparent. First, issuing top-down into the test section are the pipe jets. Each of these pipe jets contains, within their length, a high temperature ceramic honeycomb which helps straighten the flow. These honeycombs, and their effect on the flow, are addressed in more detail later. Second, moving downward into test section, through the top plate, are the seven support posts, six in a hexagonal array with one center post. The rectangular shaped test section is 217.49 mm high (fixed by the length of the cylindrical support posts) and 457 mm (18 in) wide (direction orthogonal to the incoming crossflow). This width is approximately 2.5 times the width of the hexagonal array in order to remove interaction with the flow near the cylinders and the side walls of the test section. The length of the test section is 610 mm.

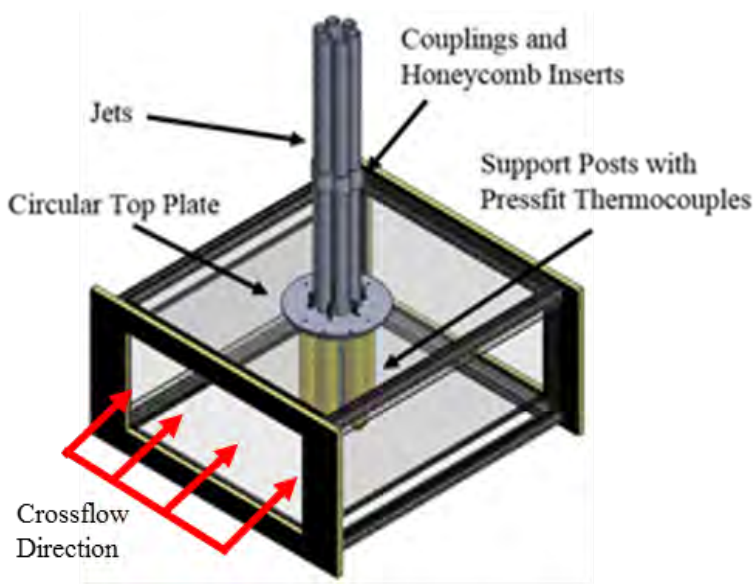

Figure 2-9. Isometric view of the test section with key design components highlighted

PIV measurements are sufficient in capturing the velocity fields, but the temperature maps of flow are a significant challenge. The thermal mixing effects for this scenario will primarily be quantified from

the temperature attenuation through the support cylinders. In order to measure the attenuation of temperature fluctuations in the posts, four thermocouples were placed in each of the six outer posts, and aligned radially towards the center post. Additionally, four thermocouples were placed in the center post. The outer 6 posts remain fixed in space, but the center post will be attached to a stepper motor enabling rotation. This is done in order to capture an azimuthal map of the temperature fluctuations in the center post, without the need to fill the post with a large amount of thermocouples. The thermocouples are inserted into each post from the top flat surface of the cylinder. The insertion depth for two of the thermocouples is 2.16 in (L/D = 0.25), while the insertion depth for the other two thermocouples is 4.33 in (L/D = 0.5). These four thermocouples are also located at different radial positions within the cylinder, namely r/D =0.131 and 0.369 for the thermocouples with L/D = 0.25, and r/D = 0.231 and 0.469 for the L/D = 0.5 thermocouples. This is illustrated in Figure 2-10. In order to achieve accurate location of the thermocouples, a "press fit insert" was designed to overcome machining limitations associated with large aspect ratio holes.

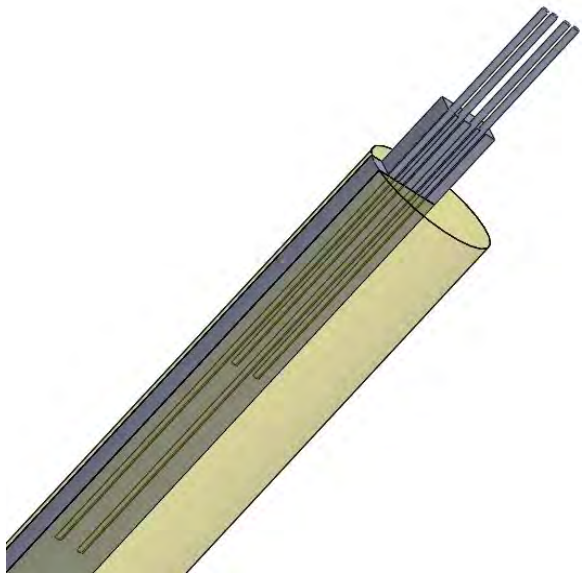

Figure 2-10. Thermocouple/Support post assembly with thermocouples shown

After appropriately identifying the functional requirements for the test section, and addressing design issues with the desired measurements, the next major concern was cross-flow conditioning. In order to take consistent, meaningful velocity measurements, it was desirable to have an easily quantifiable, near

uniform cross flow past the unit cell. In order to achieve this, standard wind tunnel design methodology was employed. After developing analytical models for the system pressure drop curves, the Greenheck mixed flow fan (model QEI-22-I-50) was selected. The QEI-22-I-50 provides a maximum flow rate of 5.66 $m^3 s^{-1}$. The fan itself has a diameter of 0.78 m, requiring that custom round-to-square transitions be fabricated to mate the fan to the rectangular 0.91 m x 0.61 m ducting.

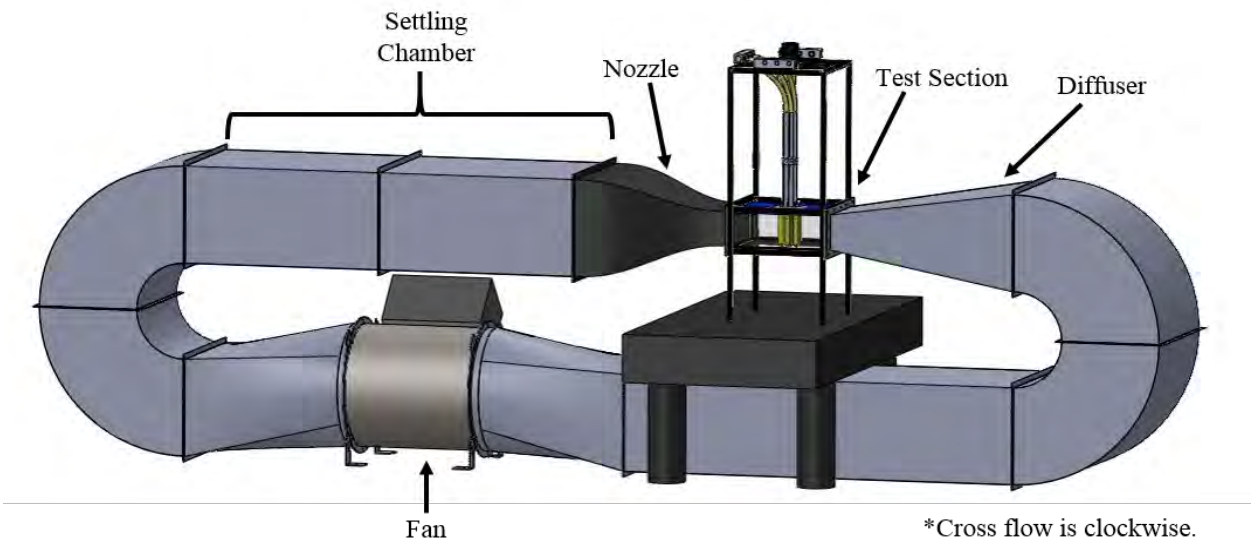

Figure 2-11. Cross flow wind tunnel design

The next component of the recirculating wind tunnel is the settling chamber. The effective length of the settling chamber was limited by the available lab space. The effective length is therefore 2.4 m long. In this length, flow straightening devices were utilized to help straighten and allow for better control of the turbulent intensity distribution in the flow. Two aluminum hexagonal honeycomb inserts were utilized to aid in reducing large scale structures such as swirl from the fan as well as lateral mean velocity variations. A stainless steel wire mesh screen was incorporated to make the flow velocity more uniform. The design of the honeycomb and wire mesh was done in accordance with studies presented by Mehta [31] and Scheiman [32]. The screen selected had a wire diameter of 1.37 mm with a spacing of 3 x 3 wires per square inch. The open area ratio for the screen was approximately 0.702, resulting in a pressure drop coefficient of 0.339 [33]. The screen was placed directly on the exit of the downstream honeycomb insert. Similar

design was used for the honeycomb flow straighteners. Based on these sources, a honeycomb hydraulic diameter of 25.4 mm was selected, with a total length of L/D_{hyd} = 6. The honeycomb inserts were placed at the entrance and exit of the settling chamber.

Following downstream of the settling chamber is the nozzle. The contraction nozzle, whose shape was determined following guidelines described by Bell and Mehta [33-34], was designed to achieve a uniform cross flow by reducing both the mean and fluctuating velocity variations to a smaller fraction of the average velocity while simultaneously eliminating flow separation and reducing Moffatt eddies in the corners. The curve of the nozzle consists of a fifth order polynomial shown in Eq. (2-8). For the horizontal contraction dimensions, the inlet radius, H_i, was 0.457 m while the outlet radius, H_e, was 0.229 m. For the vertical dimensions of the contraction, the inlet radius was 12 in while the outlet radius was approximated as 0.108 m. The total length of the contraction, L, was 0.91 m. The nozzle design has a contraction ratio, defined as the ratio of inlet to outlet area, of 8.47. The nozzle which was constructed using 2 x 2 weave carbon fiber layups (from HEXCEL Composites [35]) is illustrated in Figure 2-11. The final nozzle design dictated the 0.91 m x 0.61 m cross section for flow approaching the nozzle.

$$y(x) = H_i - \left(H_i - H_e\right)\left[6\left(\frac{x}{L}\right)^5 - 15\left(\frac{x}{L}\right)^4 + 10\left(\frac{x}{L}\right)^3\right] \tag{2-8}$$

The next portion downstream of the nozzle is the test section. Several design parameters were incorporated with the test section to allow for accurate and relevant velocity and temperature measurements to be found with the proper scaled design. First, a closer look at the test section was first presented in Figure 2-9. The first part of the test section are the jets which run vertically into the test section. Each of these jets contains two 0.305 m straight pipes with an inner diameter of 22.23 mm, and are connected with a custom made coupling. Inside each of the couplings is a high-temperature ceramic honeycomb insert for flow straightening and improved uniform turbulence statistics. These honeycomb flow straighteners are composed of Somos® NanoTool, which has a glass transition temperature of 82°C (~180°F) and consist of

L/D_{hyd} = 20. The jet array can be seen in Figure 2-12(a) while an individual honeycomb flow straightener can be viewed with a transparent version of its jet in Figure 2-12(b).

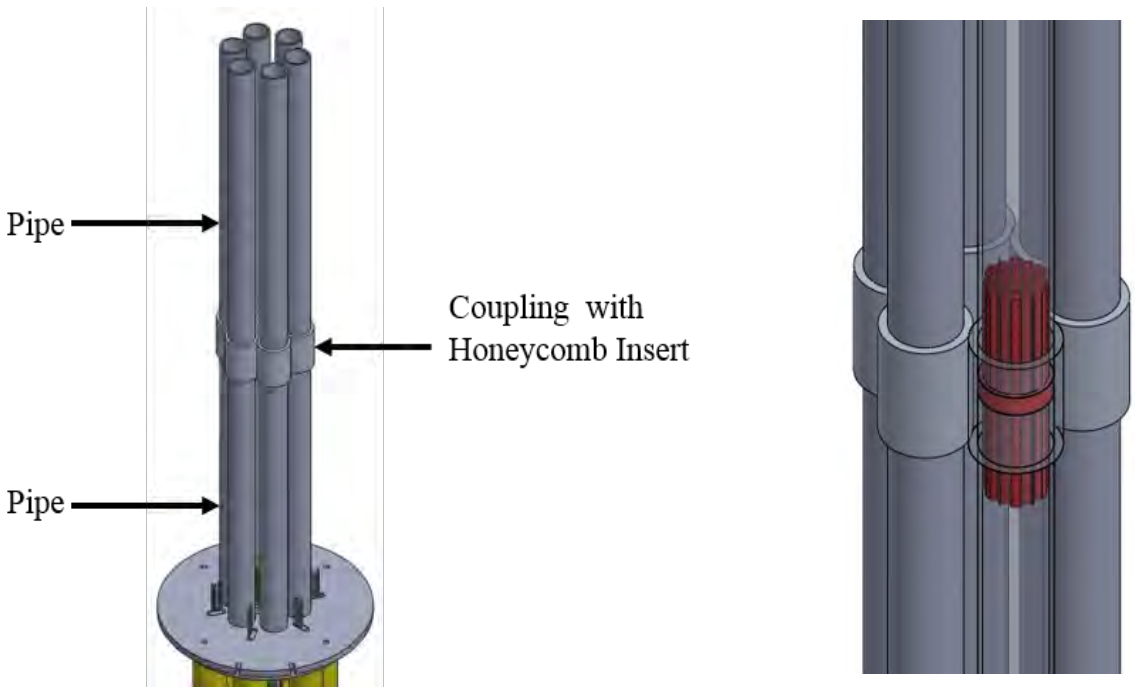

(a) (b)

Figure 2-12. (a) Array of six jets located above test section (b) transparent jet revealing internal honeycomb insert

Also seen in Figure 2-9 is the circular aluminum top plate of the test section which holds the six hexagonal posts and the central support post. The top plate supports the jets, and serves to align the outer support posts in the top wall of the test section. A more detailed view of the circular top plate with support posts, thermocouples, and jet inlets is shown in Figure 2-13. The aluminum circular plate locates each support post utilizing a four thermocouple press fit assembly (described previously), with the exception of the rotating center post, which is secured with a press fit bushing. Additionally, the aluminum plate locates each jet in space. Finally, this aluminum plate was designed such that it can be rotated 30°, to accommodate flow across an inline tube bundle (Case B in Figure 2-8) and a staggered tube bundle (Cases A and C in Figure 2-8). In order to allow PIV measurements, the side walls and bottom plate were constructed from

LEXAN®, a high-temperature polycarbonate plastic that is optically transparent. Additionally, in order to minimize the effect of surface roughness for ultimate comparison to CFD, all posts were given a high accuracy mirror finish polish after being machined. Before PIV measurements, the posts were painted with a matte black paint in order to prevent unwanted laser reflection in the test section. The top wall was constructed from a high-temperature, ultrahigh-molecular weight (UHMW) plastic.

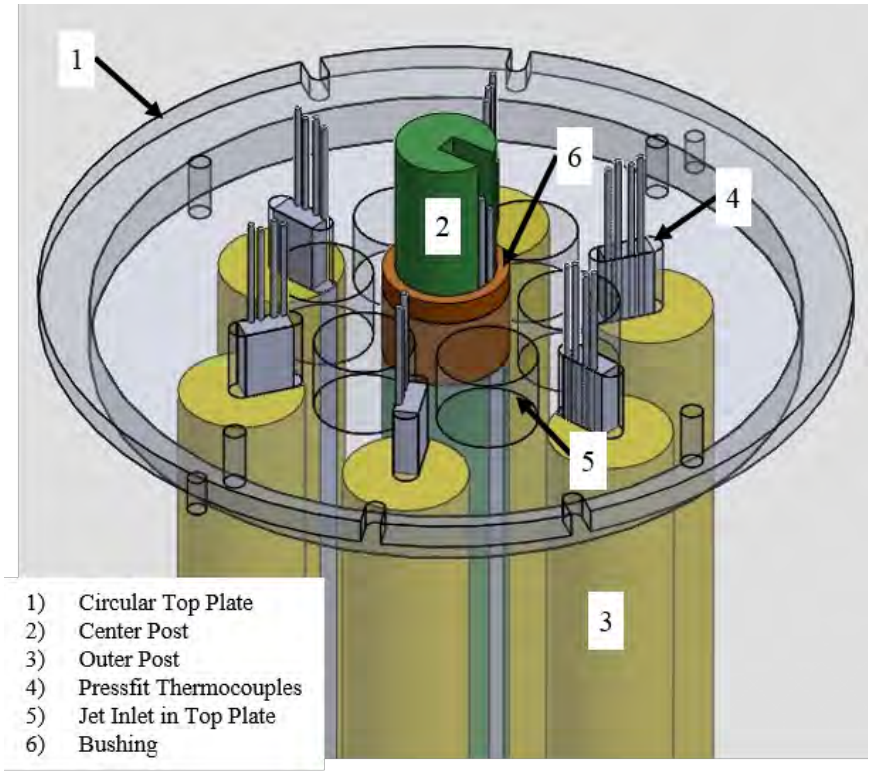

Figure 2-13: Transparent circular top plate with post configuration

Shown in Figure 2-14 are the manifolds used to connect the six jets to the flow motivation skid detailed in the previous section. This allows for up to three unique jet temperatures to be independently controlled, as is required for Case B (Figure 2-8). Similarly, by utilizing just two manifolds it is possible to have only two unique temperatures so that Case A and C (Figure 2-8) can be studied. Flexible hosing is used to connect the manifolds to each jet. Also shown in Figure 2-14 is the stepper motor. The stepper

motor is connected via long shaft to the center post of the test section so that it can be rotated to allow for sampling radial temperature distributions at multiple azimuthal locations.

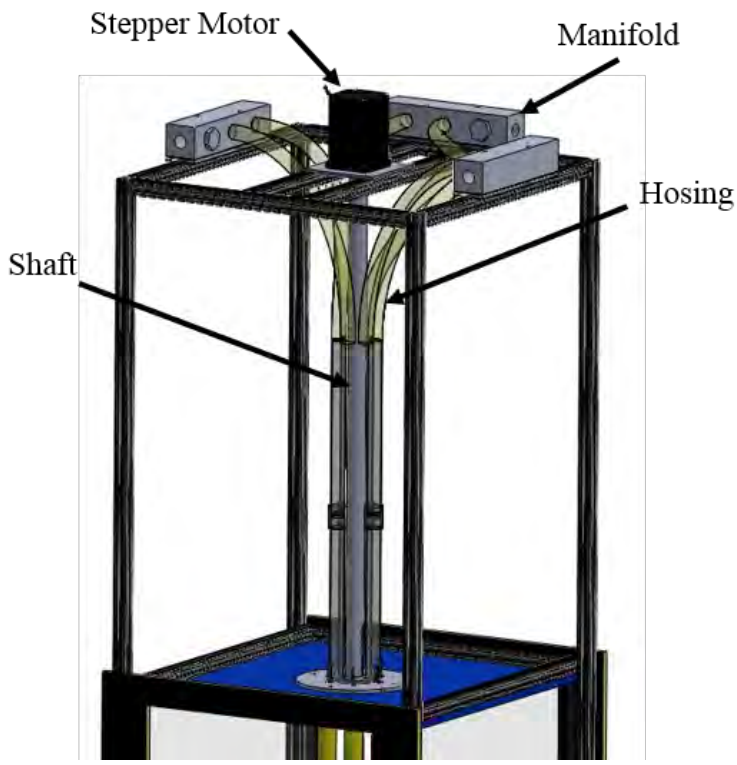

Figure 2-14: Stepper motor coupled to center post via a shaft

The last component designed was the diffuser. The diffuser design process was much simpler than that for the nozzle design since no flow conditioning characteristics need to be considered downstream of the test section. Therefore, a simple linear expansion was utilized to scale the ducting from the 0.61 m x 0.22 m cross section of the test section to that of the 0.91 m x 0.61 m ducting. For proper mating and convenient dimensioning, the diffuser is 1.22 m in length. The diffuser and the remainder of the ducting in the closed loop system, are all composed of stainless steel.

In addition to construction of the unit cell test section and cross flow conditioning setup, an ice-point reference facility has been built to act as a known temperature reference when measuring temperature with the thermocouples in the post, and is shown in Figure 2-15. The ice-point is comprised of an ice bath

placed in a refrigerator to increase the lifetime of the ice. The ice-point facility includes 30 type-T thermocouples, placed in the ice bath to act as reference junctions. In order to increase the ease of use, an input panel for type T measurement thermocouples equipped with mini-TC plugs is mounted to the side of the refrigerator. The facility uses a National Instruments TC-2095 32 Channel Thermocouple Connector, in conjunction with a SCXI-1102 32 Channel Thermocouple Amplifier, and SCXI-1600 USB Data Acquisition Module for gathering the thermocouple data. In experimental testing, the ice-point reference maintained 0°C – 0.1 °C for 56 hours, monitored using a high accuracy RTD with built in alarm (Control Company, Thermometer, LCD, -2 to 2°C).

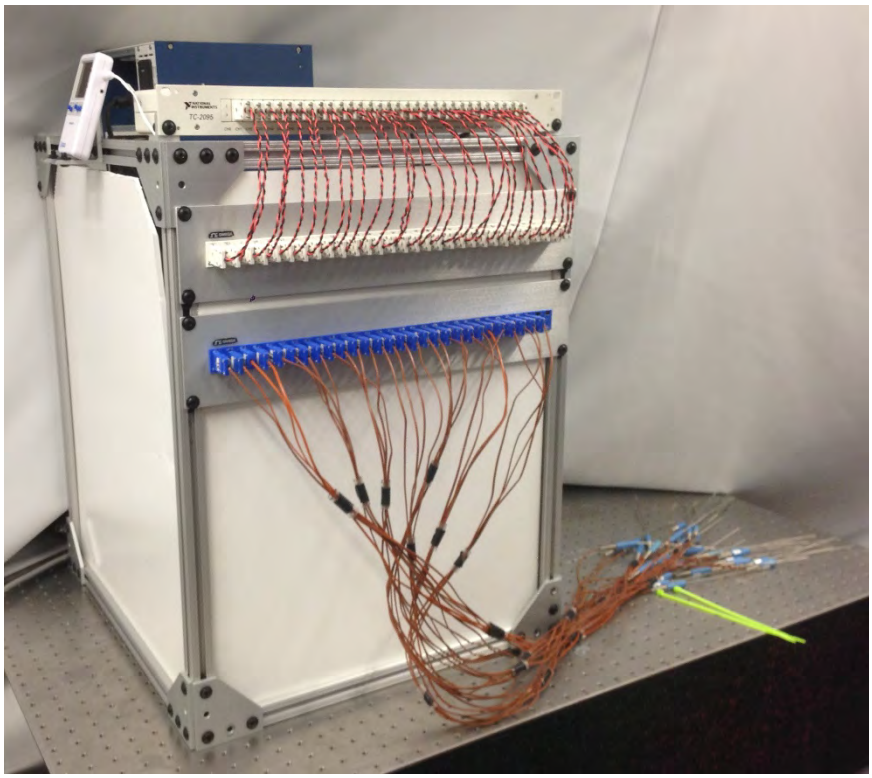

Figure 2-15. Ice point facility

With the inclusion of the ice point facility, the unit cell experimental facility design and fabrication is complete. The experimental facility is capable of creating experiments for jets, impinging jet arrays, jet array in cross flow, impinging jet in a crossflow, flow across a bank of cylinders, and the unit cell

experiment. As currently constructed, the unit cell experiment can accommodate up to six jets with Reynolds numbers ranging from 12,500 for the jets operating simultaneously, up to a maximum Reynolds number of 25,000 for a single jet. The cross-flow volumetric flow rate can reach 3.5 $m^3 s^{-1}$ for an average crossflow velocity of 35 m s^{-1} in the test section. For experimental measurements, the test section has been made of optically transparent polycarbonate for use with PIV while thermocouples have been press-fit in each post. Additionally, an ice-point reference facility has been constructed to aid with high-accuracy thermocouple measurements.

2.3 Characterization of Jet Flow Behavior

Special care was given to characterize the performance of a single jet before progressing to more complicated experiments. The previously designed flow skid was used to create a single jet. The captured single jet behavior provides both inlet data for RANS simulations, where both the mean velocity profile and kinetic energy profile are necessary to accurately capture trends in the jets. Furthermore, the single jet profiles provide a benchmark to which the triple jet inlet results can be compared and discussed.

2.3.1 Experimental Approach

In order to gather velocity measurements in the test section, a single-wire constant temperature anemometry (CTA) probe, Dantec Dynamics 55P16, was used. In order for the probe to be able to transverse the test section, a 3-axis, high temperature, linear stage setup, supplied by Parker Hannifan Inc, was used. The stages can travel 18 inches in the vertical direction, as well 10 inches in both directions within the horizontal plane. The origin of the coordinate system in this study is the center of the nozzle of the jet (i.e., entry point to the test section). The positive x axis is along the downstream direction of the jet. The positive y axis is defined as the direction away from the flow skid. The positive z axis is defined according to standard right hand rule convention based on the x and y axes. A sketch of the experimental test section, with stages included, is shown in Figure 2-16. This is a simplified illustration of the same test section previously shown in Figure 2-3.

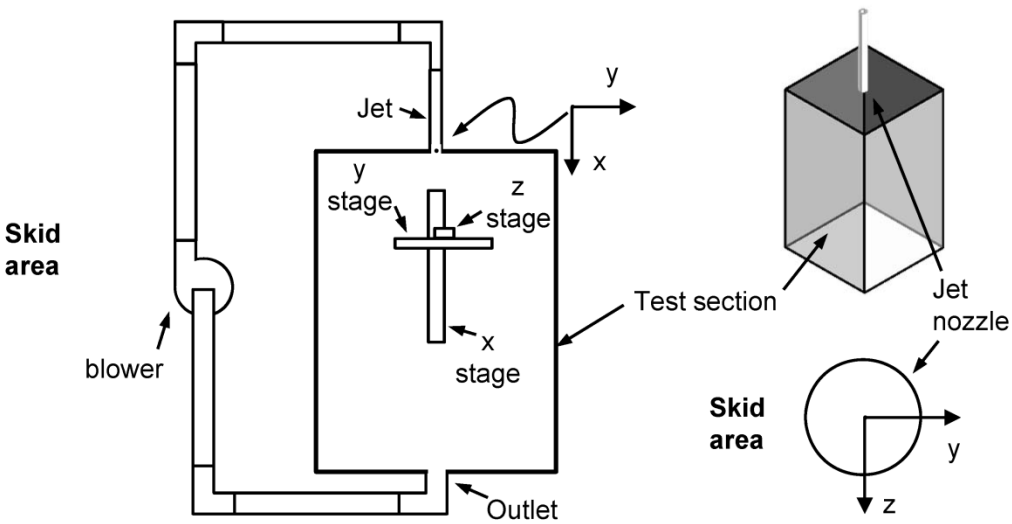

Figure 2-16. Illustration of experimental facility for studies for single round

It is desirable for experiments to have controlled, repeatable, and quantifiable conditions. Inability to meet these conditions can severely complicate quantifying and garnering new understanding into the physics involved. This is especially true when there are physical phenomena that are not yet understood. Some problems that need to be addressed in real flows are asymmetry, swirl, and non-uniform turbulent distribution. For the current work described here, special consideration is given to the first, asymmetry in the flow, with notes made regarding swirl and uniformity of turbulence. Shown in Figure 2-17(a) are velocity contours produced in the single jet experiment illustrated in Figure 2-16. In this case, only a straight pipe twenty hydraulic diameters (0.875 in) in length was used before the jet entered the test section. As seen, there are prominent asymmetries in the velocity profiles, as well as a slight offset in the direction away from the skid in the jet center relative to the axis of the measurement equipment. These issues can likely be resolved by increasing the upstream length of the pipe leading up to the nozzle. However, due to space constraints, this was not an option. Therefore, honeycomb flow straighteners were employed.

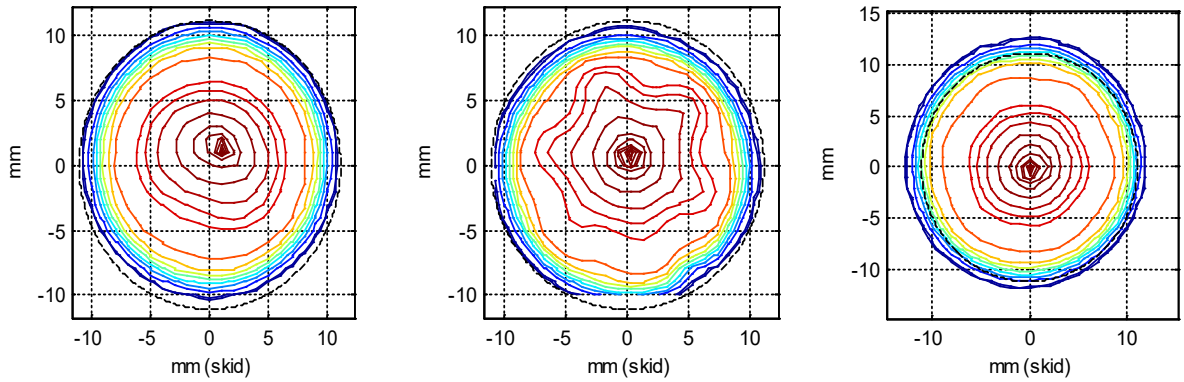

(a) (b) (c)

Figure 2-17. Qualitative velocity contours at x/D_{jet} = 0.33 for (a) straight pipe, (b) coarse honeycomb, and (c) refined honeycomb. The geometric extent of the round jet is depicted by a dashed line.

A number of prototypes were considered, consisting of different designs and materials. The first honeycomb prototype was constructed from a printed plastic, acrylonitrile butadiene styrene (ABS) utilizing fused deposition modeling (FDM). Unfortunately, poor surface finish and inadequate printing resolution created an insurmountable pressure drop which drastically reduced system performance. However, the second and third iteration of printed honeycomb, shown in Figure 2-18(a) and (b), respectively, were printed using stereolithography (SLA), which allowed much better surface finish as well as much better printing resolution.

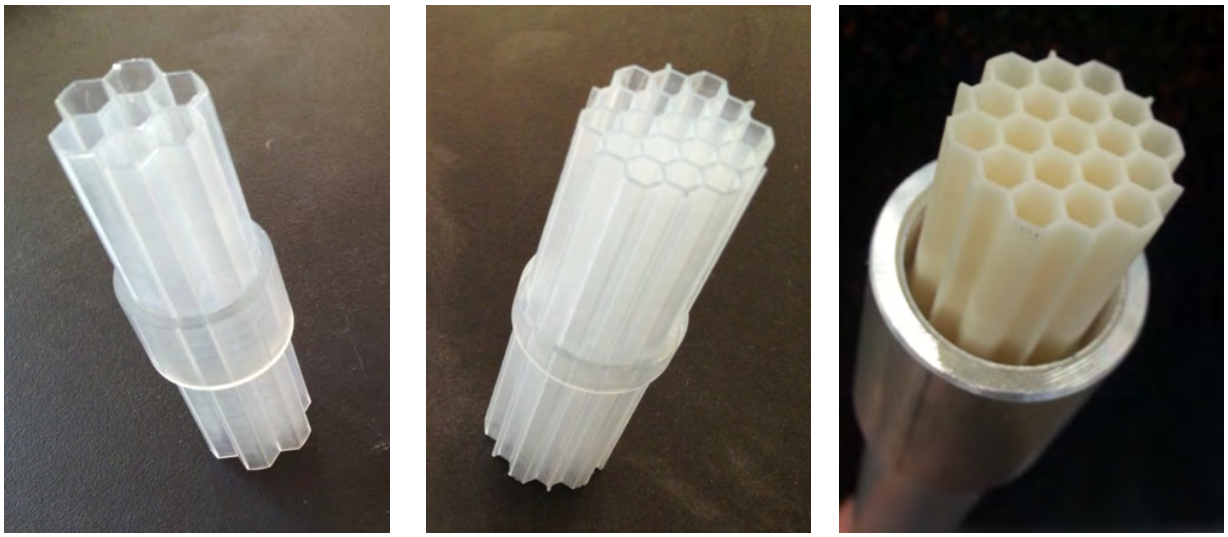

(a) (b) (c)

Figure 2-18. (a) Coarse honeycomb (b) refined honeycomb (c) ceramic honeycomb (shown in pipe coupling)

The first attempted prototype honeycomb printed in Figure 2-18(a), yielded the flow profiles seen in Figure 2-17(b). The honeycomb was designed with a hydraulic diameter of 0.26 in and a length of 11.5 hydraulic diameters. It was mounted in the pipe such that the flow develops ten pipe diameters before entering the honeycomb, and then has ten more pipe diameters to develop before entering the experimental test section. Unfortunately, these profiles strongly show the presence of the honeycomb within the pipe. In order to try and reduce the presence of the honeycomb on outlet flow profiles, a refined honeycomb with a hydraulic diameter of 0.15 in and a length of 20.2 hydraulic diameters was fabricated as shown in Figure 2-18(b), with the resultant flow profiles being shown in Figure 2-17(c). The refined honeycomb shows a much more symmetric profile. Additionally, the velocity contours, and subsequent downstream contours, do not exhibit any strong asymmetries or hexagonal pattern as observed before, suggesting a lack of asymmetric swirl and as seen later creating symmetric turbulent fluctuations. In order to accommodate the high temperatures capable of being achieved in the experimental facility, a high temperature ceramic, Samos® Nano Tool™, printed by FineLine Prototyping, was used to make six honeycombs for use in the unit cell and triple-jet experiments. These ceramic honeycombs are shown in Figure 2-18(c).

One method of experimental velocity measurement is constant temperature anemometry (CTA). The heat transfer from a long wire exposed to Joule heating is shown in Eq. (2-9), where Q is the power required to heat the wire, E is the wire voltage, R_w is the wire resistance, A is the surface area of the wire, T_w is the wire temperature, and T_∞ is the fluid temperature. From this expression, it can be seen that the wire voltage is dependent on the heat transfer coefficient, h. According to King's Law, the heat transfer coefficient for flow across a cylinder is proportional to the Reynolds number raised to an exponent. If the electrical circuity utilized to heat the wire can adaptively maintain the wire temperature, the voltage is a function of only the Reynolds number, or more specifically the velocity of the flow across the wire as shown in Eq. (2-10), where a, b, and c are curve fit coefficients. In Eq. (2-10), U_{ref} is 1 m s^{-1}. If the ambient temperature is not expected to vary, the term $T_w - T_\infty$ can be included in the curve fit coefficients a and c. For a detailed description of both the theoretical heat transfer and the signal conditioning electronics involved, see [36] and [37]. For the current work, the hot wire probe is a 5 μm gold plated wire manufactured by Dantec Dynamics, model 55P16. The signal conditioning box is a Dantec Dynamics 54T30 miniCTA.

$$Q = \frac{E^2}{R_w} = hA\left(T_w - T_\infty\right) \tag{2-9}$$

$$E^2 \propto \left(\mathrm{Re}^b + c\right)\left(T_w - T_\infty\right) \cong \left(a\left[\frac{|\mathbf{U}|}{U_{ref}}\right]^b + c\right)\left(T_w - T_\infty\right) \tag{2-10}$$

In order to express the output voltage of the CTA in terms of a velocity, the probe is first calibrated using the Dantec 54H10 hot-wire Calibrator. This is capable of creating flows ranging from 0.5 to 60 m/s. The CTA is placed in the center calibrator nozzle and approximately 10 velocities are considered ranging from 1.5 to 30 m s^{-1}. For the calibration, standard velocity is calculated relative to the pressure drop across a known geometry orifice plate. The fluid density is corrected for both the atmospheric pressure, measured

using a Conex Electro-Systems JDB-1 barometer (± 170 Pascal), and temperature, using a thermistor (± 0.2 K) internal to the calibrator. The pressure drop across the orifice plate is measured with a high-accuracy pressure transducer (Omega MMDWU10WV5P2D0T2A2) with an accuracy of 0.05 % of the full scale (10 in water column, or 2.5 kPa). Five independent tests were conducted to account for repeatability error. Shown in Figure 2-19 is a plot of the calibrator velocity versus the CTA voltage corrected using an average ambient temperature of 18.6 °C, gathered using a constant current anemometer (CCA). Note that T_w is the wire temperature, maintained at a constant 242 °C. The CTA curve fit is also shown.

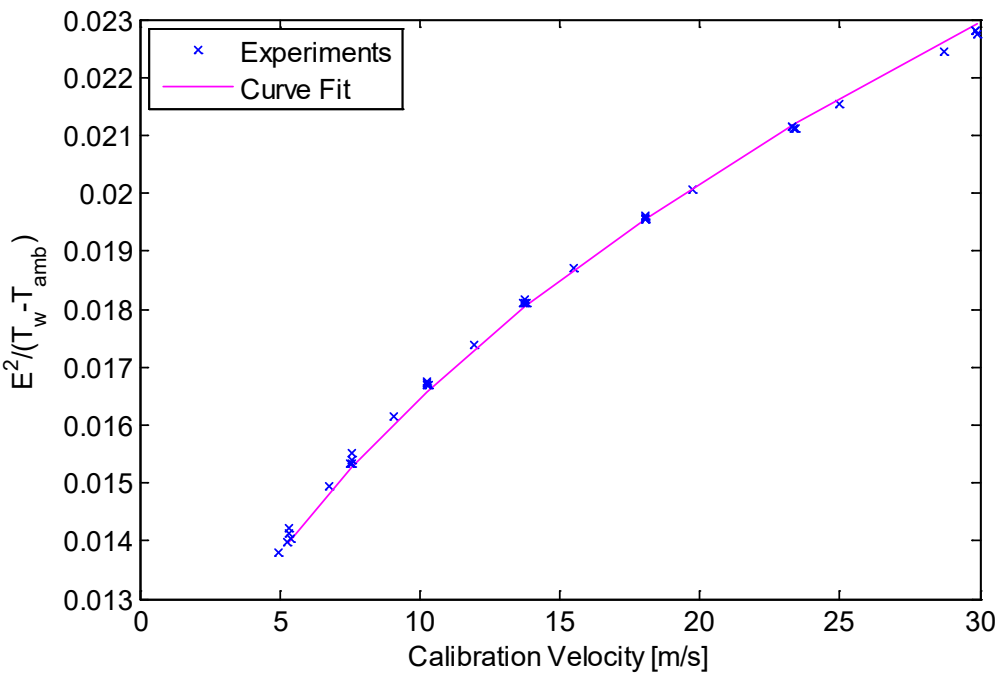

Figure 2-19. Calibration velocity versus CTA voltage corrected for temperature

For the CTA calibration, five separate voltage versus velocity curves were gathered in order to quantify the repeatability error. The average of each velocity is utilized in the calibration curve fit, the form of which is provided in Eq.(2-11), where V is the magnitude of the velocity, E is the voltage output from the CTA, which is captured via a data acquisition unit (National Instruments NI-9215A), and a, b, and c are the curve fit parameters found to be 0.003633 V^2/°C, 0.448, and 0.00627 V^2/°C, respectively. The experimental data and the corresponding curve fit are shown in Figure 2-19. The maximum error for the

curve fit is 22.10 %, while the mean absolute error for the curve fit is 2.42 %. Note that if velocities are less than 6 m s^{-1}, they are discarded due to the high uncertainty in pressure drop measurements. The mean absolute error for the curve fit of the resulting data is 2.14 % while the maximum error is 7.40 %. Figure 2-20 shows the calibration velocity versus that recovered via the curve fit. As is clearly seen, the data largely falls within 5% of the calibration velocity.

$$|\mathbf{U}| = \left(\frac{\frac{E^2}{T_w - T_\infty} - c}{a} \right)^{1/b} \tag{2-11}$$

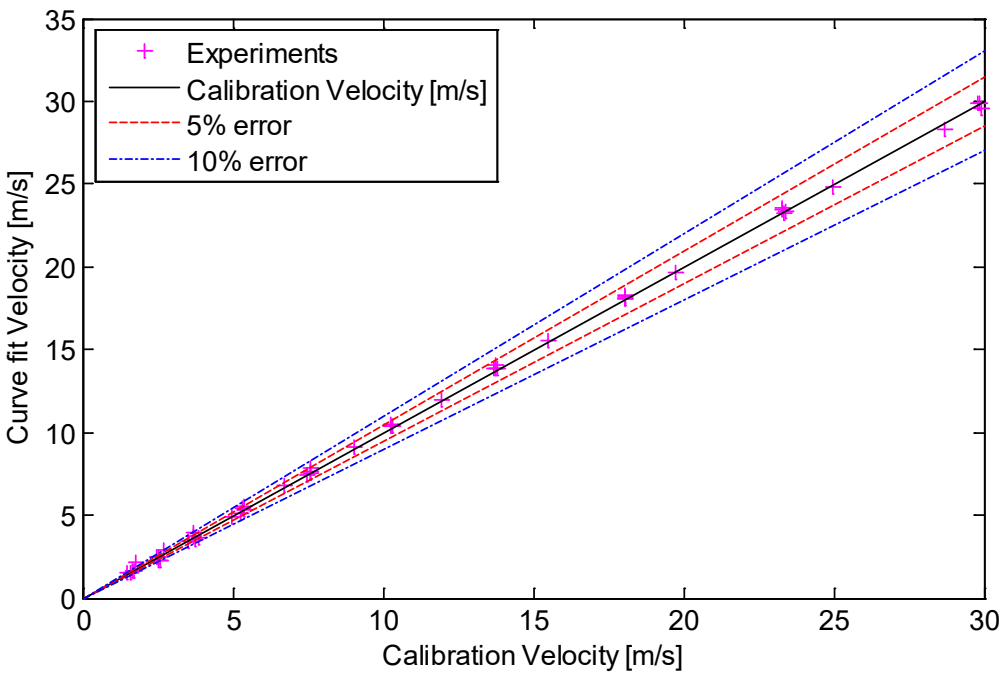

Figure 2-20. Comparison of calibration and predicted velocities

This calibration approach would be acceptable if the ambient temperature is held constant between the calibration and data acquisition steps, for the data to be collected as part of this project, the temperature difference could be as large as 50°C. The temperature differences in the domain drastically reduce the applicability of conventional hot-wire techniques, creating a need for new calibration procedures. Some

previous work has looked at increasing the applicability of CTA in non-isothermal flows, often by incorporating real time control of the wire temperature in order to fix the temperature difference in Eq. (10). However, such solutions often require hardware specifically designed for the flow being studied [36]. In order to study the effect of temperature on curve fit parameters a and c, multiple calibrations similar to that shown in Figure 2-19 were gathered for flows at various temperatures. The range of temperatures were created using a 3 kW Wattco Inc. submersion heater placed in-line with the Dantec Calibrator. For these flows, the fluid temperature was measured utilizing a higher-accuracy (±0.015°C) Omega RTD, Model HH42. Results from this study are shown in Figure 2-21, where the temperature corrected squared voltage is compared to the calibrator velocity. Not surprisingly, each unique temperature generates a different voltage and velocity relationship. A curve fit with constant coefficients would obviously introduce a large amount of error, and therefore the functional dependence of a and c with respect to temperature must be adequately captured.

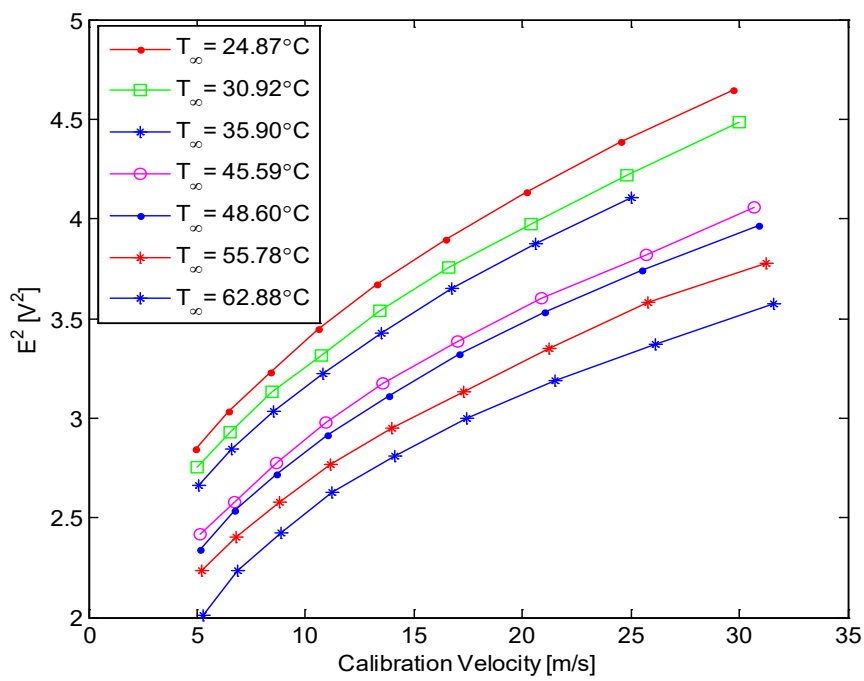

Figure 2-21. CTA calibration curves for heated flows

To address the errors when utilizing a constant curve fit, a temperature dependent curve fit was developed as shown in Eq. (2-12) where the temperature difference $(T_w - T_\infty)$ is now grouped in the coefficients $a(T)$ and $c(T)$, similar to the work in [36]. As suggested in that study, b is approximately 0.5 and independent of temperature. Moreover, a and c are expected to be linear functions of temperature. In order to check the functional dependence of a and c on temperature, each curve of data shown in Figure 2-21(a) were fit using a least squares regression. From the unique curve fit coefficients for each temperature curve, the average coefficient b was 0.3819. Then, fixing the exponential value b, the coefficients a and c are reevaluated. The new coefficients $a(T)$ and $c(T)$ are then fit linearly as a function of temperature. For the temperature dependent calibration, experimental data for 9 unique velocities and 7 unique temperatures was used as training data for the curve fits of a, b, and c. From the training data, the curve fits for $a(T)$ and $c(T)$, shown in Figure 2-22, are listed in Eqs. (2-13) and (2-14).

$$E^2 = a(T)\left(\frac{|U|}{U_{ref}}\right)^b + c(T) \tag{2-12}$$

$$a(T) = -0.0050\left[\frac{E^2}{°C}\right]T + 1.1140\left[E^2\right] \tag{2-13}$$

$$c(T) = -0.0117\left[\frac{E^2}{°C}\right]T + 1.3127\left[E^2\right] \tag{2-14}$$

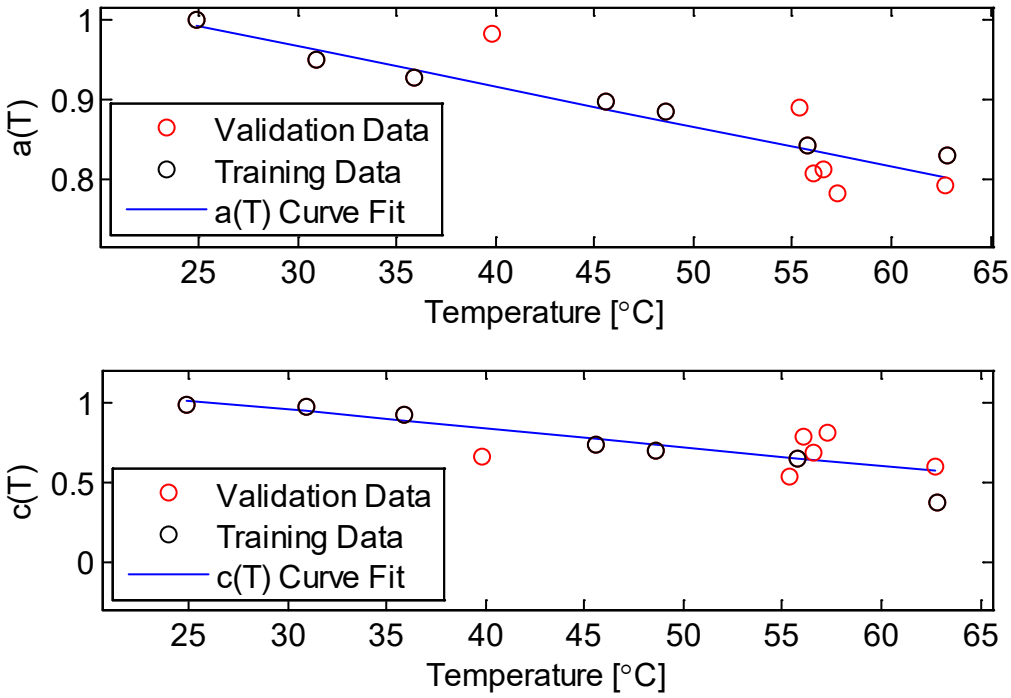

Figure 2-22. Temperature dependency of a and with curve fits shown

In addition to the training data, it was necessary to ensure the curves generated could adequately be used for all gathered data points, thus the 6 unique temperatures, each with 9 velocities, not used in the training data set are used as validation data. Additionally, to check for hysteresis and systemic errors, four different temperatures and four velocities were also gathered to be used as random data. Shown in Figure 2-23 is the curve fit velocity for the training data set, the data omitted from the training cases which was then used as validation data, and the random validation data set versus the calibration velocity. For the training data the mean absolute error was 3.68% while for all data sets the mean absolute error was 3.06%. Similarly, the maximum error for the training data and entire set of data is 15.7% and 17.7%, respectively, with both maximums occurring for the lowest velocity tested.

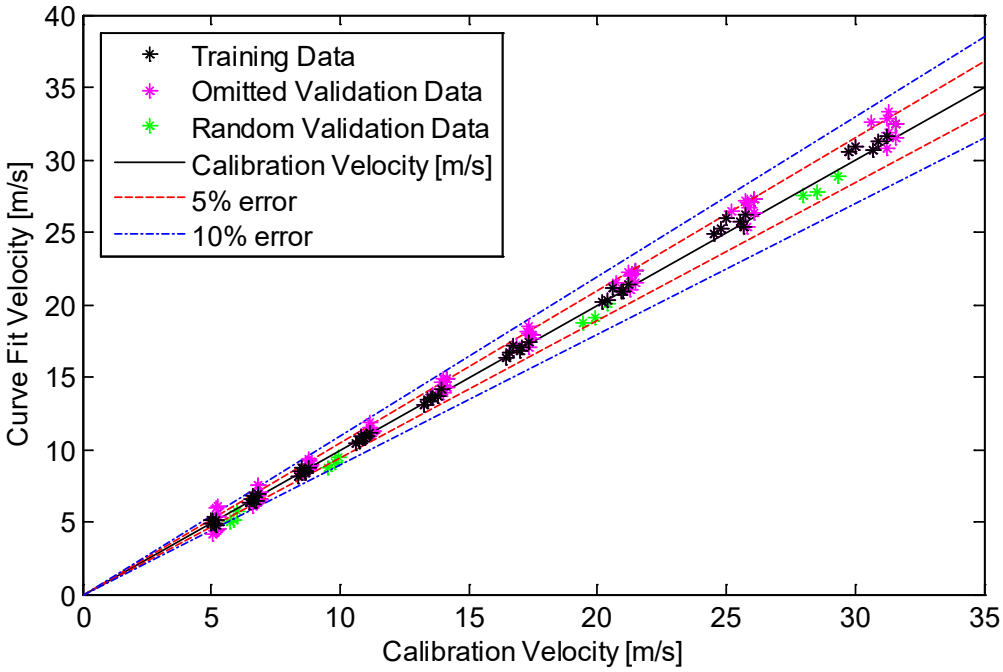

Figure 2-23. Curve fit velocity versus calibration velocity for all tested data

To correct for variation in ambient temperature from the calibration, the CTA was mounted in parallel with a constant current anemometer, referred to as the cold wire, as shown in Figure 2-24. Note that the CTA and CCA are located in parallel 4.76 mm apart. It should be noted that since the temperature and velocity measurement points are not co-located, errors exist by making that assumption. Cold wire signal conditioning was done utilizing an AA Lab Systems Inc. AN-1002 with Option 11, constant current anemometer mode. A second Dantec 55P16 5 μm gold plated wire was used for the cold wire. Calibration of the cold wire was achieved through separate experiments conducted in the actual facility. The temperature standards were taken from tightly-calibrated thermocouples placed at the direct center of the outlet of the jets. These temperatures were then used in conjunction with the CCA voltage gathered at each location to determine coefficients for a linear calibration curve for the cold-wire. For the remaining work in this section, the CCA curve fit was applied as shown in Eq. (2-15). The mean absolute error from the CCA curve fit was 1.9 %

$$T[°C] = 8.51\left[\frac{°C}{V}\right]E + 34.1[°C] \tag{2-15}$$

Figure 2-24. CTA and CCA two-wire probe

For the current work, both the CTA and CCA voltage were sampled at 2 kHz utilizing a NI-9215 BNC DAQ card. Since it is not possible to locate both wires in the same physical space, there is some offset that exists between the wires. For the probe mount designed, the CTA and CCA are located 4.76 mm apart. Multiple wire probes are available, but suffer from the same issue, namely collocated measurements are not truly possible. For reference, a specialty four-probe sensor (three for velocity and one for temperature) from Dantec Dynamics has an offset of 1.3 mm between the CCA and the center of the three CTA wires. Although this smaller offset could potentially be justified as zero under certain conditions, this must be carefully done. For the two sensor assembly used in the current study, two approaches for CTA temperature correction were considered. For the first method, it was assumed that the CCA and CTA experienced the same temperature and that all corrections to velocity can be applied in real time with the simultaneously sampled temperature field. This method is shown in Eq. (2-16) where the subscript i denotes simultaneously sampled data points while $\langle\ \rangle$ denotes the arithmetic mean. This will be referred to as the temporally congruent method. In regions where there exists a large temperature gradient, this correction method is expected to produce significant errors. The second methodology uses

collocated data points, with the assumption that temporal variation is not significant. Since the samples are no longer simultaneous only mean values for the CTA probe voltage and the CCA temperature are used, as illustrated in Eq. (2-17). This method is referred to as being spatially congruent. Note that when using mean data, any temporally dependent flow quantities, such as velocity fluctuation, cannot be calculated.

$$\left|\mathbf{U}_{\text{simultaneous}}\right| = \left\langle \left[\frac{E_i^2 - \left(c_1 T_i + c_2\right)}{a_1 T_i + a_2} \right]^{1/b} \right\rangle \tag{2-16}$$

$$\left|\mathbf{U}_{\text{collocated}}\right| = \left[\frac{\langle E \rangle^2 - \left(c_1 \langle T \rangle + c_2\right)}{a_1 \langle T \rangle + a_2} \right]^{1/b} \tag{2-17}$$

In order to quantify the error due to the limited spatial resolution of the probe, profiles for the mean velocity, calculated utilizing simultaneous but displaced data and using collocated but at separate times, were compared as shown in Figure 2-25(a) and (b), respectively, with contours of jet temperature shown in (c). For this data, the CTA and CCA wires were aligned with the z-axis with the CCA being displaced -4.76 mm from the CTA wire. For the quantification of jet profiles, only the line cooled by the heat exchanger was used, creating a single jet. Since these temperatures were relatively low (~ 30 °C) the presence of an ambient temperature gradient, most likely from the linear stage stepper motors, is observed in the $-z$ direction in Figure 2-25(c). When comparing the velocity profiles in (a) and (b), the most obvious difference is the oblong deformation in the $-y$-direction near the center of the jet when utilizing temporally congruent data. This error is expected due to the spatial resolution. To quantify this resolution, the profiles and their errors are compared and shown in Figure 2-26, where a positive error suggests that simultaneous temporal correction under predicts the velocity found using a collocated temperature correction, while oppositely a negative error suggests that the simultaneous correction method predicts a larger velocity than the mean correction method. As expected when considering the data presented in Figure 2-21(a), when the CCA is

in the warmer ambient fluid (near the $-z$ periphery of the jet), the simultaneous correction method under predicts the jet velocity. Conversely when the CCA wire "lags" behind the CTA and is still in the cold jet, the velocity is over predicted utilizing the simultaneous correction method.

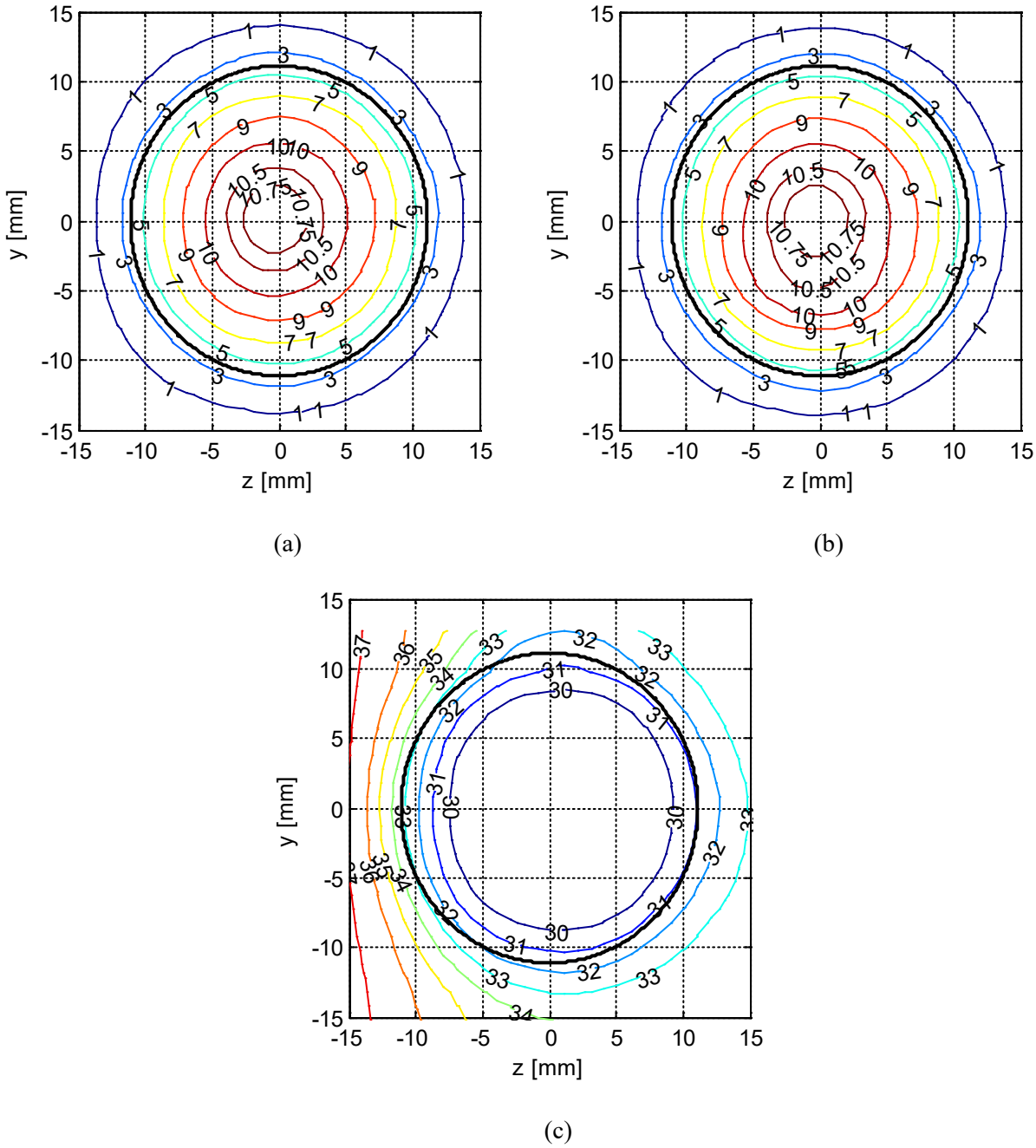

Figure 2-25. (a) Velocity magnitude with simultaneous temperature correction [m s^{-1}] (b) Velocity mangitude with collocated temperature correction [m s^{-1}] (c) Temperature [°C]. For each contour, the circular jet geometry is included for reference (solid black line, D_{jet} = 0.875 in (22.23 mm)). Re$_{jet}$ = 1.06 × 10^4

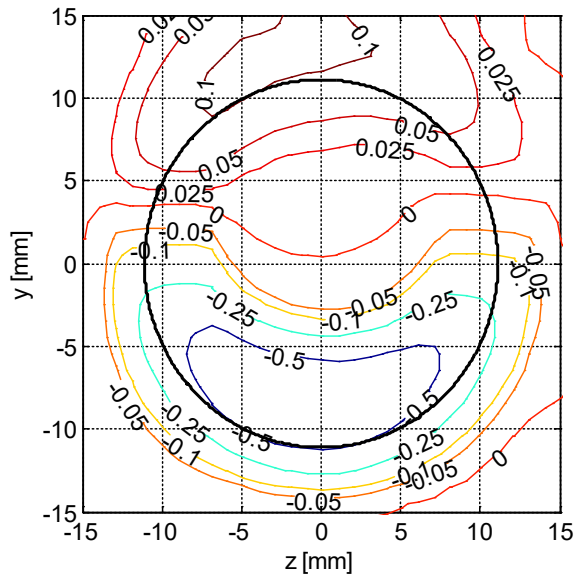

Figure 2-26. Error [m s^{-1}] between different velocity correction methods. The circular jet geometry is included for reference (solid black line, D_{jet} = 0.875 in (22.23 mm)). Re$_{jet}$ = 1.06 × 10^4

For the work in this investigation, it is generally preferred to measure velocity magnitude profiles using the collocated, spatially congruent temperature correction method introduced in Eq. (2-17). For the majority of conditions studied, there exists large temperature difference between the jets in the domain (~ 45 °C). In the presence of these large differences, and subsequently large temperature gradients, the simultaneous correction method creates unexpected artifacts in the jet profiles. This is easily seen for a typical triple jet experiment, results of which are shown in Figure 2-27(a). Note that the velocity ratio for this and all triple jet experiments is defined as $R = \frac{U_{0,cold}}{U_{0,hot}}$. The most drastic errors are seen on the $-y$-direction of all three jets. For comparison the mean corrected velocity profiles for the same case are shown in Figure 2-27(b). Note that for quantification of temporally dependent quantities, namely the fluctuating velocity magnitude and turbulent kinetic energy and turbulent intensity, it is necessary to use simultaneously corrected velocity magnitudes.

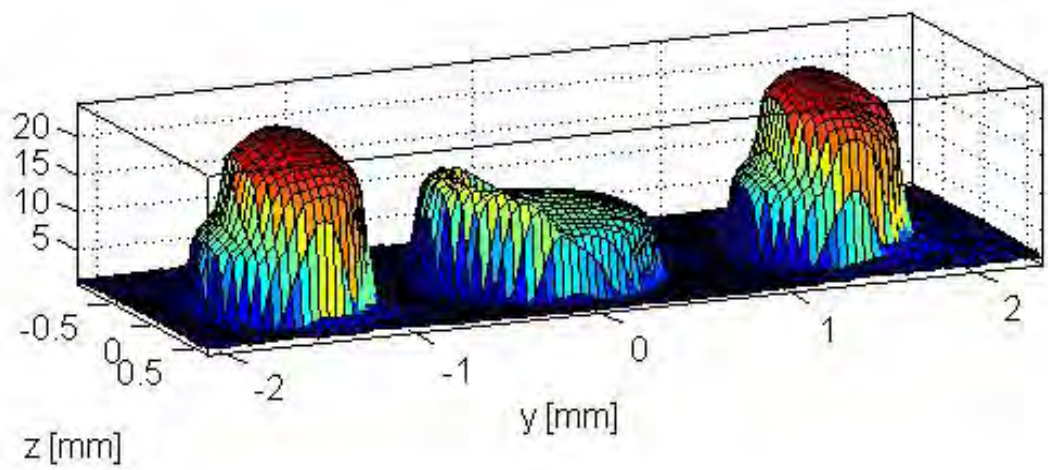

(a)

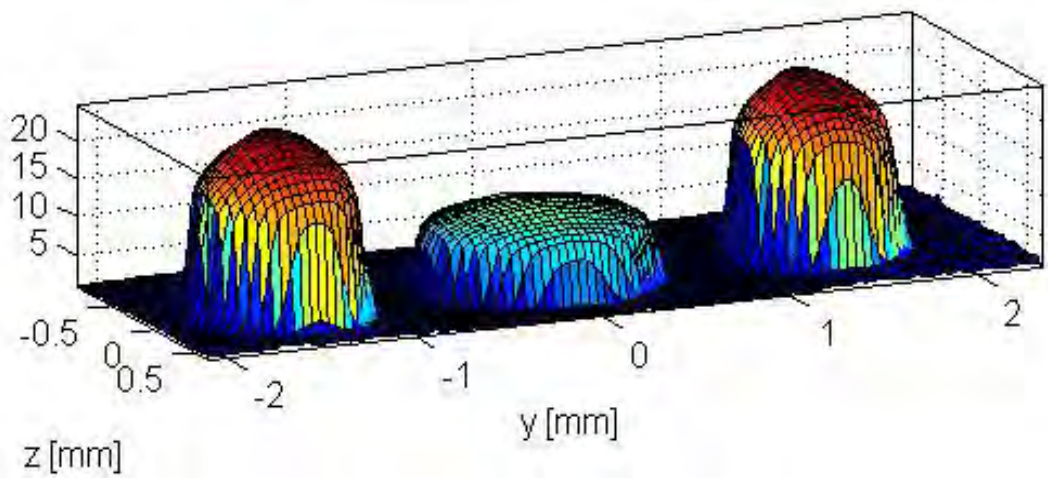

(b)

Figure 2-27. Triple-jet velocity magnitude for R = ½; ΔT = 60 °C (a) Velocity magnitude using simultaneous temperature correction (b) Velocity magnitude using collocated temperature correction.

2.3.2 Velocity Contours and Turbulence Quantification

Before studying more complex flow conditions, attributes of the single jet scenario are of interest. Extreme care is taken to ensure the jet enters completely normal to the test section, but in reality there could potentially be some misalignment between the jet and the linear stages upon which the CTA is mounted. Presently, a detailed examination of the inlet profiles for a single jet is conducted. Velocity data in the y–z plane are captured utilizing the temperature corrected single wire anemometer (Figure 2-24) at x/D_{jet} =

0.09 (slightly downstream of the jet nozzle). For these tests, the jet Reynolds number was Re_{jet} = 10.6 × 10^3 at 27 °C. Contours for the velocity, turbulent kinetic energy, and percent turbulent intensity are shown in Figure 2-28(a), (b), and (c), respectively. The black circle represents the outline of the jet nozzle. The jet is approximately a power law velocity profile, with the majority of the velocity decay occurring near the nozzle walls. For the turbulent kinetic energy (Figure 2-28(b)) and percent turbulence intensity (Figure 2-28(c)), the respective quantities are computed from the velocity data according to Eqs. (2-18) and (2-19). Similarly, surface plots for turbulent kinetic energy and percent turbulent intensity are shown in Figure 2-29(a) and (b), respectively. As shown in Figure 2-28(a) and Figure 2-29(a), the kinetic energy is approximately 0.1 $m^2\ s^{-2}$ near the center of the jet and increases to a peak value of approximately 0.2 $m^2\ s^{-2}$ just inside of the diameter of the jet, then decreases to a very small value outside the jet where the mean velocity is close to zero. Very similar trends are seen for percent turbulent intensity in Figure 2-28(b) and Figure 2-29(b). Note that the average turbulent intensity over the diameter of the jet is 8.55 %. For future studies where the experimental data will be used to validate numerical modeling efforts, it is ideal to have a symmetric, easy to quantify profile. The setup, in its current configuration, meets these requirements.

$$k = \frac{1}{2}\left\langle |\mathbf{U}| - \langle |\mathbf{U}| \rangle \right\rangle^2 \tag{2-18}$$

$$I\% = \frac{\left\langle |\mathbf{U}| - \langle |\mathbf{U}| \rangle \right\rangle}{\langle |\mathbf{U}| \rangle} \cdot 100 \tag{2-19}$$

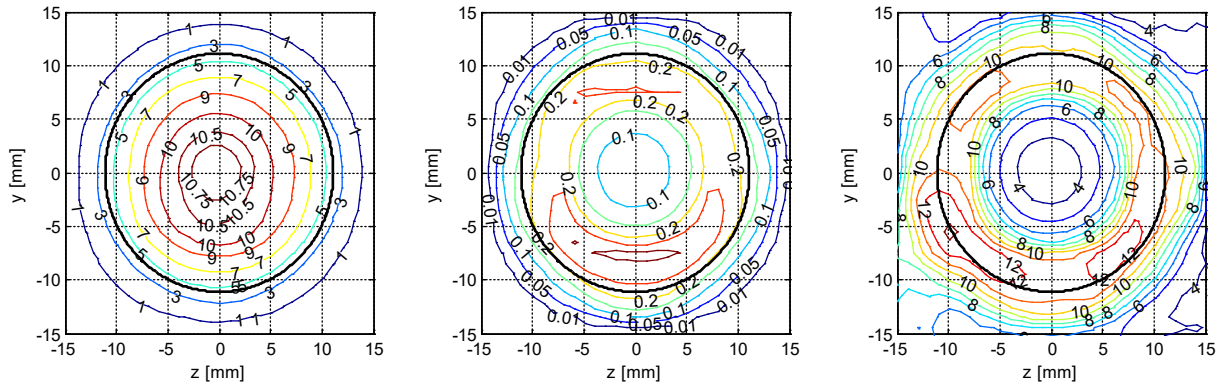

(a) (b) (c)

Figure 2-28. Contours at x/D_{jet} = 0.09. (a) Simultaneously corrected velocity magnitude (m s^{-1}), (b) turbulent kinetic energy (m^2 s^{-2}), and (c) percent turbulence intensity. For each contour, the circular jet geometry is included for reference (solid black line, D_{jet} = 22.23 mm). Re$_{jet}$ = 1.06x10^4

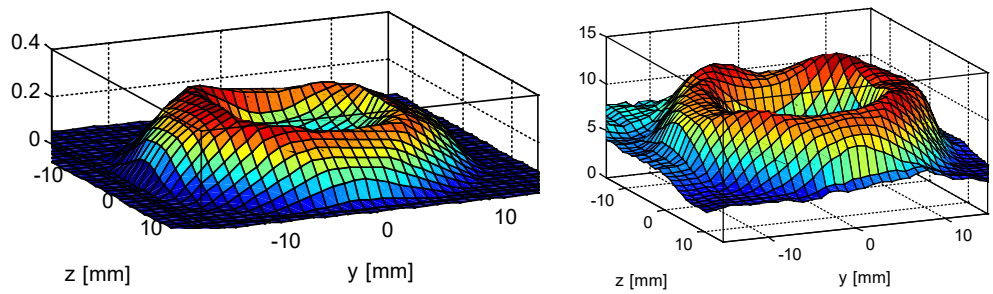

(a) (b)

Figure 2-29. Surface plots of single jet contours. (a) Turbulent kinetic energy [m^2 s^{-2}] (b) Percent turbulent intensity

2.3.3 Quantification of Jet Profile

It is important to be able to gauge and quantify the asymmetries in a manner other than a visual estimate, as well as to find an appropriate, axisymmetric curve fit. Here, it is chosen to analyze velocity data traces from six distinct lines in the contours: negative y-axis, positive y-axis, negative z-axis, positive z-axis, quadrant one (positive z, positive y) diagonal cut, and quadrant 3 (negative z, negative y) diagonal cut, as shown in Figure 2-30. This creates eight unique lines, representative of four lines "folded" onto themselves. If the jet were perfectly symmetric, these eight lines would lie exactly on top on each other.

This data is shown for the x/D_{jet} = 0.09 plane in Figure 2-31, where the velocities have been normalized by the centerline value (U_0). Investigating the data near the periphery of the jet, near r/D_{jet} = 0.5 reveals that the velocity has dropped to 20 % of the centerline velocity. In order to fit the data, a power law relationship was chosen as suggested by Schlichting [38]. It has been shown that the coefficient of the power law, n in Eq. (2-20) varies as a function of the Reynolds number; for example, Mi [39] found n = 6.5 in experiments. Pope [40] suggests the dependency of n on Reynolds number can be given by Eq. (2-21), which for the given flow of Re_{jet} = 10.6 × 10^3 yields n = 5.178. In order to account for variability in the power law coefficient, a least squares regression method was utilized. Fitting the data for 0 < $|r/D_{jet}|$ < 0.45 (90 % of the diameter of the jet), it was found that m = 1.139 with n = 6.12 and a R^2 = 0.9889. As reported, the calculated power law does not agree with that suggested by Pope. This is likely do to variations in the flow conditions upstream of the jet. Moreover, this could possibly suggest the experimental profiles are not fully developed. Investigating the curve fit, for over 90% of the domain, the mean absolute error was 0.78% with a maximum curve fit error of 3.87%, occurring at the outer most points. For comparison, several different curve fits and data ranges were tested. The results, in conjunction with those in Figure 2-28, show that the facility produces a jet with a predictable and acceptable mean velocity profile.

$$\frac{|\mathbf{U}|}{U_0} = m\left|\frac{r}{D_{jet}} - \frac{1}{2}\right|^{1/n} \tag{2-20}$$

$$\frac{1}{n} = \frac{1.085}{\ln \mathrm{Re}} + \frac{6.535}{(\ln \mathrm{Re})^2} \tag{2-21}$$

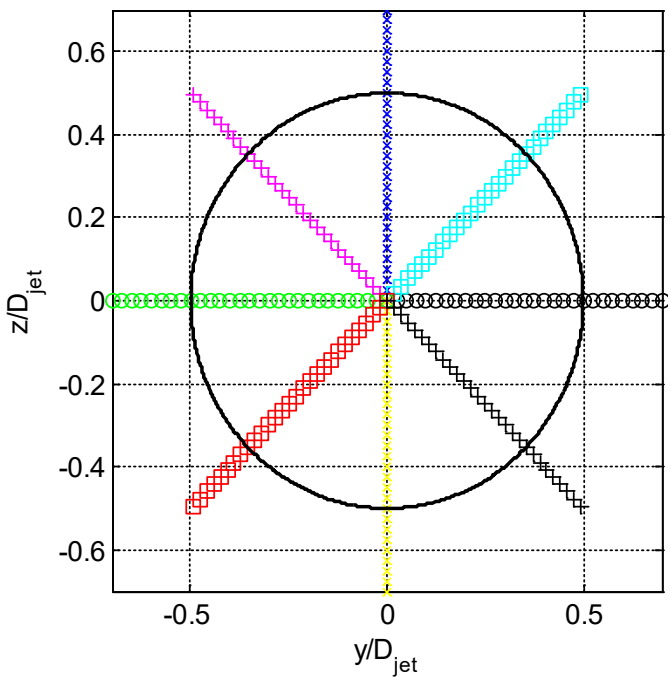

Figure 2-30. Schematic of line traces used to analyze single jet

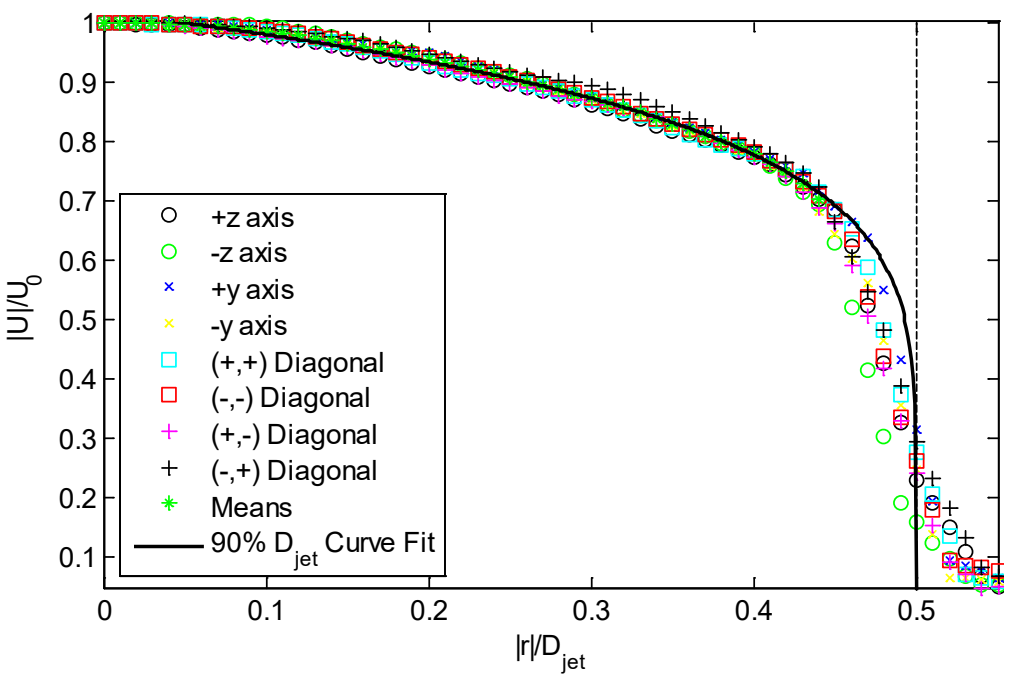

Figure 2-31. Normalized velocity contours "folded" on each other with curve over 90% D_{jet} for x/D_{jet} = 0.09 for Re_{jet} = 10.6 × 10^3, U_0 = 13.78 m s^{-1}

To further validate the curve fit present, the mass flow rate of the jet was considered. The equation for the mass flow rate is given in Eq. (2-22), where m and n are the same as in Eq. (2-20), 1.139 and 6.12, for the present case, and U_0 is the centerline velocity, equal to 13.78 m s^{-1} for the single jet study. For the given test case, the theoretical volumetric flow calculated from Eq. (2-22) is 0.00432 m^3 s^{-1}. Using Sampson's rule to integrate the numerical results shown in Figure 2-25(b), an approximation to the volumetric flow rate present in the experiment is determined. Considering only those points within the diameter of the jet, the experimentally measured volumetric flow rate is 0.004249 m^3 s^{-1}. For the given study, the flow rate was set in the PLC controller to 6.37 cfm (0.003006 m^3 s^{-1}). This suggests the error between the measured volumetric flow rate and the programmed/expected mass flow rate is 43.7 %. Additionally, using the programmed volumetric flow rate, the peak velocity estimated via the curve fit shown in Eq. (2-20) was 9.58 m s^{-1}, suggesting the peak velocity was over-estimated by 43.8 %.

$$\dot{V} = 2\pi \int_0^{\frac{D_{jet}}{2}} U_o m r \left| \frac{r}{D_{jet}} - \frac{1}{2} \right|^{1/n} \partial r \tag{2-22}$$

This seemingly large error can be attributed to a shift in the AN-1002 CCA signal conditioning box, which is a highly-sensitive electronic device. Unrelated to the current work, the laboratory was relocated, and the original calibration curve was no longer valid. As previously noted, a small error in temperature compensation can yield large differences in predicted velocities from the CTA. In order to address this calibration shift, a set of triple-jet experiments were performed and the calibration adjustments were made in response to the known temperatures (measured with tightly calibrated thermocouples) and known flow rates (quantified by the PLC controller, whose error is negligible compared to that of the temperature compensated velocity calibration approach). The triple-jet experiments used for this calibration shift are listed in Table 2-4. Note that the distance between the jets was large so that the velocity and temperature just downstream of the nozzle are assumed to be isolated from the neighboring jets.

Table 2-4. Velocity and temperature calibration experiments

R	x/D_{jet}	S/D_{jet}	$\dot{V}_{cold}$ [m^3/s]	U_{cold} [m/s]	$\dot{V}_{hot}$ [m^3/s]	U_{hot} [m/s]	ΔT [°C]
½	0.09	3.00	1.06 x10^4	9.59	6.07 x10^{-3}	19.18	22.2
½	0.09	3.00	1.06 x10^4	9.59	6.07 x10^{-3}	19.18	44.4
½	N/A	3.00	3.06x10^{-3}	9.59	6.07 x10^{-3}	19.18	44.4
½	N/A	3.00	3.06x10^{-3}	9.59	6.07 x10^{-3}	19.18	11.1

In order to account for the shift in temperature, a correction to the original equation was investigated according to Eq. (2-23), where α represents a proportional correction to the measured temperature and β represents a bias error. In order to quantify these error correction factors, it is necessary to trust velocity measurements exiting in the jets. As such, only cases where the jets are spaced sufficiently far apart enough that effects are not expected near the inlet are utilized. This is then done utilizing the experiments in Table 2-4. First, utilizing the curve fit equations m and n from the non-corrected Eq. (2-17), the peak expected velocity, based on the flowrate programmed into the PLC, was found. Then, utilizing these peak velocities α and β were found utilizing a least-squares regression method. Next, an iterative procedure was utilized where the peak expected velocities were updated using Eq. (2-23), then the coefficients were solved for again. This procedure was repeated multiple times until the coefficients no longer changed with subsequent iterations. The final coefficients were found to be α = 1.0498 and β = -9.7035 °C. Before applying the temperature correction factors, the maximum and mean absolute error between the measured velocity and expected velocity was 28.1% and 21.3%, respectively. After applying the correction factors to the calibrated data set, the max and mean absolute errors were 3.8 % and 1.0 %, respectively.

$$U = \left[\frac{\langle E \rangle^2 - a\left(\langle \alpha T + \beta \rangle\right)}{c(\langle \alpha T + \beta \rangle)} \right]^{\frac{1}{b}} \tag{2-23}$$

Reinvestigating the velocity profiles, given the new correction technique, a power law fit of the same from originally used was applied with the constants m = 1.141 and n = 5.874. Utilizing the new curve fit coefficients, the expected peak velocity, based on the skid flow rate, is 9.65 m s^{-1}. The peak measured velocity is 11.22 m s^{-1} for a 16.3% error. Calculated as done before, the measured volumetric flow rate was

0.0034 m^3 s^{-1}, which compared to the flow rate programmed into the skid of 0.0031 m^3 s^{-1}, yields an error 11.1%. Note that the temperature correction factors α and β were used when creating all of the previous velocity plots and contours.

After quantifying the velocity profile, attention was given to quantifying the temperature profiles in the jets. As shown in Figure 2-32, the same eight unique traces of the jet temperature were "folded" on top of each other and compared. Since the jet temperature deviates only slightly from the ambient, there is a steady heat up of the jet in the $-z$ direction as observed for all traces originating in the $-z$-hemisphere of the jet. Note that across 90% of the jet diameter, the mean temperature of the slices varies by 2.6% of the centreline temperature. For this reason, the jet was qualitatively considered to have a tophat temperature profile. Rigorous efforts are not spent to quantify the jet temperature profile for this case, but is given additional attention in all triple-jet experiments where the ambient temperature in the test section differs more subsequently from the jet temperatures. Moreover, it will be convenient to non-dimensionalize the temperature profile, which is more straight forward when there are two constrained jet temperatures in the domain.

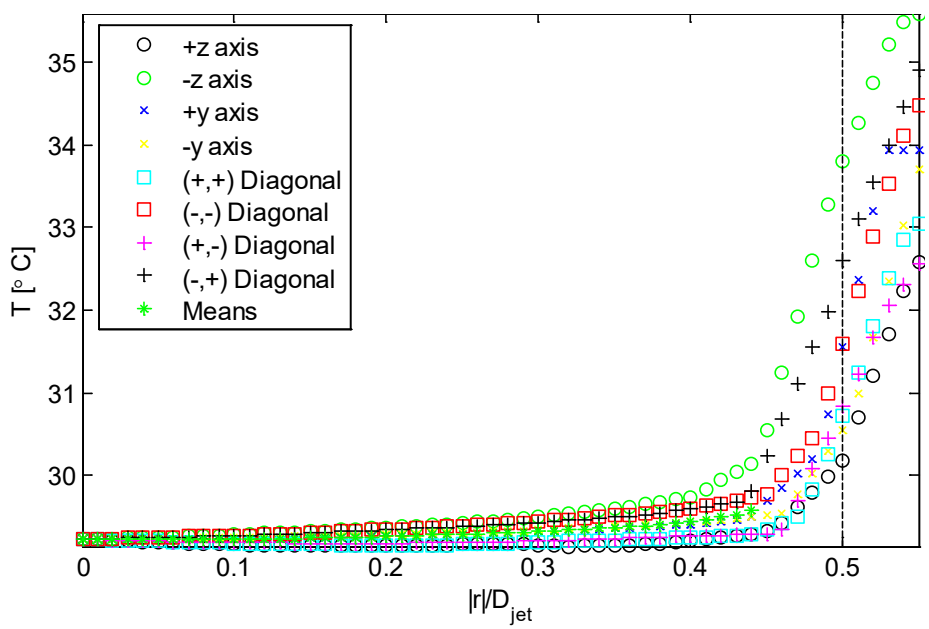

Figure 2-32. Temperature contours "folded" on each other with curve over 90% D_{jet} for x/D_{jet} = 0.09 for Re_{jet} = 10.6 × 10^3, U_0 = 13.78 m s^{-1}

2.4 Measurements in a Parallel Triple-Jet

Of primary interest in parallel triple-jets is turbulent mixing between the jets. This phenomenon in non-isothermal flows is thought to influence thermal striping in support components in the VHTR, as well as serve to prevent thermal stratification in piping connections. However, properly studying turbulent mixing can be difficult in experimental studies utilizing constant temperature anemometry. When considering a single-wire anemometer, only the magnitude of velocity, and its fluctuation, can be gathered, opposed to individual components of the velocity and the respective fluctuations. One improvement to single-wire anemometry is three-wire anemometry, where three orthogonal, simultaneous velocity measurements are captured corresponding to the entire velocity vector at a point. For the present work, the custom built two-wire CTA and CCA probe was utilized with temperature dependent curve fits. In order to study the flow in a round parallel triple-jet, a matrix of experiments was gathered in separate horizontal and vertical measurement planes. Multiple horizontal planes of data were acquired at different downstream distances. For the vertical plane data sets, each was gathered on the $y = 0$ plane. A list of the cases studied is shown in Table 2-5 and Table 2-6. In Table 2-5, the case $R = \infty$ is the case of a single free jet analyzed as previously discussed while in Table 2-6, the case $R = 0$ is the case of a round twin-jet.

Table 2-5. Matrix of cases mapped in horizontal plane

Y-Z Plane Experiments								
#	R	x/D_{jet}	S/D_{jet}	$\dot{V}_{cold}$ [m^3/s]	Re_{Cold}	$\dot{V}_{hot}$ [m^3/s]	Re_{Hot}	ΔT [°C]
H1	1/2	0.09	1.41	3.08x10^{-3}	1.05 x10^4	6.07 x10^{-3}	1.93x10^4	44.4
H2	1/2	5.09	1.41	3.08x10^{-3}	1.05 x10^4	6.07 x10^{-3}	1.93x10^4	44.4
H3	1/2	10.09	1.41	3.08x10^{-3}	1.05 x10^4	6.07 x10^{-3}	1.93x10^4	44.4
H4	1/2	0.09	3.00	3.08x10^{-3}	1.05 x10^4	6.07 x10^{-3}	1.93x10^4	44.4
H5	1/2	0.09	3.00	3.08x10^{-3}	1.05 x10^4	6.07 x10^{-3}	1.93x10^4	22.2
H6	∞	0.09	N/A	3.08x10^{-3}	1.05 x10^4	N/A	N/A	N/A

Table 2-6. Matrix of cases mapped in vertical plane through jet centerline

X-Z Plane Experiments							
#	R	S/D_{jet}	$\dot{V}_{cold}$ [m^3/s]	Re_{Cold}	$\dot{V}_{hot}$ [m^3/s]	Re_{Hot}	ΔT [°C]
V1	0	2.81	N/A	N/A	6.07 x10^{-3}	1.93x10^4	N/A
V2	1/2	1.41	3.06x10^{-3}	1.05 x10^4	6.07 x10^{-3}	1.93x10^4	44.4
V3	1/2	1.41	3.06x10^{-3}	1.07 x10^4	6.07 x10^{-3}	2.05x10^4	22.2
V4	1/2	3.00	3.06x10^{-3}	1.05 x10^4	6.07 x10^{-3}	1.93x10^4	44.4
V5	1/2	3.00	3.06x10^{-3}	1.07 x10^4	6.07 x10^{-3}	2.11x10^4	11.1
V6	1	1.41	6.07 x10^{-3}	2.15x10^4	6.07 x10^{-3}	1.96x10^4	44.4
V7	1	1.41	3.06x10^{-3}	1.06 x10^4	3.06x10^{-3}	9.66x10^3	44.4
V8	2	1.41	6.07 x10^{-3}	2.16x10^4	3.06x10^{-3}	9.73x10^3	44.4
V9	2	1.41	6.07 x10^{-3}	2.17x10^4	3.06x10^{-3}	1.02x10^4	22.2
V10	4	1.41	1.51x10^{-3}	5.31x10^3	6.07 x10^{-3}	1.93x10^4	44.4

2.4.1 Error Assessment of Triple-Jet Measurements

The first cases ran were those listed in Table 2-5. For these cases, the probe transverses in the y-z plane. Both CTA and CCA data were gathered simultaneously with a sample rate of 2 kHz at 1 mm increments in space. Data was gathered beyond the periphery of both jets to ensure that all important trends were captured. Shown in Figure 2-33 is case H1, where R = ½ and ΔT = 44.4°C. It is observed that the center jet velocity profile appears to be wider than expected. To validate the accuracy of the measurements found after application of the temperature corrected curve fit, they were compared against the controlled volumetric flow rate from the skid. Using Simpson's rule for numerical integration on the measured velocity profile, the flow rate was calculated to be 0.01622 m^3 s^{-1}, while the flow skid controls were set at 0.01505 m^3 s^{-1} (a 7.9% difference). To check these sources of error, cases H4 and H5 were considered since they had a larger center-to-center jet spacing, and therefore represented a scenario where the influence of the outer jets on the center jet could be neglected at a downstream distance so close to the jet nozzle (x/D_{jet} = 0.09). In addition, these two cases represent two different temperature ratios, allowing the impact of this factor to be explored as well. Case H4 with R = ½, ΔT = 44.4°C, and S/D_{jet} = 3.0 is shown in Figure 2-34. For this case, the volumetric flow rate programmed into the skid is 0.01505 m^3 s^{-1} while the measured volumetric flow rate was 0.0162 m^3 s^{-1}, for an error of 11.4%. For Case H5 shown in Figure 2-37, which is

identical to case H4 except the temperature difference is reduced to ΔT = 11.1 °C, the experimentally measured volumetric flow rate was 0.0143 m^3 s^{-1}, for an error of 5.2 %.

With the large temperature gradients found in the triple-jet experiment, especially for spacings of $S = 1.41D_{jet}$, additional concern was spent investigating the difference in temporally congruent and spatially congruent velocity correction methods. As shown in Figure 2-36, the error is largest at the edges of the jets nearest the outlet. As measurements are taken further and further downstream, the effect of the limited spatial resolution of the probe is reduced due to the mixing of the jets. The largest error is approximately 8 m s^{-1} and exists when the CTA is located in the edge of the heated jets while the cold wire is still in the lower temperature ambient fluid. Further downstream near x/D_{jet} = 10.09 (Figure 2-36(c)), the largest absolute velocity difference is approximately 1.5 m s^{-1} and occurs in the mixing region between the two distinct hot jets. The spatially collocated temperature and velocity profiles used in generating Figure 2-36 are shown subsequently in Figure 2-37 and Figure 2-38. It is valuable for validation to compare expected inlet conditions with measured inlet conditions. The expected inlet conditions and the actual inlet conditions measured are presented in Table 2-7 and Table 2-8. The expected centerline velocity is calculated based on Eq. (2-22), where the volumetric flow rate is that programmed into the skid.

Table 2-7. Errors in experimental inlet conditions for vertical plane mapping

#	R	ΔT [°C]	S/D_{jet}	U_0 Expected [m/s]	U_0 Actual [m/s]	R Actual	T_{jet} [°C]	ΔT_{max} [°C]
H1	1/2	44.4	1.41	$U_{0,cold} = 9.59$ $U_{0,hot} = 19.18$	$U_{0,cold} = 12.18$ $U_{0,hot,1} = 24.18$ $U_{0,hot,2} = 24.64$	0.50	$T_{cold} = 32.81$ $T_{hot,1} = 72.97$ $T_{hot,2} = 72.22$	39.79
H4	1/2	44.4	3	$U_{0,cold} = 9.59$ $U_{0,hot} = 19.18$	$U_{0,cold} = 9.92$ $U_{0,hot,1} = 19.16$ $U_{0,hot,2} = 18.86$	0.52	$T_{cold} = 31.95$ $T_{hot,1} = 78.25$ $T_{hot,2} = 75.98$	45.16
H5	1/2	11.1	3	$U_{0,cold} = 9.59$ $U_{0,hot} = 19.18$	$U_{0,cold} = 9.63$ $U_{0,hot,1} = 19.60$ $U_{0,hot,2} = 19.31$	0.50	$T_{cold} = 29.39$ $T_{hot,1} = 39.66$ $T_{hot,2} = 40.39$	10.62
H6	∞	N/A	N/A	$U_{0,cold} = 9.59$	$U_{0,cold} = 13.77$	∞	$T_{cold} = 29.22$	N/A

Table 2-8. Errors in experimental inlet conditions for vertical plane mapping

#	R	ΔT [°C]	S/D_{jet}	U_0 Expected [m/s]	U_0 Actual [m/s]	R Actual	T_{jet} [°C]	ΔT_{max} [°C]
V1	0	N/A	2.82	$U_{0,hot} = 19.18$	$U_{0,hot,1} = 20.84$ $U_{0,hot,2} = 20.71$	N/A	$T_{hot,1} = 41.89$ $T_{hot,2} = 42.31$	N/A
V2	1/2	44.4	1.41	$U_{0,cold} = 9.59$ $U_{0,hot} = 19.18$	$U_{0,cold} = 11.96$ $U_{0,hot,1} = 24.25$ $U_{0,hot,2} = 24.11$	0.49	$T_{cold} = 32.94$ $T_{hot,1} = 73.01$ $T_{hot,2} = 72.28$	39.70
V3	1/2	22.2	1.41	$U_{0,cold} = 9.59$ $U_{0,hot} = 19.18$	$U_{0,cold} = 10.48$ $U_{0,hot,1} = 21.40$ $U_{0,hot,2} = 21.35$	0.49	$T_{cold} = 30.83$ $T_{hot,1} = 51.07$ $T_{hot,2} = 51.00$	22.30
V4	1/2	44.4	3.00	$U_{0,cold} = 9.59$ $U_{0,hot} = 19.18$	$U_{0,cold} = 10.03$ $U_{0,hot,1} = 19.35$ $U_{0,hot,2} = 19.21$	0.52	$T_{cold} = 31.41$ $T_{hot,1} = 77.54$ $T_{hot,2} = 75.39$	45.05
V5	1/2	11.1	3.00	$U_{0,cold} = 9.59$ $U_{0,hot} = 19.18$	$U_{0,cold} = 9.67$ $U_{0,hot,1} = 19.39$ $U_{0,hot,2} = 19.15$	0.51	$T_{cold} = 29.59$ $T_{hot,1} = 39.78$ $T_{hot,2} = 40.39$	10.49
V6	1 (Re_j = 21.2x103)	44.4	1.41	$U_{0,cold} = 19.18$ $U_{0,hot} = 19.18$	$U_{0,cold} = 22.89$ $U_{0,hot,1} = 22.57$ $U_{0,hot,2} = 22.37$	1.02	$T_{cold} = 31.48$ $T_{hot,1} = 72.67$ $T_{hot,2} = 71.96$	40.83
V7	1 (Re_j = 10.6x103)	44.4	1.41	$U_{0,cold} = 9.59$ $U_{0,hot} = 9.59$	$U_{0,cold} = 11.16$ $U_{0,hot,1} = 12.22$ $U_{0,hot,2} = 12.12$	0.92	$T_{cold} = 32.32$ $T_{hot,1} = 71.98$ $T_{hot,2} = 72.41$	39.87
V8	2	44.4	1.41	$U_{0,cold} = 19.18$ $U_{0,hot} = 9.59$	$U_{0,cold} = 22.88$ $U_{0,hot,1} = 12.44$ $U_{0,hot,2} = 12.11$	1.86	$T_{cold} = 30.51$ $T_{hot,1} = 69.21$ $T_{hot,2} = 69.50$	38.85
V9	2	22.2	1.41	$U_{0,cold} = 19.18$ $U_{0,hot} = 9.59$	$U_{0,cold} = 21.11$ $U_{0,hot,1} = 11.01$ $U_{0,hot,2} = 11.10$	1.91	$T_{cold} = 29.38$ $T_{hot,1} = 49.64$ $T_{hot,2} = 49.97$	20.43
V10	4	44.4	1.41	$U_{0,cold} = 19.18$ $U_{0,hot} = 4.79$	$U_{0,cold} = 22.54$ $U_{0,hot,1} = 6.66$ $U_{0,hot,2} = 6.47$	3.43	$T_{0,cold} = 30.19$ $T_{0,hot,1} = 69.90$ $T_{0,hot,2} = 70.28$	39.90

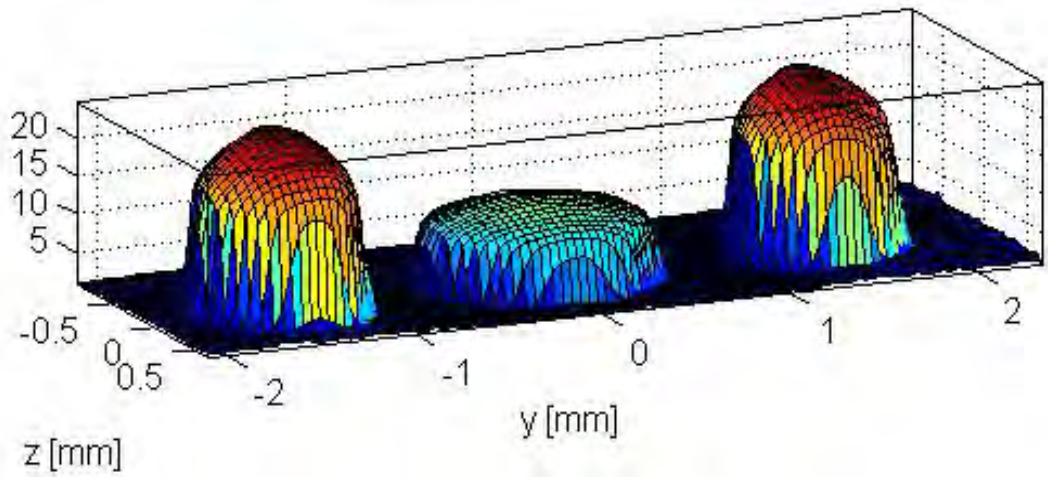

(a)

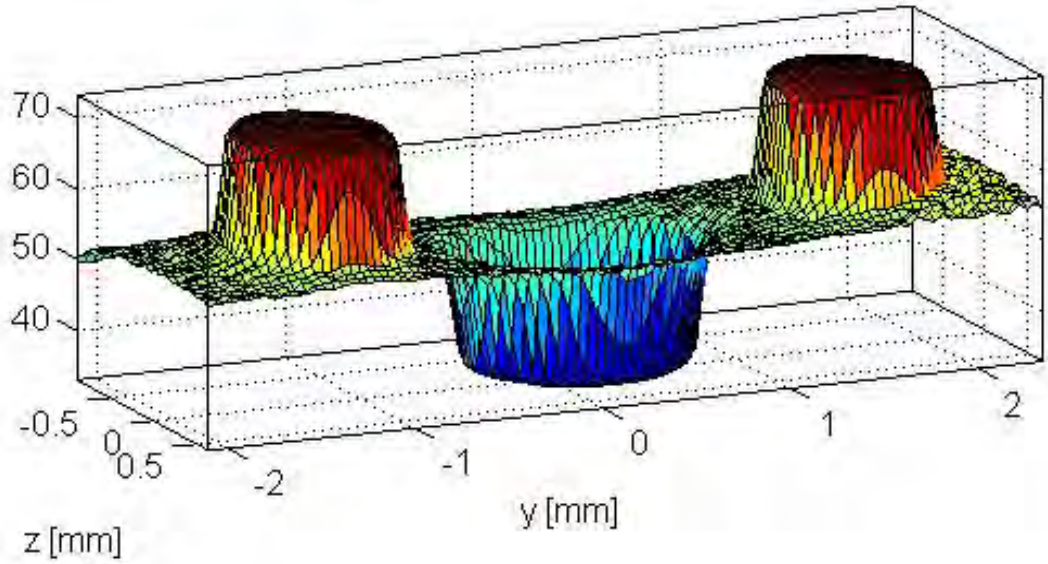

(b)

Figure 2-33. Case H1: R = ½, ΔT = 44.4 °C, S/D_{jet} = 1.41 measured at x/D_{jet} = 0.09 (a) profiles of velocity magnitude [m s^{-1}], and (b) temperature profiles [°C]

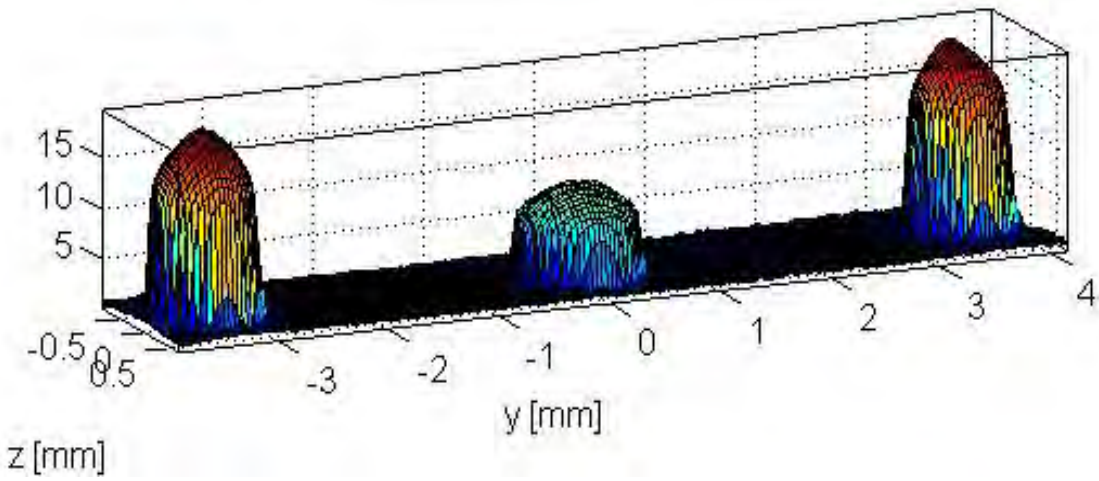

(a)

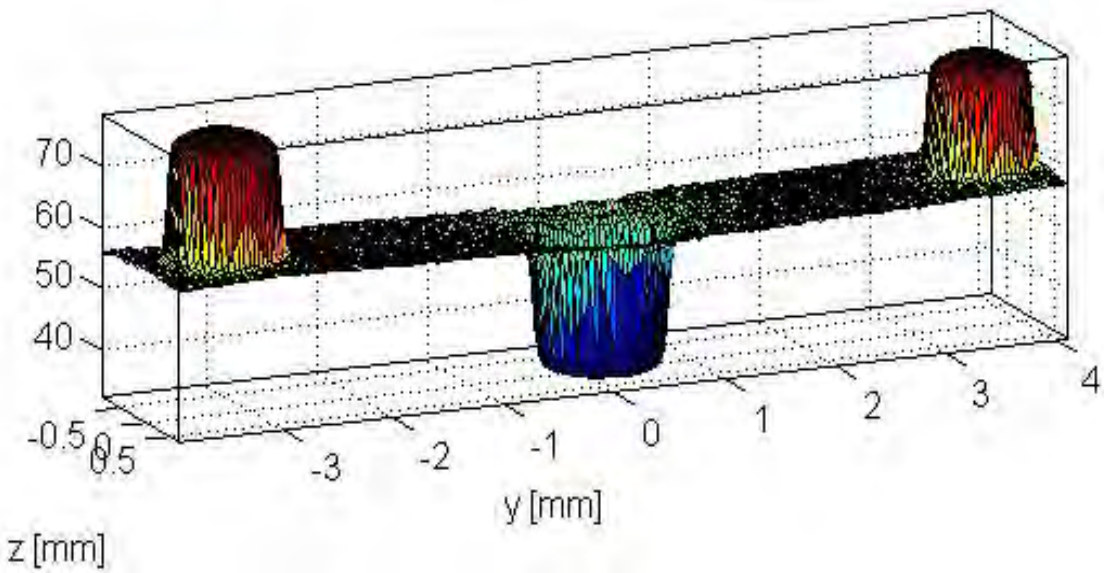

(b)

Figure 2-34. Case H4: R = ½, ΔT = 44.4 °C, S/D_{jet} = 3 measured at x/D_{jet} = 0.09 (a) profiles of velocity magnitude [m s^{-1}], and (b) temperature profiles [°C]

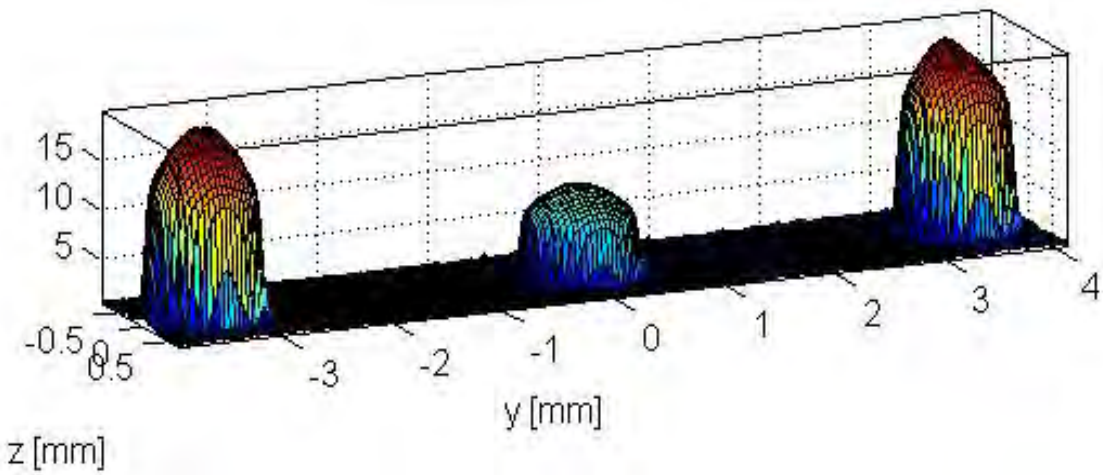

(a)

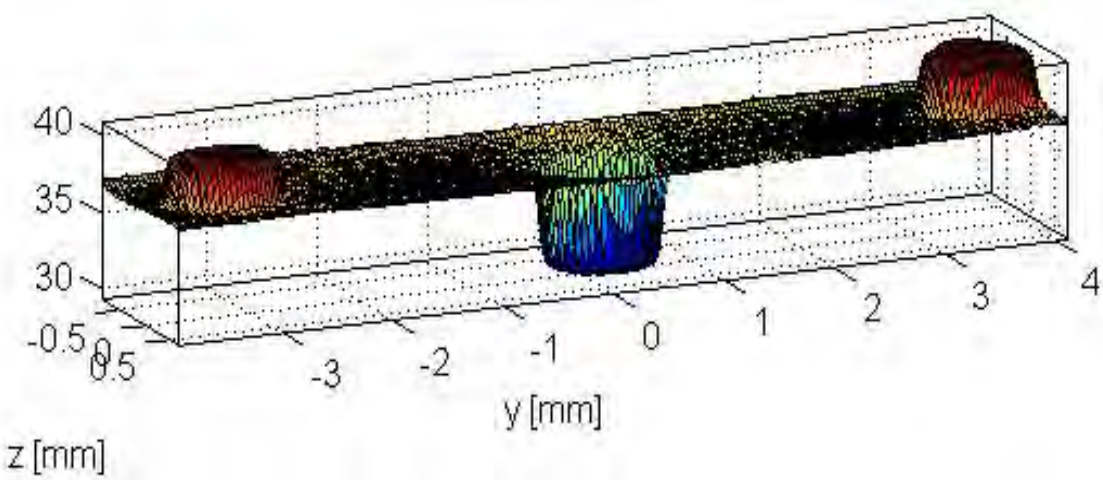

(b)

Figure 2-35. Case H5: R = ½, ΔT = 11.1 °C, S/D_{jet} = 3 measured at x/D_{jet} = 0.09 (a) profiles of velocity magnitude [m s^{-1}], and (b) temperature profiles [°C]

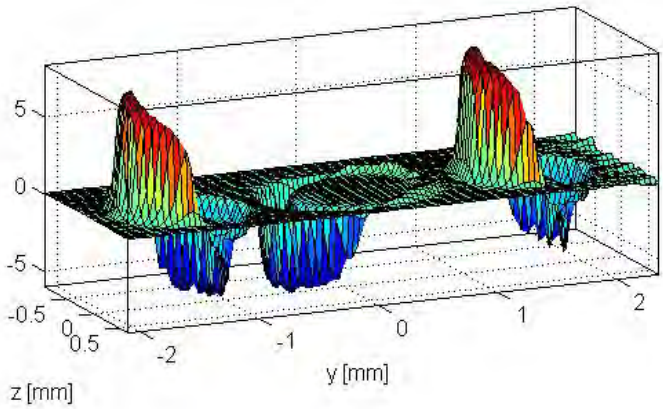

(a)

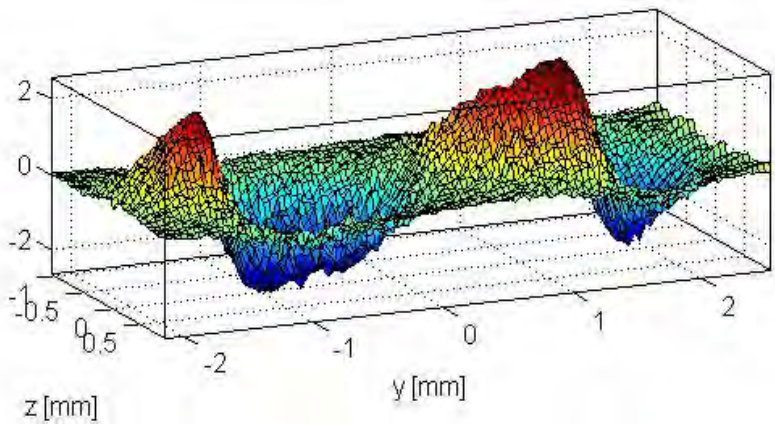

(b)

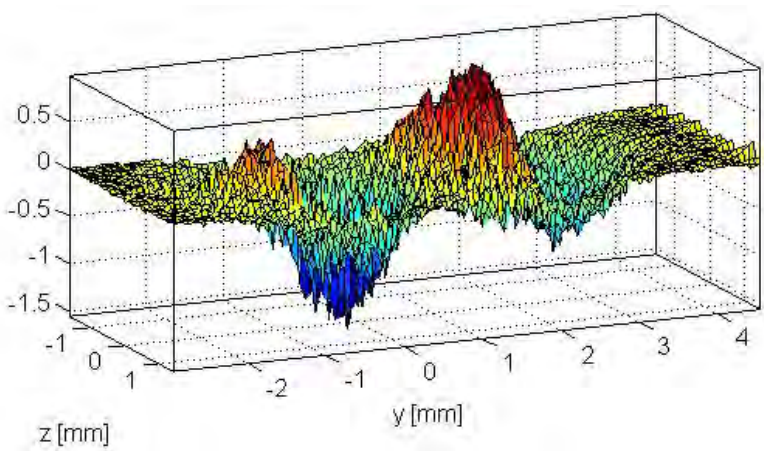

(c)

Figure 2-36. Difference in temporally congruent and spatially congruent velocity correction methods [m s^{-1}]

(a) Case H1: measured at x/D_{jet} = 0.09, (b) Case H2: measured at x/D_{jet} = 5, and (c) Case H3: measured at x/D_{jet}= 10

2.4.2 Analysis of Triple-Jet Profiles

Of major concern in triple-jet behavior is the turbulent mixing of the jets. In order to study the mixing in the jets, profiles of the jets were considered first. As listed in Table 2-7 as cases H1, H2, and H3, data was gathered for three different downstream distances, x/D_{jet} = 0.09, 5.09, and 10.09 respectively. As illustrated in Figure 2-37(a), the first cross-section shows three distinct jets. However, by x/D_{jet} = 5.09 (Figure 2-37(b)), the jets have begun to spread and mix significantly with only a small distinct cold peak existing where the center jet once had a prominent profile. This is further exacerbated by x/D_{jet} = 10.09, shown in Figure 2-37, where there now only exist two distinct peaks associated with the hot outer jets.

Considering contours of temperatures, similar trends are seen as those found with the velocity profiles. Shown in Figure 2-38 is the development of the triple-jet temperature profile at each of the three downstream planes for which data was captured. These uniquely represent case H1, H4, and H5, respectively. As observed in Figure 2-38(a) the temperature profiles in both the hot jets and the cold is qualitatively a top-hat, in agreement with the single jet analysis documented previously. Looking in the downstream contours in Figure 2-38(b) and (c) reveals evidence of mixing, which is seen as the hot jet temperatures are spreading and decreasing as they mix with the cold jet, whose temperature is increasing. Interestingly evident in both Figure 2-37(a) and Figure 2-38(a), the cold jet appears wider than both the hot jets in terms of temperature profile and velocity profile.

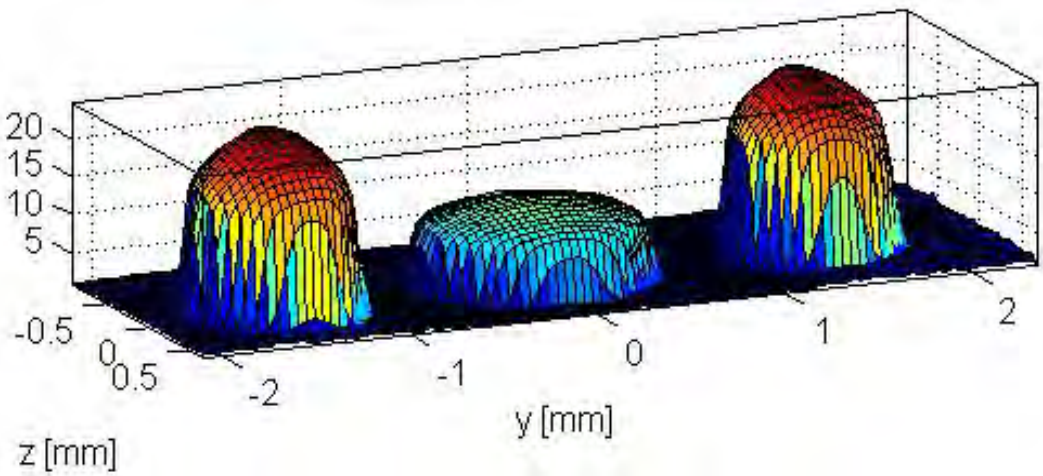

(a)

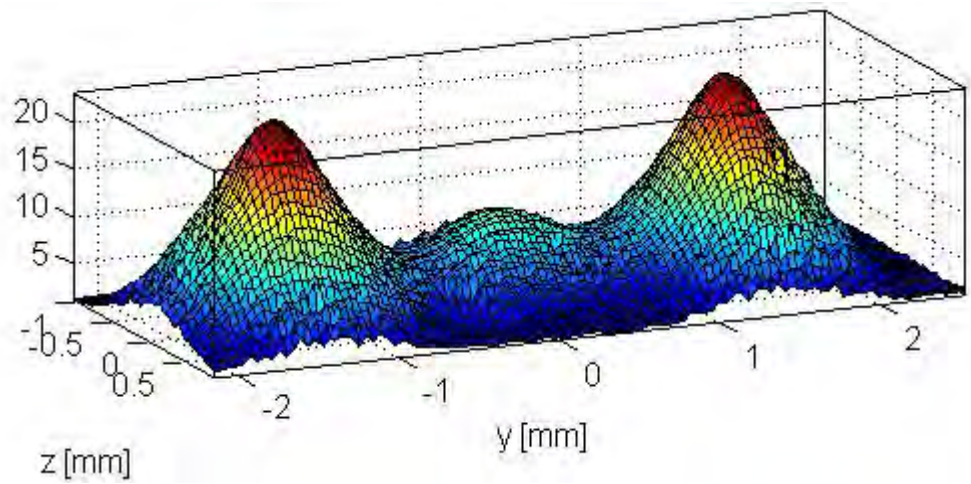

(b)

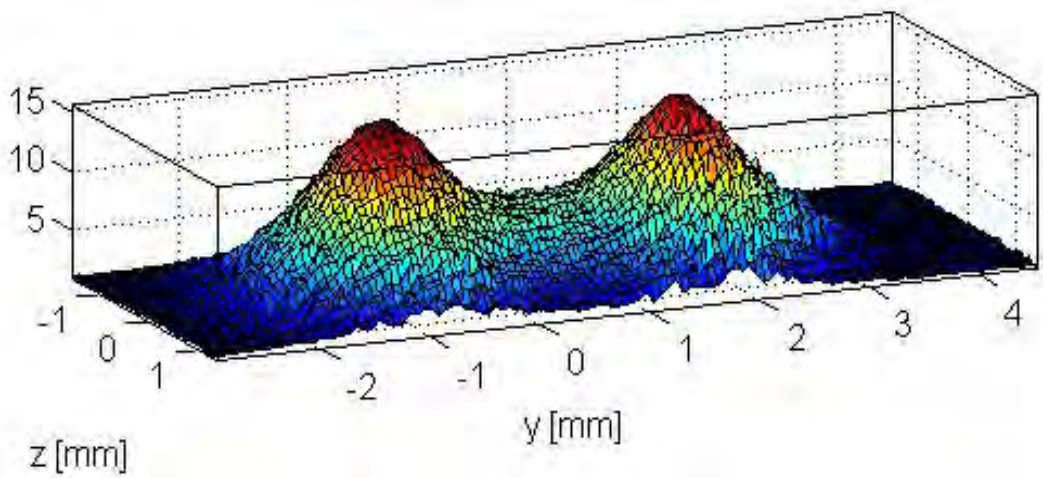

(c)

Figure 2-37. Velocity contours [m s^{-1}] for R = ½, ΔT = 44.4 °C, S/D_{jet} = 1.41 (a) measured at x/D_{jet} = 0.09, (b) measured at x/D_{jet} = 5.09, and (c) measured at x/D_{jet} = 10.09

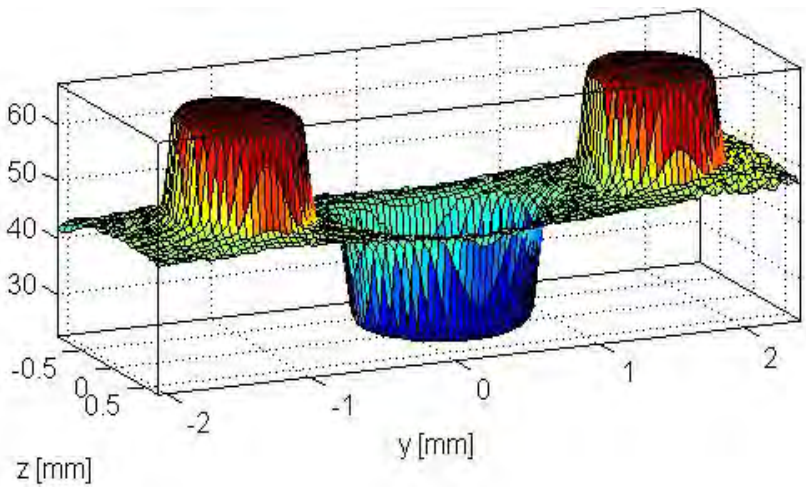

(a)

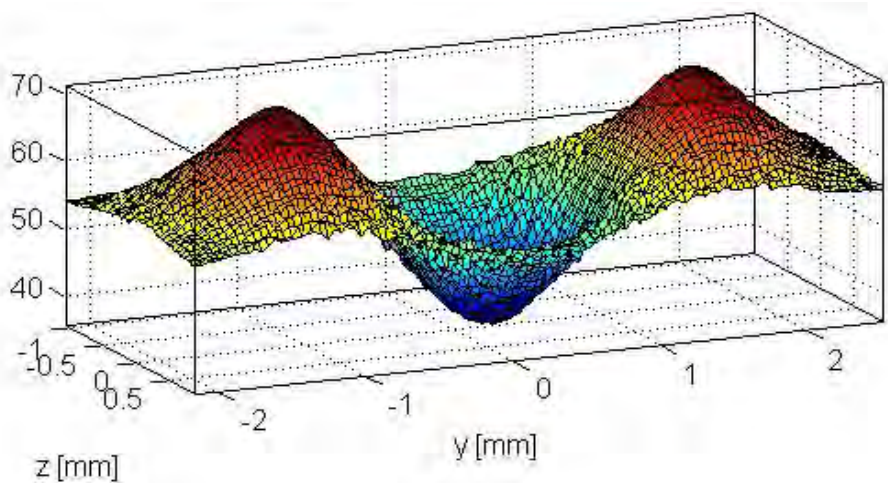

(b)

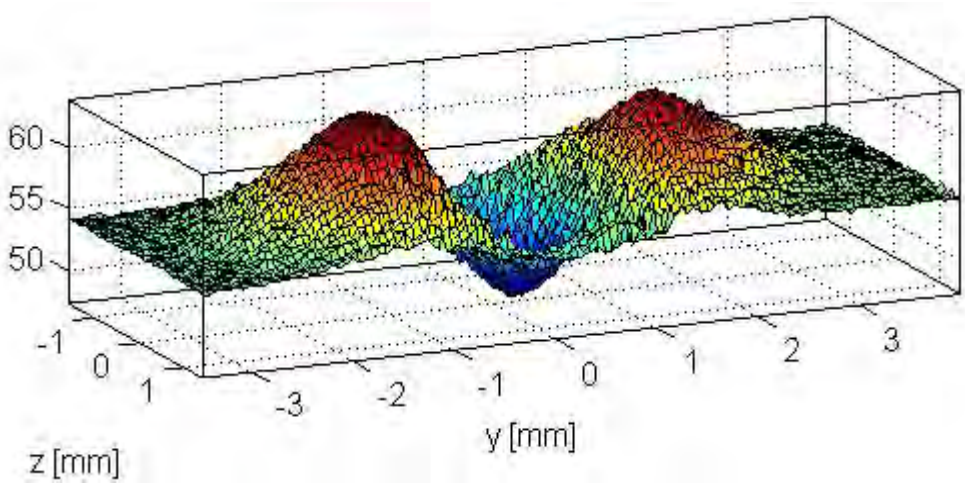

(c)

Figure 2-38. Temperature contours [°C] for R = ½, ΔT = 44.4°C, S/D_{jet} = 1.41 (a) measured at x/D_{jet} = 0.09, (b) measured at x/D_{jet} = 5.09, and (c) measured at x/D_{jet} = 10.09

To investigate the increased spreading of the center jet, line traces for each of the jets are gathered similar to that done in Figure 2-30. In order to sample the triple-jet inlet profiles in a logical manner, eight traces were taken of each jet then averaged with those traces with which symmetry was expected. The traces are shown in Figure 2-39 where a common nomenclature was used for all traces where symmetry was expected. Utilizing this sampling technique, profiles are shown for the H1 case in Figure 2-40. Investigating Figure 2-40(b) reveals that the radius of the jet in the horizontal is approximately 10% larger than expected from the single jet curve fit. Conversely the jet appears to be oblong in profile as the single jet curve fit agrees well with the vertical traces. As would be expected for a jet stretching in the horizontal direction, the average of the diagonal traces falls between that of the horizontal and vertical traces.

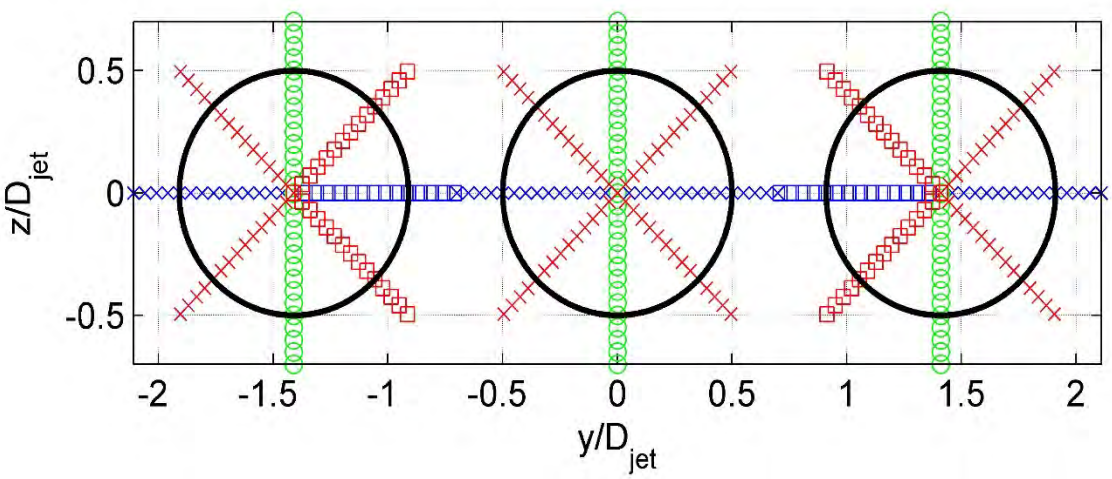

Figure 2-39. Traces for triple-jet study and the averaging applied – □ inner horizontal averages, x outer horizontal averages, o vertical averages, □ inner diagonal averages, x outer diagonal traces. Black circle represents jet.

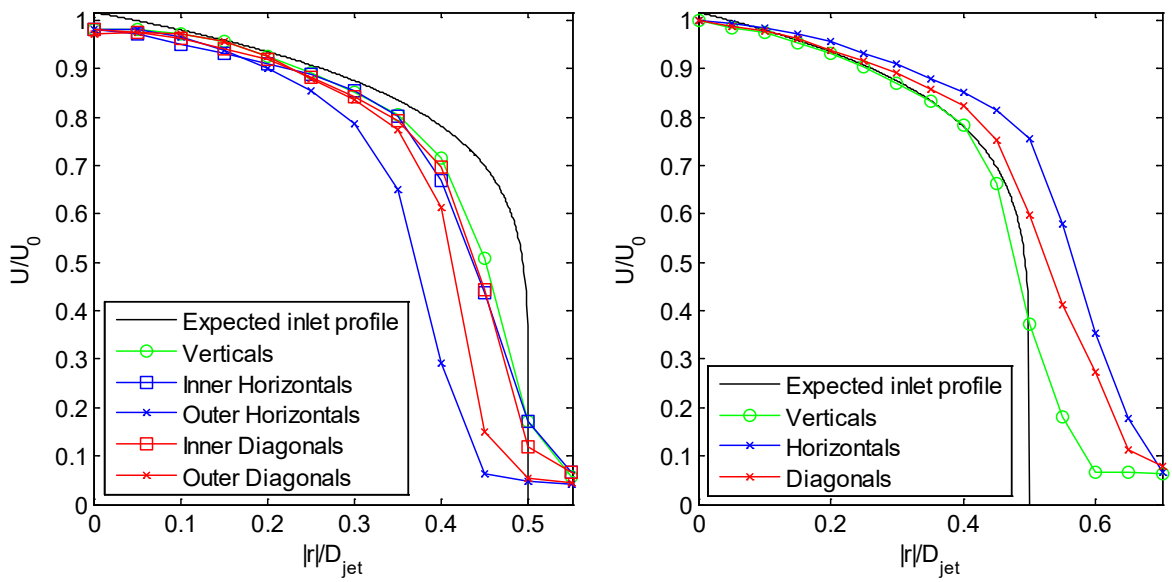

Figure 2-40. Symmetrically averaged inlet profiles the Case H1 measured at x/D_{jet}=0.09. (a) averaged traces for both hot jets; (b) averaged traces for cold jet

Similar to the analysis done for the cold jet in Figure 2-40(b), part (a) shows averages of the traces for the hot jets. Examining the profiles, it is first apparent that the hot jets appear much narrower than that of a single jet. However, more interesting is the trend in outer traces, both for the horizontal and diagonal, which appear narrower than those for the vertical and horizontal traces. This suggests that the hot jets are "necking" in towards the cold jet even at distances of only x/D_{jet} = 0.09. Furthermore, the cold jet is spreading horizontally towards the hot jets. To investigate if this is an effect of the tight jet spacing (S/D_{jet} = 1.41), similar analysis was conducted for Cases H4 and H5, which having a non-dimensional jet spacing of S/D_{jet} = 3.0. Shown in Figure 2-41 and Figure 2-42 are the profiles for Case H4 and H5, respectively.

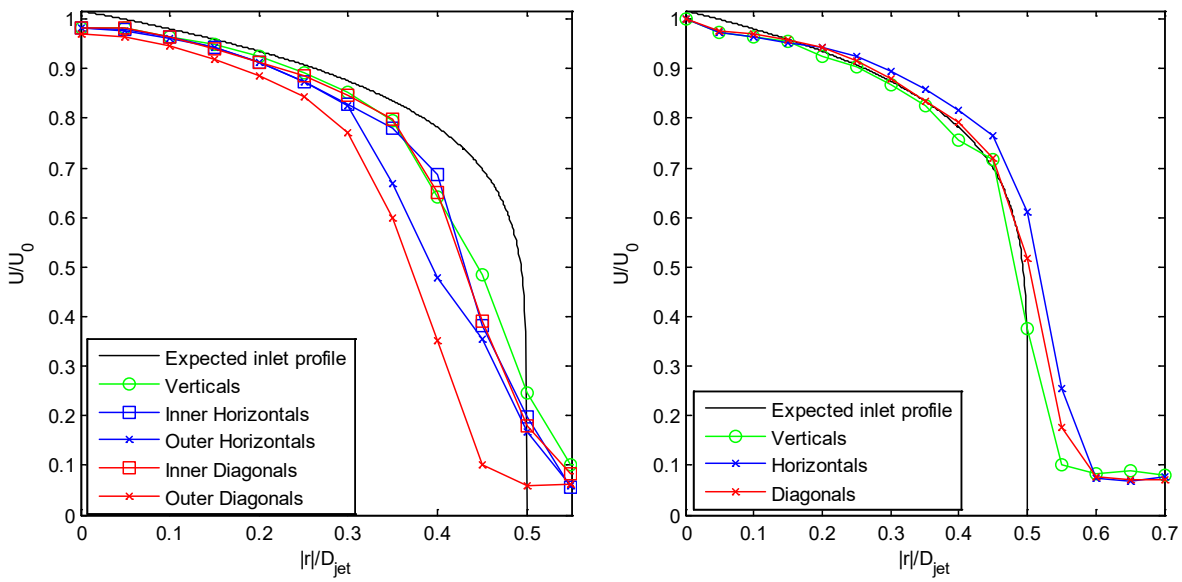

(a) (b)

Figure 2-41. Symmetrically averaged inlet profiles the Case H4 measured at x/D_{jet} = 0.09. (a) averaged traces for both hot jets; (b) averaged traces for cold jet

For the wider spacing in cases H4 and H5 (Figure 2-41(b) and Figure 2-42(b)), the cold jet inlet averages suggest that the cold jet does not spread as it does in the closer spaced Case H1 (Figure 2-40(b)). In fact, it is observed that the jet behaves according to expectations. When looking at the hot jet inlet traces, it is noticed for both Case H4 and H5 that the profiles are slightly narrower than expected from the single jet measurements. Additionally, for Case H4, there appears to be a slight degree of necking occurring in the hot jet, as evident by the outer traces decreased velocity profiles seen in Figure 2-41(a). This under-prediction of velocity on the outside of the triple jet is not likely due to the correction method. In all cases, the CCA was offset from the CTA in the –z-direction. Thus, when comparing temporally congruent and spatially congruent data the largest errors are not symmetric, but in fact occur in the –z-direction. For Case H5, the hot jet appears narrower than expected, but does not exhibit any necking towards the center jet. This necking is likely due to the symmetric behavior the triple-jet array. It seems plausible that as the number of jets in the array is increased, the degree to which jets neck will decrease for jets closer to the

center then compared to those closer to the end of the array. Furthermore, changes in behavior may even exist for arrays with an odd number of jets compared to those with an even number of jets.

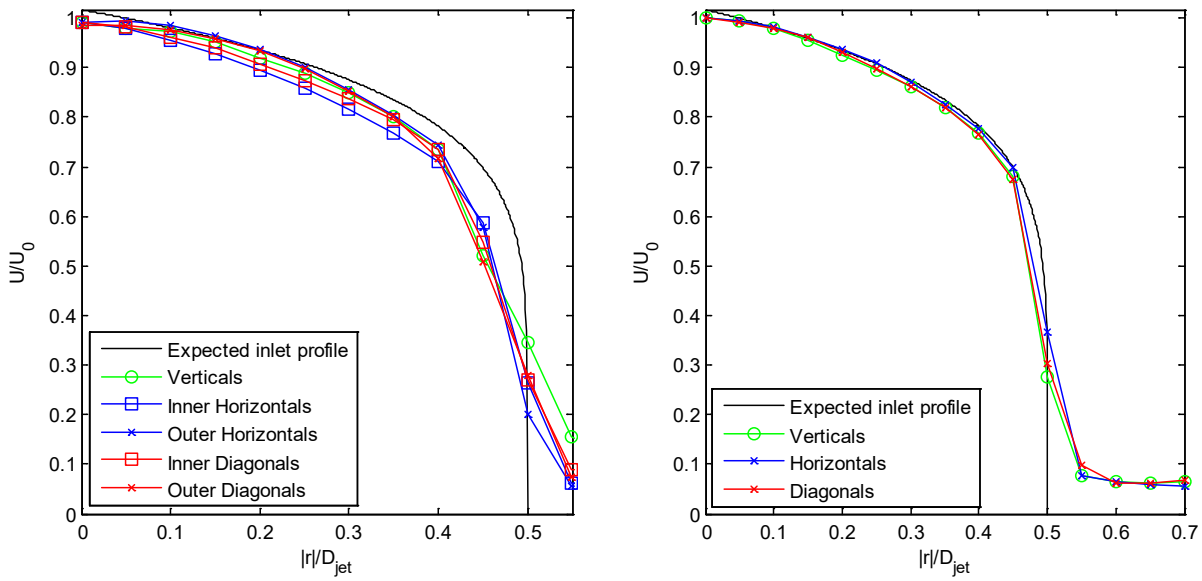

(a) (b)

Figure 2-42. Symmetrically averaged inlet profiles the Case H5 measured at x/D_{jet} = 0.09. (a) averaged traces for both hot jets; (b) averaged traces for cold jet

2.4.3 Trends in the Triple-Jet

In order to quantitatively talk about mixing in a parallel triple-jet, vertical traces of multiple cases, shown in Table 2-6, were mapped in the xy-plane through $z = 0$. Contours of velocity and temperature data were gathered in the vertical plane. To compare the different behaviors of each case, line traces were gathered at various downstream distances and symmetrically averaged to better understand trends in the temperature and velocity profiles. An example of these trends is shown in Figure 2-43, which is used to investigate the effect of temperature difference on the velocity profiles.

Shown in Figure 2-43 are symmetrically averaged velocity profiles, normalized by the maximum velocity, in the profile for different downstream distances. The cases presented were uniquely selected to represent three distinct velocity ratios, $R = \frac{U_{0,cold}}{\langle U_{0,hot} \rangle}$, each having two unique temperature differences. As

shown by the close agreement between Case V2 and V3, agreement between Cases V3 and V5, and agreement between Cases V8 and V9, the temperature difference does not have any apparent effect on the velocity profiles. Similar to the profiles shown in Figure 2-43, effort was taken to investigate how for these same cases the non-dimensional temperature profiles in the domain varied as a function of the temperature difference. The non-dimensional temperature was defined according to Eq. (2-24). As shown in Figure 2-44, even at large downstream distances, there are no significant variations in the non-dimensional temperature profile in and/or near the periphery of the jet. However, in areas between and/or outside of the jets, the temperature appears to vary slightly from case to case. This difference can be attributed to different inlet temperatures and flow rates for the different cases. As the inlet boundary conditions were not the same in all cases, the average temperature in the test section changed to case to case. To approximate the effects of each inlet condition on the test section temperature, the bulk inlet temperature was calculated for each case according to Eq. (2-25). As anticipated, the cases with the largest observed peripheral temperatures also have the largest inlet bulk temperature. As the test section is an insulated box this is to be expected.

$$\theta = \frac{T - T_{inner}}{T_{outer} - T_{inner}} \tag{2-24}$$

$$T_{bulk} = \frac{\dot{V}_{hot,1} T_{hot,1} + \dot{V}_{hot,2} T_{hot,2} + \dot{V}_{cold} T_{cold}}{\dot{V}_{hot,1} + \dot{V}_{hot,2} + \dot{V}_{hot,1}} \tag{2-25}$$

Table 2-9. Estimated bulk temperature of flow into test section for each case

#	U_0 Expected [m/s]	T_{jet} [°C]	T_{bulk} [°C]	#	U_0 Expected [m/s]	T_{jet} [°C]	T_{bulk} [°C]
V1	$U_{0,hot} = 19.18$	$T_{hot,1} = 41.89$ $T_{hot,2} = 42.31$	42.1	V6	$U_{0,cold} = 9.59$ $U_{0,hot} = 9.59$	$T_{cold} = 32.32$ $T_{hot,1} = 71.98$ $T_{hot,2} = 72.41$	58.9
V2	$U_{0,cold} = 9.59$ $U_{0,hot} = 19.18$	$T_{cold} = 32.94$ $T_{hot,1} = 73.01$ $T_{hot,2} = 72.28$	64.7	V7	$U_{0,cold} = 19.18$ $U_{0,hot} = 19.18$	$T_{cold} = 31.48$ $T_{hot,1} = 72.67$ $T_{hot,2} = 71.96$	58.7
V3	$U_{0,cold} = 9.59$ $U_{0,hot} = 19.18$	$T_{cold} = 30.83$ $T_{hot,1} = 51.07$ $T_{hot,2} = 51.00$	47.0	V8	$U_{0,cold} = 19.18$ $U_{0,hot} = 9.59$	$T_{cold} = 30.51$ $T_{hot,1} = 69.21$ $T_{hot,2} = 69.50$	49.9
V4	$U_{0,cold} = 9.59$ $U_{0,hot} = 19.18$	$T_{cold} = 31.41$ $T_{hot,1} = 77.54$ $T_{hot,2} = 75.39$	67.5	V9	$U_{0,cold} = 19.18$ $U_{0,hot} = 9.59$	$T_{cold} = 29.38$ $T_{hot,1} = 49.64$ $T_{hot,2} = 49.97$	39.6
V5	$U_{0,cold} = 9.59$ $U_{0,hot} = 19.18$	$T_{cold} = 29.59$ $T_{hot,1} = 39.78$ $T_{hot,2} = 40.39$	38.0	V10	$U_{0,cold} = 19.18$ $U_{0,hot} = 4.79$	$T_{0,cold} = 30.19$ $T_{0,hot,1} = 69.90$ $T_{0,hot,2} = 70.28$	47.4

While the profiles presented in Figure 2-43 and Figure 2-44 support the notion that the temperature behaves as a passive scalar, more detail about the triple-jet behavior can be examined by comparing cases for a fixed temperature difference where velocity ratio is varied. This is the situation considered in Figure 2-45 where the temperature difference for all four cases shown is ΔT = 44.4 °C. The first observation noticed is that for Cases V6 and V7, there is very little difference. This suggests that for the limited range of jet velocities tested, there is not a significant dependence of the flow field on the Reynolds number of the jets. However, by contrast there does appear to be significant differences associated with the velocity ratio. When comparing Cases V2 and V8, several distinct trends are seen. It appears that in Case V2, with R = ½, the center jet has slightly narrowed compared to the R = 1 cases, while the opposite is true for Case V8 in which the center jet is slightly wider than that of the iso-velocity cases. One possible explanation for this behavior may be tied to single jet behavior. From early theoretical work on a free jet [38], it is expected that in order to maintain momentum across the half width of the jet, mass must be entrained. Thus, as the

momentum of each outer jet is twice that of the center jet for R = ½, it may be that the outer jets are entraining the center jet's mass into their own. In order to quantify this behavior, it would be necessary to define the apparent width of each jet, and explain the complicated mechanism by which they combine. To aid in this analysis, higher resolution experimental data, with multiple component velocity and stress measurements, are suggested for future studies.

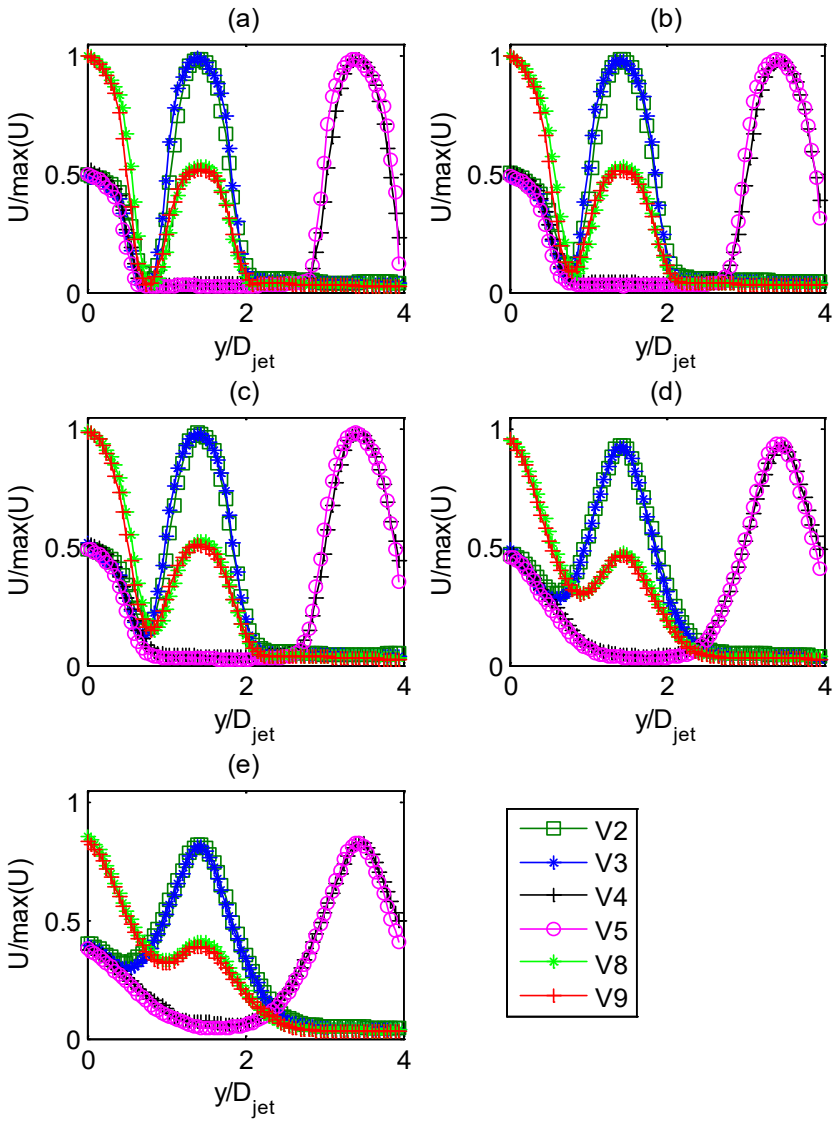

Figure 2-43. Effects of temperature on the non-dimensional triple-jet velocity profile for different downstream distances (a) measured at x/D_{jet} = 0.09; (b) measured at x/D_{jet} = 0.59; (c) measured at x/D_{jet} = 1.09; (d) measured at x/D_{jet} = 4.09; (e) measured at x/D_{jet} = 6.09

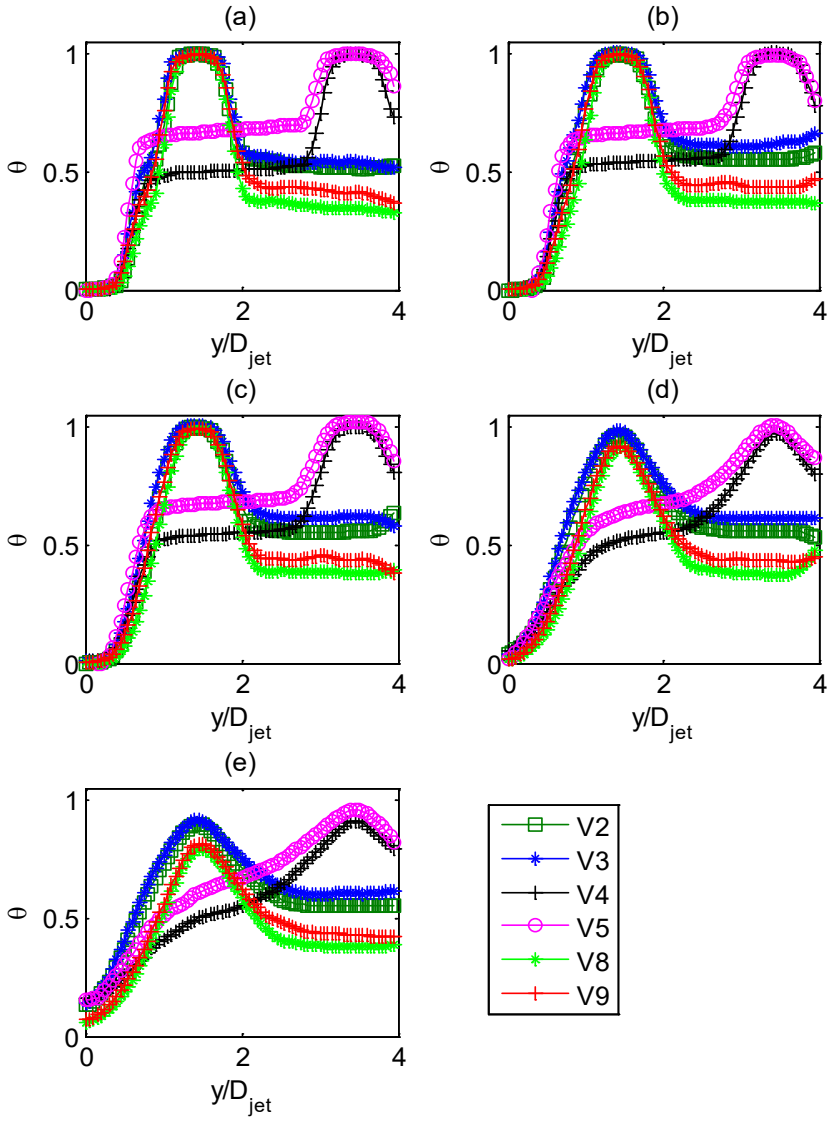

Figure 2-44. Effect of temperature difference on the non-dimensional triple-jet temperature profiles at different downstream distances (a) measured at x/D_{jet} = 0.09; (b) measured at x/D_{jet} = 0.59; (c) measured at x/D_{jet} = 1.09; (d) measured at x/D_{jet} = 4.09; (e) measured at x/D_{jet} = 6.09

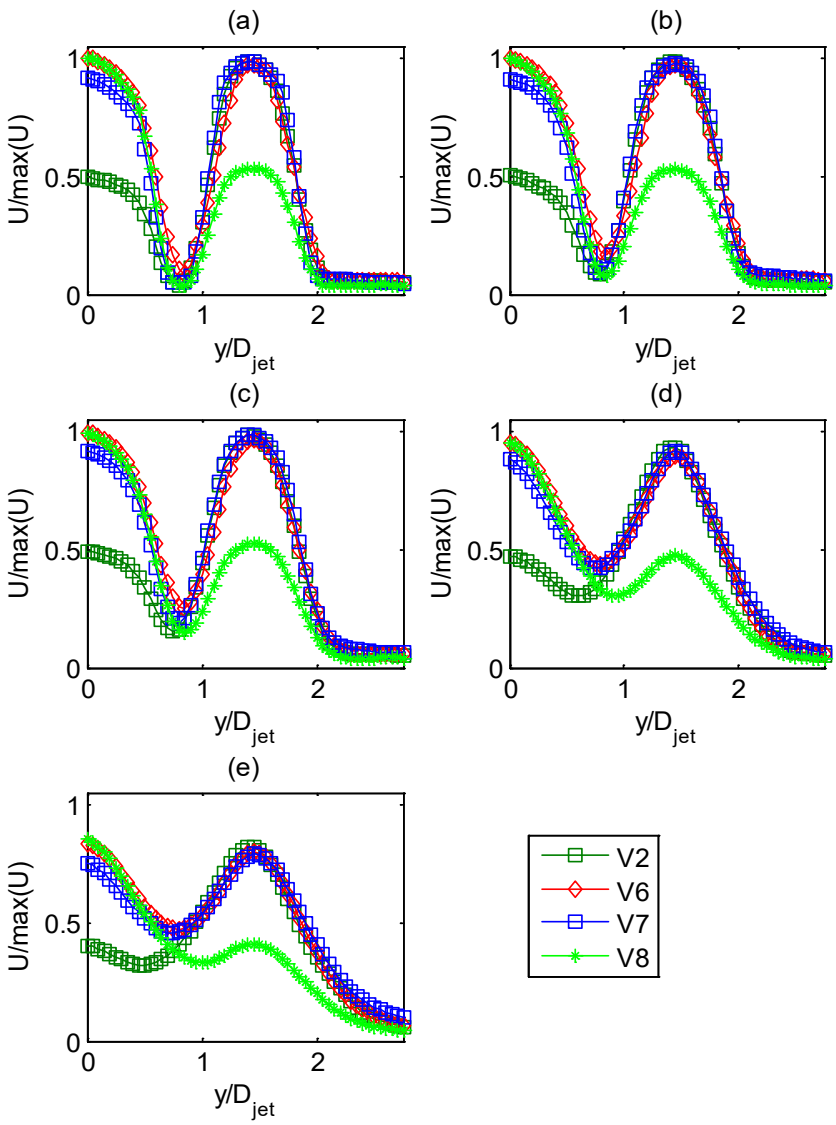

Figure 2-45. Differences related to velocity ratio for triple-jet velocity profiles at different downstream distances (a) measured at x/D_{jet} = 0.09; (b) measured at x/D_{jet} = 0.59; (c) measured at x/D_{jet} = 1.09; (d) measured at x/D_{jet} = 4.09; (e) measured at x/D_{jet} = 6.09

For the case of a parallel round triple-jet, the effects of temperature difference, velocity ratio, and jet spacing on velocity and temperature profiles have been studied. It was seen that the temperature difference does not present any significant impact on the velocity profiles measured in the jet. Moreover,

any noticeable differences were less than those currently observed due to the uncertainty associated with the dual CTA and CCA measurement compensation techniques. Furthermore, it is seen that non-dimensional spacing does have an effect on the behavior of the center jet near the inlet. For the small S = 1.41 case, the center jet appeared wider than expected. However, when increasing the spacing to S = 3.0, the center jet behavior near the inlet was as expected.

This assessment has provided additional understanding into the expected flow behavior in a round parallel triple-jet. Additionally, an unexpected physical behavior was observed for the spreading of a round jet. The present analysis provides encouraging results and suggests that future work should focus on more complete resolution of the flow field in the triple-jet as it is reasonable to expect the spacing of the jets influences and creates different flow regimes between the jets. Based on these observations, first level approaches to validation and verification of turbulence models are possible. For future work, care should be given to better understanding the physics associated with the spreading of the center jet and the effects on velocity profiles near the jet.

2.5 Non-Isothermal Triple Jet Near Solid Wall

For additional temperature validation opportunities, experiments were run with a heated triple jet configuration and a solid wall positioned parallel to the jet axes. For these experiments, the primary measurement is full field temperatures captured via an infrared camera (FLIR SC5000) with an accuracy of ±1°C. The triple jet facility previously described was outfitted with a solid wall running parallel to the three jets and infrared viewports as illustrated in Figure 2-46. The parallel wall is composed of polycarbonate and is painted with Krylon 1602 paint with an emissivity (ε) of 0.95 [41]. The thermal conductivity of the polycarbonate plate is 0.19 W m^{-1} K^{-1} and has a melting temperature in the range of 230-260 ˚C. The parallel plate is composed of polycarbonate due to its optimal thermal properties regarding the proposed temperatures the plate is subjected to. Its low thermal conductivity prevents “smearing” of the temperature profiles on the front surface of the plate, enabling a better quantification of the thermal loading functions themselves, and not an attenuated version of them.

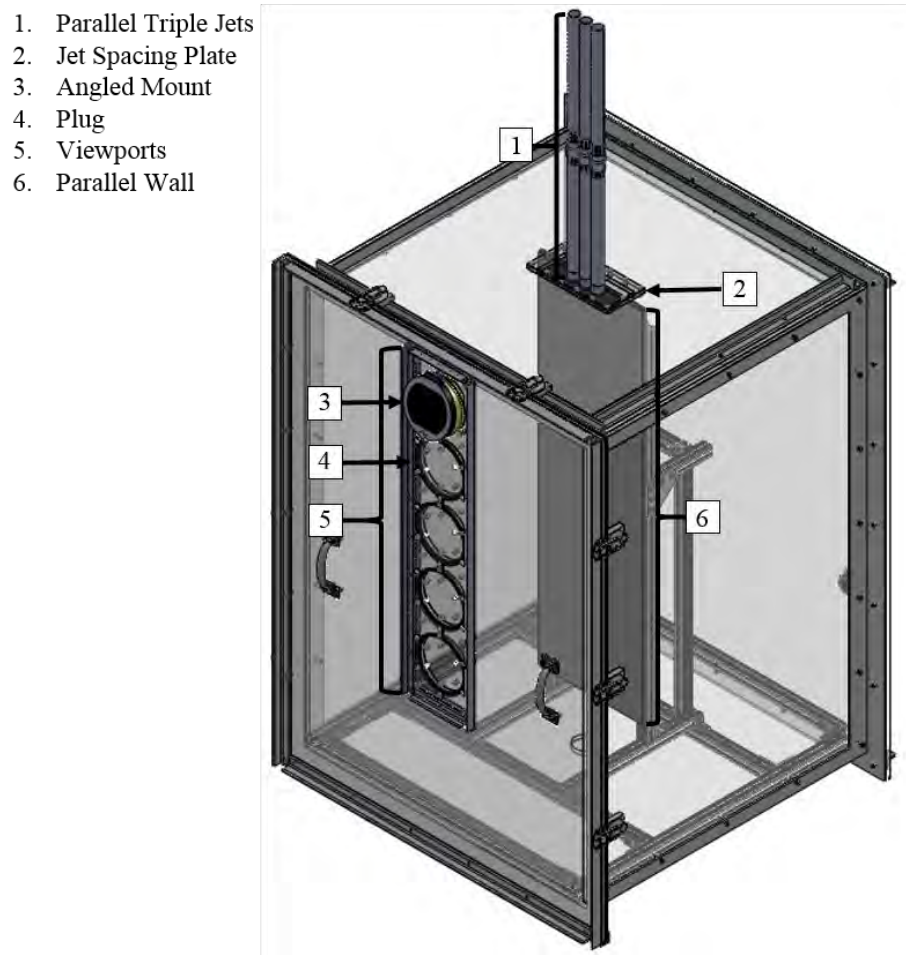

Figure 2-46. Isometric view of triple jet near solid parallel wall

2.5.1 Experimental Parameters

The three jets consist of a center cold jet with an adjacent hot jet on either side. The hot jets are consistently set to the same temperatures and flow rates for each test case. The test cases are categorized by the velocity ratio previously defined (R) between the cold and hot jets. For each test case, the temperature difference between the jets is 22.2 °C, providing for a sufficiently high temperature gradient between the hot and cold jets for clear temperature profile visualization. Since the area of each jet is the same, and the absolute temperature range is fairly small, the velocity ratio can be calculated using the experimentally specified volumetric flow rates. The test cases are presented in Table 2-10.

Table 2-10. Experimental triple jet configurations for parallel plate experiments

Case Name	*Hot Jet*			*Cold Jet*			ΔT (°C)	R
	$\dot{V}_H$ (m^3/min)	Re_H	T_H (°C)	$\dot{V}_C$ (m^3/min)	Re_C	T_C (°C)		
Case 1	1.133	15432	44.7	0.566	7716	22.5	22.2	0.5
Case 2	0.566	7716	45.6	0.566	7716	23.3	22.2	1.0
Case 3	0.377	5144	47.8	0.566	7716	25.6	22.2	1.5

The plate spacing from the jets, herein defined as 'δ', provides another experimental parameter of interest. The plate spacing, "δ", is defined in terms of the number of hydraulic diameters the plate is from the axial centerline of the three jets. For this study, the plate is fixed directly tangent to the outlets of the jets (δ = 0.5). This provides the most apparent temperature profile of the jet potential cores possible, with minimal effects from the ambient air of the tank, since there is no free stream gap between the jet flows and the plate. The spacing of the jets relative to one another (S) also influences the mixing on the plate surface. The spatial coordinate in the streamwise direction is normalized by the jet spacing (Y*=Y/S). These parameters are illustrated in Figure 2-47 and Figure 2-48. The minimum center-to-center spacing at the outlets of the jets, which is based on a scaled mock-up of the General Atomics gas turbine modular helium reactor (GT-MHR) [26], is S = 3.13 cm. This minimal spacing was chosen for this analysis.

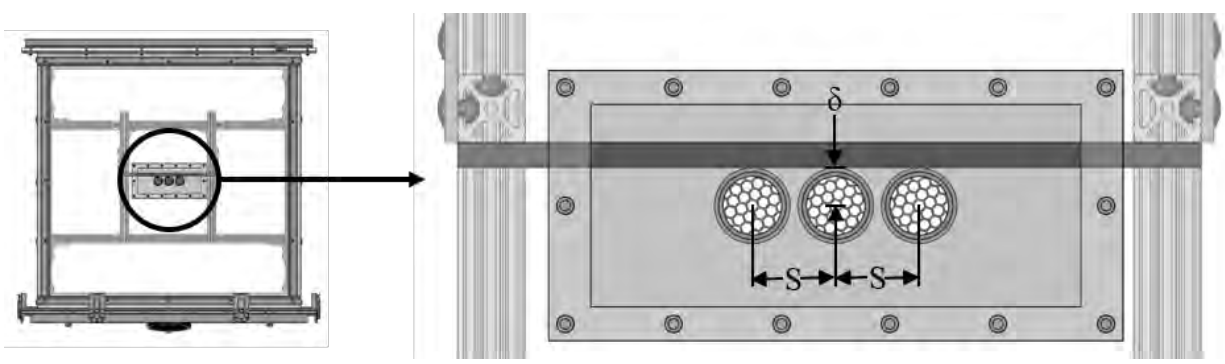

Figure 2-47. Top view of triple jet test section with confining wall

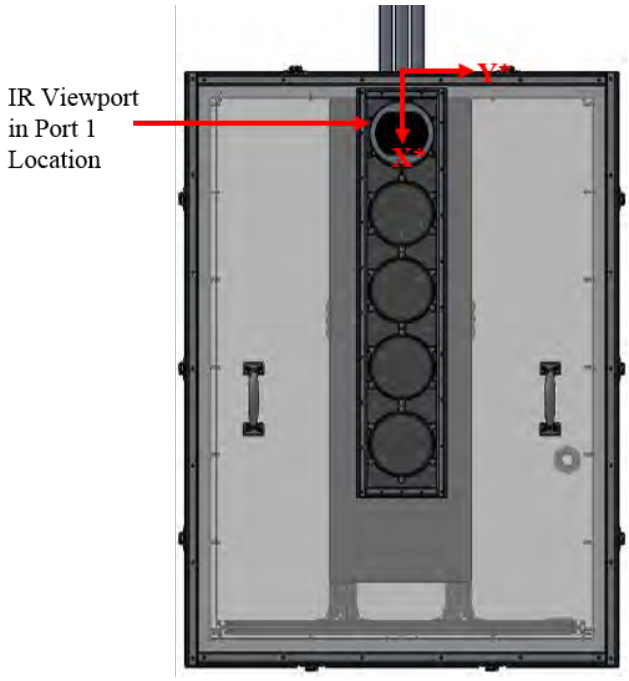

Figure 2-48. Front view of test section and IR viewports

2.5.2 Experimental Methods

The volumetric flow of the individual jets are held constant by the temperature and flow control skid's automated valves after the jet temperatures reach steady state. The jet outlet temperatures are determined experimentally by placing a type-T thermocouple with a resolution of +/- 0.5 °C at the outlet of each jet. A FLIR SC5000 IR camera with a resolution of +/- 1.0 °C is used to acquire the temperature signatures induced by the jets on the parallel plate. The test section walls are composed of 1.11 cm thick polycarbonate and have poor infrared transmittance in the wavelength spectrum of the IR camera (2.1-5.1 μm). For this reason, a FLIR 4 in Infrared (IR) viewport (model IRW-4C) is incorporated, which includes a lens composed of calcium fluoride with a maximum operating temperature of 260 °C. The camera is placed approximately 55.88 cm from the front surface of the parallel plate. To avoid reflection of the camera on the window, the window is mounted at a 10° angle with respect to the camera lens. Additionally, a shroud is placed between the camera lens and the viewport which eliminates any incident radiation. Accommodation for 5 viewports were created on the front surface of the test section with a center-to-center

distance of 15.24 cm for each adjacent viewport. The angled mount and IR window can be placed in any of these five viewports with the remaining viewports sealed with plugs. Each viewport allows for a view of the parallel plate with an image approximately 7.7 jet diameters in height, and 6.0 jet diameters in width of the parallel plate. The viewport design can be better visualized in Figure 2-48.

Only the top three viewports are utilized here. The overlap between the three viewports in the X-direction has been determined, providing for one coherent study of the thermal loading on the plate from the outlets of the triple jet configuration. For this study the non-dimensionalized X* axis is used as seen in Figure 2-48, where $X^*=X/D_{hyd}$ where D_{hyd} is the hydraulic diameter of an individual jet.

2.5.3 Experimental Results – Temperature Contours

The temperature profiles captured by the IR camera at each viewport for each case in Table 2-10 can be found in Figure 2-49. The temperature scaling of each figure is held constant to enable qualitative and quantitative comparisons. From this figure, it is clear that the most apparent difference in the surface temperature of the polycarbonate plate is in the R = 0.5 Port 1 temperature field. For this test, the results show the immediate effect of the individual jet flows on the plate surface in the entrance region of the jets, before any notable mixing has taken place. The effect of the velocity ratio is most apparent in this region in that the hot jets dominate the temperature profile seen on the plate and all three jets are clearly defined. The entrance region is easily classified because negligible change in temperature has occurred directly at the outlets of the cold and adjacent hot jets which is in good agreement with the same behavior described in the experiments conducted by Tokuhiro and Kimura [10]. In the corresponding downstream thermal fields for the R = 0.5 case, the convective mixing region becomes more apparent, specifically in Port 2. By the lower half of Port 3, the profile is almost in the post mixing regime with near uniform temperatures across the surface of the plate. The entrance region seen in the R = 1.0 Port 1 case is less clear than in the R = 0.5 Port 1 case, since the velocities are now equal. The "squeezing" experienced by the cold jet becomes slightly less apparent in the isovelocity case Port 2 image. This is due to the isovelocity condition itself, in which the viscous effects are minimized and the differences in physical properties of air at these absolute temperatures (T_c = 24.3˚C and T_h = 46.2 ˚C, for the cold jet and hot jets, respectively) are assumed

negligible. Therefore, for the R = 1.0 case, the convective mixing of the jets is now based primarily on the temperature difference between the jets. The post mixing region appears most prominent in the R = 1.0 Port 3 case. In the R = 1.5 case, the cold jet velocity is sufficiently higher than the two adjacent hot jets' velocities such that the cold jet dominates the temperature field seen on the plate, even as far downstream as Port 3. Thus the squeezing experienced by the cold jets due to the hot jets in the R = 0.5 case is now reversed, and in the R = 1.5 case the cold jet is instead beginning to push out the adjacent hot jets in Port 2. Interestingly, the thermal mixing behavior seen in the R = 0.5 Port 3 case seems sufficiently mixed, characteristic of the post mixing region, similar to that of the R = 1.0 Port 3 temperature field. As expected, the main difference between the post mixing regions in these two cases are the absolute temperatures seen in each. The R=0.5 case consists of a total volumetric flow between the three jets of 2.832 m^3/min while that of the R=1.5 case is 1.321 m^3/min. For this reason, the R=0.5 case should have a higher post mixing temperature in the plate due to the significant increase in mass flux of the fluid and increased heat transfer through the plate. The 9 plots in Figure 2-49 provide a comprehensive example of the three mixing regions previously described by Tokuhiro and Kimura [10]. The mixing regions are visualized for the three proposed velocity ratios (R = 0.5, 1.0, 1.5) with a constant temperature difference at the outlets of the jets.

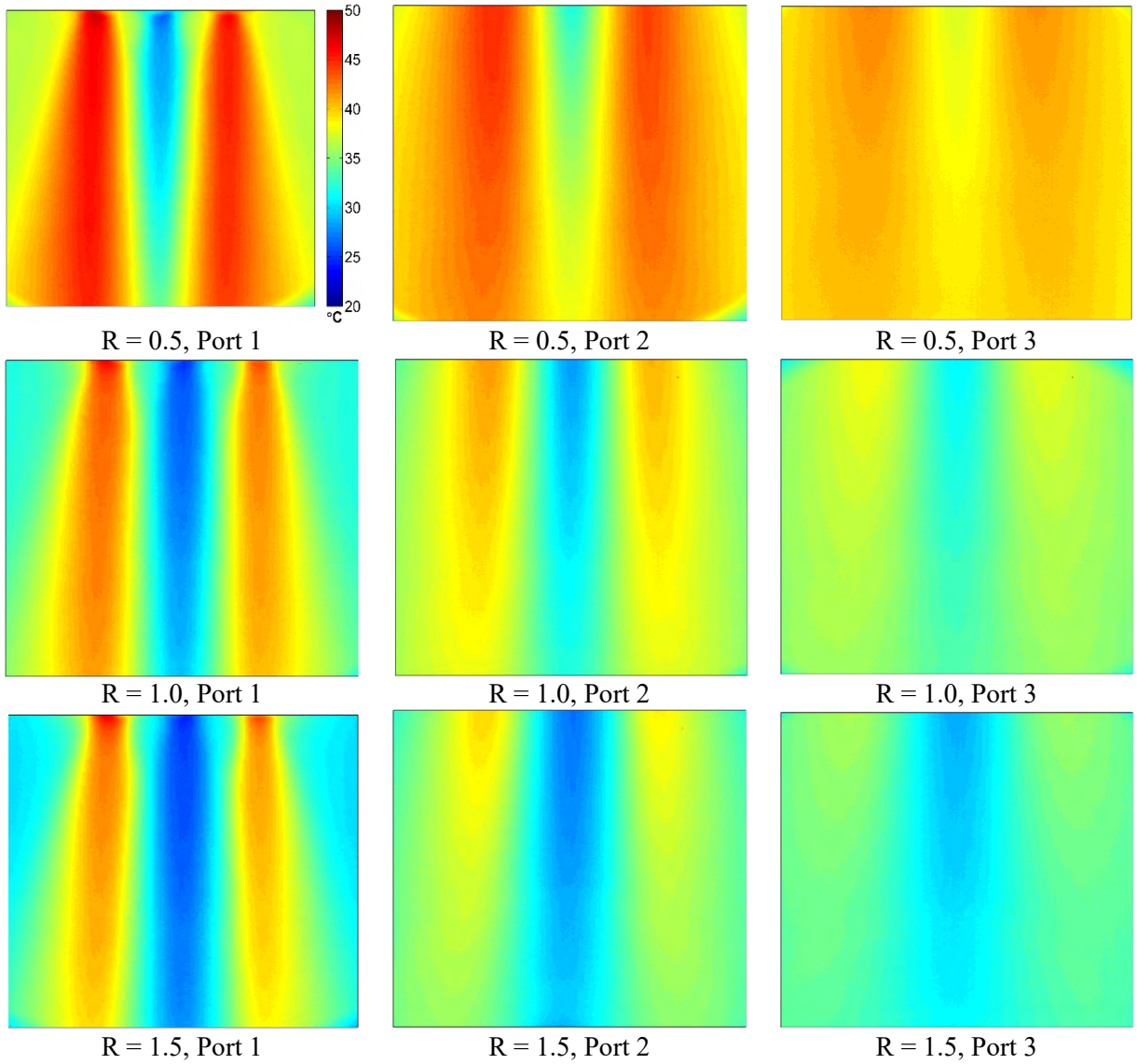

Figure 2-49. Contours of triple jet-induced temperature fields across parallel wall. Approximate size of each image is 13.4 cm x 17.1 cm

2.5.4 Experimental Results – Jet-Induced Temperature Peaks

Line traces of the temperature data were utilized in X*=2 increments in the downstream non-dimensionalized X*-direction for each temperature field. A total of 10 line traces were evaluated accounting for a range of X* values between X*=2-20 downstream. As an example, a visualization of the line traces and the corresponding temperatures are seen in Figure 2-50 for the R = 1.0 (isovelocity) Port 1 case with the X* = 2, 4, 6 line traces.

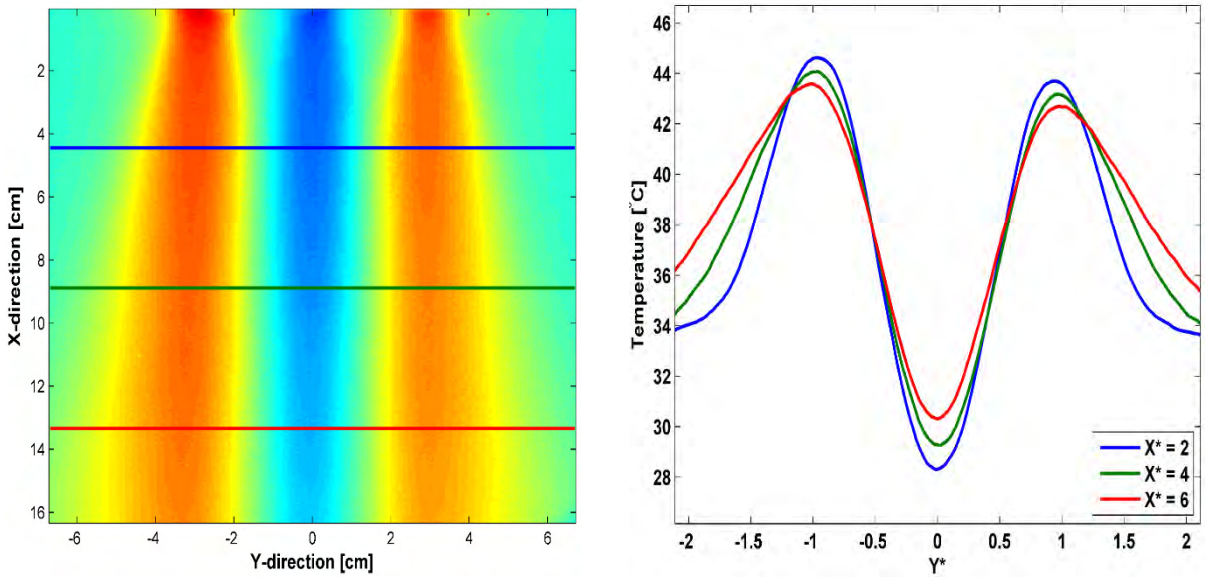

(a) (b)

Figure 2-50. (a) Case 1, Port 1 temperature field with imposed line traces (b) Case 1, Port 1 polycarbonate plate surface temperatures

As previously stated, the X*-direction length scale for each viewport is relative to the overall length downstream. The line traces provide an array of temperatures along the width of the plate, in the Y*-direction (as depicted in Figure 3). For an improved understanding of the characteristic behavior of the line traces, the asymmetry of each trace was resolved by averaging each line trace about its center-most point, the cold jet center. The maximum relative asymmetric error for two individual symmetrically averaged pixels was found to be 7.8, 3.5, and 4.1% for Case 1, 2, and 3, respectively. Additionally, the notable relative asymmetric error for each case was found on the outside of the hot jets where the relative asymmetric error inside the three jets (Y* = -1 to Y*= 1) was less than 3% for each case. This implies that the slight asymmetry in the jets for each test case was acceptable and the majority of the asymmetry was due to dissipation outside of the mixing area of the triple jet configuration.

Additionally, the non-dimensionalized temperature, $\theta = \frac{T-T_C}{T_H-T_C}$, is introduced such that the minor differences in the hot and cold jet temperatures for each test case are now considered negligible when comparing the three proposed test case in Table 2-10.

Where T is the temperature at a given pixel, T_H is the maximum hot jet outlet temperature, and T_C is the cold jet outlet temperature. The line temperatures for the X*=2-20 distances downstream for each case can be seen in Figure 2-51.

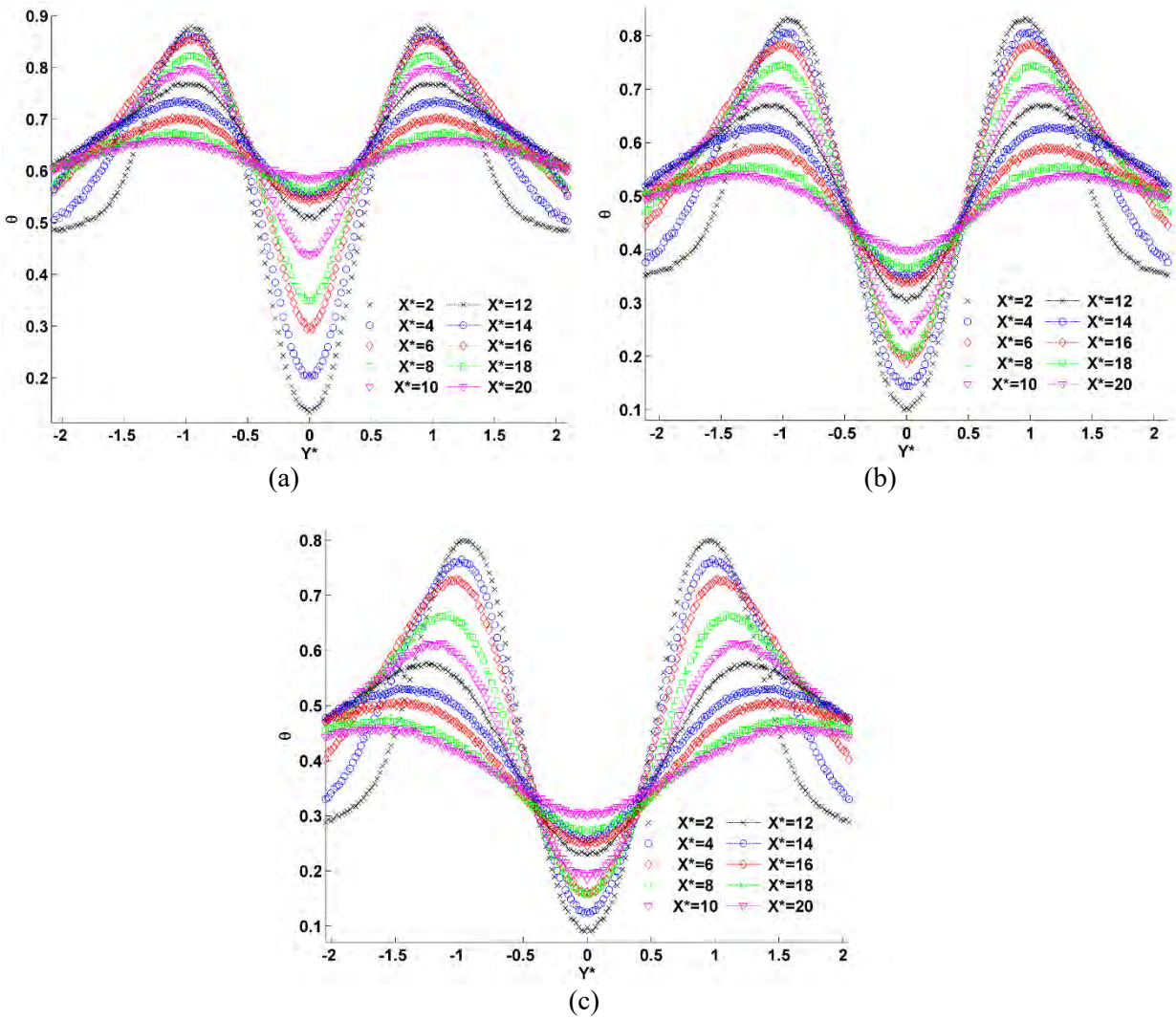

Figure 2-51. Temperature line profiles for (a) Case 1, (b) Case 2, and (c) Case 3

In Figure 2-51(a), Case 1 shows the effect of the hot jets' dominance over the line temperature profiles with increasing X* intervals downstream. This is due to the R=0.5 parameter in which the mass flux from the hot jets dominates the temperature profile seen on the plate. The line temperatures become increasingly horizontal with downstream distance in the X*-direction implying that the temperature profile

on the plate is becoming more evenly mixed. The same could be said for Case 2 and 3 in Figure 2-51(b) and (c), however in Case 1 the line temperature horizontal averages are higher than Case 2, and likewise, the horizontal averages in Case 2 are higher than Case 3. Additionally, the "spreading" of the jets in the Case 1 and Case 3 line temperature plots show inverse behavior. In Case 1 where the hot jets dominate, the cold jet "spreads" far more with downstream distance as the line temperatures reach thermal equilibrium downstream. The opposite behavior is seen in Case 3 where the hot jets spread more aggressively downstream where the cold jet mass flux dominates. These aggressive shifts in surface temperatures along the plate with downstream distance suggest areas of potential thermal striping concern.

The analysis found in Figure 2-51 allows for evaluation of the maximum temperature of the hot jets relative to the X* and Y*-direction on the plate surface. The location of the maximum temperature of each downstream line trace for each case are provided in Figure 2-52.

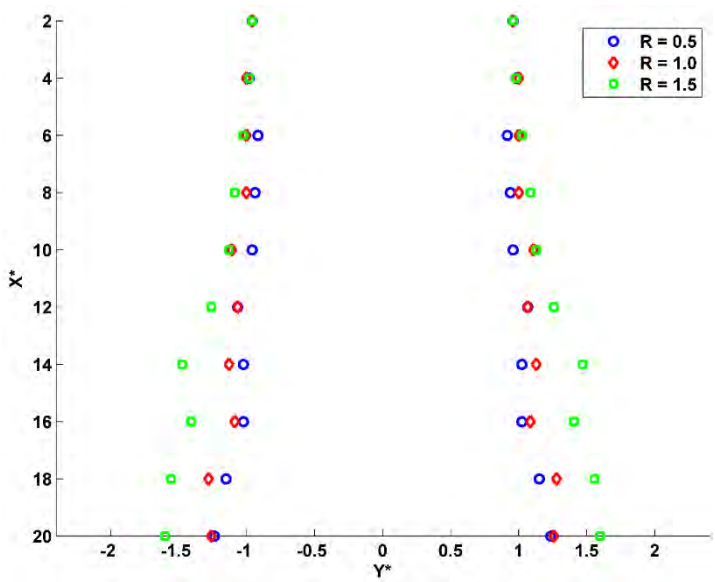

Figure 2-52. Peak temperature location for each line trace shown in Figure 2-51.

For the case with the highest hot jet velocity (R = 0.5), the peak temperature of each line trace was relatively close to the jet center lines. As the hot jet velocities were reduced for the R = 1.0 and R = 1.5 cases, the peak temperatures gradually move position further outside from the two jet centerlines, as the cold jet flow contributes more to the mixing taking place on the surface of the plate. Also worth noting is

the downstream behavior of each case. For each case, the Port 2 line traces provide peak temperatures that were slightly further outside than that of the Port 1 peak temperatures. The same comparison can be made for the peak temperatures seen in Ports 2 and 3, in that the peak temperatures are even further out from the jet centerlines. This moving peak temperature away from the hot jet centerlines shows the dissipation in the heated flow across the plate in the Y*-direction. This implies that the heat is being conducted more outwardly along the surface of the plate as the flow moves downstream and is highly dependent on the velocity ratio between the center cold jet and outer hot jets.

The temperature fields provide comprehensive examples of the three regions of flow experienced by the triple round jet to parallel wall configuration. These temperature profiles are in good agreement with profiles determined using a similar slot jet to parallel wall configuration in previous studies [10, 12, 42-43]. The spreading of the temperature profiles for each case and the moving peak temperature found as a function of the line traces across the plate and downstream location hint at the possibility of an empirically determined probability function of crack propagation in the plate as induced by thermal striping. Future research will look more closely at the movement of the line temperature profiles and peak temperature downstream along the plate and will utilize additional temperature differences, as well as plate spacings and jet spacings that are geometrically comparable to those seen in the scaled version of the lower plenum of the VHTR core.

2.6 Unit Cell Experiments

Design of the unit cell experimental test section has been previously detailed in Section 2.2.2. Key modeling parameters involving the geometry of the test section are reiterated here. The unit cell test section depicted in Figure 2-53 consists of a hexagonal array of seven aluminum cylinders (herein referred to as posts) with a cross flow inlet moving in the +x-direction and six interstitial jets, also in a hexagonal arrangement, issuing vertically downward into the test section in the +z-direction.

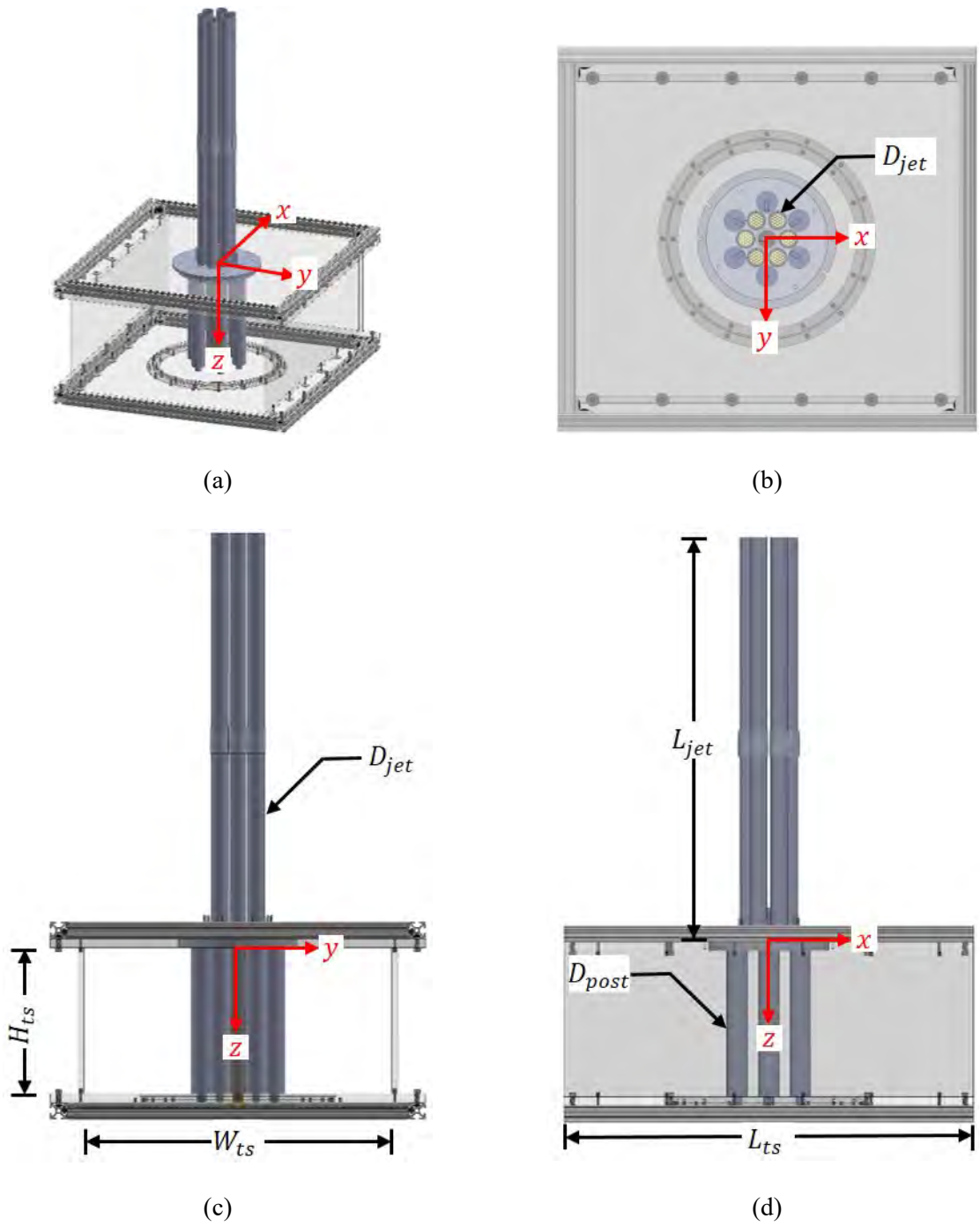

Figure 2-53. Unit cell test section (a) isometric view, (b) top view, (c) front view, and (d) side view

The cross flow is generated by a wind tunnel at approximately room temperature and the non-isothermal jets are motivated by a temperature and flow control system. The working fluid for both systems is air. The system is capable of producing three unique flow rates and fluid temperatures via corresponding

flow meters and heaters. The three lines are then separated via manifolds into the corresponding six jets. The test section side and bottom walls are composed of clear 9.525 mm thick polycarbonate allowing for optical access. The bottom wall consists of a rotating insert to allow for an inline or staggered array of posts as depicted in Figure 2-54. This figure also introduces the lettering scheme for the posts and numbering scheme for the jets in both orientations. Critical test section dimensions are presented in Table 2-11 where the nomenclature references Figure 2-53 and Figure 2-54.

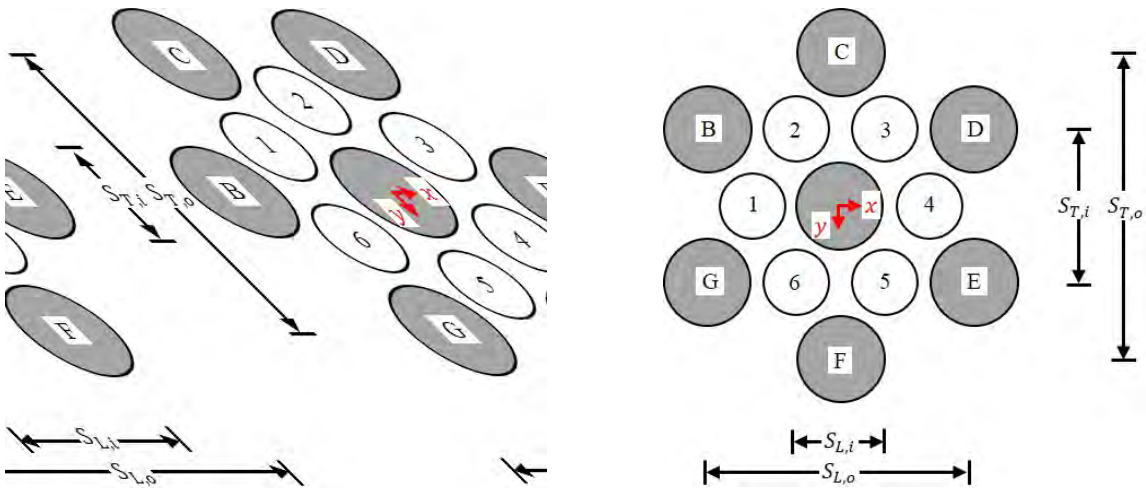

(a) (b)

Figure 2-54. Top view of unit cell test section depicting (a) inline cylinder array and (b) staggered post array. Cross flow is in $+x$-direction and jets are flowing in the $+z$-direction (into page).

A PIV system from LaVision Inc. is utilized with three high-speed cameras, each operating in planar 2D-2C (2 dimension, 2 component) with a two-dimensional laser sheet. The cameras are Phantom Miro M120's with 1920 × 1200 pixel resolution and 12-bit dynamic range. Each camera is equipped with a Nikon AF NIKKOR 50 mm f/1.8D lens and a LaVision Inc 527 nm lens filter with 10 nm band pass and 70% transmission efficiency. The horizontal light sheet is produced by a dual cavity pulsed DM30-527-DH laser from Photonics Industries Inc. with a maximum power of 60 mJ/pulse at 527 nm and a maximum

pulse rate of 10 kHz. The cross flow is seeded with dioctyl sebacate via a TSI Six-Jet Atomizer Model 9306 with an approximate seeding size of 2.2 μm [13].

Each camera utilizes a 25.4 mm × 25.4 mm front silvered mirror rotated at 45° from the $+y$-direction toward the $+z$-direction. The mirrors are placed at strategic locations underneath the test section where the laser sheet provides optimal illumination (no interference from posts, i.e. shadowing) around the posts. These locations include a direct inline view of posts E and G as well as the cross flow inlet. A simplified schematic of the experimental setup with one camera and mirror assembly is provided in Figure 2-55. Each of the other three cameras and mirror assemblies follow a similar arrangement. All cameras and mirrors are mounted on linear bearing optical table top mounts whose position can be measured to within 0.5 mm.

Table 2-11. Unit cell test section dimensions

	Name	**Nomenclature**	**Dimension [mm]**
Consistent	Test section width	W_{ts}	457.84
	Test section height	H_{ts}	217.42
	Test section length	L_{ts}	609.60
	Post diameter	D_{post}	31.75
	Post length	L_{post}	217.42
	Jet diameter	D_{jet}	22.23
	Jet length	L_{jet}	615.95
In-line array	Inner streamwise pitch	$S_{L,i}$	54.00
	Outer streamwise pitch	$S_{L,o}$	107.95
	Inner transverse pitch	$S_{T,i}$	31.19
	Outer transverse pitch	$S_{T,o}$	93.49
Staggered array	Inner streamwise pitch	$S_{L,i}$	31.19
	Outer streamwise pitch	$S_{L,o}$	93.49
	Inner transverse pitch	$S_{T,i}$	54.00
	Outer transverse pitch	$S_{T,o}$	107.95

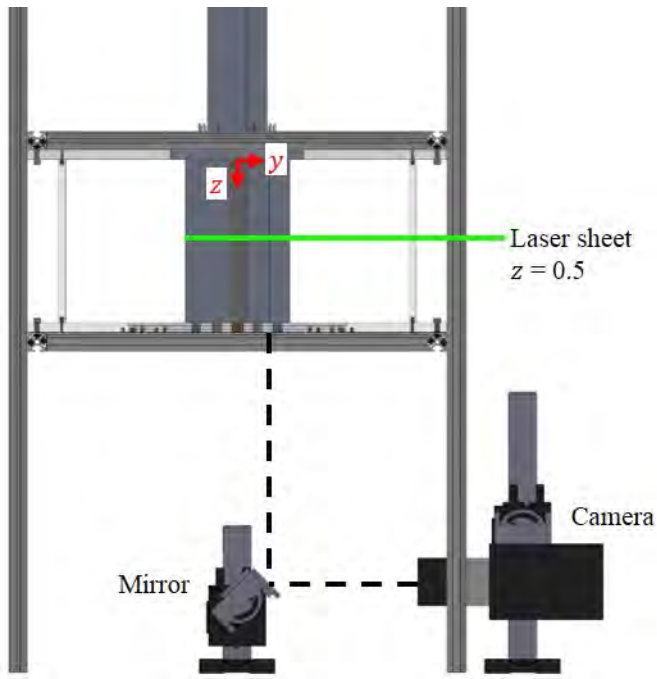

Figure 2-55. Basic PIV arrangement utilized for experimental testing

The tight space constraint underneath the test section as well as between the posts inside the test section provides a challenge for calibration of the cameras. An optimal configuration would include the use of automated linear stages for an accurate calibration of the cameras using a calibration target outside of the test section. In the absence of linear stages, a 'dry run' is conducted in which the laser is illuminated, the cross flow is seeded, and the cameras are focused on the seeder particles. Reference images are acquired for each camera which include known distances between the adjacent posts. These distances yield a scaled calibration factor for cameras 1 and 3, which are focused on posts G and E, respectively. Considering current experimental limitations, the scale factor provides a reasonable calibration for these two cameras, given that there is a reference geometry in each field of view. Camera 2 however, is focused on the cross flow inlet and as such, does not have a reference geometry in its field of view. In lieu of a reference geometry, the closest reference geometry available to the inlet is that of post G and as such, the scale factor found for camera 1 is adopted for camera 2 as well. A summary of these scale factors is provided in Table

2-12. The capture parameters are provided in Table 2-13 and are consistent for all PIV results in the current work including all inlet testing and experimental results unless otherwise noted.

Table 2-12. High speed camera scale factor calibrations.

		Scale factors [mm/px]		
Camera	**In field of view**	**Case 1**	**Case 2**	**Case 3**
1	Post G	8.81889	9.22382	8.99888
2	Cross flow inlet	8.81889	9.22382	8.99888
3	Post E	9.35883	9.41079	9.13384

Table 2-13. PIV recording parameters.

Laser sheet thickness [mm]	≅1.0
Numerical aperture	4.0 (All cameras)
Field of view [mm^2]	150.36 mm × 206.38 mm (Cam 1)
	135.07 mm × 246.57 mm (Cam 1)
	171.13 mm × 205.14 mm (Cam 2)
Pulse separation [μs]	25 (Case 1)
	25 (Case 2)
	40 (Case 3)
Sampling frequency [Hz]	1000
Number of image pairs [frames]	1000

Vector calculation and basic post processing is provided by LaVision's DaVis version 8.3 software. A complete description of the vector field processing steps is provided in Table 2-14. The instantaneous and mean velocity components, turbulence statistics, and velocity gradients are then computed from the processed vector fields.

Table 2-14. Vector field processing parameters

Procedure (numbered) and options	User input
1. Subtract time filter	
Subtract average	Use all images
2 PIV (particle image velocimetry): vector calculation: double frames	
Number of passes	2
Final interrogation area size [pixels]	32 × 32
Interrogation overlap [%]	50
3. Vector length filter	
Upper threshold [m/s]	30
4. Denoising and robust smoothing	
Number of passes	1
Smoothing mode	Simple averaging
Number of vectors for smoothing	16
Filling	No filling

The lower plenum unit cell experiment resides in a large warehouse laboratory environment with ample fluorescent lighting. The lighting promotes an undesirable ambient noise and lowers the seeder intensity count in the PIV measurements. Modifications to the physical experiment aid in reducing lighting noise, including camera band pass filters which limit environmental noise and painting of the posts with Keyacid™ Rhodamine WT to reduce laser light reflection. Of particular help is the subtract time filter referenced in Table 2-14. The subtract time filter subtracts the ensemble average intensity of the frame set from each individual frame, thereby greatly diminishing the ambient noise [44]. An example of this subtraction filter is displayed in Figure 2-56, using the 'worst offender' optical configuration. Figure 2-56 also aids in providing a qualitative view of the typical seeder density used in a given experiment. These challenges induce a lower than desirable intensity count for the seeder particles, but in post-processing, still provided ample vector field information.

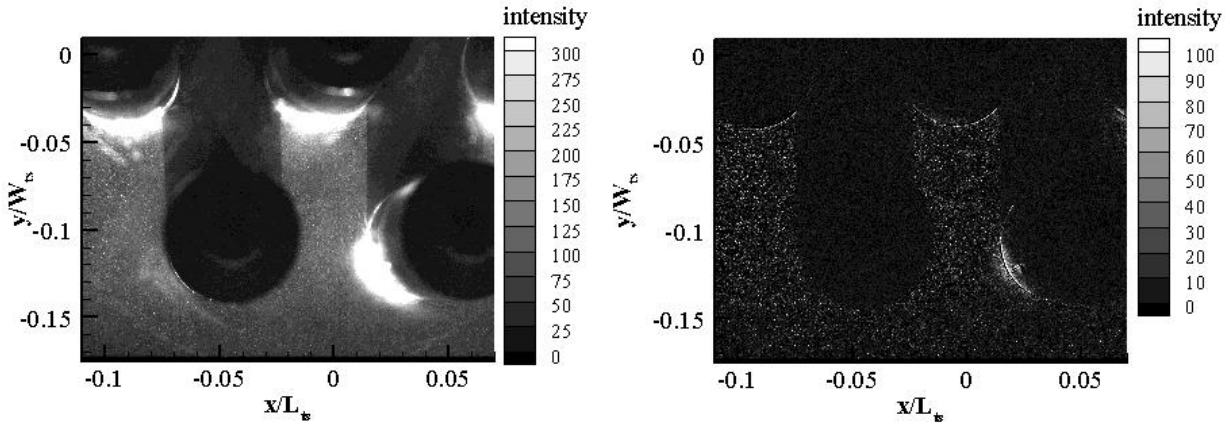

(a) (b)

Figure 2-56. Example of image subtraction feature using the case 2 post G optical configuration (a) raw image and (b) after image subtraction filter

With the velocity measurement system fully defined, the experimental design concludes with a brief description of the temperature measurement system. Type T thermocouples are placed radially along each of the aluminum posts. The thermocouples are calibrated using a fifth order polynomial curve fit with a reference OMEGA hot point® Dry Block Probe Calibrator with an accuracy of +/- 0.83 °C and maximum operating temperature of 130.0 °C. All unit cell operating temperatures are within the bounds of the calibration. While all outer posts (posts B-G) thermocouples remain fixed towards the center, the center post (post A) rotates clockwise along the *z*-axis and collects data in 30° increments, such that center post radial temperature profiles are available across the entire 360° domain. The post is turned with a high accuracy rotational stage with a resolution of 1.0°. For each case, both the center post and outer post thermocouples collect data at 500 Hz for 3 minutes. For each rotation of post A, steady-state was ensured before an additional measurement is collected.

With the geometry and measurement systems fully defined, the motivations behind the experimental tests are discussed from which test cases are proposed. The lower plenum unit cell involves a highly non-linear turbulent process promoted by the individual mass flux and momentum contribution from the cross flow and each of the impinging jets. The introduction of a non-isothermal condition for the jets implies that the energy equation is also introduced into the system of coupled equations describing the fluid

behavior. The experimental test cases look to investigate each of these influences by emphasizing either a strong cross flow velocity or jet velocity with some disparity in jet temperature amongst adjacent jet inlets. The experimental test conditions are provided in Table 2-15. In regards to Table 2-15, it should be noted that in lieu of proper pressure readings at the cross flow and jet inlets, the working fluid is assumed to be an ideal gas with a constant pressure of 1 atm. This is a reasonable approximation for fluid densities and dynamic viscosities, given the low gage pressure found in the unit cell test section via a pressure transducer mounted on the test section ceiling (digital signal not logged).

Table 2-15. Experimental test cases for unit cell studies

		Mean Inlet Temperature, $\overline{T}_{inlet}$ [deg C]	**Density, ρ [kg/m^3]**	**Dynamic Viscosity, μ [kg/(m*s)]**	**Mean Inlet Velocity, $\overline{V_{inlet}}$ [m/s]**	**Reynolds Number, Re_{inlet}**
Case 1	**Cross flow**	25.24	1.18	1.85E-05	12.53	2.36E+05
	Jet 1	83.26	0.99	2.11E-05	7.69	4.83E+03
	Jet 2	75.01	1.01	2.07E-05	7.83	8.49E+03
	Jet 3	41.19	1.12	1.92E-05	4.08	5.29E+03
	Jet 4	39.33	1.13	1.91E-05	6.74	8.86E+03
	Jet 5	34.62	1.15	1.89E-05	6.95	9.40E+03
	Jet 6	69.96	1.03	2.05E-05	4.63	5.17E+03
Case 2	**Cross flow**	26.67	1.18	1.85E-05	14.72	2.77E+05
	Jet 1	72.72	1.02	2.06E-05	12.07	1.33E+04
	Jet 2	45.92	1.11	1.94E-05	11.52	1.47E+04
	Jet 3	44.92	1.11	1.94E-05	11.27	1.43E+04
	Jet 4	71.28	1.02	2.06E-05	11.44	1.26E+04
	Jet 5	58.54	1.06	2.00E-05	11.53	1.36E+04
	Jet 6	55.94	1.07	1.99E-05	12.09	1.45E+04
Case 3	**Cross flow**	24.81	1.19	1.84E-05	7.68	1.46E+05
	Jet 1	50.44	1.09	1.96E-05	9.02	1.12E+04
	Jet 2	50.36	1.09	1.96E-05	9.48	1.17E+04
	Jet 3	70.81	1.03	2.05E-05	10.01	1.12E+04
	Jet 4	76.62	1.01	2.08E-05	9.44	1.02E+04
	Jet 5	68.62	1.03	2.04E-05	5.83	6.54E+03
	Jet 6	42.74	1.12	1.93E-05	5.40	6.97E+03

Case 1 issues a strong cross flow velocity into the domain relative to the jet inlet velocities. Case 2 provides proportional cross flow and jet velocities and a larger disparity in the temperature amongst adjacent jets. Case 3 introduces higher jet inlet velocities relative to the cross flow. Figure 2-57 acts as a visual aid to identify the non-isothermal jets by their corresponding manifold configuration, i.e. red is "hot", yellow is "medium", and blue is "cold". As opposed to conventional experiments where nominal test variables may be inferred from system specifications (i.e. inferring an inlet velocity based on the associated upstream flow rate reading or PLC controller input), each of the inlet temperature and velocity are directly measured via inlet tests which precede or are sequential with the actual experimental test cases. The following section provides a detailed description of each of these quantified inlet conditions before moving forward with the experimental test results.

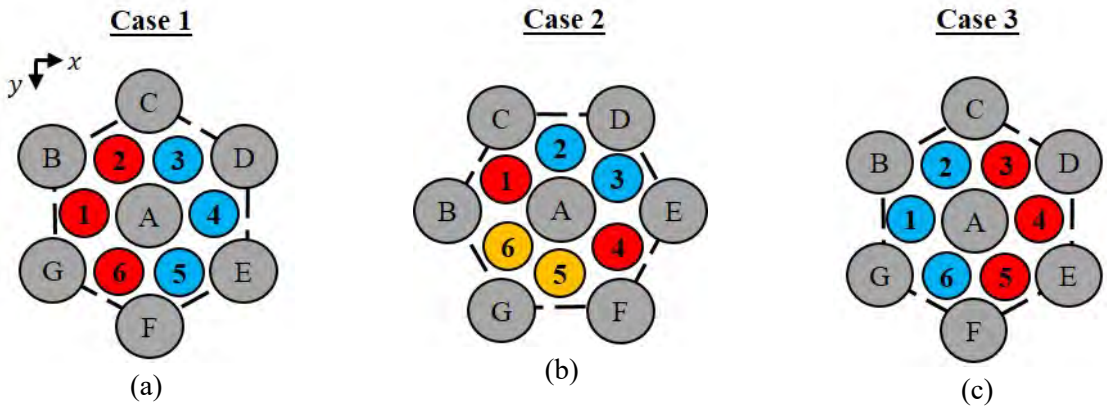

Figure 2-57. Visualization of non-isothermal jet configuration for each of the proposed test cases. Note: coordinate system in (a) is consistent for each figure, jet flows are into the page ($+z$-direction), and cross flow is in $+x$ direction

2.6.1 Boundary Conditions – Jet Inlet

Inlet temperature testing consists of positioning supplementary type-T thermocouples at the center of each jet inlet in the unit cell test section. For each unit cell test case, the thermocouples sample at 100 Hz every 30 seconds. The reported outlet temperatures are the ensemble average of these measurements over the course of 2 hours once a steady-state condition has been achieved. The ensemble averaged jet inlet temperatures were presented previously in Table 2-15. A repeatability study is also performed for the case

involving the highest proposed absolute jet inlet temperatures, namely case 1, the results of which are presented in Table 2-16. Five total tests for case 1 are performed for this assessment.

Table 2-16. Repeatability assessment for case with highest absolute jet inlet temperatures (case I)

Jet number	$\overline{\mathbf{T_{inlet,jet}}}$ **[°C]**
Jet 1	83.26 +/- 1.51
Jet 2	75.01 +/- 1.61
Jet 3	41.19 +/- 1.73
Jet 4	39.33 +/- 1.76
Jet 5	34.62 +/- 1.92
Jet 6	69.96 +/- 1.95

The difference in jet inlet temperatures for a given case is attributed to the asymmetric manifold flow channels and implies a corresponding disparity in flow rates. An optical view of the jet inlets in the x-z plane is limited, due to the optical obstruction from the posts. A secondary test section is utilized to capture the jet inlet velocity profiles. The secondary test section consists of a 738.19 mm × 749.3 mm × 1068.39 mm enclosure with three jets issuing into the domain from the top surface. The jets are geometrically identical to those of the unit cell test section. The manifold connections and temperature and flow conditioning are replicated for each set of jets used for the three test cases. An example of the manifold configuration for three jets is presented in Figure 2-58.

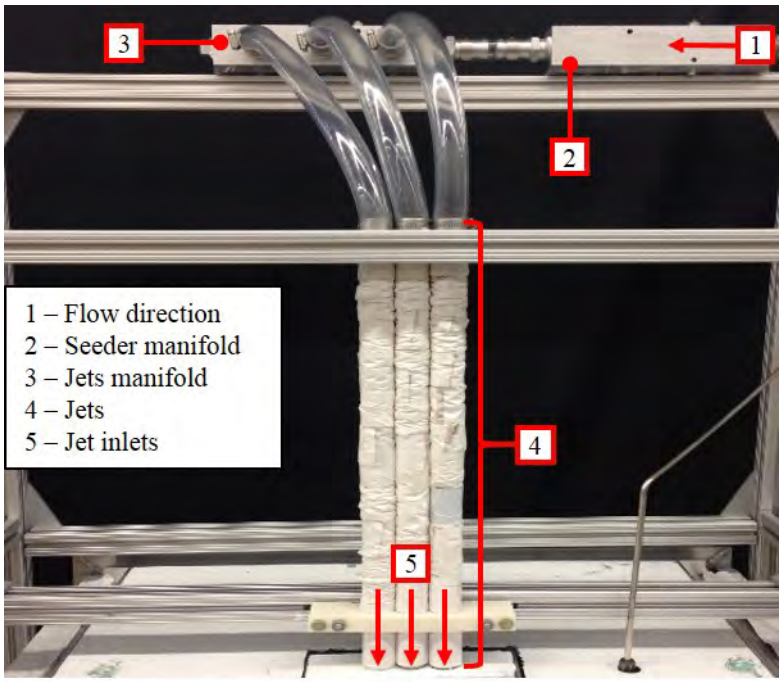

Figure 2-58. Three jet manifold configuration for jet inlet testing

Gage pressure during testing in the enclosure was found to be very small and comparable to the gage pressure found in the unit cell test section during inlet temperature testing (note that this did not involve the presence of a cross flow). As such, the difference in gage pressure between the two test sections was found to be negligible. A high speed camera with a planar 2D-2C PIV configuration is used to record the inlet velocity profiles of the jets. The camera has a scale factor of 11.063 mm/pixel and identical recording parameters to that of Table 2-13 with the exception of a field of view of 177.89 mm × 66.53 mm and pulse separation of 25μs. The jet inlet velocities were evaluated at the trace z/H_{ts} = 0.0266. Convergence of the inlet jet velocity means, standard deviations, second moments, and third moments are evaluated using the maximum error criteria, ϵ_{max}, presented in Eq. (2-26) for a given inlet line trace:

$$\epsilon_{max}(x,y,t) = max\left(\frac{\left|\phi_{ens,x,y,t} - \phi_{ens,x,y,t-1}\right|}{\left|\phi_{ens,ij,t}\right|}\right) \leq \epsilon_{tol} \qquad t \in 2{:}N \tag{2-26}$$

where ϕ_{ens} is an arbitrary ensemble averaged parameter at a given location x,y at time, t and N corresponds to the total number of frames needed to reach convergence ($N \leq$ total number of available frames). All jet

inlet trace velocity statistics for each manifold configuration converged to within 0.5% in the available 1000 frame PIV data sets. An example convergence study of all velocity statistics for a given jet is presented in Figure 2-59. Examples of this disparity in flow rate can be seen in Figure 2-60(a-b) for an arbitrary two jet scenario and Figure 2-60(c-d) for an arbitrary three jet scenario.

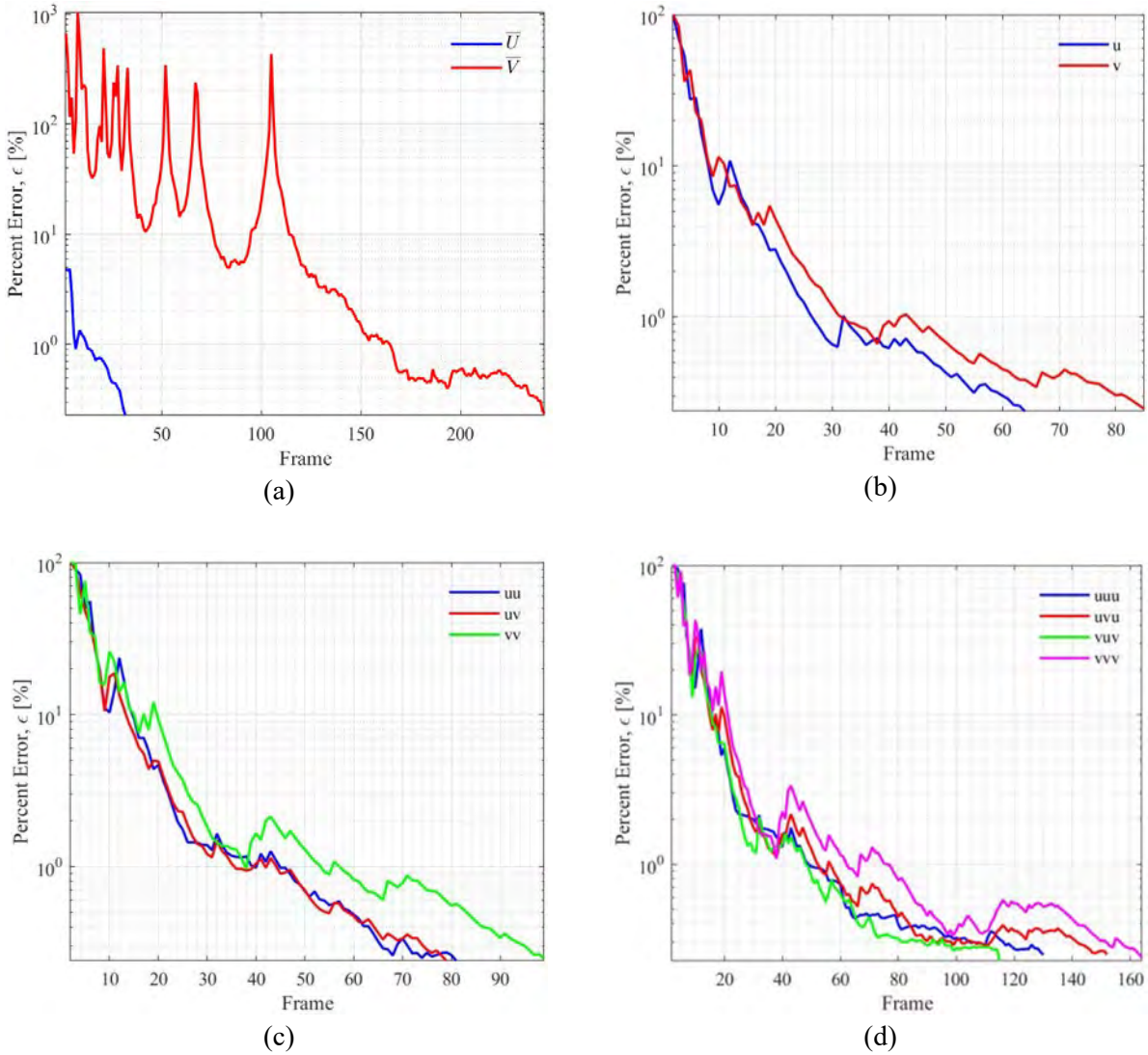

Figure 2-59. Convergence of case 1 jet 6 inlet velocity statistics (a) mean velocities, (b) standard deviation of velocities, (c) second order moments, and (d) third order moments

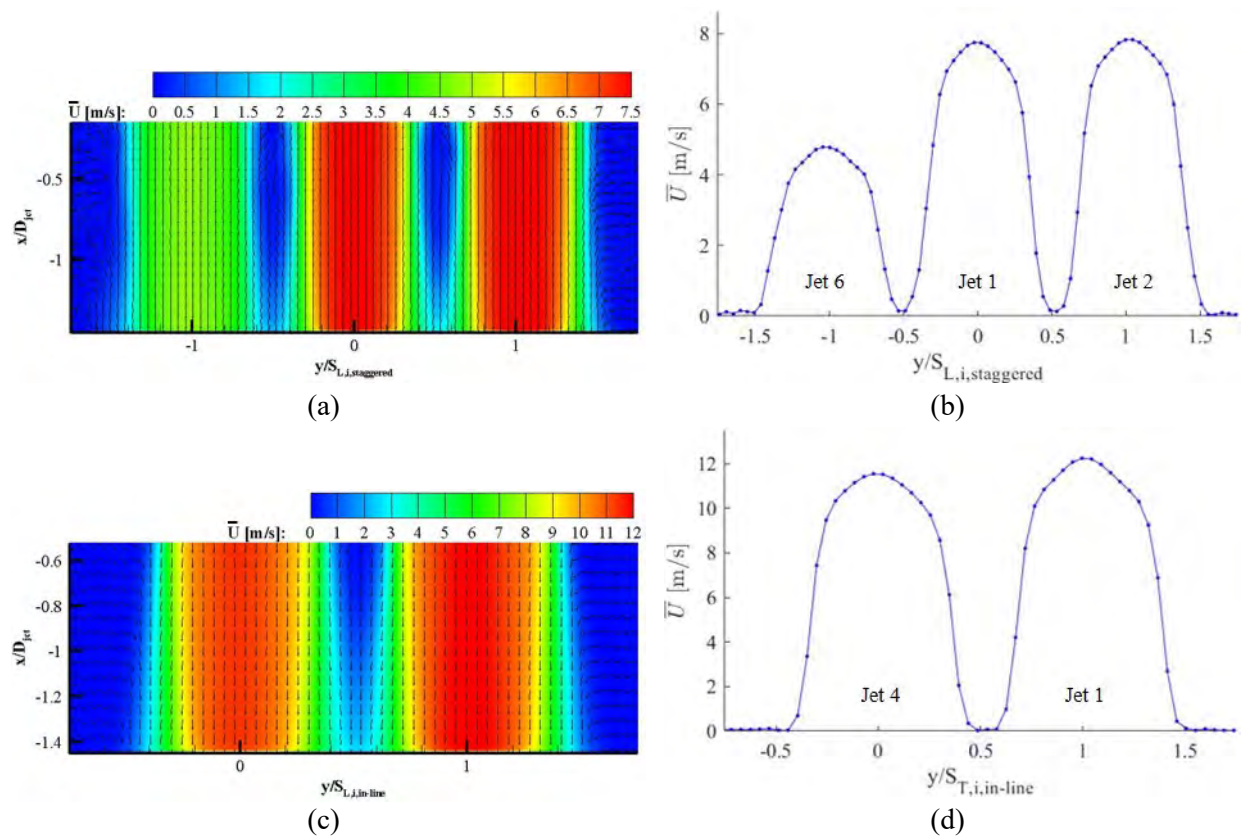

Figure 2-60. Case 1 'hot' manifold (a) velocity contour and (b) inlet velocity profile and case 2 'hot' manifold (c) velocity contour and (d) inlet velocity profile

For a given jet inlet profile, the averaged outlet velocity for an arbitrary jet, $\overline{V_{inlet,jet}}$ is obtained according to Eq. (2-27)

$$\overline{V_{inlet,jet}} = \frac{\int_0^{D_{jet}} U(y)}{D_{jet}} \tag{2-27}$$

where, in this instance, $\overline{V_{inlet,jet}}$ is equivalent to the streamwise flow component, namely, $\overline{U}$ at the inlet as depicted in Figure 2-60(b) and (d). The averaged inlet velocities can be used for RANS simulations, while for LES, the instantaneous velocity profile for each jet is used as the boundary condition in the simulation and is updated every 1 millisecond since the PIV data capture rate is 1000 Hz. Since high speed data acquisition was not employed for temperature measurements, the average values would be used for both RANS and LES approaches.

2.6.2 *Boundary Conditions – Crossflow*

A total of six supplementary thermocouples are placed along the periphery of the cross flow inlet to the test section; one in each corner and two along the y-centerline of the inlet ceiling and floor. These correspond the locations (x/L_{ts},y/W_{ts},z/H_{ts}) = (-0.5,-0.5,0.0), (-0.5, 0.0, 0.0), (-0.5,0.5,0.0), (-0.5,-0.5,1.0), (-0.5,0.0,1.0), and (-0.5,0.5,1.0).The same data acquisition protocol is followed for steady-state cross flow inlet temperatures. The temperature measurements are then averaged across all six thermocouples for each case to yield crossflow inlet temperatures of $(\overline{T_{inlet,cross}})$ = 25.24, 26.67, and 24.81 °C for case 1, 2, and 3, respectively. These values are slightly above room temperature and it is clear that for each case, the non-isothermal jet's added heat into the wind tunnel (whose flow is room temperature air upon startup) provides a minor increase in the steady state operating conditions.

Cross flow inlet velocity is captured during the experimental test cases. One of the three high speed cameras is positioned at the inlet to the test section and captures data in parallel with cameras positioned at posts E and G. PIV data acquisition setup and parameters were provided in the previous section. The cross flow inlet velocity is evaluated at the trace x/L_{ts}= – 0.4946 (a few millimeters from the inlet to the test section). Convergence of the inlet profiles was ensured using the same methodology as described for the jet inlets. All cross flow inlet velocity statistics were found to converge to within 0.5% in the allotted 1000 frame data sets with the exception of the spanwise velocity component V for case 1, which converged to 1.35% after 1000 frames. The cross flow inlet is expected to have a strong uni-directional flow in the +x-direction and as such the V-component of velocity is quite small. Based on the convergence criteria presented in Eq. (2-26), a small change in the magnitude of the V-component from one frame to the next can have a drastic effect on the maximum error across the inlet trace. Convergence details for the case 1 cross flow inlet velocity are provided in Figure 2-61. The evaluation of the cross flow inlet profile proceeds explicitly with the U-component.

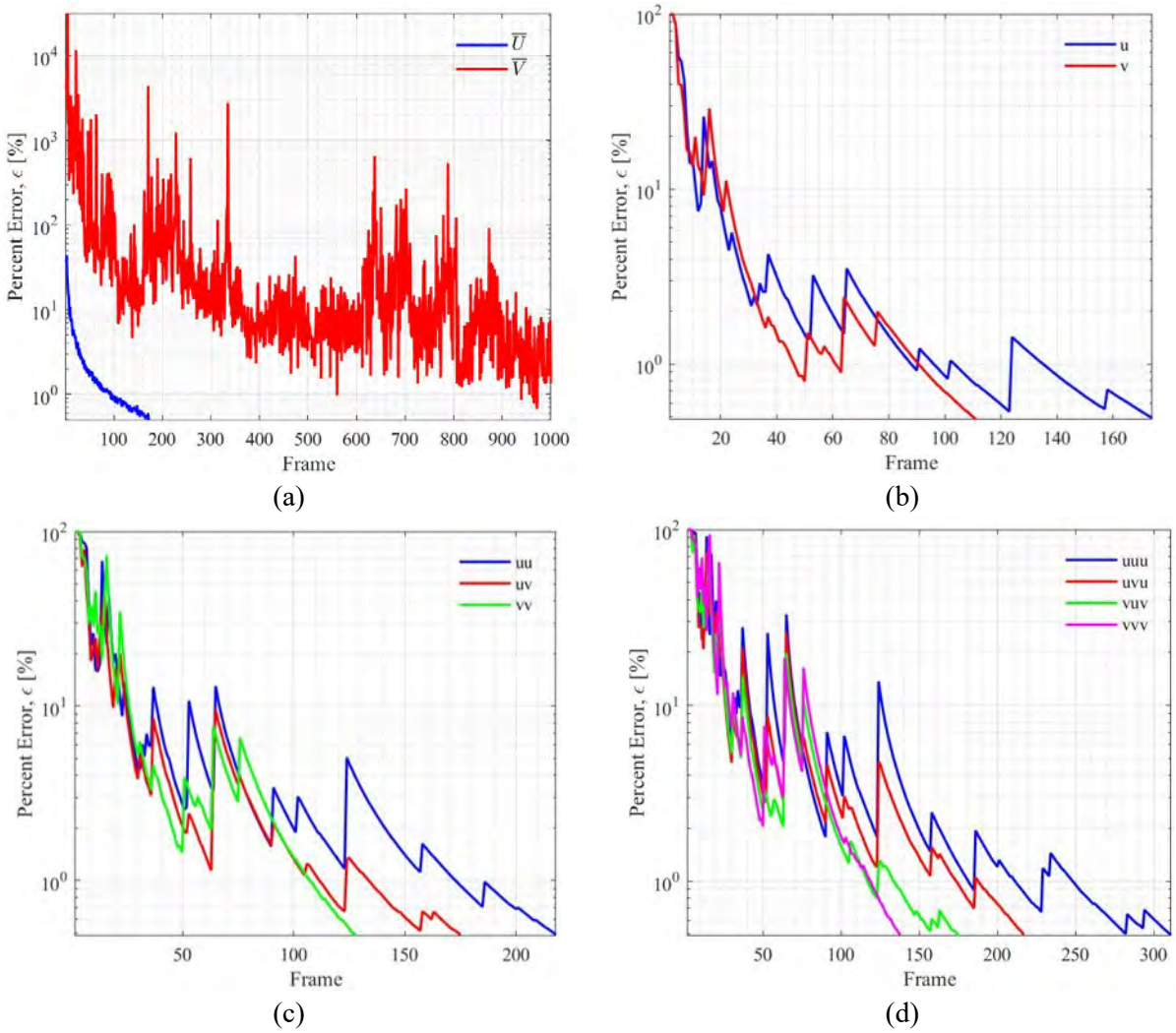

Figure 2-61. Convergence of case 1 cross flow velocity statistics (a) mean velocities (b) standard deviation of velocities (c) second order moments and (d) third order moments

Similar to the jet inlet profiles, line traces of the cross flow inlet are used to determine the inlet velocity. The cross flow inlet velocity testing is currently limited by several factors. A non-transparent test section top wall limits spanwise (y-direction) velocity measurements to underneath the test section. There is a limited amount of space underneath the test section. Ideally, cross flow inlet data is captured simultaneously with the post measurements. The current configuration, as discussed in the Experimental Methods section, allows for a maximum of three cameras in this confined space. As such, the camera

measuring the cross flow inlet is able to capture approximately 20% of the width (y) of the test section at a discrete height of z/H_{ts} = 0.5. The cross flow inlet velocity for each case can be seen in Figure 2-62.

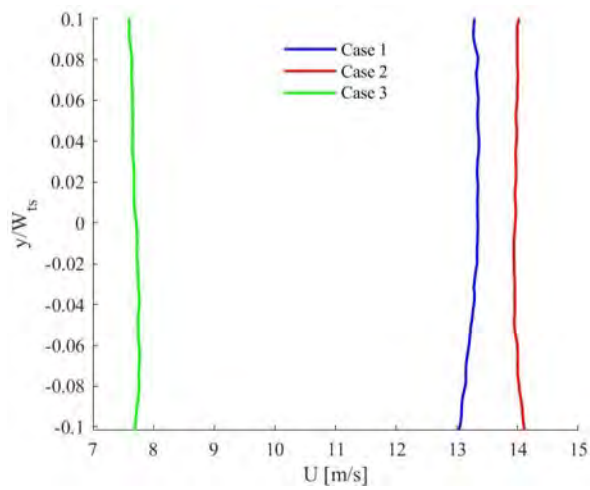

Figure 2-62. Cross flow inlet velocity trace for each case

As mentioned prior, the cross flow inlet velocity ideally has a 'flat' profile. The velocity should be nominally uniform across the test section inlet with the exception of near wall behavior. The 'flatness' of the cross flow inlet velocity is evaluated according to the following expression:

$$Uniformity = max\left(\frac{U_{inlet,cross}(y) - \overline{U_{inlet,cross}}}{\overline{U_{inlet,cross}}}\right) \cdot 100\% \tag{2-28}$$

where Eq. (2-26) is used to determine the average inlet velocity (with the evaluated cross flow inlet width substituted for jet diameter). From Eqs. (2-26) and (2-27) the cross flow inlet conditions are evaluated and presented in Table 2-17.

Table 2-17. Cross flow inlet average velocities and uniformity

Case	$\bar{U}_{inlet,cross}$ [m/s]	$Uniformity$ [%]
1	13.2755	1.83
2	13.9842	0.91
3	7.6993	1.34

2.6.3 Experimental Results

2.6.3.1 Temperature Measurements

As previously discussed in the design of the unit cell experiment section, each of the posts consists of four embedded thermocouples aligned radially towards the center. A total of twenty-eight thermocouples were utilized and are organized according to post letter and thermocouple number. For a given post, thermocouple '1' implies the sensor closest to the radial center of the post and thermocouple '4' implies the sensor furthest from the center. The center post thermocouples axial position remains fixed during testing and is unavailable for adjustment due to a permanent coupling to the central shaft. The outer post thermocouples however, are subject to some maneuverability in axial height. As a preliminary test, the thermocouple heights are adjusted and it is determined that the thermocouple temperatures for a given post and height are constant to within 1.0 °C regardless of radial position. This behavior is promoted by the post material, aluminum, which was chosen based on its ease of machining, yet exhibits an undesirably high thermal conductivity. To assuage the lack of interest in radial temperature profiles, alternative heights for the outer post thermocouples are proposed to provide more meaningful insight into the post temperatures as a function of axial height and radial position. Table 2-18 includes these positions and reports all average temperatures for the outer post thermocouples for the unit cell cases.

Table 2-18. Outer posts mean temperature measurements for unit cell test cases

TC	Mean Temperature, $\overline{T}$ [°C]			Height, z [mm]	Non-Dim. Height, z/H_{ts}	Radius, r [mm]	Non-Dim. Radius, r/D_{post}
	Case 1	Case 2	Case 3				
B1	59.19	44.64	62.98	42.86	0.20	3.33	0.21
B2	50.58	36.19	53.99	107.16	0.49	5.87	0.37
B3	49.1	32.49	54.44	21.43	0.10	9.37	0.59
B4	57.32	40.52	61.73	85.73	0.39	11.91	0.75
C1	51.84	38.9	59.63	42.86	0.20	3.33	0.21
C2	52.18	36.62	61.65	107.16	0.49	5.87	0.37
C3	44.78	32.14	52.45	21.43	0.10	9.37	0.59
C4	42.18	29.5	51.17	85.73	0.39	11.91	0.75
D1	54.5	38.99	69.23	42.86	0.20	3.33	0.21
D2	42.26	29.78	55.29	107.16	0.49	5.87	0.37
D3	49.54	37.44	63.34	21.43	0.10	9.37	0.59
D4	46.15	33.79	60.59	85.73	0.39	11.91	0.75
E1	51.5	39.61	62.37	42.86	0.20	3.33	0.21
E2	47.49	35.78	59.05	107.16	0.49	5.87	0.37
E3	54.39	44.61	65.37	21.43	0.10	9.37	0.59
E4	42.01	31.31	53.31	85.73	0.39	11.91	0.75
F1	46.4	38.42	55.42	42.86	0.20	3.33	0.21
F2	49.92	37.57	59.09	107.16	0.49	5.87	0.37
F3	54.13	47.01	63.99	21.43	0.10	9.37	0.59
F4	38.85	28.82	45.52	85.73	0.39	11.91	0.75
G1	43.6	28.3	46.73	42.86	0.20	3.33	0.21
G2	41.55	25.57	46.88	107.16	0.49	5.87	0.37
G3	50.44	36.84	56.07	21.43	0.10	9.37	0.59
G4	49.25	33.95	53.05	85.73	0.39	11.91	0.75

The center post mean temperatures as a function of rotational position about the z-axis are reported in Table 2-19 through Table 2-21. It should be noted that the 0° orientation aligns the center post thermocouples with the $+x$-direction and that the post is rotated clockwise (from the $+x$-direction towards +y-direction in reference to Figure 2-53(b)).

Table 2-19. Case 1 center post mean temperatures as a function of rotational position

Rotational Position, θ [°]	Mean Temperature, $\overline{T}$ [°C]			
	TC A1	TC A2	TC A3	TC A4
0	35.77	39.35	35.21	45.57
30	34.34	35.36	30.78	41.18
60	33.71	33.19	28.54	38.94
90	33.37	31.75	27.04	37.44
120	33.11	30.62	25.87	36.25
150	32.92	29.71	24.91	35.34
180	32.67	29.02	24.13	34.53
210	32.52	28.57	23.60	33.99
240	32.49	28.26	23.28	33.62
270	32.53	28.01	23.06	33.34
300	32.39	27.78	22.74	33.04
330	32.27	27.60	22.50	32.79

Table 2-20. Case 2 center post mean temperatures as a function of rotational position

Rotational Position θ [°]	Mean Temperature, $\overline{T}$ [°C]			
	TC A1	TC A2	TC A3	TC A4
0	34.20	34.62	30.17	39.92
30	34.13	34.10	29.57	39.35
60	34.03	33.72	29.21	39.05
90	33.98	33.39	28.85	38.68
120	33.93	33.21	28.58	38.47
150	33.98	33.00	28.47	38.28
180	33.97	32.88	28.32	38.16
210	33.97	32.92	28.32	38.15
240	34.05	33.05	28.38	38.19
270	34.14	32.97	28.27	38.11
300	34.14	33.02	28.29	38.15
330	34.23	33.00	28.36	38.21

Table 2-21. Case 3 center post mean temperatures as a function of rotational position

Rotational Position θ [°]	Mean Temperature, $\overline{T}$ [°C]			
	TC A1	TC A2	TC A3	TC A4
0	39.54	45.75	42.15	52.17
30	38.20	41.57	37.76	47.89
60	37.74	39.50	35.87	45.97
90	37.39	38.18	34.43	44.53
120	37.12	37.24	33.43	43.41
150	36.91	36.02	32.25	42.13
180	36.65	35.53	31.65	41.46
210	36.33	34.85	30.81	40.68
240	36.13	34.41	30.26	40.07
270	36.06	34.16	29.96	39.73
300	35.95	33.90	29.61	39.35
330	35.87	33.62	29.24	39.06

2.6.3.2 Flow Field Measurements

Two high-speed cameras are aligned with the axial centerlines of posts E and G as previously described. Planar 2D-2C PIV measurements are especially useful in the interstitial areas between the posts. The predominant areas of interest lie in the areas where ample laser lighting is available with no interference from post shadows. This section analyzes the flow downstream of post G as an example, wherein a similar procedure is possible for the interstitial region upstream and downstream of post E. The areas of interest for post G in the staggered and in-line configurations are displayed in Figure 2-63.

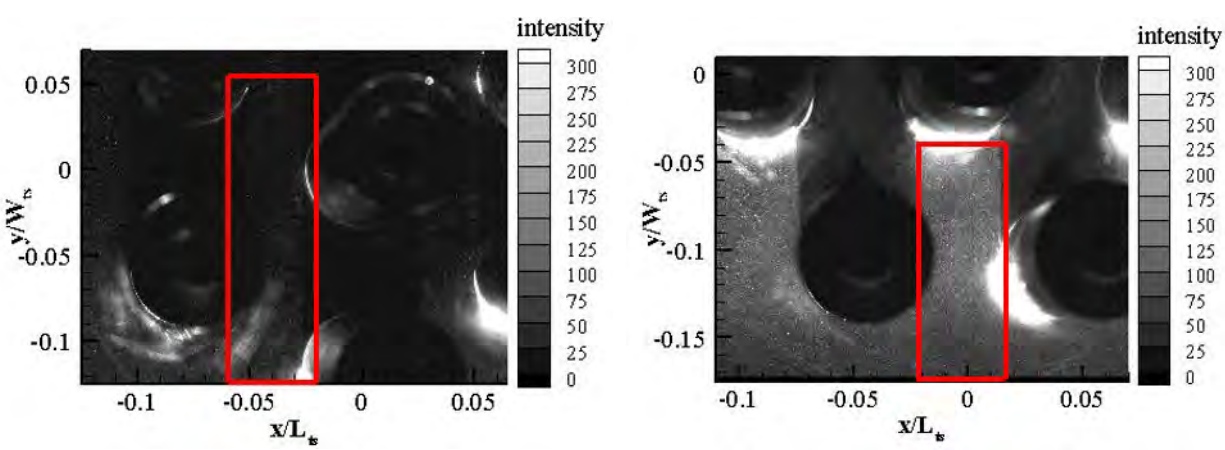

(a) (b)

Figure 2-63. Areas of interest for the (a) staggered and (b) in-line post configurations

The wake region behind post G exhibits a complex flow behavior as the result of several factors. The geometric orientation of the posts disrupts the classic flow past a cylinder arrangement with an adverse pressure gradient caused by the tight interstitial spacing between posts A. F, and G. At the center point of these three posts is a jet (jet 6 and 5 for the staggered and in-line arrays, respectively) which further disrupts the momentum of the flow past post G with the introduction of a strong pressure gradient in the z-direction. Analysis of the behavior is very complex and provides a significant challenge for investigation. A qualitative arrangement of the ensemble averaged and standard deviation of the velocity components for each case is presented in Figure 2-64.

The streamwise velocity component,U, delineates a clear impingement on the front surface of the post for cases 1 and 3 as seen in Figure 2-64(a) and (i), respectively, with an obvious increase in magnitude for the higher cross flow scenario (case 1). A slightly more interesting behavior is the flow reversal behind post G exhibited in Figure 2-64(e). The reversal encompasses a larger region behind post G for the inline configuration than either of the two staggered cases. The spanwise component of velocity exhibits a symmetric affect around the staggered post configurations as portrayed by Figure 2-64(b) and (j). It is also clear from Figure 2-64(f), that there is a very weak spanwise velocity component for the inline configuration post G. The velocity standard deviations, representing the fluctuating components of velocity, appear to exhibit similar contours for cases 1 and 3 as seen in Figure 2-64(c-d) and (k-l). Interestingly, these quantities have similar magnitudes as opposed to the case 1 and 3 mean components of velocity from Figure 2-64(a-b) and (i-j) which represent scaled formations of one another. The fluctuations present in the inline formation show peculiar peaks in fluctuations at different locations as referenced in **Error! Reference source not found.**(g-h).

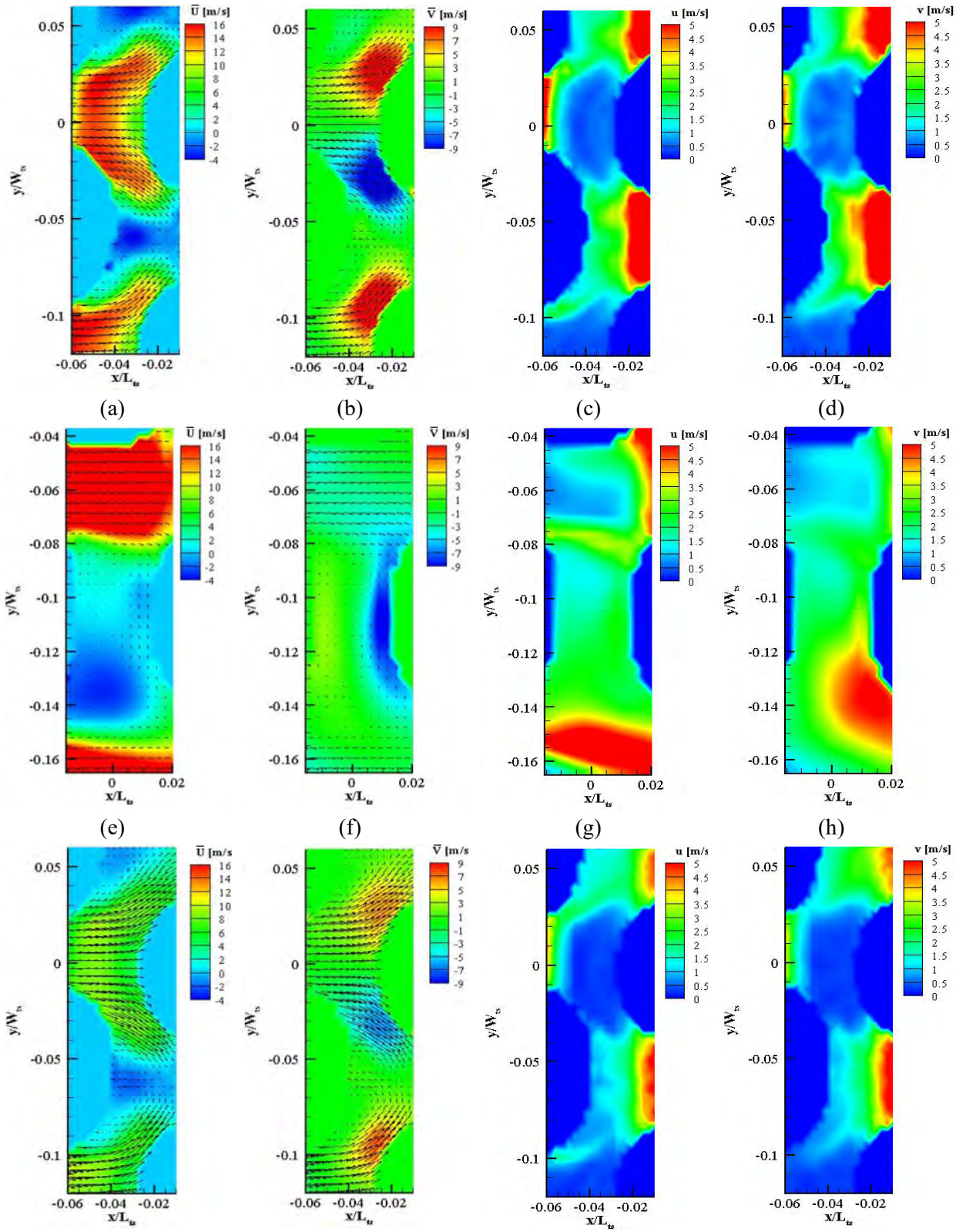
Ū [m/s]
V̄ [m/s]
u [m/s]
v [m/s]
y/W_ts
x/L_ts
(a)
(b)
(c)
(d)
(e)
(f)
(g)
(h)
(i)
(j)
(k)
(l)

Figure 2-64. Contours of ensemble averaged and standard deviation of velocity components for (a-d) case 1, (e-h) case 2, and (i-l) case 3

A deeper look into each individual flow scenario is accompanied by traces of the velocity statistics in the interstitial regions presented in Figure 2-63. The ensemble averaged ($\overline{U}$ and $\overline{V}$) and standard deviations (u and v) for case 1 are presented in Figure 2-65. From Figure 2-65(a), the streamwise component, $\overline{U}$, exhibits a clear dip in the profile around y/W_{ts}=0.0 due to the immediate halt in flow at the front of post A, which is immediately downstream of the line trace. The spanwise flow symmetry behind post G is clear in Figure 2-65(b) around y/W_{ts}=-0.04. The velocity fluctuations exhibit similar behaviors, both in the shape of their profiles and their magnitudes, as mentioned previously, yet here a deeper understanding of the peak locations of these fluctuations is apparent. From Figure 2-65(c-d), it is clear that both components are peaking in the y/W_{ts}=-0.05 area with similar magnitudes. For additional insight, the Reynolds stresses, uu, uv, and vv are presented in Figure 2-66.

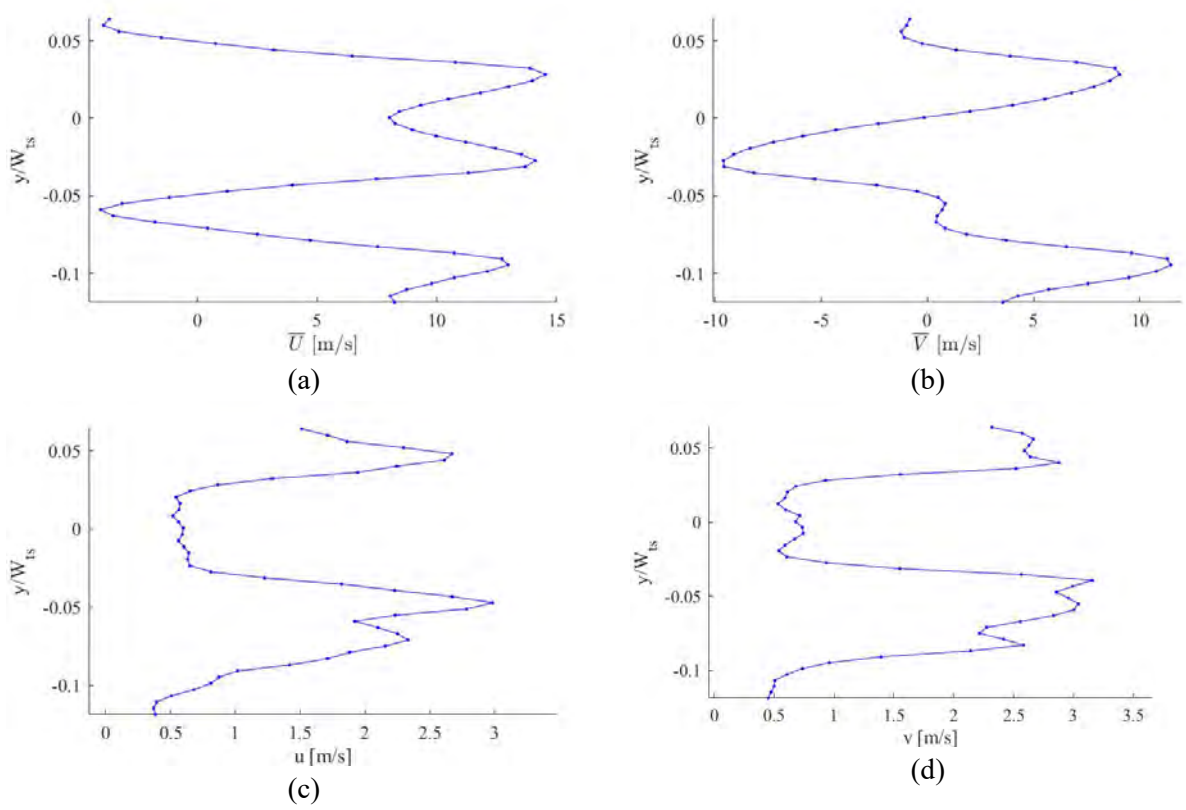

Figure 2-65. Case 1 mean velocity components along x/L_{ts} = -0.03

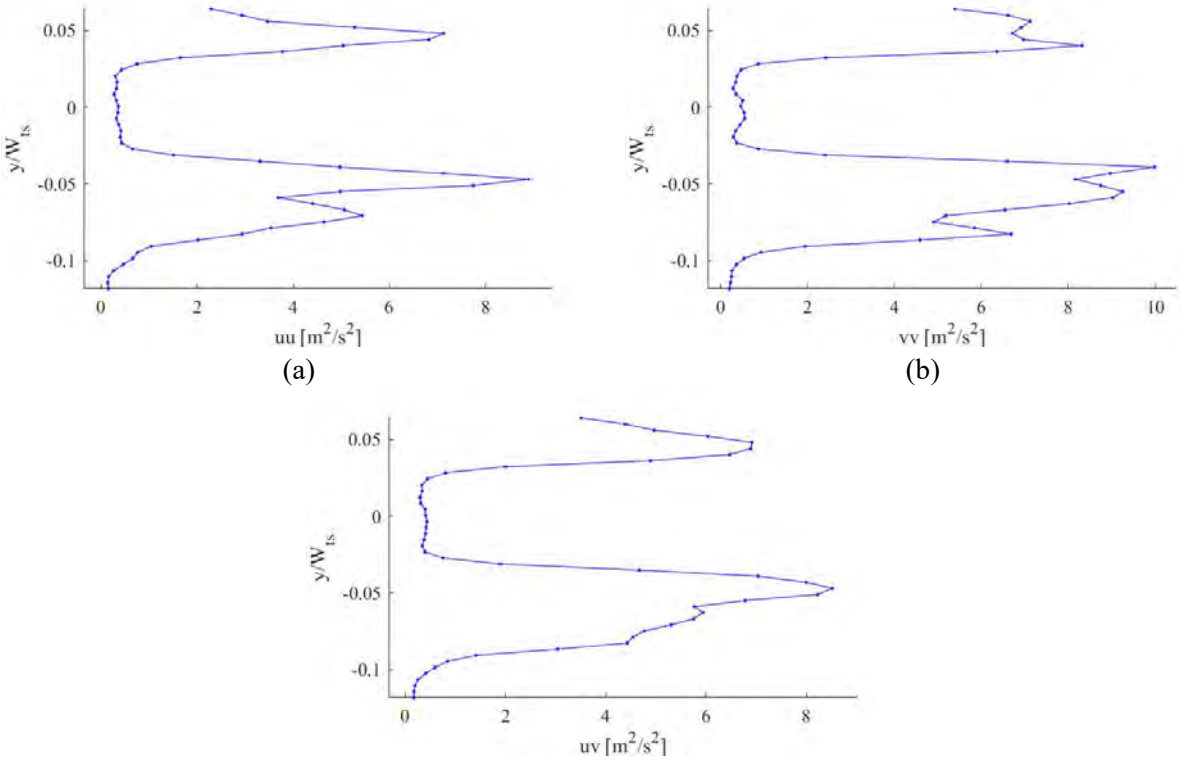

Figure 2-66. Case 1 Reynolds stress components along x/L_{ts} = -0.03

As expected, the normal components of the Reynolds stresses found in Figure 2-66(a) and (b), each have a peak magnitude almost in the exact same location, namely, y/W_{ts}=-0.05, similar to the individual fluctuating components. The shear component found in Figure 2-66(c) is a function of both fluctuating components of velocity, and as such, exhibits a slightly smoother profile with notable peak behaviors reminiscent of both normal components. The staggered array mean and fluctuating components of velocity are presented in Figure 2-67 as well as the Reynolds stresses in Figure 2-68.

From Figure 2-67(a), the streamwise component, $\overline{U}$, takes a much sharper dip directly behind post G. The wake region is perturbed by the immediate solid boundary enforced by post F in this inline configuration. The spanwise component, $\overline{V}$, exhibits a very erratic behavior with a much smaller magnitude than that exhibited in case 1. The velocity components in Figure 2-67(c) and (d) once again exhibit similar shapes, with the u-component exhibiting a higher peak than that of the v-component.

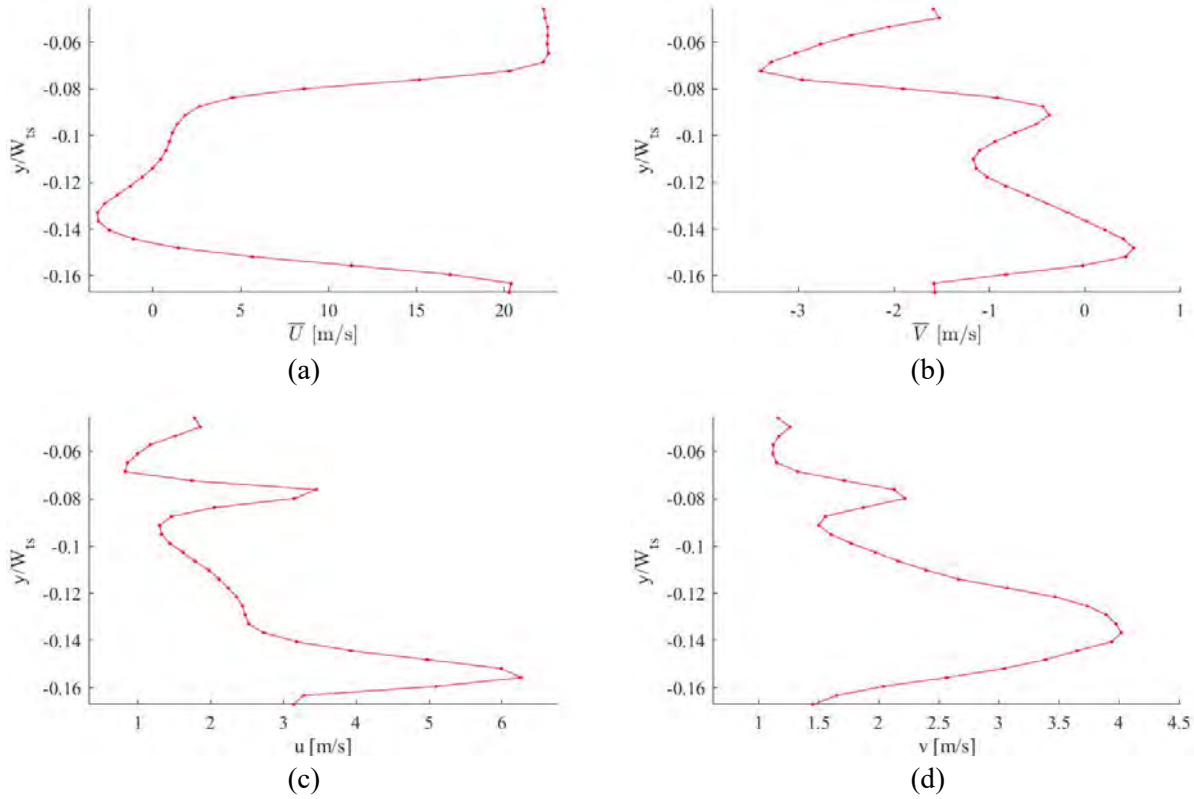

Figure 2-67. Case 2 mean velocity components along x/L_{ts} = -0.0

Of particular interest is the significantly higher peak values in all three Reynolds stresses found in Figure 2-68 for case 2. With the cross flow being the biggest momentum contributor, and the three cases having similar magnitude cross flows, it is surmised that the considerably larger Reynolds stresses found in case 2 are induced by the orientation of the posts. The inline array of posts would appear to facilitate higher Reynolds stresses directly behind post G than that of the inline array. To complete the flow field analysis, the velocity profiles and Reynolds stresses for case 3 are presented in Figure 2-69 and Figure 2-70, respectively.

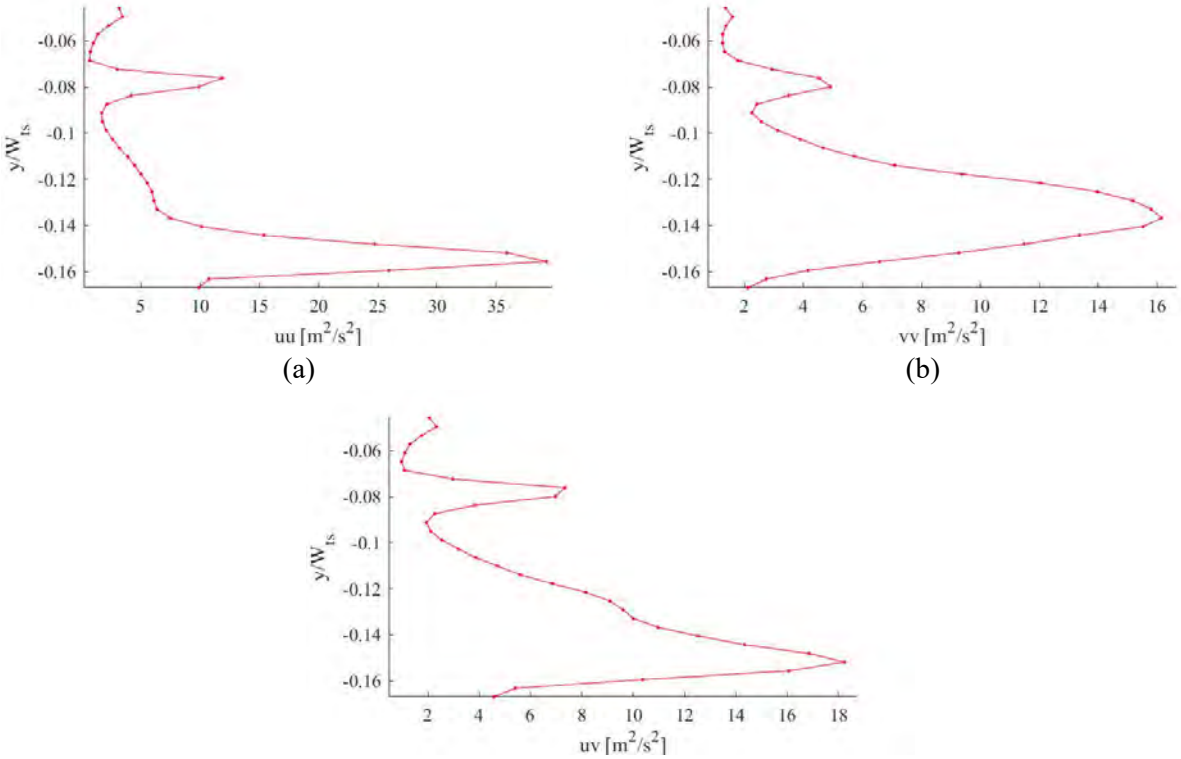

(a) (b)

(c)

Figure 2-68. Case 2 Reynolds stresses along x/L_{ts} = -0.0

As expected, the mean velocities in Figure 2-69 provide similar shapes with scaled magnitudes to those of case 1. The velocity fluctuations however, promote a more uniform profile but additional peaks in Figure 2-69(c) and (d) than those observed in Figure 2-65(c) and (d). This is reflected in the Reynolds stresses in Figure 2-70 which yield considerably smaller magnitudes than those of case 1 in Figure 2-66.

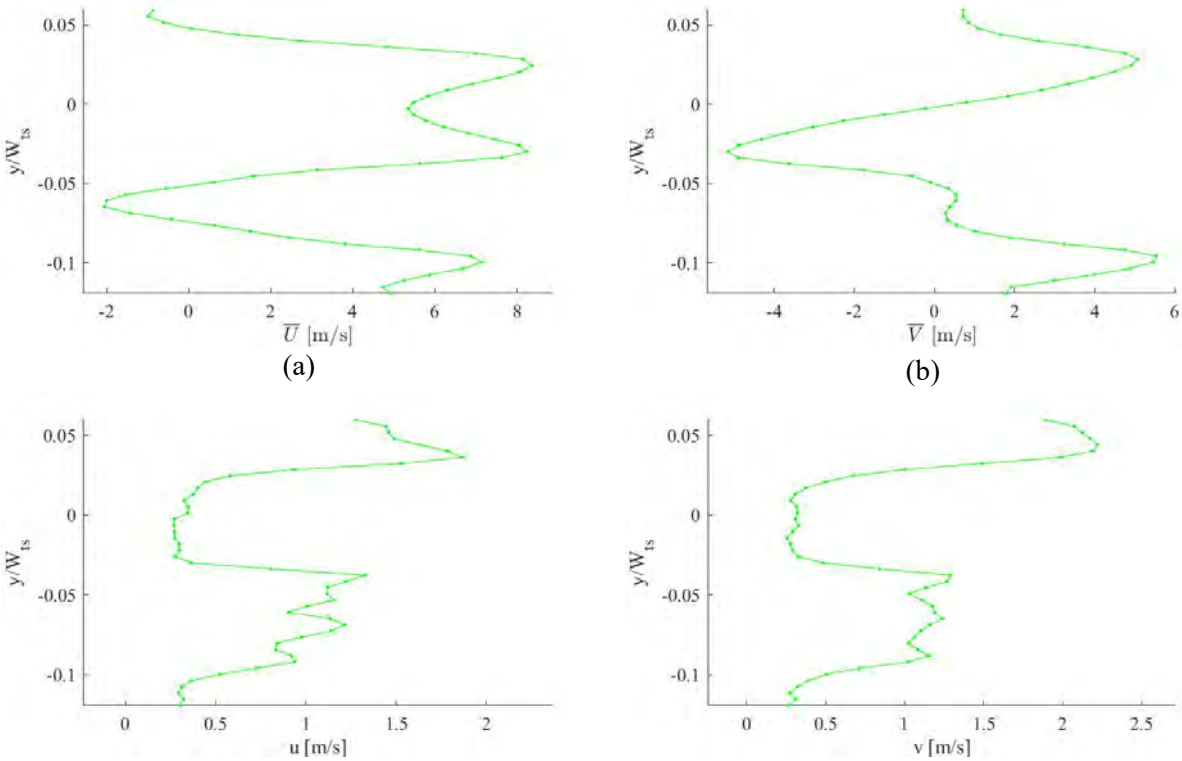

Figure 2-69. Case 3 mean velocity components along x/L_{ts} = -0.03

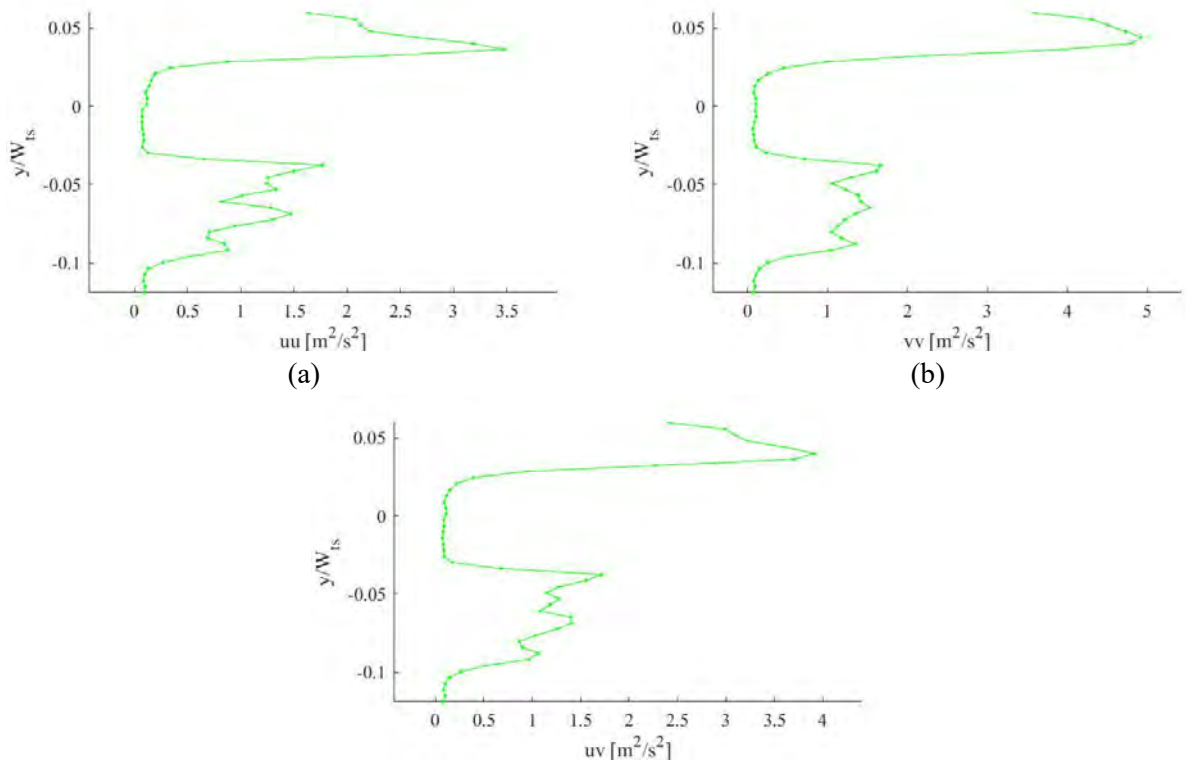

Figure 2-70. Case 3 Reynolds stress components along x/L_{ts} = -0.03

In conclusion, the lower plenum unit cell experimental testing involves a complex geometry which successfully combines several canonical flow types into one experiment. These include flow past a bank of cylinders (with both staggered and inline configurations), impinging jets, and non-isothermal jets in a cross flow. Any one of these flow types provides a rich and complex look into the behavior of fluid interactions in highly turbulent scenarios. By combing each into a single experiment relevant to the VHTR lower plenum, the authors hope not to exhaust the fundamental analysis of any of these individual flow features, but to provide a comprehensive look at the combination of features in an experimental test bank for future VHTR lower plenum validation. There are several caveats to this preliminary investigation, which is an ambitious attempt and as a result, includes several "lessons learned" from the design of experiment, construction, and experimental testing herein. Any future testing of the unit cell experiment should look to isolate certain thermal or hydraulic variables in the experimental facility. Namely, the independent roles and effects from the inlet velocities and temperatures of the cross flow and jets. By isolating these variables,

both experimental and modeling efforts will better deduce the individual contribution to the turbulent mixing experienced in the lower plenum unit cell from those inputs specifically. As an example, the cross flow inlet velocity could be varied while the jet inlet velocities remained fixed, or vice-versa. By limiting the number of input variables for a given case, repeatable data sets are much more feasible, i.e. the time to complete experimental test cases is much more manageable and implies a faster turnaround for repeated experiments. With repeatable data sets, a proper uncertainty quantification of the inlets or test metrics is possible. The acquisition of automation hardware, namely linear stages for the high-speed cameras, laser, and calibration target are essential tools for future efforts towards accurate and repeatable data sets.

It is the intent of this preliminary investigation then, to provide a brief look into three intricate thermal hydraulic scenarios that may prove challenging from a modeling perspective. Several test metrics are provided including internal temperature measurements of the posts as a function of radial and axial location, mean and fluctuating components of velocity, and corresponding Reynolds stresses. All included metrics serve as validation for fluid and fluid-to-structure simulations of the VHTR lower plenum unit cell and will be used for such comparisons later in this report.

3 Computational Studies

Computational Fluid Dynamics (CFD) has become a standard modeling approach for many industries. It provides the engineer with the opportunity to conduct detailed investigations where the only expense is a computational one. Flow features can also be thoroughly investigated in a non-invasive way, as opposed to experimental techniques which almost always require some amount of intrusion into the flow. However, these significant advantages of CFD must be viewed with some degree of skepticism, especially for complex or turbulent flows, where a given modeling approach, although numerically stable and able to produce seemingly reasonable results, may not be physically valid depending on the underlying assumptions on which it is based. Recognizing these limitations, there has been a concerted effort over the past number of decades to establish formal guidelines one can use to quantify the uncertainty of CFD generated results. The computational work here focuses on flow physics that relate to the VHTR lower plenum and range from fundamental to applied. In each case, the aim is to provide insight into modeling requirements for capturing the turbulent quantities of interest. First, a full scale Reynolds-averaged Navier Stokes (RANS) model of the lower plenum is conducted with two primary objectives: (i) to document and reasonably understand the non-isothermal conditions of the inlet jets and the flow inside the lower plenum, and (ii) to get judicious first hand estimates of the temperature and flow conditions at locations A, B and C (see Figure 2-8). This is followed by a RANS study of a single turbulent jet.

It is important to realize the ultimate goal is to study the thermal striping phenomenon. The temperature fluctuations that dictate this process can be directly produced by turbulence, in which case they are non-coherent. However, coherent fluctuations may be superimposed under certain conditions [12], in which case, other modeling approaches are needed. LES models can capture, with sufficient accuracy, both the turbulent and coherent fluctuations, and is therefore of great interest in such an application. LES explicitly solves the large, energy containing scales of turbulence that have a strong dependence on the specifics of each flow, while modeling the smaller, dissipative scales that have a more universal character [40, 45]. In contrast, unsteady Reynolds-averaged Navier-Stokes (URANS) models cannot capture the

details of the non-coherent fluctuations (e.g., its spectral content), while direct numerical simulations (DNS) of the lower plenum would be prohibitively expensive. Turbulent jets and flow past cylinders are of great interest and do not require additional experiments since a wealth of trusted data already exists in regard to these types of flows. The RANS studies previously mentioned are followed by results from LES for a turbulent jet and flow past a cylinder. The final assessment is that of our own unit cell data, which is also conducted using LES, and shows promise in capturing the complex flow physics present in such a condition. For all of these computational studies (RANS and LES), the open source, finite volume, computational fluid dynamics package, OpenFOAM®, is used.

3.1 RANS Model of VHTR Lower Plenum

The full-scale CFD model of the lower plenum geometry is presented in Figure 3-1. The model was build using Gambit. The geometry extended 1.4 m x 7.2 m x 2.9 m along the three coordinate directions. Only half of the lower plenum geometry was built across the line of symmetry. The CFD model has a total of 138 inlets through which Helium entered the lower plenum (4 half inlets along line of symmetry). The domain has 97 supporting posts (8 along line of symmetry). All the support posts and the inlets were separately identified to aid in the analysis and extraction of data. The details about the geometry were obtained from comprehensive small-scale geometry specifications given in McCreery and Condie [26]. The small scale geometry was 1:6.55 of the full-scale model and has been widely used to study the flow characteristics in the VHTR lower plenum under isothermal conditions. A snapshot of the mesh used for the simulations is shown in Figure 3-2. The mesh is generated in Gambit and is converted to OpenFOAM readable format using the "fluentMeshToFoam" conversion utility in OpenFOAM. Note that the converter did not use Fluent during the mesh conversion process even though it is named so. The geometry had a total of 7.91 million tetrahedral cells. The cell size near the walls was 1.5 cm. The maximum mesh size inside the domain was 5 cm. The idea was to get a reasonable first-hand estimate of the flow conditions inside the lower plenum.

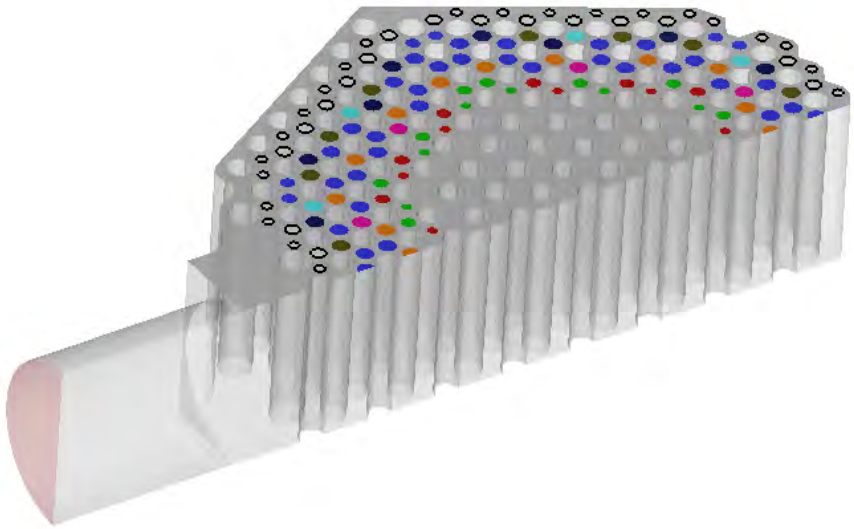

Figure 3-1. CFD Model of the lower plenum geometry

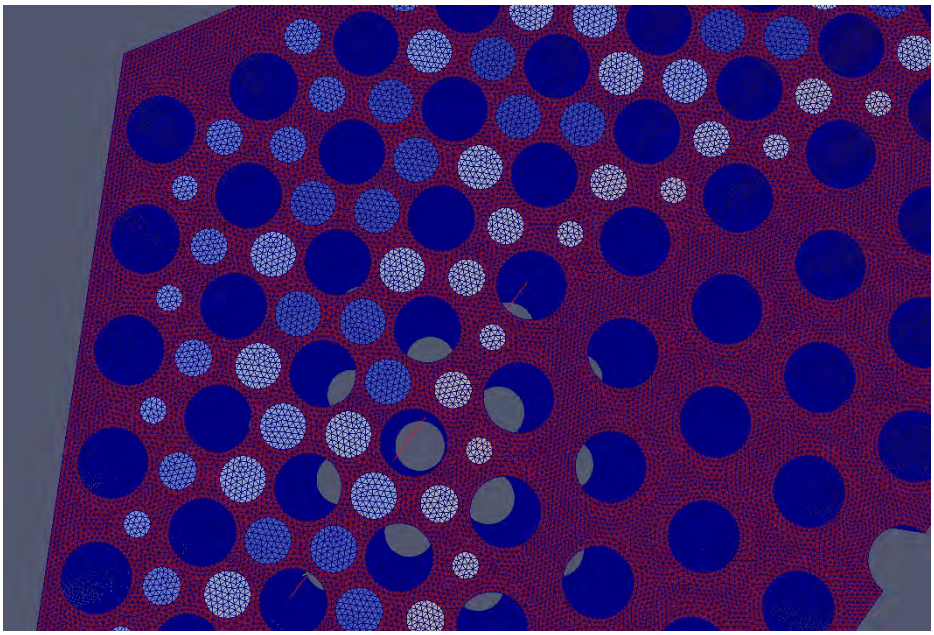

Figure 3-2. Snapshot of the mesh at the top surface using ParaView

The inlet flow conditions were obtained from a combined literature and data presented in McCreery and Condie [26] and Anderson et al. [2]. McCreery and Condie [26] presents details about nine region flow map of the flow coming into the lower plenum and corresponding RELAP5/ATHENA system code model

components as used by Bayless [4] to model the different heat transfer regions of the lower plenum. The 138 inlets were subdivided into nine heat transfer regions which correspond to the nine core regions of the VHTR. The distribution of the number of inlets based on pipe diameters in shown the Table 3-1. The 134 inlets plus the 4 half channels along the line of symmetry of the full-scale lower plenum geometry is divided into 3 different inlet pipe diameters of 3.3", 4.6" and 5.7" respectively. The inlets are identified with a color code to portray their physical location in the lower plenum geometry shown in Figure 3-1. Each color code corresponds to a heat transfer zone as used by Bayless [4]. Note that the nine heat transfer zones have different quantities and combinations of inlet pipe diameters

Table 3-1. Distribution of inlet pipe diameters

	D = 3.3"	D = 4.6"	D = 5.7"	Total
	6	6	0	12
	6	8	0	14
	0	0	10 + 1/2 x 2	11
	0	6	30 + 1/2 x 2	37
	0	0	8	8
	0	0	4	4
	0	0	4	4
	0	0	8	8
	22	16	0	38

Table 3-2. The flow condition at the inlets

	Temperature (K)	Mass flow (kg/s)	Density (kg/m^3)	Velocity (m/s)
	1304.7	5.201	2.551	20.52
	1371.4	9.747	2.428	33.12
	1338.6	9.961	2.487	22.13
	1198.1	19.307	2.776	12.08
	1097.8	59.267	3.028	148.70
	1049.6	7.715	3.166	37.03
	1100.7	14.442	3.020	72.66
	1112.8	14.283	2.987	36.32
	1113.2	19.560	2.986	21.92

The flow conditions at the inlets were obtained from Anderson et al. [2] and are presented in Table 3-2. Note it was assumed that the nine region model used by Anderson et al. [2] is the same as those used by Bayless [4]. The simulations assumed the flow conditions to be uniform at the inlet. It was also assumed that the information of conditions at the inlet/heat transfer zones was also presented in the same order. The inlet temperatures varied from 1049 K to 1371 K, i.e. a temperature spread of more than 300 K. This resulted in a density variation about 0.7 kg/m3 (from 2.4 kg/m3 to 3.2 kg/m3) for the Helium flowing in the lower plenum. The pressure inside the domain was assumed to be 69.53 bar based on the average pressure conditions of the RELAP5/ATHENA system code simulations. Density was obtained from NIST's thermo-physical data [46]. The inlet flow velocities ranged from 12 m/s to 149 m/s. The flow velocities in heat transfer zone were calculated from the information on mass flow rates in each heat transfer region and the calculated density and flow area of each region. The flow area of each heat transfer region was calculated from the information on number of channels in each zone and the inlet pipe diameters (Table 3-1). This resulted in a Reynolds number variation from 75,000 – 1,300,000 for the incoming flow as shown in Table 3-3. (note N.A. means the region does not have the mentioned tube diameter). The viscosity of helium at the inlet condition was also obtained from NIST's thermo-physical data.

Table 3-3. Reynolds number of flow at the inlets

	Re (D = 3.3")	Re (D = 4.6")	Re (D = 5.7")
	79555	110816	N.A.
	118017	164393	N.A.
	N.A.	N.A.	140422
	N.A.	75371	92484
	N.A.	N.A.	1319887
	N.A.	N.A.	354601
	N.A.	N.A.	642065
	N.A.	N.A.	315078
	111200	154897	N.A.

The Realizable k-ε model was used to simulate the turbulent flow inside the domain [47]. The solver algorithm "BuoyantBoussinesqSimpleFoam" was used for the simulations. Steady RANS simulations were done to get a first-hand understanding of the non-isothermal flow phenomenon inside the lower plenum. Note that a uniform velocity, k and ε condition were used at the inlet. The k and ε conditions at the inlet were obtained from standard fully-developed pipe flow correlations for turbulent flow [48]. Zero gradient conditions for k and ε was set at the walls as no available walls functions would be applicable for such a wide range of flow conditions as seen in the lower plenum. The walls of the lower plenum were considered adiabatic [4, 26]. This was based on the calculations by Bayless [4] which showed that the heat transfer effects of hot or cold surfaces in the lower plenum need not be modeled as internal components have less mass than the walls. The bypass flow in between lower plenum sections was not modeled. The pressure gradient at the outlet was calculated according to Hagen–Poiseuille flow correlations. This ensured no recirculating flow into the domain from outside. A reference pressure of 69.53 bar was set near one of the lowest (12.08 m/s) velocity inlet. The initial k and ε conditions inside the domain were set to the lowest value of the inlet flow conditions. The thermo-physical properties for viscosity and thermal conductivity used for the simulations were:

$$\mu = -3.563 \times 10^{-12} \cdot T^2 + 3.958 \times 10^{-8} \cdot T + 1.022 \times 10^{-5} \text{ [kg/m-s]} \tag{3-1}$$

$$k = -2.940 \times 10^{-8} \cdot T^2 + 3.093 \times 10^{-4} \cdot T + 8.414 \times 10^{-2} \text{ [W/m-K]} \tag{3-2}$$

where the temperature is given in units of Kelvin. The specific heat was taken as a constant (C_p = 5190 J/kg.K) and the density was calculated based on the ideal gas law.

The correlations were obtained by curve fitting NIST's thermo-physical data in the range of operating temperatures. The error in the calculated properties using the correlations was within 0.1%. The "hRhoThermo" module with "polynomialTransport" was used in OpenFOAM. An aggressive under-relaxation factor of 0.3, 0.7, 0.7 and 0.7 was used for P, V, k and ε in the simulations.

The case was computed using 36 CPUs and was simulated for 5 days of simulation time. Simulation was done in two steps for faster convergence. Flow inside a coarse grid domain was simulated first for a day which had approximately 0.5 million meshes. The mesh sizes were not refined near the boundaries for this case. The flow results of the coarse grid simulation were used as initial condition for the fine mesh geometry of 7.91 million cells. The converged residuals for solving V_x, V_y, V_z, T, P, k and ε were less than 10^{-9}, 10^{-8}, 10^{-9}, 10^{-8}, 10^{-7}, 10^{-7} and 10^{-7} respectively.

Figure 3-3 shows the temperature contours at the outer surface of the lower plenum and in the supporting posts at Locations A, B and C. The internal core is much hotter than the temperatures on the surrounding outer walls. At each location the supporting posts towards the internal core is more heated than the outward facing posts. The central supporting post at locations A and C had similar mean temperatures of 1204 K (Max: 1258K; Min. 1169K) and 1202 K (Max: 1253K; Min: 1171 K) respectively. The central post at Location B had a mean temperature of 1194 K (Max: 1206 K, Min: 1185 K). The temperature variation in location B is much lesser than in Location A and C.

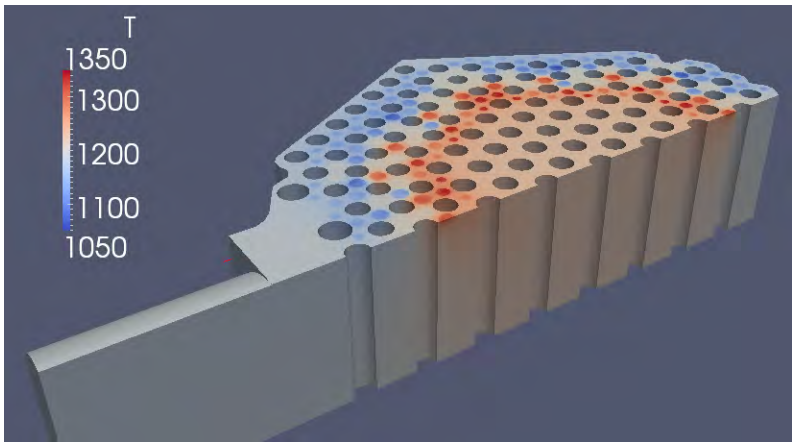

(a)

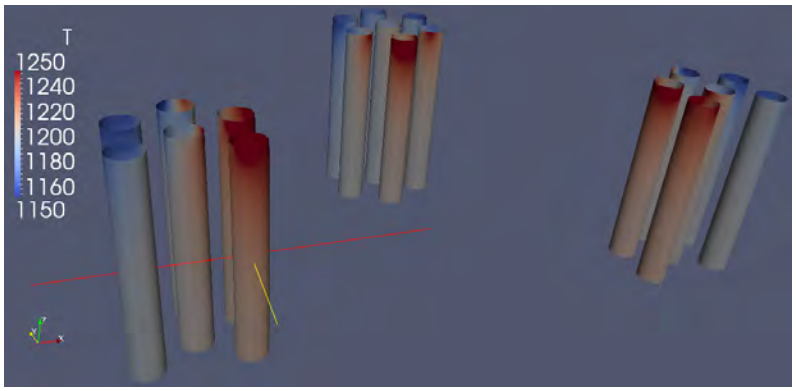

(b)

Figure 3-3. (a) The simulated temperature at the surface of the lower plenum; and (b) at locations A, B and C (from left to right)

Figure 3-4 shows a much more detailed picture of the Helium temperatures at locations A, B and C where measurements and experimental work is targeting. As expected, the fluid temperatures are higher at Locations A and C compared to B. Helium temperatures at a height of 0.7 m above the floor of the lower plenum is also shown. Location A and C seem to have similar temperature conditions even though A is located close to the outlet of the lower plenum.

The difference between locations A and C becomes evident when flow of Helium at the locations are compared as provided in Figure 3-5. As expected the flow velocities at location A is much higher due to its location being close to the outlet of the lower plenum. The flow velocities at locations B and C are generally lower than 20m/s while at location A they are about 40 m/s or higher. Plans are being made to simulate the high crossflow in the lower plenum as well in the experimental facilty as seen at location A.

The CFD model of the lower plenum developed for this study can be effectively used to model the flow and temperature conditions in the experimental and computational prototypes planned hereafter.

H = 0.7 m above the lower plenum floor

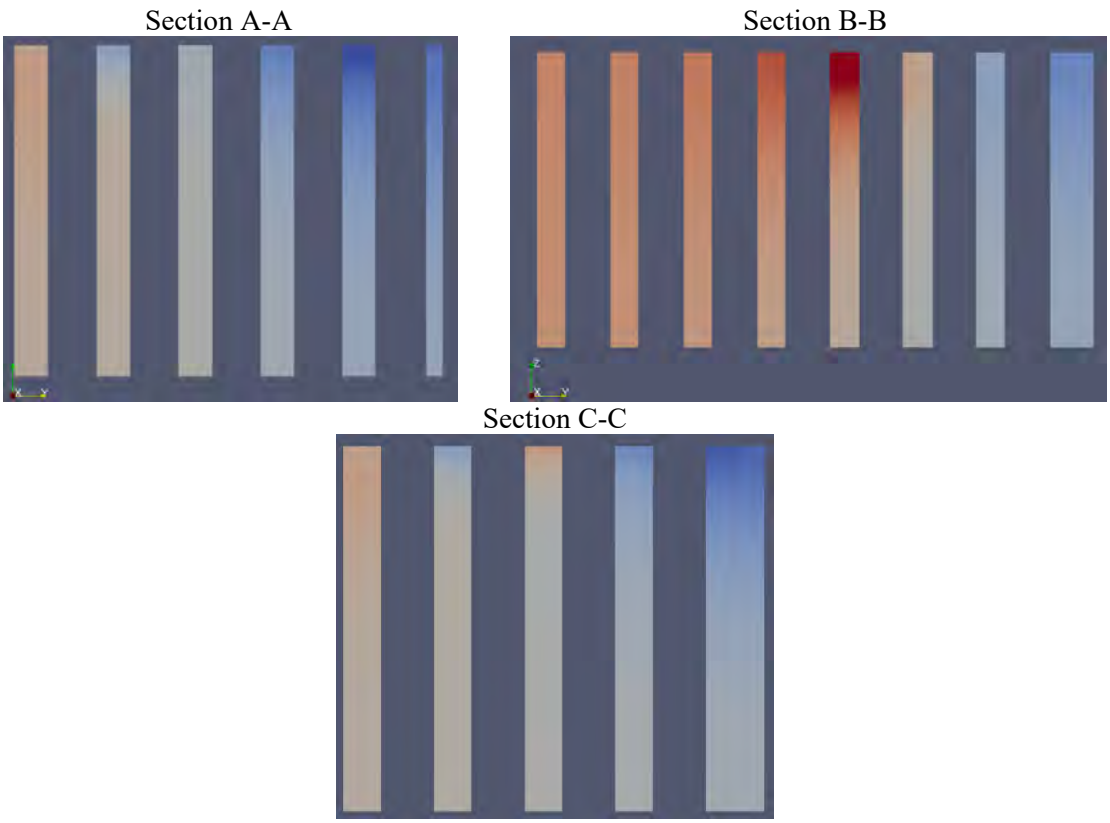

Figure 3-4. Simulated helium temperatures at the different cross-sections where measurements are of interest in the non-isothermal prototype model

H = 0.7 m above the lower plenum floor

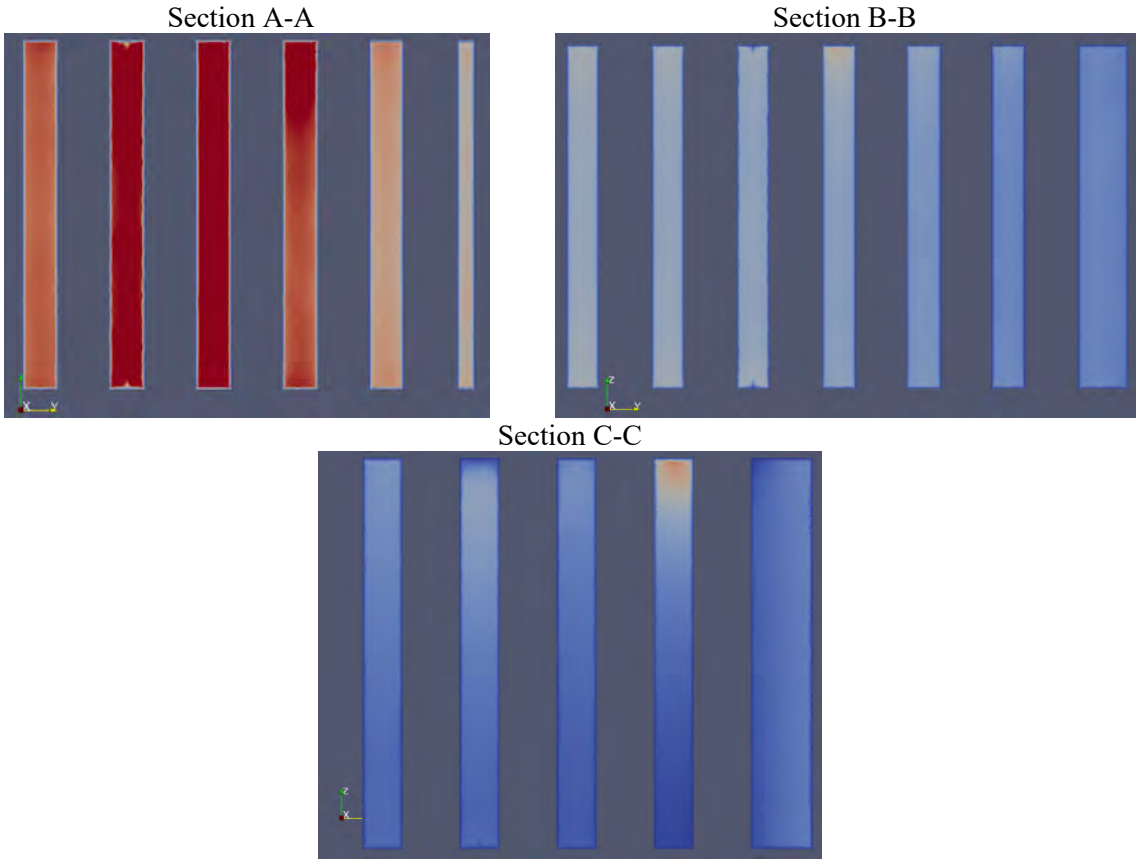

Figure 3-5. Simulated veloctity magnitudes at the different cross-sections where measurements are of interest in the non-isothermal prototype model

A full-scale CFD model of the lower plenum of a VHTR has been built and simulated to study the non-isothermal conditions inside the lower plenum. The CFD model was built with the intension of providing reasonably accurate estimates of flow conditions inside the lower plenum to aid in the design of experimental and computational models prototypes of different sections inside the lower plenum planned

henceforward. The temperature conditions in the support posts at the planned mesurement locations are presented. The temperature and flow characteristics at the planned prototype builtup locations are significantly different from each other. The data from the CFD model can later be used for proper planning of the experimental and computational work in the future, with goals of modeling and understanding the thermal striping phenomenon in the small sectional models more accurately.

3.2 RANS Simulations of Isothermal Turbulent Round Jets

Turbulent round jets are of obvious importance to lower plenum flow modeling and represent the first step in ultimately establishing a trusted model of the unit cell. Both isothermal and non-isothermal jets are analyzed in this project. Since the fluctuating components of velocity are of importance, ultimately, a large-eddy simulation (LES) is conducted (see next section). In order to initialize those studies, a Reynolds Averaged Navier Stokes model for an isothermal, high Reynolds number confined jet is presented. The enclosure around the confined jet is set large enough such that the results can be compared with previous well-known experimental studies. Detailed comparisons are made with experimental data for the velocities and higher order moments and excellent agreement is found in all cases.

The most widely used experimental studies for CFD validation of isothermal round jets are the works of Panchapakesan & Lumley (P&L) [49], Wygnanski & Fiedler (W&F) [50], and Hussein et al. (HCG) [51]. P&L reported measurements for a jet with $Re = 1.1 \times 10^4$. In contrast, the Reynolds number of incoming jets in the VHTR lower plenum are expected to exceed 8×10^4 [12]. It has been observed that flow characteristics can be vastly different between a $Re = 1.1 \times 10^4$ [49] jet and a $Re = 9.55 \times 10^4$ [51] jet, as demonstrated by Hussein et al. [52, 53]. The jet Re for the experiments of W&F ($Re = 10 \times 10^4$) and HCG ($Re = 9.55 \times 10^4$) were quite similar; however, W&F used stationary hot wires (SHW) for their measurements which give erroneous results for high turbulent intensity flow, especially at locations far from the centerline of the jet. Hence, the experimental laser Doppler anemometer (LDA) and flying hot wire (FHW) measurements of HCG are used for the current validation study.

3.2.1 Computational Model

The computational domain simulated for the study is shown in Figure 3-6. It is assumed that the round jet from a nozzle of diameter D = 1 inch ejects out into a cylindrical domain of diameter $D_{enclosure}$. The selection of the geometry inherently assumes an axisymmetric flow inside the computational domain. Note that the experimental data of Hussein et al [51] and Wygnanski and Fiedler [50] both showed axisymmetric flow characteristics. Hence an axisymmetric simulation is set up in OpenFOAM using a 2° wedge section of the cylindrical enclosure to reduce computational efforts without compromising on accuracy. Periodic boundary condition was applied to the two lateral sides of the wedge, and appropriate symmetry conditions were applied to the wedge axis, following standard procedure for axisymmetric simulations in OpenFOAM. The domain length specifications are the same as that of Hussein et al [51].

A script was developed in Matlab to generate a non-uniform structured mesh for the simulation domain. The radius of the jet was divided into 10 equal sized mesh elements, i.e. the mesh size at the inlet was $D/20$. The mesh size was kept the same as that at the inlet up to X=30D and up to Y=7.5D. The mesh expanded after X=30D along the X direction, and after Y=7.5D in the Y direction. Finally, near the enclosure wall, a boundary layer mesh is applied. An expanding mesh was also made towards the back wall from the inlet. The total number of finite volume cells was 0.35 million for the meshed simulation domain.

Figure 3-6. Schematic of the RANS simulation domain mimicking HCG experiments [51]

Table 3-4. The boundary conditions for the simulation domain. P refers to the pressure in Pa scaled by density in kg/m^3

Location	V (m/s)	P (m^2/s^2)	k (m^2/s^2)	ε (m^2/s^3)
Wall	$V = 0$	$\frac{\partial P}{\partial n} = 0$	$\frac{\partial k}{\partial n} = 0$	$\frac{\partial \varepsilon}{\partial n} = 0$
Inlet	$V_X = 56.2$ $V_Y = V_z = 0$	$\frac{\partial P}{\partial n} = 0$	0.159375	5.88
Outlet	$\frac{\partial V}{\partial n} = 0$	$\frac{\partial P}{\partial n} = P_{gradient}$	$\frac{\partial k}{\partial n} = 0$	$\frac{\partial \varepsilon}{\partial n} = 0$

Our simulation of the turbulent round jet is based on the Reynolds Averaged Navier Stokes (RANS) equations with the Boussinesq approximation for the Reynolds stresses. The turbulent eddy viscosity in our simulations is computed using the realizable k-ε turbulence model [47]. The realizable k-ε model resolves the round-jet anomaly, i.e., it predicts the spreading rates of axisymmetric jets as well as that of planer jets reasonable well. The OpenFOAM solver *simpleFoam*, which is an implementation of the standard finite volume-based Semi-Implicit Pressure Linked Equation (SIMPLE) algorithm, was used for the simulations.

The boundary conditions used for the simulations are presented in Table 3-4. Note that a uniform velocity, k and ε condition is used at the inlet. The averaged flow condition is the same as that of the HCG measurements. The constant value of k at the inlet is calculated using the relationk $= {}^{3}/_{2}\,(\mathrm{I}_t \mathrm{U}_{inlet})^2$, based on the measured jet inlet velocity $\mathrm{U}_{inlet} = 56.2 m/s$ and turbulent intensity at inlet of I_t=0.58% at the inlet reported by Hussein et al. The constant value of ε at the inlet is then obtained from standard fully-developed pipe flow correlations for turbulent flow [48]. Since in all cases, the enclosure walls are very far from the turbulent jet, the boundary layer along the walls are expected to be laminar, and hence there is no need to apply wall functions. Instead, zero gradient conditions for k and ε are set at the walls, together with standard no-slip condition for the mean velocity. A reference pressure of zero was set at a selected cell center near the inlet. It was observed that for incompressible flow condition, such a setting gave faster convergence compared to a specified reference pressure of zero at the outlet. A constant pressure gradient corresponding to the fully developed Hagen-Poiseuille flow was specified at the outlet. Finally, it was found that its best to initialize the k and ε conditions inside the domain with the inlet k and ε values. A high gradient of k and

ε near the inlet is avoided in such a case for the initial iterations thus allowing the use of high under-relaxation factors for the simulations. The relaxation factors for *P*, *V*, k and ε was set to 0.1, 0.3, 0.3 and 0.25 respectively during the initial part of the simulation. It was progressively increased to 0.3, 0.7, 0.7 and 0.7 as the solution approached convergence. Under steady state conditions, the simulated results at the centerline, X=70*D* (i.e. the location at which HCG presented the results) and at the outlet did not change over 20000 iterations. The converged residuals for solving V_x, V_y, V_z, *P*, k and ε were less than 10^{-11}, 10^{-10}, 10^{-7}, 10^{-6}, 10^{-10} &10^{-9} respectively. The sampling utility in OpenFOAM was used to extract and analyze the results.

3.2.2 Results and Discussion

Figure 3-7 shows the centerline velocity profiles for different enclosure sizes along with measured stationary hot-wire (SHW) data of Hussein et al. [51]. The location X=4*D* is also shown in the plot which corresponds to the position of the virtual origin predicted from Hussein et al's SHW measurements. Hussein et al measured data in between 50 to 122 jet diameters in their experiment. On the other hand, Wygnanski & Fiedler presented results in between 20 to 100 jet diameters. Hence for comparison purposes, results here are shown up to X/D_{jet} of 120. Also shown for reference in Figure 3-7 are two additional curves where the enclosures are smaller than that reported by HCG. For the location of 70 diameters downstream, there is almost no difference between an enclosure exactly mimicking the HCG facility (192 *D*) and one half as big (96 *D*), which corresponds to Wygnanski & Fiedler's enclosure size. By comparison, another decrease in the enclosure size (48 *D*) begins to show deviation from the other results, revealing pronounced differences around X = 60*D*. The results are contrary to what was concluded by Kandakure et al. [54] for a confined free jet. Note that the velocities of the jet remain close (within 1%) to that of the inlet flow conditions until X≈8 *D* for all the enclosure sizes. This corresponds to the potential core region.

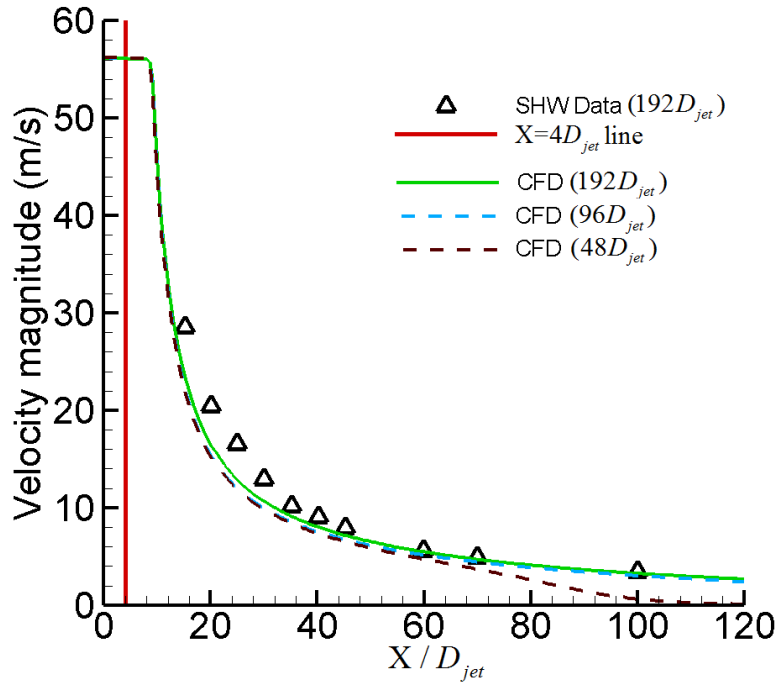

Figure 3-7. Centerline velocity for RANS models of turbulent jet

Figure 3-8 shows the flow at a downstream location of X=70*D* for different enclosure sizes. HCG presented their experimental results at this same location. The centerline velocities reduce as enclosure size decreases. The centerline velocities at X=70D_{jet} for enclosure sizes of 48D_{jet}, 96D_{jet} & 192D_{jet} are 3.66 m/s, 4.40 m/s & 4.68 m/s respectively. Backflow is observed for enclosure size of 48D_{jet} above 12 jet diameters. The centerline velocity predicted by CFD matches fairly well with measured data (4.82 m/s) for HCG case. The flow magnitudes in between 6-15D_{jet} are nearly identical for HCG and Wygnanski & Fiedler's enclosures. With confidence in the RANS modeling capabilities to capture the first order statistics for HCG, we now look to Large Eddy Simulations (LES) to analyze the higher order statistics in more detail and determine the modeling approach needed to capture the metrics important for turbulent mixing.

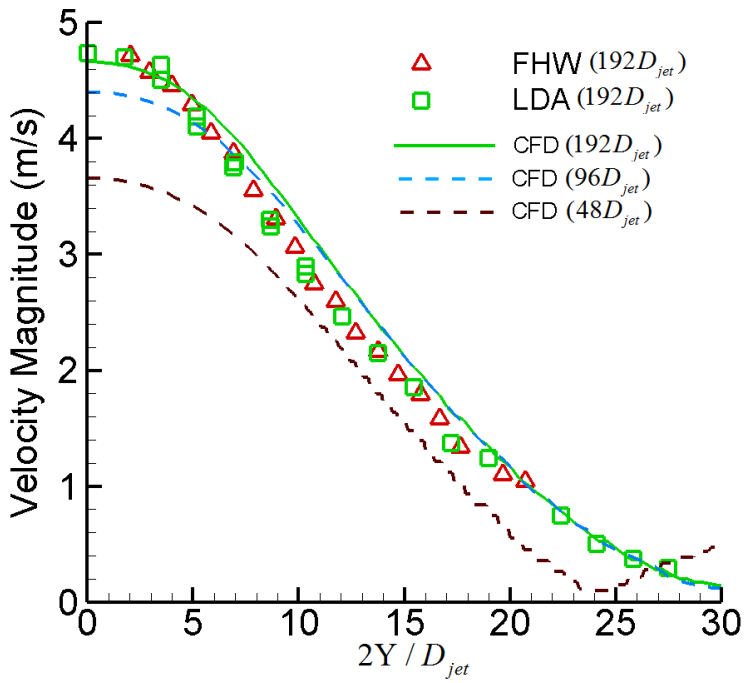

Figure 3-8. Velocity profiles at X=70*D* for different enclosure sizes

3.3 Large Eddy Simulations of Isothermal Turbulent Round Jets

A comprehensive LES study of the HCG experiments is noticeably absent from the literature. Studies like Kim & Choi [52], which investigated the effects of the jet inflow conditions on the downstream evolution of a circular jet for Reynolds numbers of 3600, 10^4, and 10^5, only used axial domain length of 18 D (D being the diameter of the jet) for the Re = 10^5 jet (i.e., only the near field). HCG did the bulk of their flow measurements in the self-similar far-field region, at a downstream axial location of 70D, and therefore these authors could not make direct comparisons. Bogey & Bailly (B&B) [53] reported that the distance required to achieve self-similarity of flow in their LES simulations was around 60D for a Re = 1.1×10^4 jet (similar to P&L's experimental measurement). Moreover, even though B&B performed LES simulations for an axial domain length of 75D, they found that flow characteristics were vastly different from HCG. In addition, their Reynolds number (Re = 1.1×10^4) was an order of magnitude less than that of HCG. The potential core length simulated was also much longer than what was observed in the experiments of P&L. In other words, although they matched the far field (i.e., self-similar region), their near field computational

results were significantly different than the experimental data they meant to mimic. For many applications (VHTRs included), the domain of interest can be entirely comprised of the near field region due to geometric constraints. Comprehensive and systematic LES modeling is needed to help resolve these discrepancies for isothermal jet flow. The work presented here uses an appropriate domain size for effective validation with experimental measurements and addresses the issue of potential core length for a high Reynolds number turbulent jet akin to HCG. It also addresses the inconsistencies in the literature regarding the turbulent statistics.

3.3.1 Computational Model

The simulated isothermal round jet computed by LES is compared to that of the jet studied experimentally by HCG with the jet Reynolds number $\mathrm{Re} = \frac{U_{inlet}D}{\nu} = 95{,}000$, where U_{inlet} is the jet exit velocity, D is the jet diameter, and ν is the kinematic viscosity of air. In their experiments, HCG used a jet with D = 1 in, and the experimental jet facility was surrounded by a large enclosure. As shown in Figure 3-9(a), the nozzle of the jet was placed within the enclosure such that the distance of the back wall to the nozzle was 34 ft (408D) and the distance from the nozzle to the downstream exit of the facility was 48 ft (576D). The width of the domain was 16 ft (192D). The jet was centered in the cross-section of the enclosure.

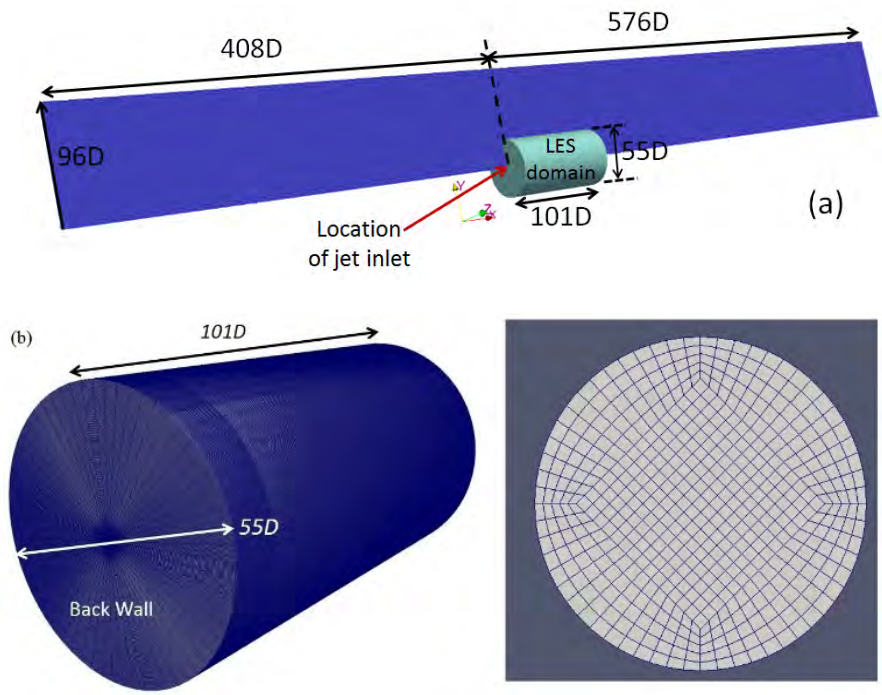

Figure 3-9. Comparison of the size of the LES simulation domain (R = 55D/2) and HCG experimental domain (R = 96D). The wedge geometry shown for the experimental domain is the axisymmetric domain (b) Views of the mesh near the inlet and at the side walls for the LES model

Simulating such a large domain is computationally prohibitive with LES. Therefore, a subset computational domain was simulated in the current study. The LES domain used for this study is shown in relation to the experimental HCG domain in Figure 3-9(a) and (b). The computational domain has dimensions of $101D$ in the axial direction ($100D$ from jet inlet to the downstream outlet and $1D$ from back wall to jet inlet) and $55D$ in the radial direction. It should be noted that the downstream location of $x = 70D$ (location where detailed experimental results are reported in HCG) is within the LES computational domain. The radial dimension of the LES domain was selected based on an axisymmetric RANS simulation of the full scale HCG facility, where near zero axial velocities were seen at 45 jet radii from the center for a downstream location of $100D$. Hence, a domain width of $55D$ was deemed large enough such that the influence of radial side walls is minimal. RANS simulations were performed for the smaller domain to ensure this assumption. The incompressible flow simulation employs wall conditions for the back and side surfaces and an outflow condition at $x = 100D$.

The mesh used for the simulation is shown in Figure 3-9(b). The domain has a total of 16 million cells. As shown in Figure 3-10, different mesh grading is applied in both the axial and radial directions. For the axial direction, a stepwise increasing cell size is used from the inlet to the location $x = 15D$ downstream to ensure that the inner core of the jet is well-resolved at entry. In this region, the mesh size transitions from $D/120$ to $D/8$ in axial length. For the remainder of the downstream domain ($15D < x < 90D$), the axial mesh size is $D/8$. The last $10D$ of the domain in the axial direction is used to form a sponge layer with a mesh size that linearly increases from $D/8$ to $D/2$. To minimize reflection from the outlet boundary of the computational domain, a non-reflecting boundary technique known as a numerical sponge layer is used. This technique is actually a combination of numerical beach and grid expansion to absorb reflective waves coming from the outlet of the computational domain [55] and is vastly used in LES studies like B&B and many other recent studies [56, 57]. In the radial direction, a 15 × 15 Cartesian mesh is used at the jet inlet as shown in Figure 3-9(b). Each square cell in this Cartesian grid is $D/25\sqrt{2}$ (~$0.028D$) in size on each side. The very center cell of this grid is collocated with the overall domain centerline, thereby eliminating the need to interpolate for any centerline data for which experimental results are widely available. As can be seen in Figure 3-9(b) and Figure 3-10, five radial layers of cells are placed between the center of the Cartesian grid and the edge of the circular inlet ($r = D/2$). Outside of this circular inlet, a uniform mesh size is used between $r = D/2$ and $r = D$. The mesh size in this region is similar to the average mesh size contained within the jet diameter. An expanding grid is then used from $r = D$ to $r = 5D$. A uniform grid size of $D/8$ is then applied from $r = 5D$ to the outside edge of the computational domain ($r = 27.5D$). The number of azimuthal divisions is dictated by the 15 × 15 Cartesian array (4 × 15 = 60 divisions). Recent investigations by Kim [52] showed that 60 equal azimuthal divisions is appropriate for LES to capture the flow for a turbulent jet.

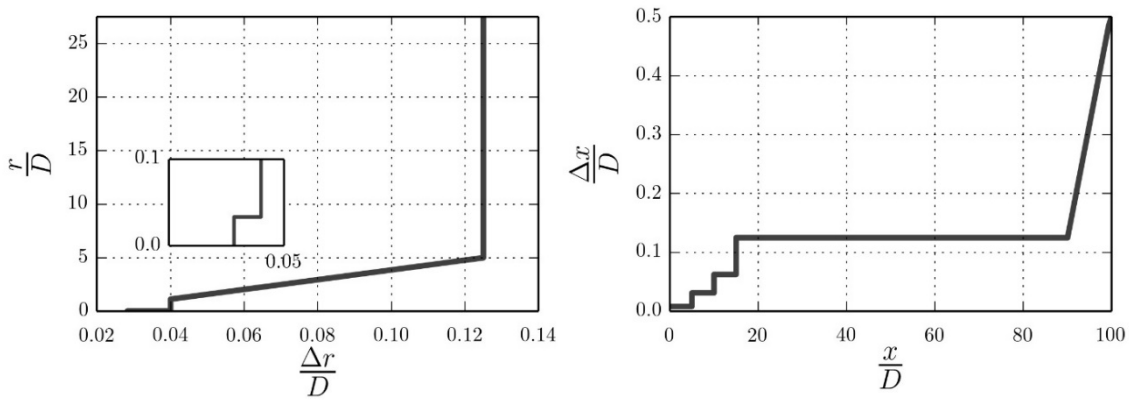

Figure 3-10. Mesh spacing in radial and axial direction. The grid is symmetric with respect to the jet axis

The open source, finite-volume, computational fluid dynamics package OpenFOAM® is used for the present study. The selection of the LES sub-grid scale (SGS) model is done by a systematic CFD study; six different models were compared:

1. Smagorinsky model [58]
2. Homogeneous dynamic Smagorinsky model [59]
3. Dynamic local averaged Smagorinsky model [60, 61]
4. k-equation eddy-viscosity model [62]
5. Dynamic k-equation eddy-viscosity model [62]
6. Localized dynamic k-equation eddy-viscosity model

Initial simulations were performed using each of the models. Each LES run was initialized with the previously conducted RANS simulation. The incoming flow was assumed to have no fluctuations. A comparison of the simulation results is provided in Figure 3-11(a), where the inverse of the centerline velocity (U_C) is shown as a function of the downstream distance (x/D). This is often referred to as the decay rate of centerline velocity and for the results shown, they represent the time-averaged solution from 0 to 6.65×10^2 residence times, where the residence time for the jets is D/U_{inlet}. For reference, the stationary hotwire measurements (SHW) from HCG are included along with the RANS results. From this comparison, it is apparent that the simulation which shows the most promise for fast convergence to the measured data

is the Dynamic local averaged Smagorinsky model. This SGS model also predicts a smaller potential core length compared to the other models. For these reasons, this model is used within the LES framework for the HCG jet. The model is an implementation of the dynamic Smagorinsky model with coefficients C_D and C_I computed as local averages of their face values corresponding to values by Fureby et al. [61]. Note that without the effect of inlet fluctuations, the potential core of the jet is incorrectly predicted and does not compare well with the RANS simulations. However, this first phase of numerical explorations provides valuable insight into the different SGS models and their impact on the results.

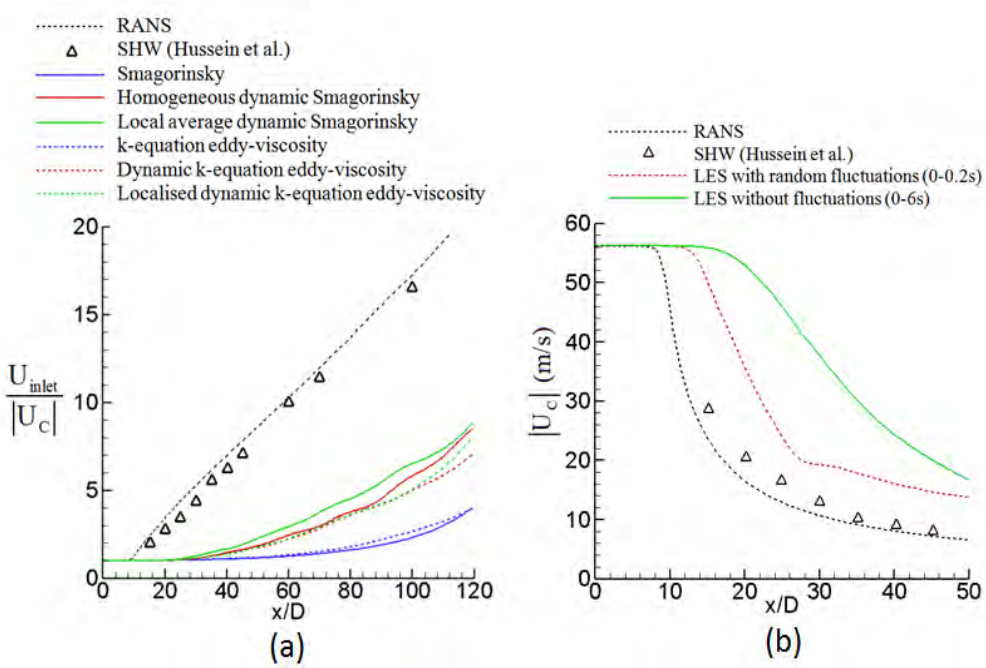

Figure 3-11. (a) Comparison of mean centerline time averaged velocities for different LES models ($|U_C|$ - centerline velocity magnitude; U_{inlet} – average velocity at inlet); (b) The effect of inlet fluctuations on the simulated potential core length

After adopting the SGS model as described above, the effect of including random fluctuations at the jet nozzle is investigated, with results shown in Figure 3-11(b), where the centerline velocity is plotted against the downstream distance from the nozzle. From the two LES curves shown, it is easily seen that fluctuating inlet conditions have a large impact on the length of the potential core. For the case with no random fluctuations, even a longer simulation time (0 - 1.33 × 10^4 residence times) does not decrease the

potential core length nearly as much as when those fluctuations are included, even for a short simulation time (0 - 4.5×10^2 residence times). The fluctuation at the inlet in the simulation is generated using a random fluctuation generator (*turbulentInlet* boundary condition) option in OpenFOAM. The turbulent intensity at the nozzle in the simulation is adjusted to match the reported intensity measurements of 0.58% from the HCG experiments. In the simulation, the potential core length stabilizes within the first 2.5×10^2 residence times. However, even though the turbulent intensity matches at the inlet, it still over-predicts the length of the potential core. Recent LES studies have also predicted a longer potential core length compared to that seen in similar experiments [53, 63]. Other studies suggest that the potential core length simulated using LES can vary significantly from measured data and is very sensitive to the inlet flow conditions [52].

Multiple factors can govern flow conditions at the jet nozzle [64], and several complicated methods for generating synthetic turbulence exist to address this. However, it is difficult to generate a synthetic turbulence profile which would exactly give the correct spectrum associated with the turbulence as seen by HCG in their experiments. Therefore, the most straightforward and accurate approach, albeit computationally expensive, is to perform a precursor simulation of the flow in the upstream nozzle assembly, completely independent from the LES model of the large enclosure. From this precursor simulation, the fluctuations at the jet nozzle itself can be sampled and transferred to the inlet boundary of the jet simulation.

In their experiments, HCG used two different contractions beginning with a 12 in duct opening to eventually reach the exit jet diameter of 1 in which was then directed into the large enclosure previously described. The first upstream contraction was a cubic design and the second was a fifth-order polynomial design. A faithful model for this double contraction is created and shown in Figure 3-12. Tetrahedral cells were used to mesh the contraction geometry; the model had a total of 0.445 million cells. A very low value of turbulent fluctuation is prescribed at the inlet of the contraction model as would be expected close to the screen mesh of a wind tunnel [64]. Instead of modeling the large enclosure downstream of the nozzle, the flow is directed into a pipe with a diameter twice the size of the jet diameter. This is done in order to reduce computational effort without losing any accuracy in the simulated flow inside the contraction nozzle. The

flow inside the contraction domain is first initialized with steady-state RANS data. A Spalart-Allmaras detached-eddy simulation (DES) model was then used to obtain accurate flow conditions at the jet nozzle. The detached-eddy model uses RANS equations at regions near solid boundaries, thus reducing the computational cell requirement. LES is used for the rest of the domain [65]. Adjustable time stepping is used for the contraction simulation with a maximum courant number set at 0.5. As illustrated in Figure 3-12, transient velocity data is probed and saved at 180 locations (5 equally spaced radial locations at 10° angular increments at the nozzle exit plane).

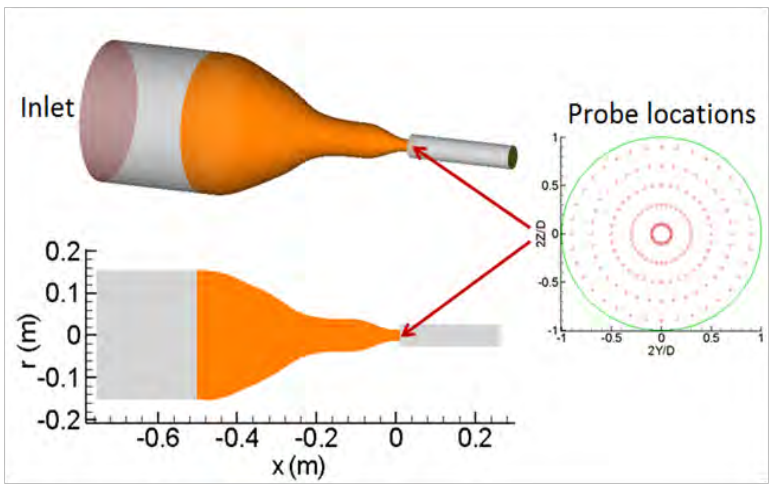

Figure 3-12. Computational model of the double upstream contraction used in the experiments of HCG

The precursor contraction simulation is performed for a period of 0.18 s. The distribution of vorticity magnitude at the nozzle exit at five different time instances is shown in Figure 3-13. Data during the initial 2.5×10^2 residence times of the simulation is not used. The effect of simulation time on turbulent intensity at the nozzle exit is shown in Table 3-5. HCG reported unsteadiness of the fan as the major cause of the turbulent intensity at the nozzle exit. The present simulations show that similar turbulent intensity is observed from the flow at the exit of the contraction nozzle without the effect of unsteadiness of the fan. The difference in turbulent intensity calculated using data saved with 90 probed locations and 180 locations was 0.002%. During the period of 0.1 - 0.18 s, the turbulent intensity is found to be 0.579%, which is nearly

identical to the measured 0.58% value reported by HCG. This 0.08 s (0.1 - 0.18 s) of data from the precursor contraction nozzle simulation in then used as an inlet condition for the isothermal jet simulation for the domain in Figure 3-9 and is periodically cycled for the duration of the jet simulation. For example, if the simulation time of the LES domain (refer to Figure 3-9) is 2 s, this 0.08 s of data is cycled 25 times during that period (2 s / 0.08 s = 25). It is interesting to note that the radial component of turbulent intensity is twice that of the axial component at the nozzle exit.

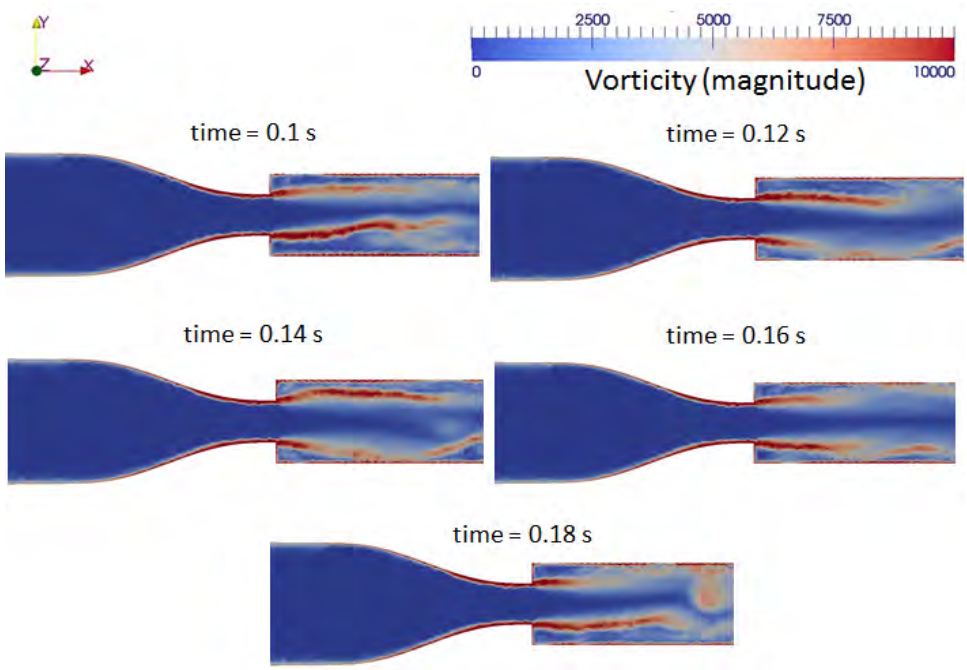

Figure 3-13. Contours of vorticity magnitude near the nozzle exit at different time instances

Table 3-5. Effect of simulation time on turbulent intensity at the nozzle exit

Time interval [s]	*Turbulent Intensity (%)*
0.1 - 0.12	0.670
0.1 - 0.14	0.657
0.1 - 0.16	0.578
0.1 - 0.18	0.579

With accurate inlet conditions from the precursor nozzle simulation, LES studies of a single, isothermal round jet (Re = 95,000) are performed using the dynamic local-averaged Smagorinsky model. Adjustable time-stepping with a maximum courant number of 0.5 is used for each of the simulations. Time-averaging of the flow quantities is initiated at 3.5×10^2 residence times, i.e. after two cycles of data from the precursor contraction nozzle simulation. Nearly 50,000 hours of computational effort were used to obtain 2 s (4.4×10^3 residence times) of time-averaged LES data.

3.3.2 Results and Discussion

1.1.1.1. Mean Velocities and Near-Field Parameters

Figure 3-14 shows the distribution of vorticity magnitude in the jet at various time steps. With a diameter of $18D$ and a length of $50.5D$, these snapshots display a small section of the entire LES domain. The jet development from the potential core region to a fully turbulent state is presented. The largest Kelvin–Helmholtz rollers of the two mixing layers at the jet edge appear very clearly. These mixing layers develop symmetrically and start breaking down into small scales. Vortical flow structures are originally generated in the shear layers, and then merge at the end of the potential core. Later, a rapid breakdown of the large structures with a growth of the small structures occurs, and the development of the jet becomes asymmetric. The radial spreading of the jet becomes visible just downstream of the potential core. From this figure, it is also apparent that the flow becomes highly mixed as the jet develops. This is due to the increase in turbulent length scales and/or the sizes of the vortical flow structures further downstream. Although LES captures the large-scale structures, the small-scale features are absent, as would be expected. Moreover, the assumption of laminar flow at a large radial distance from the centerline looks appropriate since there is no turbulence manifesting in the flows at these locations (very top and bottom edges of images shown in Figure 3-14).

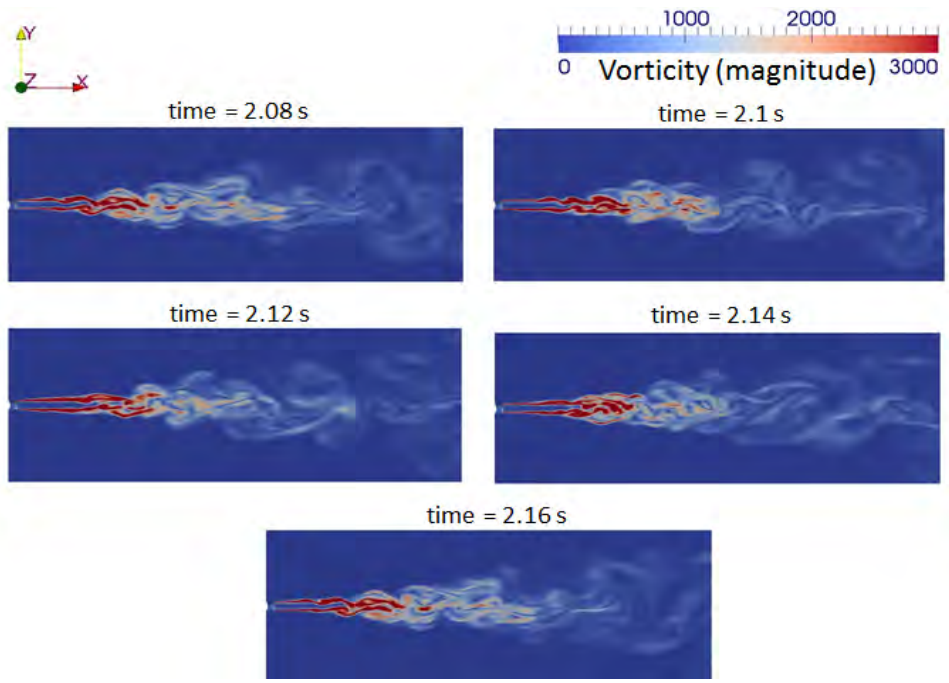

Figure 3-14. Contours of vorticity magnitude at the nozzle exit for the LES domain at different time instances

The effect of time-averaging on velocity magnitude is presented in Figure 3-15. The establishment of a steady-state condition is investigated by considering the evolution of centerline velocities. When only averaging between 3.5×10^2 and 1.46×10^3 residence times, the behavior still reveals some time dependence as shown in Figure 3-15. The time-average of the flow reaches its steady value after 3.5×10^3 residence times, evident from the fact that the centerline velocity magnitude remains constant for the remaining three averaging windows included. Also worth noting is that near the inlet, the velocity magnitude of the jet predicted by LES is different from analogous RANS data. This gap is due to the fact that the inlet condition for LES also includes fluctuating components in both the radial and axial directions, while the RANS simulation is initialized with only the turbulence intensity. In reality, the fluctuations present end up contributing to the time-averaged downstream velocity component, so this is not entirely unexpected. Figure 3-15(b) compares the inverse centerline velocity of the LES simulation with measured data from HCG. Plotting the inverse of the velocity data enables better analysis of the low velocity regions sufficiently far downstream of the jet nozzle. This further reveals that with advancing simulation time, the centerline

velocity predicted by LES matches the experimental data very precisely. The length of the potential core found by determining the downstream location x, where $u_c(x) = 0.95U_{inlet}$, is found to be $4D$. Although detailed near-field experimental data is not available from HCG, the simulated centerline velocity accurately following the measured data downstream suggests correct prediction of the potential core length. Other LES simulations of jets typically over predict the potential core length. For example, B&B reported $6.5D$, while the experimental data from P&L reported a value of $1.75D$. Also, based on linear fitting of the simulated inverse centerline velocity between x = 15 and $75D$ using time-averaged data from 3.5×10^2 - 5.75×10^3 residence times, the virtual origin (x_0) [66] was calculated to be $4D$, as was observed by HCG from their measurements. Thus, properly accommodating the fluctuating velocities yields results more indicative of the actual flow physics in both the near and far-field, and good agreement can be realized.

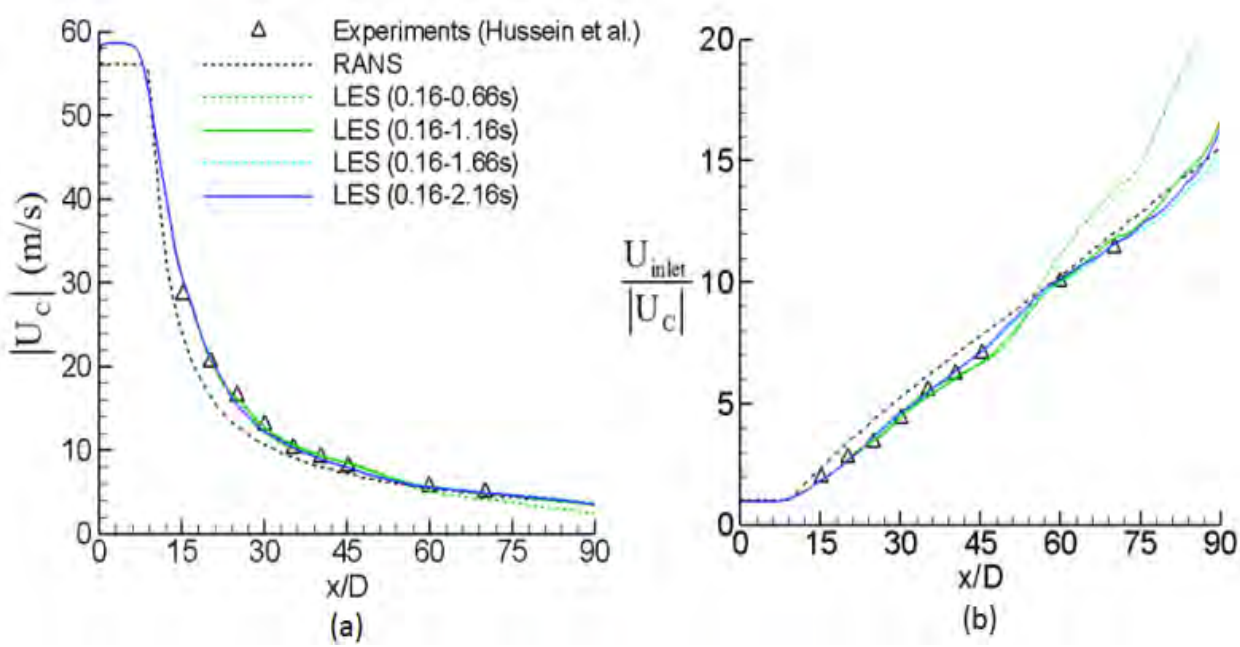

Figure 3-15. Effect of time-averaging on (a) the centerline velocity magnitude ($|U_C|$) and (b) inverse centerline velocity for the LES simulation. Data in the initial 3.5×10^2 residence times is not considered in the time-averaging.

1.1.1.2. Reynolds Stresses

In addition to the time-averaged velocities within the domain, other key physical quantities are compared to the HCG data. The accurate prediction of the potential core enables the ability to sample data at the exact locations reported by HCG, namely $x = 70D$. Figure 3-16(a) shows the time-averaged axial stresses for various time intervals at this downstream location. Just as observed for the centerline data, the simulation results approach a time-independent solution, such that further averaging would have no impact. The need of azimuthal averaging can be visualized by comparing Figure 3-16(a) with Figure 3-16(b). For this reason, data reported for all subsequent plots makes use of azimuthal averaging.

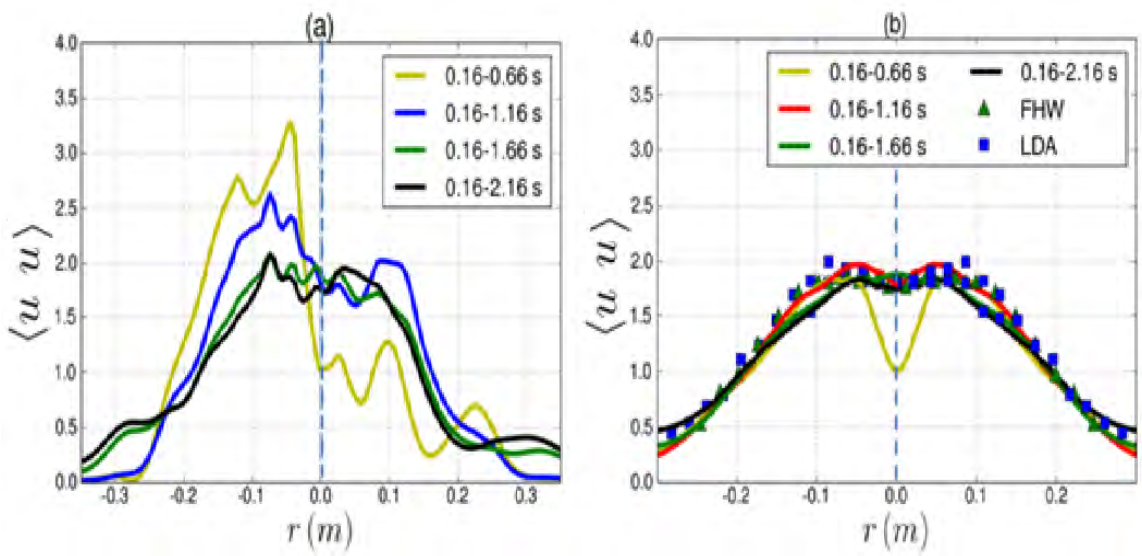

Figure 3-16. Comparison of axial stress profiles at $x = 70D$ for different time average interval (a) without azimuthal averaging and (b) with azimuthal averaging. (FHW: flying hot wire measurements; LDA: laser Doppler anemometer measurements)

As can be seen in Figure 3-17, LES data also compares very well with the higher-order experimental data reported by HCG. The profile of the axial normal stress $\langle uu \rangle$ calculated by LES successfully detects the distinct off-axis peak measured by the LDA/FHW. This peak is consistent with experimental measurements and is due to the strong off-axis peak in the production of turbulence energy by the Reynolds stress working against the mean shear.

The radial and azimuthal components of Reynolds stresses are presented in Figure 3-18 and Figure 3-19, respectively. The radial component near the centerline is very close to the LDA measurements of HCG. In addition, the radial stress $\langle vv \rangle$ and azimuthal stress $\langle ww \rangle$ ($u'_\theta u'_\theta$) closely mimics that from HCG. Figure 3-20 exhibits turbulent shear stress data $\langle uv \rangle$ ($u'_x u'_r$) which is consistent with both FHW and LDA data reported by HCG along the radial direction at $x = 70D$. The location of the off-axis peak (~ 0.1 m) for shear stress is close to the radial distance of the same off-axis peak in Reynolds stress shown in Figure 3-17. The Reynolds stresses also exhibit significant anisotropy, which is revealed both by comparing the shear stress shown in Figure 3-20 and by the difference in the normal stresses (Figure 3-17, Figure 3-18 , and Figure 3-19). On the centerline, the turbulence intensity is about 25% of the mean velocity. Although HCG did not report this number, it can be calculated from their data, and was found to be 24.4%. For this turbulent jet, it is expected to be an axisymmetric flow, a condition that is satisfied when the radial and azimuthal components of turbulent kinetic energy are identical. As can be seen in Figure 3-18 and Figure 3-19, this expectation is a valid one.

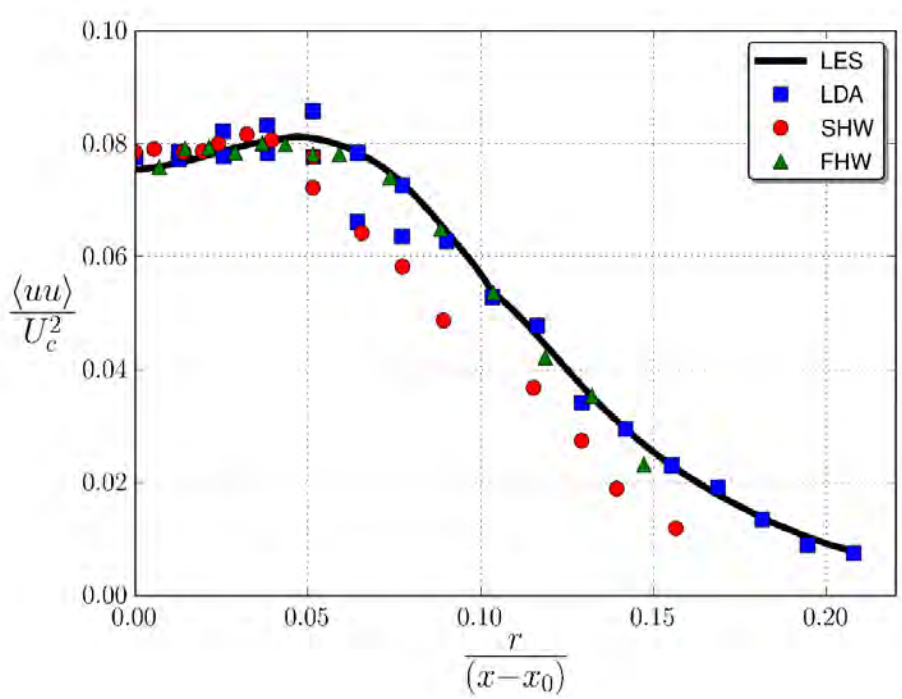

Figure 3-17. Comparison of axial component of turbulent kinetic energy at $x = 70D$

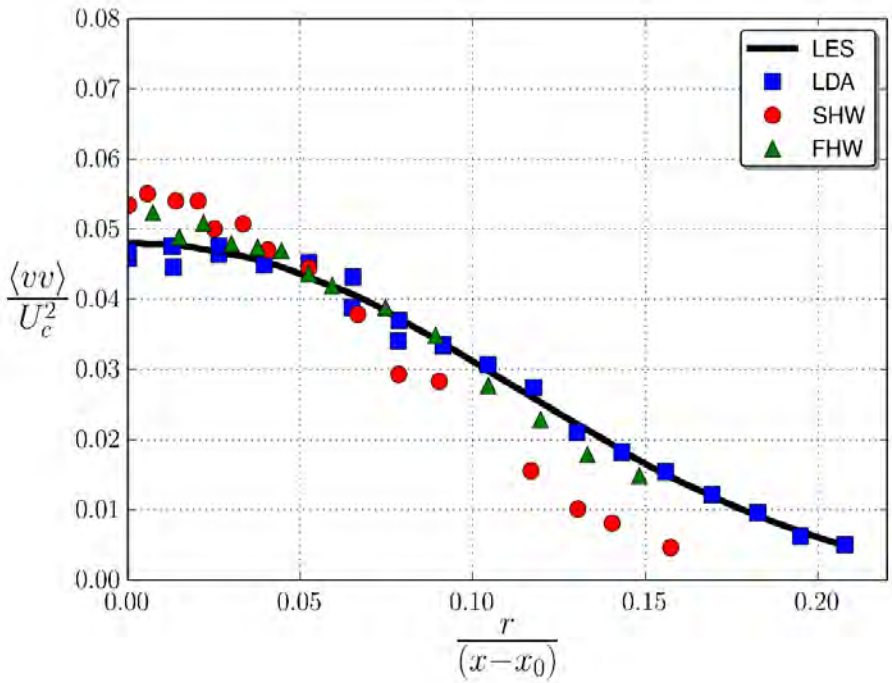

Figure 3-18. Comparison of radial component of turbulent kinetic energy at $x = 70D$

Another feature worth exploring is the self-similarity of the flow features downstream of the nozzle. The evolution of axial velocity at different axial locations is shown in Figure 3-21. It shows that axial velocities reveal self-similar behavior in the range of $20D < x < 80D$. Therefore, for a location where self-similarity is reached, an increase in downstream length of the domain would not provide additional insight. However, it is important to realize that although self-similarity may be reached for the velocities, other quantities like turbulence statistics (e.g., second moments of velocities), might show very different trends in self-similarity. The fact that the same region of self-similarity does not apply for the axial stress component is evident in Figure 3-22. Close to the jet nozzle ($x = 20D$), the behavior is not consistent with experimental or computational results at $x = 70D$. However, these second moments do show self-similar behavior in the range of $50D < x < 70D$. Therefore, the self-similar region can occur at different locations, depending on which flow metrics are of interest.

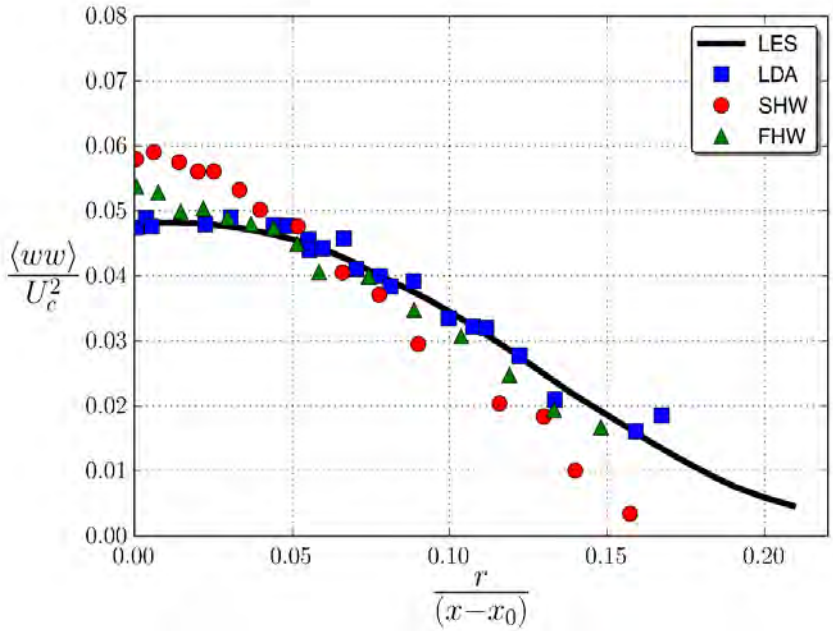

Figure 3-19. Comparison of azimuthal component of turbulent kinetic energy at $x = 70D$

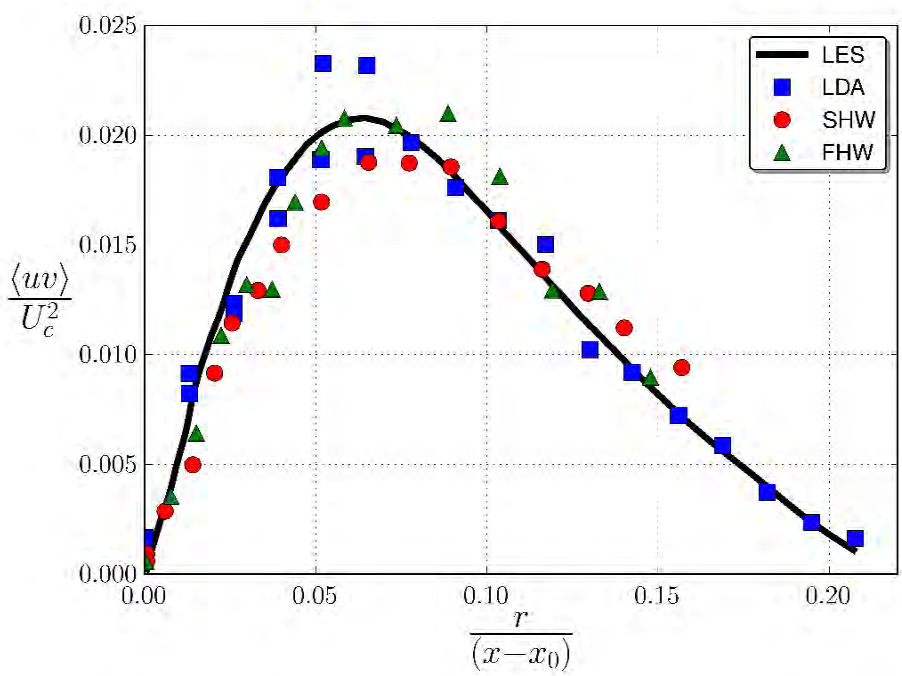

Figure 3-20. Comparison of turbulence shear stress at $x = 70D$

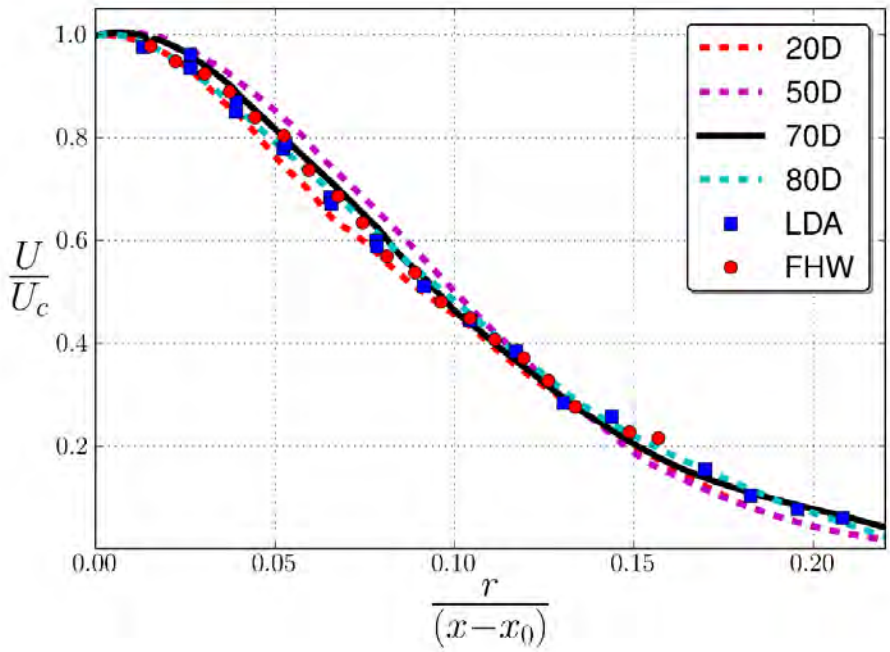

Figure 3-21. Normalized axial velocity profiles at different axial locations

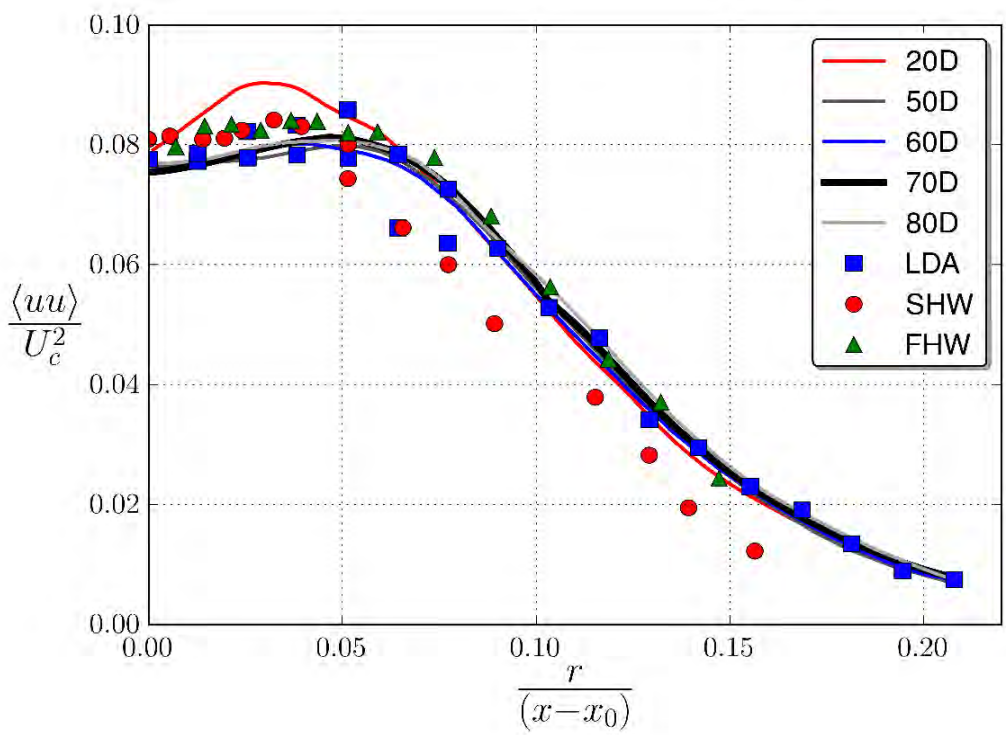

Figure 3-22. Normalized axial stress profiles at different axial locations

1.1.1.3. Profile of Triple Correlations

The main importance of third order moments is their principal role in the turbulent energy and Reynolds stress budgets. Both slope and magnitudes of the third order moments indirectly appear in those budgets with the potential to greatly affect the flow physics. Therefore, it is important to resolve the inconsistent trends seen in the literature.

The profile for $\langle u^3 \rangle$ in Figure 3-23 shows both LES studies have a shape similar to their corresponding experimental curves, but with a lower magnitude. It is should be noted that the LES from B&B, which is also meant to mimic P&L experimental conditions, exhibits this trend as well, but the difference between LES-PL and B&B is coming from the fact that they solved incompressible flow with a compressible solver. The mesh set-up and initial conditions are also different in B&B compared to LES-PL. Both of these factors play an important role in higher turbulent statistics. Also, near the centerline, both sets of LES data (as well as B&B) show similar trends, namely an initial decrease, followed by an upward trend and subsequent drop after a peak value is reached. Figure 3-24, Figure 3-25, and Figure 3-26 show negative values near the centerline, which according to P&L, has an important influence on the turbulent transport of the jets. Although all three figures exhibit similar shape experimentally and computationally, magnitudes and in some cases peak locations differ in Figure 3-24 and Figure 3-26. Moreover, all the LES results are in agreement with P&L for $\langle uw^2 \rangle$ within Figure 3-25 rather than the LDA measurements of HCG, which appear to be extremely noisy. This noisy behavior is to be expected since very high turbulent intensity was observed away from the core region of the jet (the explanation offered by HCG). The LES-PL results show a very good agreement with P&L data in these three mentioned figures, but, near the centerline for $\langle uv^2 \rangle$ shows a smaller magnitude similar to that of B&B and HCG results (see Figure 3-26). The LES-HCG data, on the other hand, have maximum locations similar to the HCG data, but far from the centerline they follow trends common to P&L data. Figure 3-27 clearly displays each LES result and their corresponding experimental data for $\langle v^3 \rangle$. Here, LES-PL shows a similar shape to B&B, but both have

higher magnitudes in comparison to experimental data of P&L, particularly around the peak location. The LES-HCG again follows HCG trend wise, but with a slightly lower magnitude.

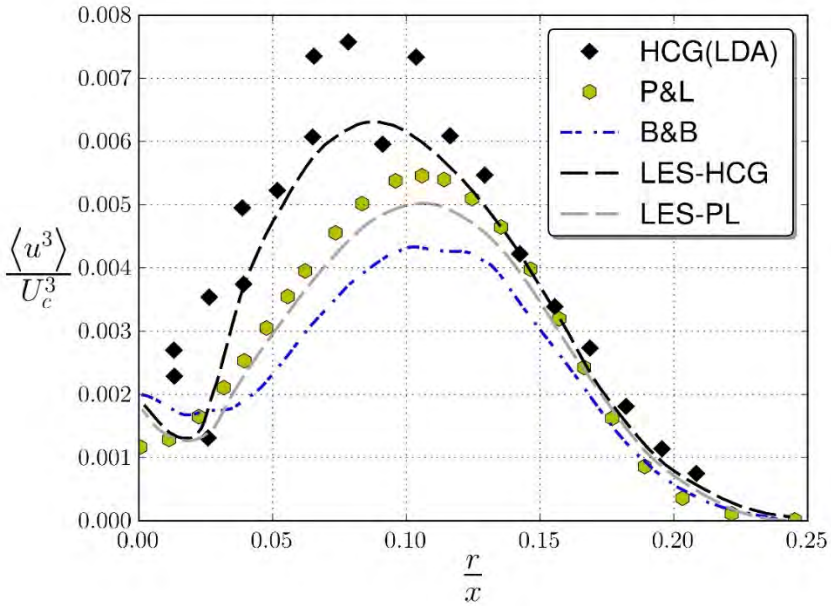

Figure 3-23. Comparison of axial flux of $\langle uu \rangle$

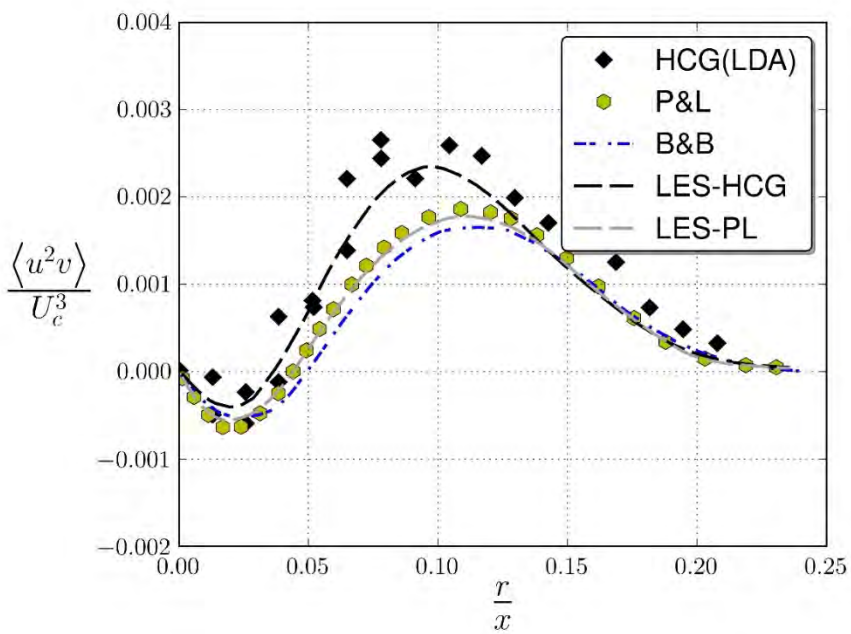

Figure 3-24. Comparison of axial flux of $\langle uv \rangle$

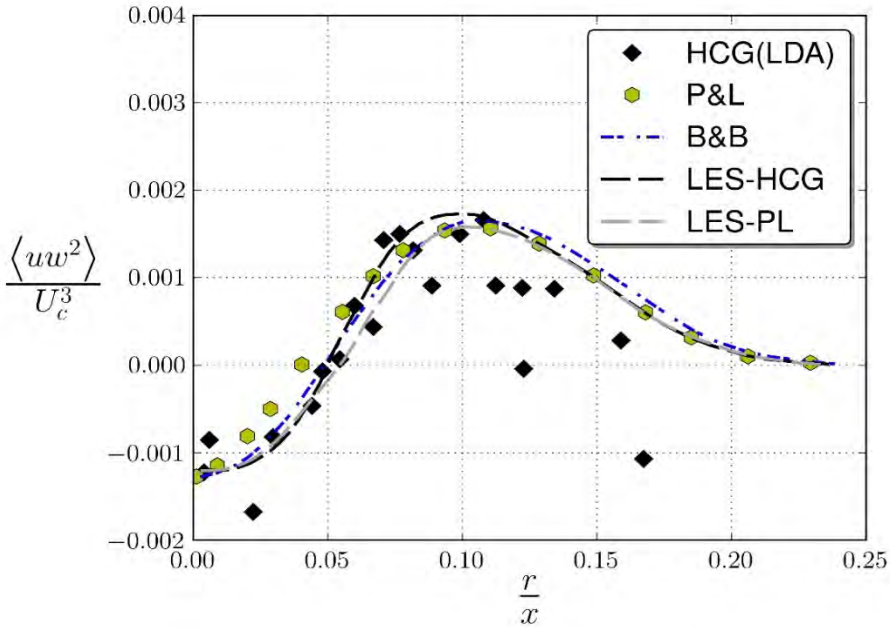

Figure 3-25. Comparison of axial flux of $\langle ww \rangle$

For the $\langle vw^2 \rangle$ trends shown in Figure 3-28 (where no experimental data is available), it is worth noting the magnitude is around half of the $\langle v^3 \rangle$ data shown in Figure 3-27. With this result, the common approximation of both HCG and P&L, $\langle v^3 \rangle = \langle vw^2 \rangle$ seems very questionable. This approximation is used in both experimental studies to evaluate turbulence diffusion terms due to difficulty of acquiring thorough actual measurements.

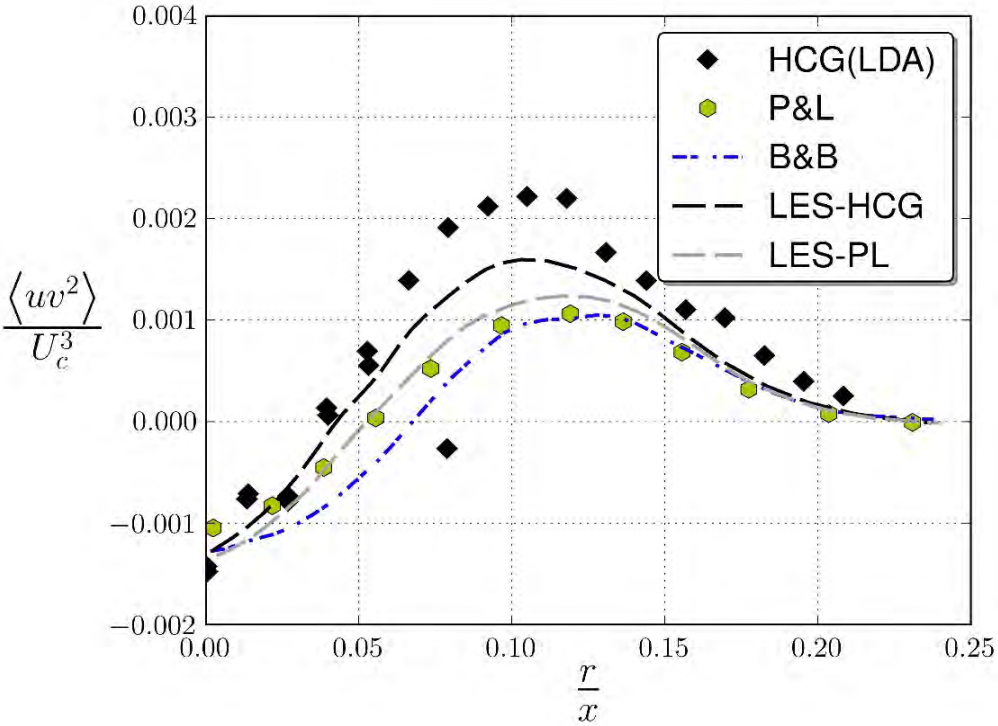

Figure 3-26. Comparison of radial flux of $\langle uv \rangle$

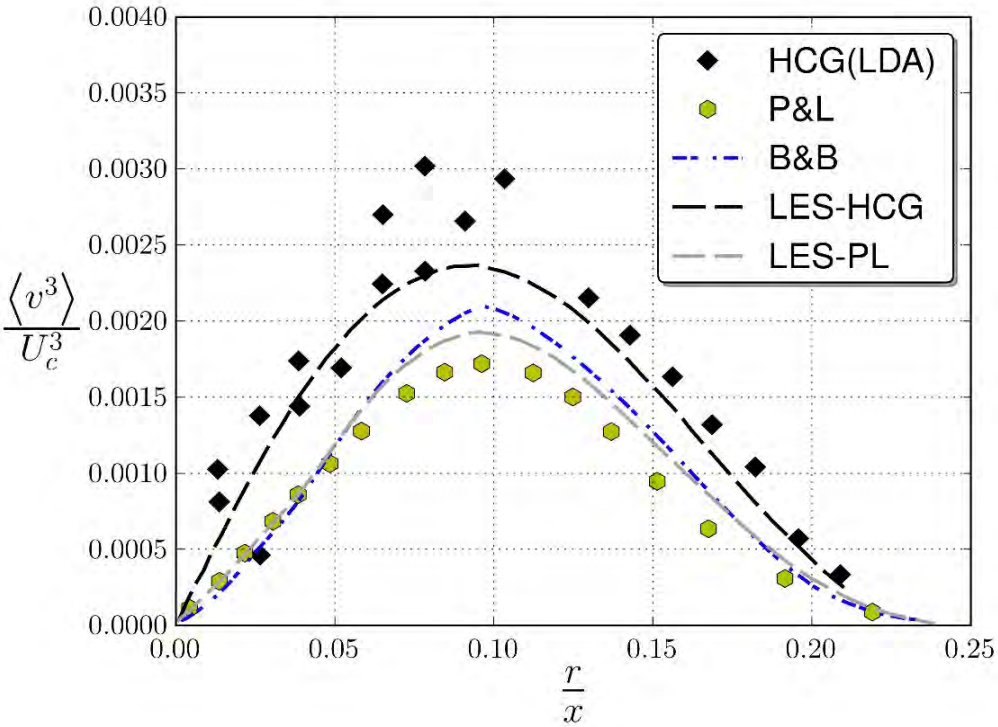

Figure 3-27. Comparison of radial flux of $\langle vv \rangle$

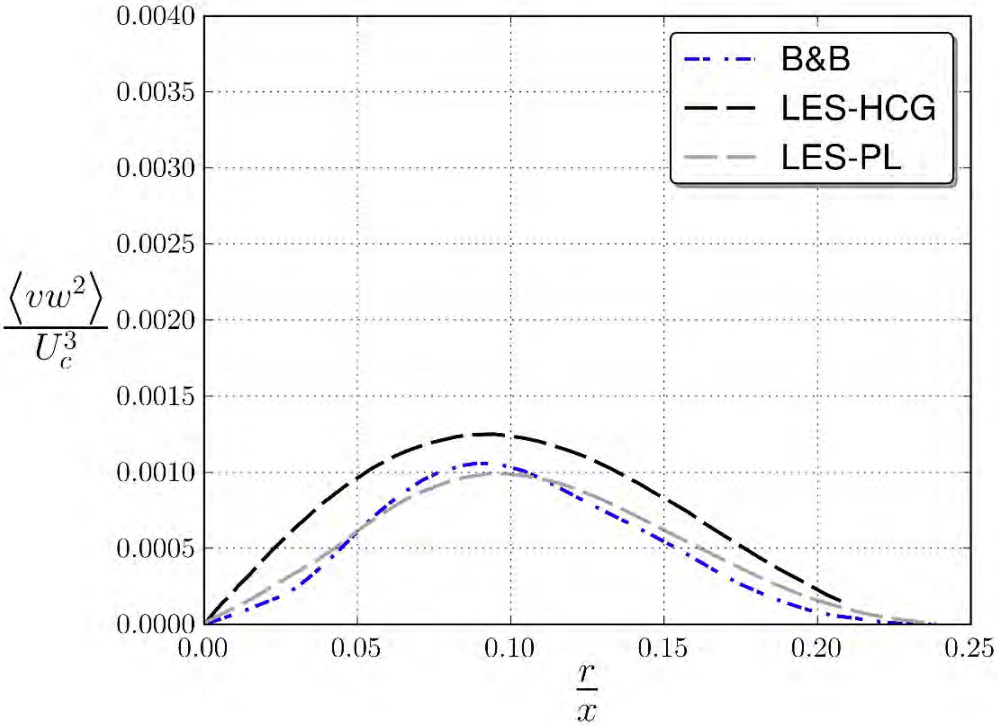

Figure 3-28. Comparison of radial flux of $\langle ww \rangle$

1.1.1.4. Turbulent Kinetic Energy Budget

The turbulent kinetic energy budget is one of the physically descriptive criteria to assess evolution of a turbulent jet flow. This budget, by which the contribution and balance of different mechanisms such as convection, dissipation, diffusion and production can be assessed, provides valuable insight into the physics of the turbulent jet. The measurement of the turbulent kinetic energy budget of the jet has been a topic of large interest in several previous studies, both of an experimental and computational nature, including HCG, P&L, and B&B. To address some serious discrepancies regarding the turbulent kinetic energy budget in the aforementioned studies, this is now investigated in greater detail. In addition to the two Reynolds numbers considered for duplicating HCG and P&L studies, another LES study is included with Reynolds number of Re = 2000 (hereafter as LES-2000), which corresponds to a recent DNS study by Taub et al. [67].

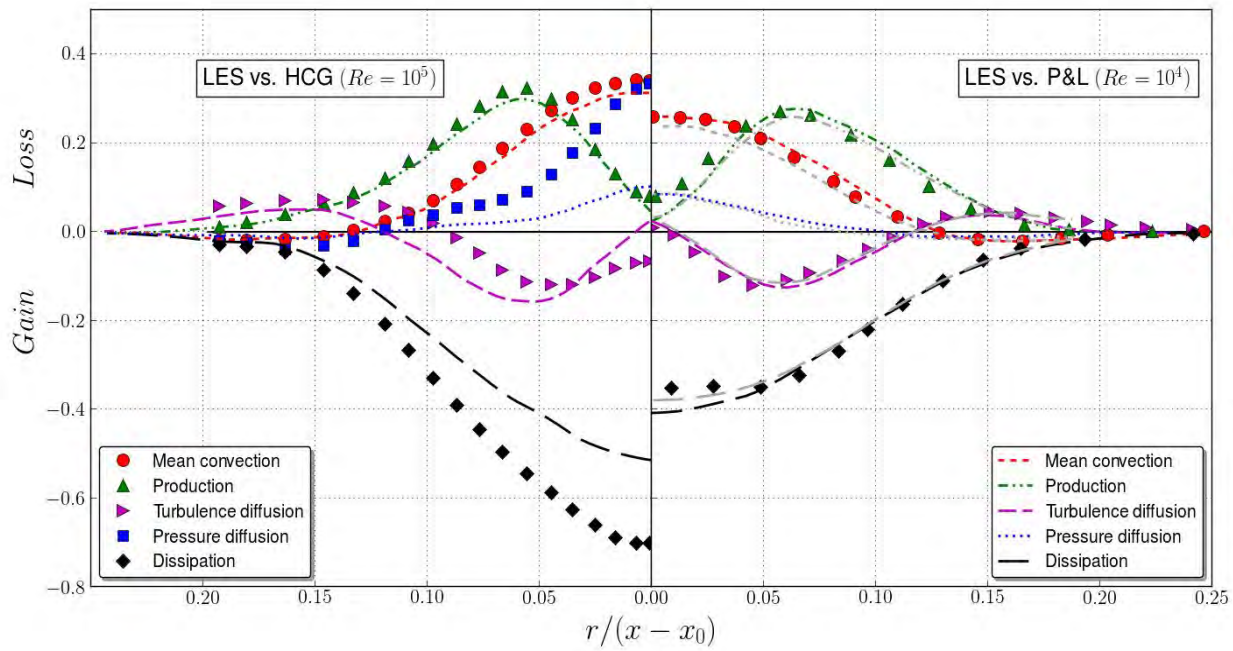

Figure 3-29. Turbulent kinetic energy budget in self-similar region, quantities are normalized by $\langle U_c^3 \rangle$. Grey lines corresponding to LES data of B&B

The budget for the turbulent kinetic energy in the self-similarity region of the jet is presented in Figure 3-29 for the Re = 10^5 (same as HCG) and Re = 10^4 (same as P&L) on the left and right sides of the figure, respectively. Note that for the Re = 10^4 case, the B&B LES results are also provided for comparison. The LES reported values are calculated explicitly from the LES data without any assumptions similar to those adopted by HCG and P&L. LES-PL reveals a very good agreement with both P&L and B&B for the mean convection, production, dissipation and turbulence diffusion. However, P&L neglected the pressure diffusion term altogether, and quantified dissipation as the balance after accounting for all the other terms. This assumption by P&L of neglecting the pressure diffusion term seems unsubstantiated given the non-negligible magnitude of the current LES results, which are also consistent with the LES from B&B.

The LES-HCG results (left side of Figure 3-29) find very good agreement for mean convection and production, but cast serious doubt on assumptions used by HCG to calculate pressure diffusion and dissipation. In the HCG study, dissipation was evaluated by a mathematical model called *axisymmetric*

turbulence, which results in a higher magnitude for dissipation in comparison to the LES results as well as measurements from P&L. Consequently, evaluation of pressure diffusion as the closing term of the energy budget appears to have magnified the difference between both LES and P&L data compared with the HCG measurement of the pressure diffusion term. In reality, the pressure diffusion profiles are similar for both HCG and P&L. Turbulence diffusion of LES-HCG, on the other hand, follows a similar trend as P&L and B&B particularly near the centerline, which is not consistent with the experimental results of HCG. This is a direct result of the fact that HCG could not capture negative values near the centerline for those mentioned triple correlations which determine turbulence diffusion.

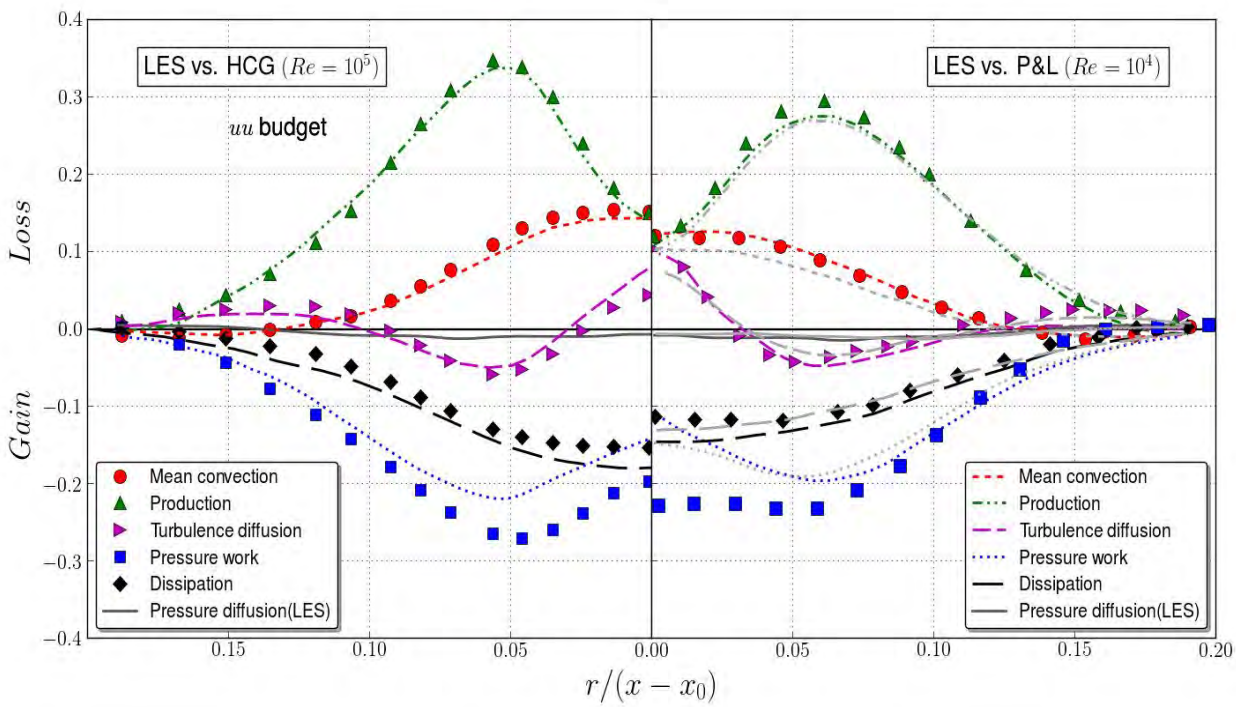

Figure 3-30. Balance of $\langle uu \rangle$ in self-similar region, quantities are normalized by $\langle U_c^3 \rangle$. Grey lines corresponding to LES data of B&B

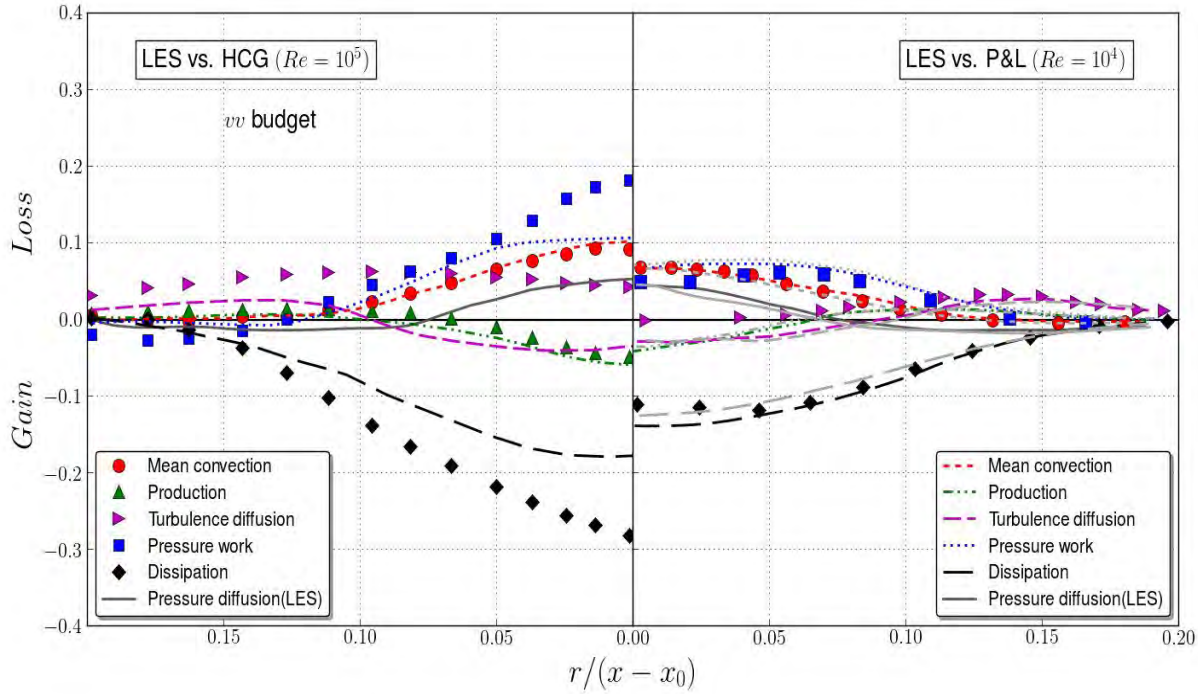

Figure 3-31. Balance of $\langle vv \rangle$ in self-similar region, quantities are normalized by $\langle U_c^3 \rangle$. Grey lines corresponding to LES data of B&B

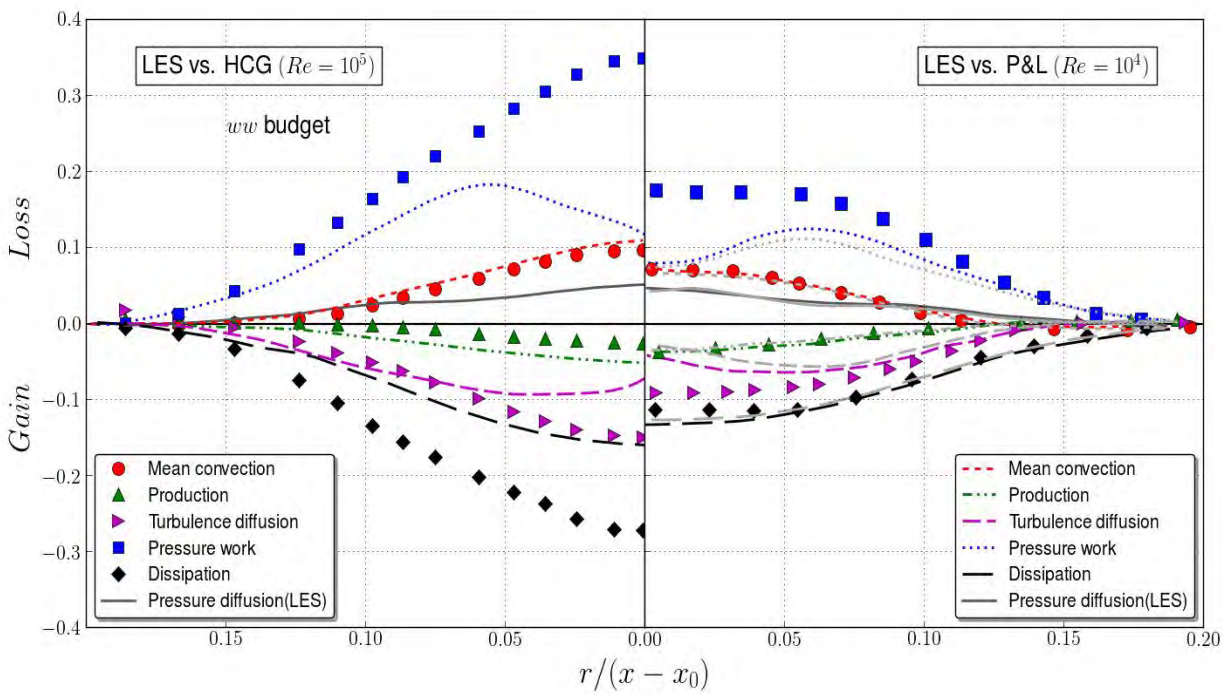

Figure 3-32. Balance of $\langle ww \rangle$ in self-similar region, quantities are normalized by $\langle U_c^3 \rangle$. Grey lines corresponding to LES data of B&B

To examine the role of the different mechanisms in the turbulent kinetic energy within the jet, the budgets for the three energy components $\langle uu \rangle$, $\langle vv \rangle$, and $\langle ww \rangle$ of LES-HCG and LES-PL are presented in Figure 3-30, Figure 3-31, and Figure 3-32, respectively. In each of the aforementioned figures, they are compared with the energy component budgets obtained by HCG, P&L, and B&B. To evaluate these components, P&L neglected the pressure diffusion and also assumed small-scale isotropy for the dissipation components and finally evaluated the remaining pressure terms as the balance. HCG, instead, used the axisymmetric dissipation assumption and solved the closing balance as pressure work. Both HCG and P&L assumed $\langle vw^2 \rangle = \langle v^3 \rangle$ for their respective turbulence diffusion calculations.

For the three energy components, there is a good agreement between the LES-PL and P&L terms related to mean convection, production, and dissipation. This agreement supports the assumption of isotropic dissipation made by P&L. As mentioned in the work of B&B, the difference between turbulence diffusion terms in radial and azimuthal components is coming from the assumption of $\langle vw^2 \rangle = \langle v^3 \rangle$ in P&L and HCG for their calculation of turbulence diffusion. This discrepancy of turbulence diffusion near the centerline, which is trivial in the radial component and significant for the azimuthal component, indirectly affects pressure work terms. Similar behavior is observed for the HCG measurement of pressure work. In the radial component, P&L reported zero production, while all the LES calculations and data of HCG measurements show small, but negative magnitude near the centerline which rapidly goes to zero toward the outer radius of jet. The effect of the dissipation assumption of HCG both on the dissipation itself and indirectly on pressure work terms can be seen by comparing LES-HCG data with P&L and B&B.

The budget of the Reynolds stress is lastly presented in Figure 3-33. Both of the LES data sets agree well with their corresponding experimental measurements, but the effect of Reynolds number on production and pressure work is much more obvious in this figure. Mean convection and turbulence diffusion terms of the Reynolds stress budget seem identical for both experimental and computational values in both Reynolds number studies.

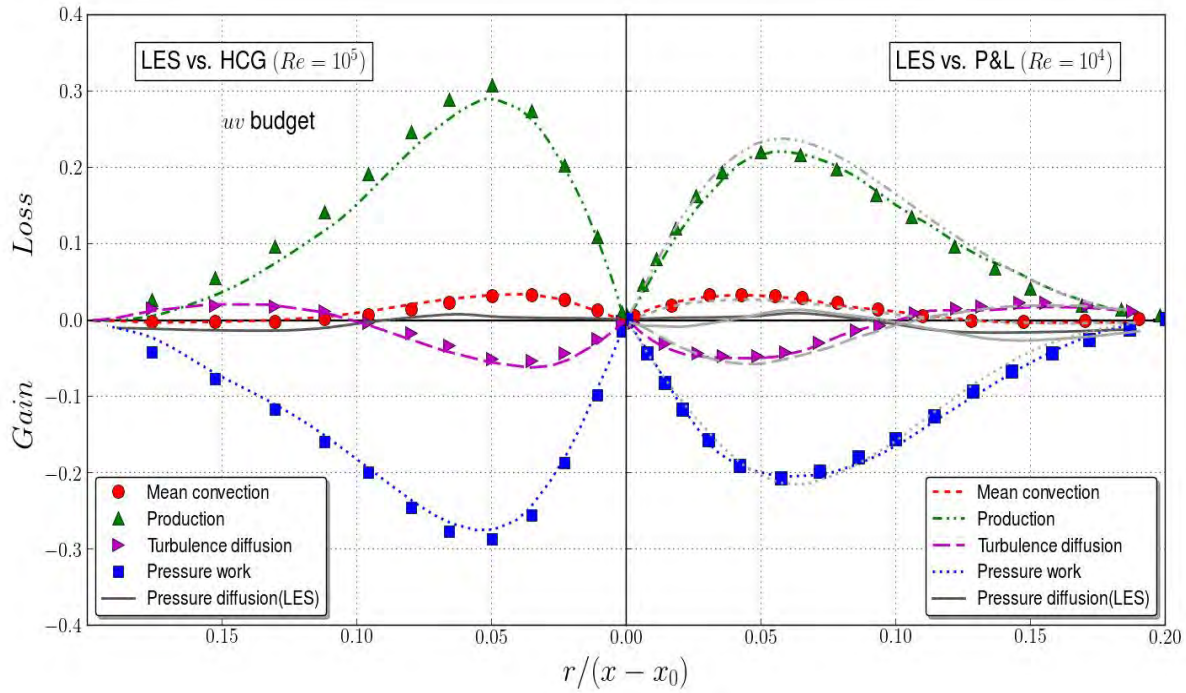

Figure 3-33. Balance of $\langle uv \rangle$ in self-similar region, quantities are normalized by $\langle U_c^3 \rangle$. Grey lines corresponding to LES data of B&B

With the purpose of clarifying the differences between the data from two Reynolds numbers which differ by an order of magnitude, particularly in terms like mean convection and production which can be measured reliably [67], the LES-2000 study is conducted. Together, these three simulations provide the perspective needed to accurately quantify the budget for turbulent kinetic energy through comparison with the two benchmark experiments of HCG and P&L (along with the corresponding LES from B&B) and the DNS study of Taub et al. [67]. The accommodated Reynolds numbers for this comparison are 10^5, 10^4, and 2000 for LES-HCG, LES-PL, and LES-2000, respectively. The results of this comparison are shown in Figure 3-34 and Figure 3-35. Both LES and experimental results show that magnitude and peak location of mean convection and production terms vary with Reynolds number, while this dependency is negligible in pressure diffusion results of LES. Turbulence diffusion also reflects a Reynolds number dependence on both magnitude and maximum locations.

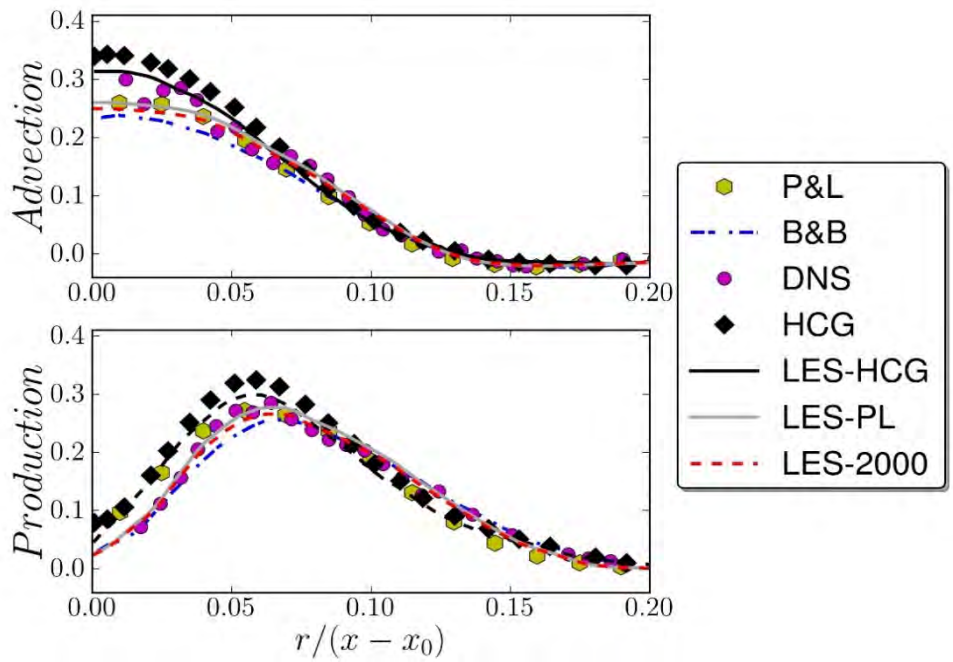

Figure 3-34. Comparison of mean convection (advection) and production of turbulent kinetic energy budget in self-similar region, quantities are normalized by $\langle U_c^3 \rangle$

The difference between LES-HCG and LES-PL is larger than the gap from LES-PL to LES-2000, so the dependency on Reynolds number appears to be higher as Reynolds number increases. The location of peak in diffusion terms vary significantly with Reynolds number in comparison to other terms. As shown in Figure 3-35, peak locations of diffusion terms move to further downstream location as the Reynolds number grows. In general, each jet can be characterized by its Reynolds number in terms of higher turbulent statistics and turbulent energy budget.

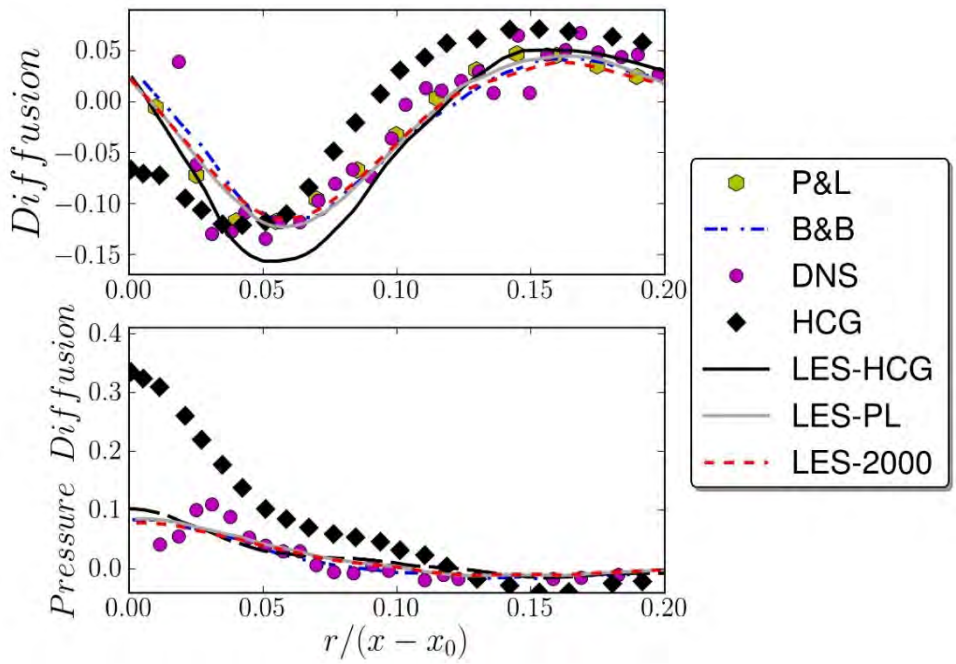

Figure 3-35. Comparison of turbulence diffusion and pressure diffusion of turbulent kinetic energy budget in self-similar region, quantities are normalized by $\langle U_c^3 \rangle$

In summary, LES studies of turbulent jets between Re = 2000 and Re = 10^5 have been conducted. This has enabled characterization of turbulence properties of a round jet by its turbulence statistics and the budget for turbulent kinetic energy and each of its components. The directly obtained flow statistics from these LES studies have been compared to experimental data of HCG and P&L.

The LES results have shown that the approximation regarding $\langle vw^2 \rangle = \langle v^3 \rangle$ made by both HCG and P&L is inaccurate. Turbulence diffusion has also been found to be trivial in the budget of turbulent kinetic energy, which is in agreement with P&L, but casts doubt on turbulence diffusion and hence, dissipation calculations. The effect of Reynolds number on turbulence statistics, particularly on third order moments and the energy budget, have been studied. Terms like mean convection and production are found to be influenced by Reynolds number and inlet conditions.

Therefore, for the complex geometries with a range of jet Reynolds numbers like the VHTR lower plenum, this study emphasizes the significance of both Reynolds number and the upstream flow conditioning. Even though this LES work has been computationally costly, it provides key insights into the

physics tied to an isothermal turbulent round jet. This critical first step greatly enables the development of a trusted approach to eventually modeling the VHTR lower plenum. It is important to note that having such highly detailed experimental results like HCG and P&L has greatly aided the computational simulation in different stages of this study. The more statistics available, the more useful they are in terms of validating a computational model. In general, the luxury of experimental data does not always exist, which is where V&V becomes even more important, especially in the simulation of complex geometries and physics. The high fidelity results are also due in part to the fact that HCG provided detailed measurements of the upstream flow conditioning components. Without such details, the modeler is forced to fill in the gaps, which in some cases, creates otherwise non-existent problems as evidenced by the preliminary work of this investigation.

3.4 Non-Isothermal Turbulent Round Jets

Similar to isothermal turbulent jets, experimental investigation of non-isothermal turbulent jets also has a rich history. One of the first comprehensive studies was conducted by Corrsin & Kistler [68] which years later, in more detail, was followed by another key investigation by Chevray and Tutu [69]. In both of these studies, the authors made detailed investigations of temperature and velocity fields in a round heated air jet issuing from a contraction into an insulated test section. Values of the mean velocity and temperature (above ambient) at the jet exit were 25 m/s and 20 °C respectively, while measured turbulence intensity at the same location was around 0.5%. Those two mentioned articles had been among the very few measurements aimed at quantifying the Reynolds shear stress and heat flux in a turbulent round jet. Chua and Antonia [70] measured those quantities, as well as the turbulent Prandtl number, for a circular jet at a Reynolds number of 17,700. Antonia and Mi [71] also made some measurements of temperature dissipation with the aid of a parallel cold wire for a jet at Reynolds number of 1.4×10^4. They measured the temperature derivative and dissipation in each of the three directions and found that the radial and azimuthal values of temperature dissipations were almost equal and only slightly larger than the axial component. The subsequent departure from isotropy of the temperature dissipation was found to be very minor. The influence of initial flow conditions on the passive scalar field of a slightly heated turbulent free jet was

investigated by Mi et al. [72]. Detailed experimental data was reported for jets at a Reynolds number of 16,000 issuing from two nozzle types: a smooth contraction and a long straight pipe. Significant differences between the flows issuing from the two nozzles were found across the flow region covering an axial range from 0 to 70 jet exit diameters downstream. Mi and Nathan [73] complimented this study by investigating the centerline evolutions of turbulent statistical properties of non-isothermal air jets issuing from nine differently-shaped nozzles. The loss of jet axisymmetry at the jet exit caused faster mean velocity decay, and enhanced the growth of the fluctuating intensity in the near field. However, the asymptotic decay rate of the centerline velocity in the far field seemed to remain independent of nozzle shape.

In spite of various experimental investigations, the number of computational simulations is surprisingly limited. Among those rare simulations, Smith et al. [74] did a RANS simulation to evaluate the capability of the κ-ε turbulence model to predict flow physics influenced by variation of nozzle shape in heated turbulent round jets. Not surprisingly, it was found that RANS is incapable of correctly predicting key aspects of the near-field flow in addition to the rates of spread and decay caused by changes to nozzle shape. Suto et al. [75] performed LES of four different Reynolds numbers ranging from 1200 to 10^6 for a heated jet and found the dynamic Smagorinsky model to be in better agreement with mean velocity than the standard Smagorinsky model. However, discrepancies were observed between LES and experimental measurements of scalar fluctuation intensity in the near field. Colombo et al. [76] used the LES solver within the FLUENT CFD code to simulate a non-isothermal air jet at Reynolds number of 95,500. Mean velocity, mean temperature, and second-order moments of velocity components calculated from LES were compared with different available experimental results. Key features of the non-isothermal jets like temperature fluctuations and its RMS are absent in their studies.

1.1.1.5. Computational Model

In order to computationally verify the experimental data of [72] for non-isothermal jet flow and to resolve the discrepancies surrounding the presence of a hump in centerline RMS temperature fluctuations in the jet near-field, large-eddy simulations are constructed and evaluated using the OpenFOAM toolbox. To address the above objectives, two separate LES studies are conducted: one for jet precursor to provide

correct boundary conditions for the jet inlet region and one LES study corresponding to the work of [72] to explicitly validate against their experimental measurements. To mimic their experimental work, the non-isothermal round jet diameter is set to D = 14 mm and is 50 K above the ambient temperature of 288 K. Similar to the previous isothermal jet studies, the LES domain is $100D$ in length from the jet nozzle to the outlet of the domain. This enables direct comparison with data from [72], where measurements were made up to $70D$ downstream of the jet nozzle. The overall diameter of the domain is $55D$. The Reynolds number (Re_D) of the jet based on the average jet velocity and diameter at the exit of contraction nozzle is 16,000. The back and side wall temperatures of the simulation domain are set to ambient temperatures (288 K). Accurate fluctuating inflow velocity conditions are used from the precursor contraction nozzle simulation analogous to that mentioned in the previous isothermal investigation. Adjustable time stepping with a maximum courant number of 0.4 is used for the present simulations. The non-isothermal round jet simulation is performed using the *rhoPimpleFoam* compressible flow solver within the OpenFOAM CFD toolbox. The *dynLocalAverageSmagorinsky* SGS model is implemented into the present LES study as the incompressible *dynLocalAverageSmagorinsky* SGS model gave accurate predictions of turbulent statistics for an isothermal round jet as previously reported. For this reason, OpenFOAM was modified to accommodate this using a compressible flow solver.

A RANS simulation is first performed in order to initialize the flow field and temperatures inside the domain. This approach also motivates the mesh creation process for LES through adjusting the local mesh size depending on the turbulence length scale found from RANS data.

The mesh used for the simulation is similar to that of used for isothermal jet. The domain has just over 16 million cells. As seen in Figure 3-36, different mesh grading is applied in the axial direction from the inlet to the location $x = 15D$ downstream to ensure that the inner core of the jet is well resolved at entry. For the remainder of the downstream domain ($15D < x < 100D$), the axial mesh size is $D/8$. Using a compressible solver enables the use of a non-reflecting boundary condition at the outlet. In the radial direction, a 15 × 15 uniform square grid is used at the center of the jet inlet in a manner similar to the

isothermal jet mesh design Each square cell in this Cartesian grid is $D/25\sqrt{2}$ (~$0.028D$) in size on each side. The very center cell of this grid is collocated with the overall domain centerline, thereby eliminating the need to interpolate for any centerline data at which experimental results are widely available. As can be seen in Figure 3-36, three additional radial layers of cells exist between the bounds of the Cartesian grid and the edge of the circular inlet ($r = D/2$). Outside of this circular inlet, a uniform mesh size is used between $r = D/2$ and $r = D$. The mesh size in this region is similar to the average mesh size contained within the jet diameter. An expanding grid is then used from $r = D$ to $r = 5D$. A uniform structured square grid size of $D/8$ is then applied from $r = 5D$ to the outside edge of the computational domain ($r = 27.5D$). The number of azimuthal divisions is dictated by the 15 × 15 Cartesian array (4 × 15 = 60 divisions), which was found to be more than adequate for the isothermal work.

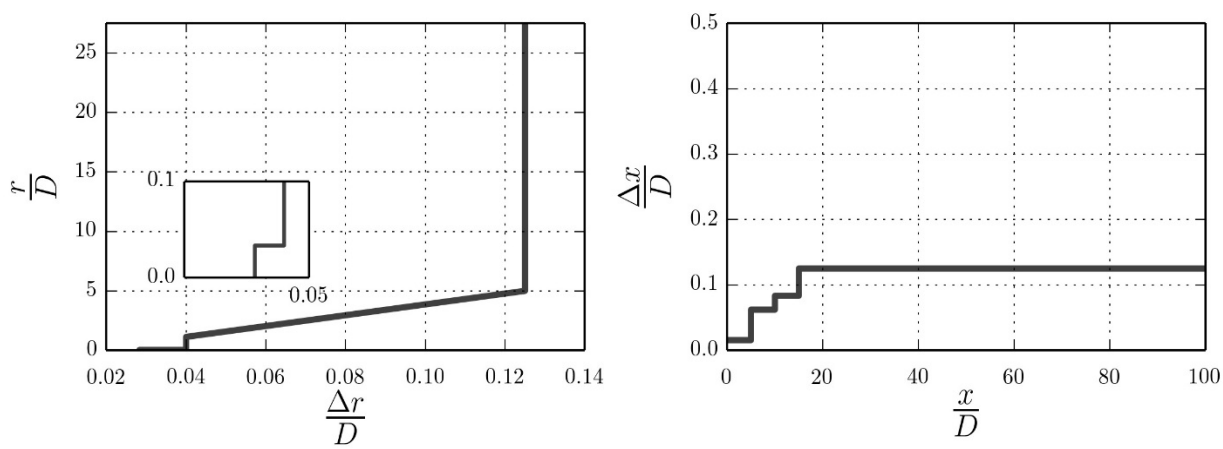

Figure 3-36. Mesh spacing in radial and axial direction. The grid is symmetric in respect to the jet axis

1.1.1.6. Precursor Simulation

In their experiments, Mi et al. [72] used two different nozzles: a long straight pipe and a smooth contraction, the latter of which is the subject of current study. The contraction begins with a duct opening of 80 mm, which transitions down to the exit jet diameter of 14 mm. A faithful model for this contraction is created and shown in Figure 3-37. Tetrahedral cells were used to mesh the contraction geometry. The model had a total of 2.02 million cells. A very low value of turbulent intensity (with scale of 0.001) is

prescribed at the inlet of the contraction model, which would be expected close to the screen mesh of a wind tunnel [51]. Instead of modeling the large enclosure downstream of the nozzle, the flow is directed into a domain with a diameter 25 times the size of the jet diameter in order to reduce computational costs. The flow inside the contraction domain is first initialized with steady-state RANS data. Isothermal wall boundary conditions are used for the entire contraction. The mesh near the wall is fine enough ($y^+ = 0.01$) to avoid the use of a wall model. This mesh resolution is very computationally expensive, but it proves to be the only attainable solution for providing the correct inlet boundary conditions for non-isothermal jets as delayed detached-eddy simulation (DDES) and other methods failed. In addition to velocities and temperature fluctuations, SGS measurements from the contraction model p play a vital role in precisely capturing the near-field physics of the problem, particularly RMS of temperature at the jet centerline. The *rhoPimpleFoam* solver with the same SGS model is then used to obtain accurate flow conditions at the jet nozzle.

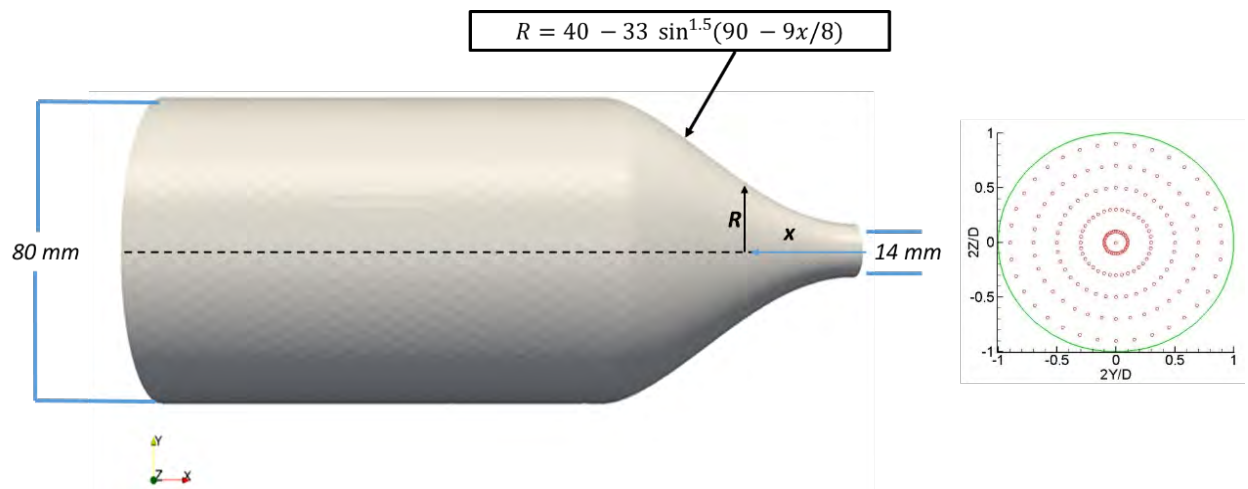

Figure 3-37. Computational model of the upstream contraction used in the experiments of Mi et al. [47]

1.1.1.7. Results and Discussion

Similar to the isothermal jet work, adjustable time-stepping is used for the contraction simulation, with maximum Courant number set at 0.4. As illustrated in Figure 3-37, transient velocity data is probed

and saved at 181 locations (5 equally spaced radial locations at 10° angular increments at the nozzle exit plane as well as center of the jet) to precisely capture and serve as inlet boundary conditions for of the jet.

Figure 3-38 shows the axial variation of temperature normalized with respect to the mean inlet temperature of the jet. The variable θ is the difference between the temperature at a point and the ambient temperature. Good agreement between LES and experimental data can be seen particularly in downstream locations where the self-similar region is achieved, which is located at the $20D$ downstream location of the domain. From this figure, the virtual organ (x_{01}) and decay constant ($K1$) are determined as $3.58d_\epsilon$ and 4.37 respectively, which is in great agreement with the reported data of [72], which is calculated to be $3.5d_\epsilon$ and 4.48 respectively. More information regarding the effective diameter (d_ϵ) can be found in [47]. The authors of that experimental paper argued that since the ratio of the Grashof number (Gr) to the square of the Reynolds number ($\mathrm{Gr/Re^2}$) at the jet exit was extremely small for their experiment ($\mathrm{Gr/Re^2} \approx$ 10-5), the effect of buoyancy was negligible and thus the measured temperature field would be similar to that observed for a passive contaminant/tracer. Figure 3-38 also shows that the present simulation data agrees well with the results of [72], which means that the temperature calculation by LES is correctly assumed passive scalar. Also seen in this figure, specifying accurate inlet conditions from the contraction model significantly improves the near-field data predictions.

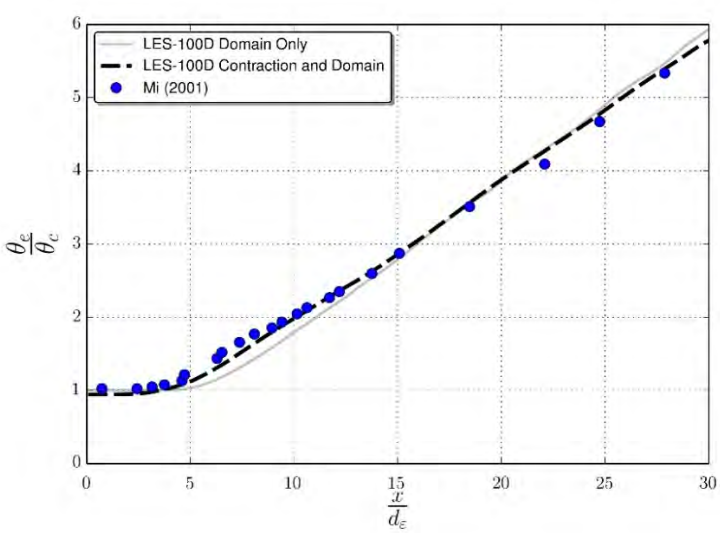

Figure 3-38. Centerline normalized inverse temperature

Figure 3-39 depicts a different form of the normalized mean temperature, and shows that beyond downstream location of $10D$, the LES result is in a very good agreement with experimental measurements. Although the near-field data does not match perfectly, the behavior of both experimental and LES are extremely similar. Once more, the effect of including a contraction simulation is noticeable, especially in near-field. This better prediction has an impact both in terms of the mean temperature as well as the virtual organ (x_{01}) values.

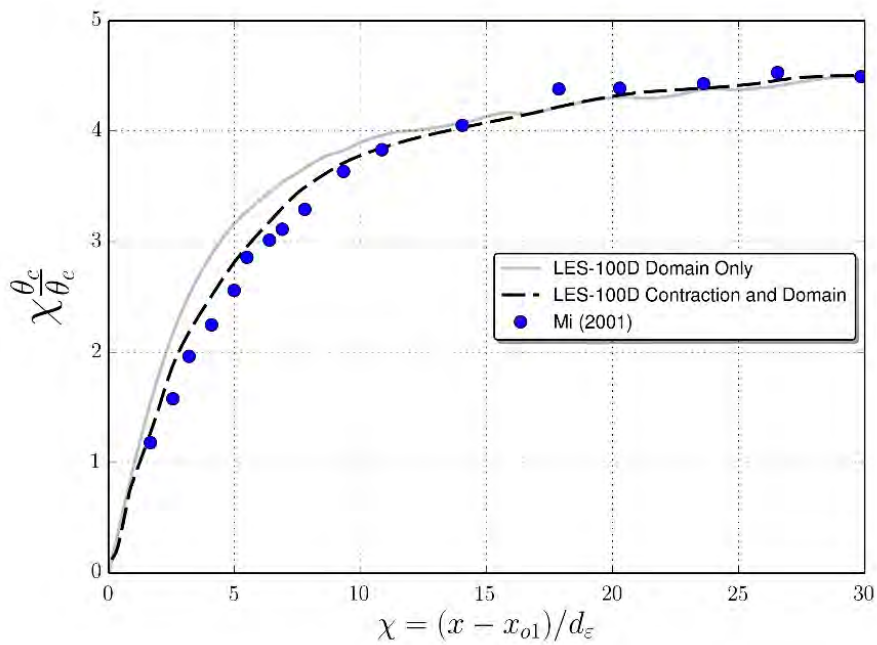

Figure 3-39. Streamwise versions of the normalized temperature mean

Figure 3-40 displays the spreading rate of the LES jet by examining the streamwise variations of the temperature half-radius ($r_{1/2}$), which is the location where the value of temperature is equal to half of the centerline temperature. The spreading rate of the half-radius is 0.115, which is very close to its experimental value of 0.11 reported by [72].

Figure 3-41 shows the radial variation of temperature for different axial locations in the compressible LES simulation with temperature-dependent fluid properties. The LES self-similar behavior of temperature has been captured well and agrees with the data of [72]. It seems that the experimental results

reach ambient temperature sooner away from the jet centerline in comparison to the LES results. Further investigation and comparison with other experimental data should be performed in future. The computational domain, on the other hand, seems to be large enough since self-similar behavior is captured well and LES results in the radial direction agree with the presented experimental data.

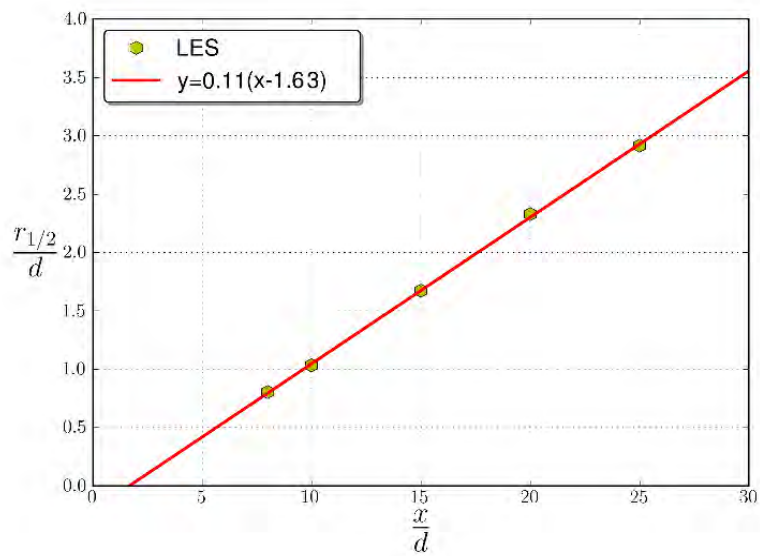

Figure 3-40. Streamwise versions of scalar half-radius

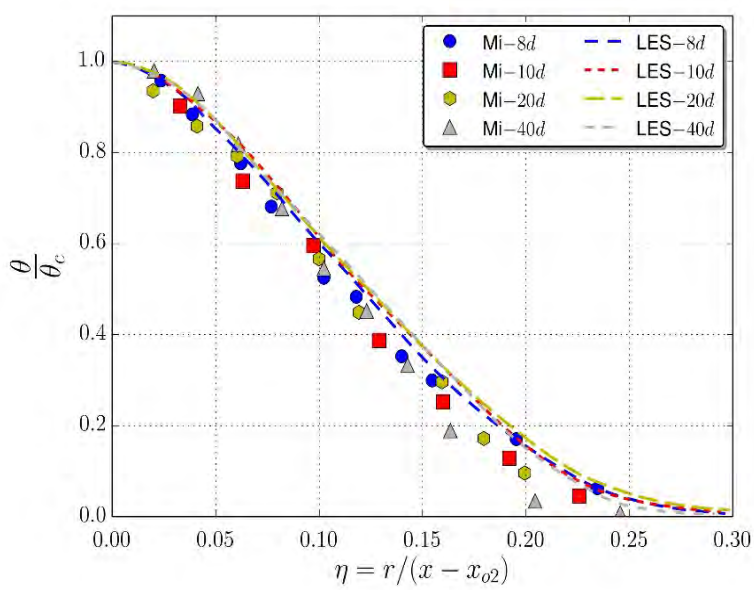

Figure 3-41. Radial profile of normalized mean temperature at several locations

Figure 3-42 and Figure 3-43 compare the streamwise development of the centerline RMS temperature fluctuations for the non-isothermal jet. Two normalization procedures are shown. The normalization by the exit mean temperature gives a reference for the absolute intensity of temperature fluctuations, while the locally normalized result provides a ratio which has been found by previous researchers to asymptote to a constant in the self-similar far-field region. As seen from Figure 3-42, the effect of contraction simulation on the precise prediction of RMS temperature fluctuations is vital. It is the main reason why all the previous computational studies (both RANS and LES) failed to accurately capture the physics of the problem.

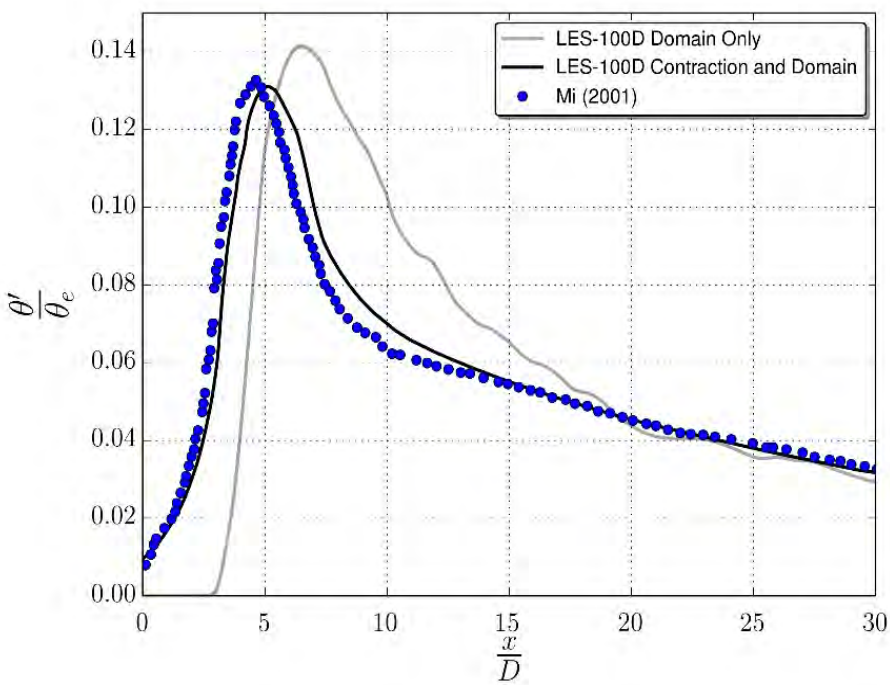

Figure 3-42. Streamwise variation of the temperature RMS along the jet centerline

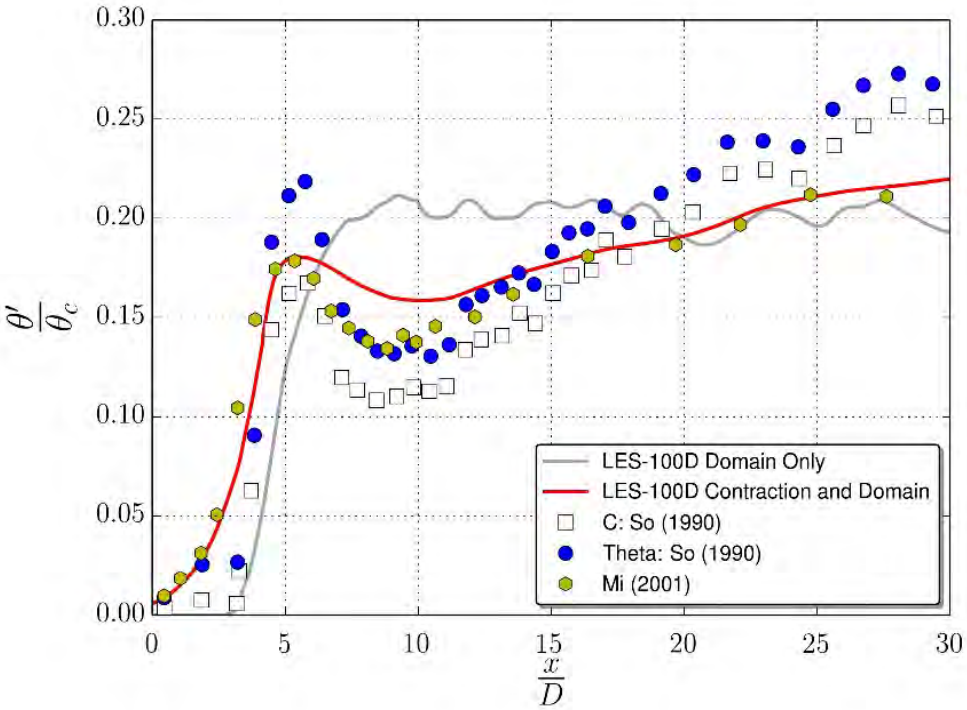

Figure 3-43. Streamwise variation of the temperature RMS over centerline along the jet centerline

Figure 3-43 shows that for a jet coming from a smooth contraction nozzle, a local maximum, or a hump, exists in the near-field temperature variations. This observation also repeated in concentration data of So et al. [77]. On the other hand, there is no equivalent hump in a jet issuing from pipe as comprehensively mentioned in Mi et al. [72]. From Figure 3-43, the aforementioned hump can be seen in both experimental and the LES results and is associated with the initial conditions, which is in contrast with what some previous studies mentioned as experimental errors [78, 79]. Mi et al. [72] argued that for a jet issuing from a smooth contraction, strong large-scale "engulfment" of ambient cold air by the highly coherent vortex structures results in a high amplitude of the temperature fluctuations (i.e. the hump). By contrast, for a jet coming from a pipe, the shortage of the large-scale coherent structures causes a fairly weak "engulfment" of surrounding cold air into the jet in the near-field region.

Once again, the effect of the contraction simulation is noticeable in Figure 3-43, accurately feeding the inlet condition results in near-field data improvement. This includes close to inlet data improvement as

well as capturing the hump. The difference between the experimental data of [72] and LES can be pointed to the fact that an experimentally isothermal condition is impossible. Also, the effect of SGS seem to be very significant for accurate LES simulations.

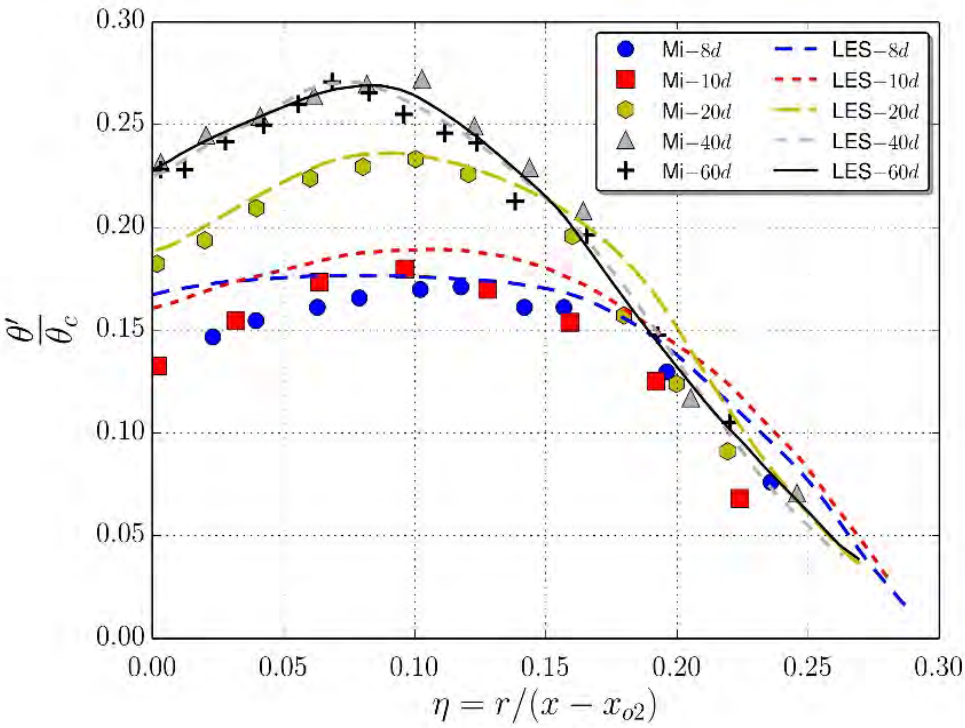

Figure 3-44. Radial profiles of the normalized temperature RMS over centerline

Figure 3-44 presents radial profiles of the normalized RMS temperature fluctuations over centerline mean temperature. Relative to the mean temperature field, the RMS temperature develops to the self-similar state further downstream from the nozzle exit. Similar to experimental data, the self-similar state of the RMS scalar is reached at $x > 40D$ for the LES case.

The present study has explored large-eddy simulation of a non-isothermal axisymmetric free jet similar to experimental study of Mi at el. [72]. The present LES is conducted at a Reynolds number of 16,000 using a compressible solver in OpenFOAM. The present study has revealed that to correctly simulate the turbulent scalar properties throughout the jet flow field in LES, very accurate inlet conditions should be provided. Existence of the hump for a jet issuing from a contraction is proven to not just be experimental

noise, but in order to correctly capture those near-field fluctuations, a separate contraction simulation has been conducted and data from this simulation has been fed accurately as inlet condition for a larger domain jet simulation.

3.5 Flow Past a Circular Cylinder

3.5.1 Isothermal Flow Over a Cylinder

In order to assess the accuracy and dependability of the OpenFOAM toolbox's LES capabilities, a 3D LES simulation of isothermal flow over a circular cylinder at Re = 3900 is performed. The Reynolds number for this preliminary evaluation was selected in such a way that results can be compared with well-known experimental and simulation data; flow over a cylinder at Re = 3900 has been extensively studied in previous investigations. Lysenko et al. [56] reviewed the available literature at the time for both LES and experimental work at Re = 3900. The experimental work of Lourenco and Shih [80] and Parnaudeau et al. [81] are the most widely used data to compare flow characteristics in the near field wake behind the cylinder, while the Ong and Wallace [82] experiment is used for far field comparisons with simulation data. It has been observed that the span wise length of the computational domain can have a significant effect on simulation results at such Reynolds numbers. Kravchenko and Moin [83] studied the effect of span wise domain length and showed that the drag coefficient (C_D) predicted can vary from 1.65 for a 2D simulation to 1.07 for a domain length of πD, as shown in Table 3-6.

Table 3-6. Effect of grid points in span-wise direction (N_z) and span-wise length (L_z) on simulated Strouhal number (St) and average drag coefficient (C_D) using LES [58]

Case	N_z	L_z	$\overline{C}_D$	St
1	1	0	1.65	0.230
2	4	$\pi D/2$	1.36	0.190
4	8	πD	1.38	0.193
3	24	$\pi D/2$	1.07	0.212
5	48	πD	1.04	0.210
6[a]	48	πD	1.07	0.206
Expt	···	···	0.99±0.05 (1)	0.215±0.005 (2), (3) 0.21±0.005 (4)

[a]Coarse grid in radial and circumferential directions.

1.1.1.8. Computational Model

To construct a computational model of canonical isothermal flow over a circular cylinder, a classical O-type grid, as shown in Figure 3-45, is employed. The mesh design in the present investigation is based on an analogous study performed by [56]. The computational domain has a radius of $50D$ and a span-wise extension of πD, which was identical to the previous work of [56]. The domain had slightly less than 3 million computational cells with 300 × 300 orthogonal grids in the cross-sectional plane and 24 cells in the span-wise direction. Grid points were clustered near the surface of the cylinder ($\Delta r/D \approx 10^{-3}$) with a mesh expansion factor of 1.025 in the radial direction. For the analyzed flow Reynolds number of 3900, the diameter of the cylinder (D) was fixed to unity (1 m) and the incoming flow velocity (U_∞) was set to 0.0589 m s^{-1}. Cyclic boundary conditions were used for the front and back faces in the span-wise direction.

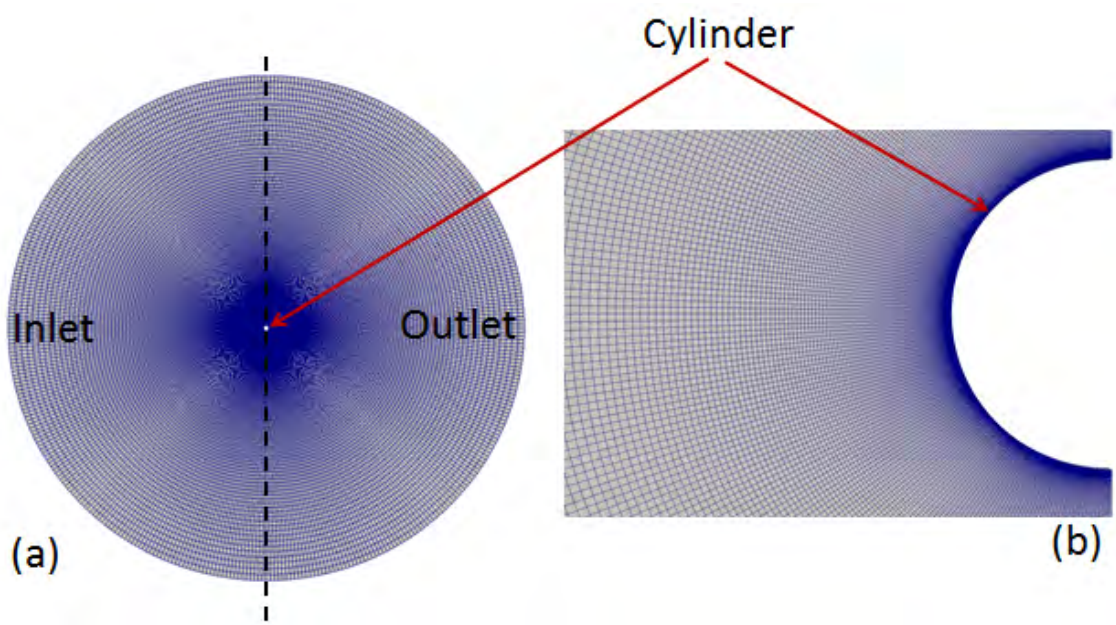

Figure 3-45. (a) The computational domain; and (b) Mesh near the surface of the cylinder

The sub-grid scale (SGS) model selected for the performed LES simulation was the dynamic local-averaged Smagorinsky model; the selection of the appropriate SGS model was based upon the findings presented for an isothermal and non-isothermal single jets. The LES simulation results were compared with the experimental measurements of [80] and [81] for flow characteristics in the near field wake behind the

cylinder while for the far field comparison, the measurements of [82] were used. The simulation was run for about 300 vortex shedding cycles while the time-averaging of the flow statistics was initiated after approximately 15 vortex shedding cycles.

1.1.1.9. Results and Discussion

Figure 3-46 shows the distribution of vorticity magnitude at different time instances during a single vortex shedding cycle. Based on the Strouhal number (St) observed in the experiments and cylinder dimension in the simulation setup, the time period of one shedding cycle (t_c) was about 80 seconds. Table 3-7 shows the minimum and maximum cell dimensional wall distance (y^+) near the cylinder wall during a single vortex shedding cycle. The maximum y^+ value never exceeds 0.32. Thus, the grid resolution in the viscous sublayer was adequate and no wall modeling was required.

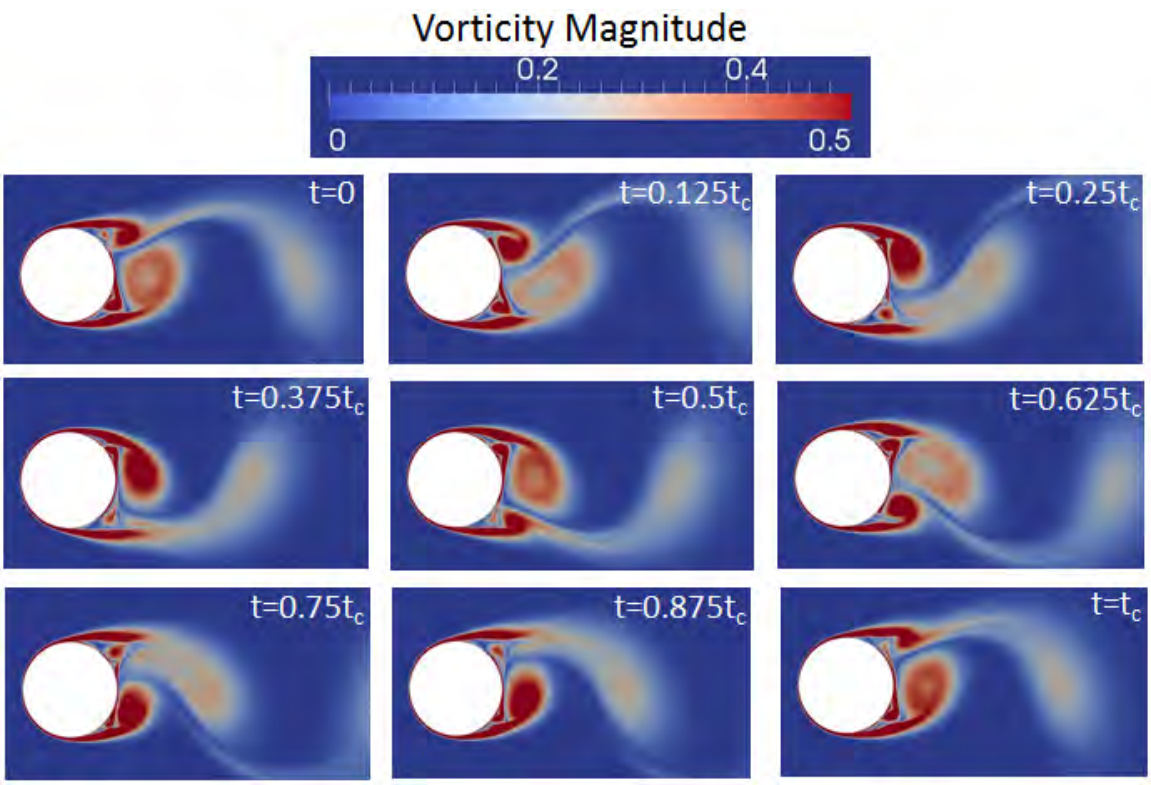

Figure 3-46. Contours of vorticity magnitude at different time instances during a single vortex shedding cycle

Table 3-7. Minimum and maximum y^+ near the cylinder wall during a single vortex shedding cycle

Time	Minimum	Maximum
0	0.0083	0.3052
0.125 tc	0.0103	0.3068
0.25 tc	0.0141	0.3177
0.375 tc	0.0105	0.3187
0.5 tc	0.0084	0.3092
0.625 tc	0.0092	0.3026
0.75 tc	0.0140	0.3154
0.875 tc	0.0078	0.3193
tc	0.0102	0.3124

Figure 3-47 shows a comparison of the stream-wise velocity (u) in the wake centerline simulated for the present case with published data from LES simulations and experimental measurements. The LES simulation of [56] with conventional Smagorinsky SGS model (LES-SMAG) and dynamic κ-equation eddy viscosity subgrid scale model (LES-TKE) is shown in the figure along with the LES simulation of [83] with a dynamic subgrid scale model. Lysenko et al. [56] obtained averaged turbulence statistics over 150 shedding cycles while [83], which is the closest to the data, obtained statistics over approximately 7 vortex shedding cycles. Franke and Frank [84] concluded that more than 40 vortex shedding periods are required to obtain converged mean flow statistics. The experiments of [81] collected data of about 60 vortex shedding cycles to obtain averaged turbulence statistics. Lysenko et al. [56] and [80] conducted measurements over 29 vortex shedding cycles. As pointed out by [56], the PIV data of [81] differed from those measured by [80], but were consistent with hot-wire anemometry (HWA) data of [82]. The LES-SMAG simulation of [56] would be the most appropriate LES simulation to compare with as time-averaged data over 150 vortex shedding cycles was presented. The present study's simulation results of mean stream-wise velocity compare well with the LES simulations of [56] with dynamic SGS model and the experiments of [81]. The current LES simulation only used 24 cells in the span-wise direction compared to 64 cells by [56].

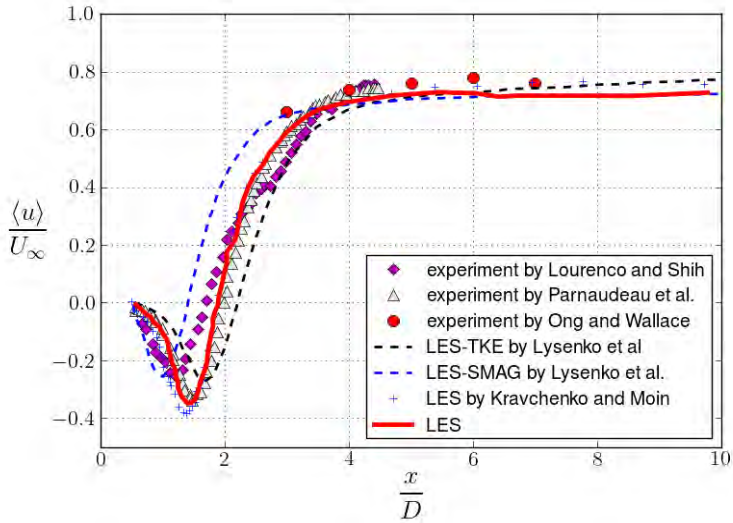

Figure 3-47. Comparison of mean stream-wise velocity in the wake centerline for isothermal flow over a circular cylinder at Re = 3900. x = D/2 is the surface of the cylinder.

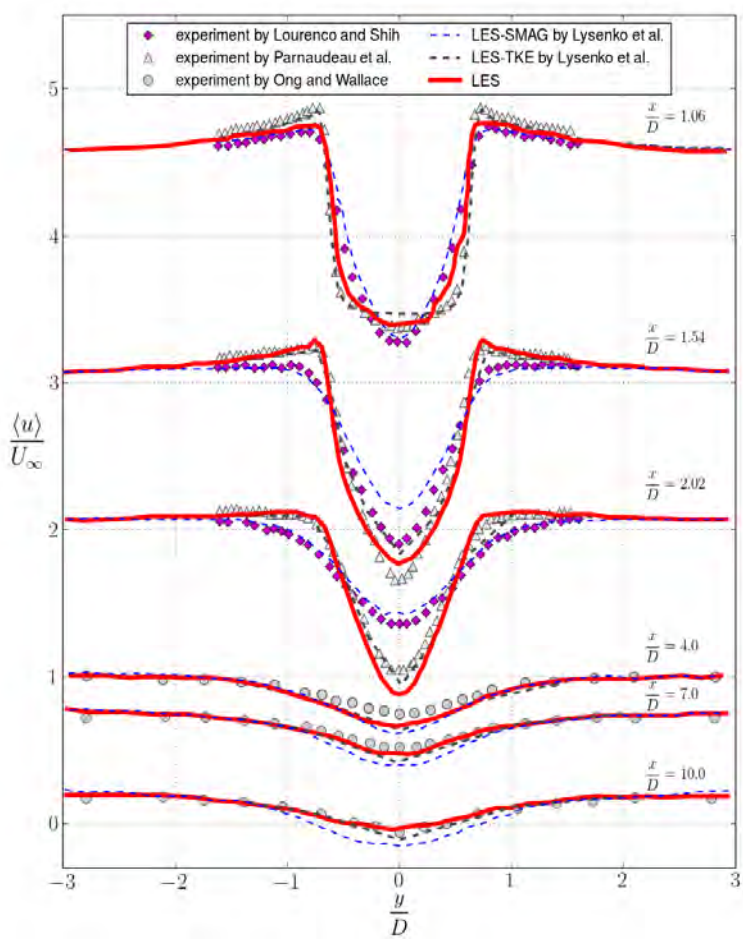

Figure 3-48. Comparison of mean stream-wise velocity at different locations in the wake of a circular cylinder at Re = 3900

Figure 3-47 and Figure 3-48 show the mean stream-wise and transverse velocities, respectively. The figures compare the statistics in between $1 \leq x/D \leq 10$ with the experiments of [80] and [81] at three different downstream locations in the very near wake (x/D = 1.06, 1.54, and 2.02) and with the experiments of [82] at downstream locations of x/D = 4.0, 7.0, and 10.0. The stream-wise velocity compared well with the measurements of [81] and [82], as well as the LES simulation of [56] with the dynamic SGS model. It is evident from the results of [56] that the conventional Smagorinsky SGS model is not appropriate for simulating the isothermal flow over a cylinder. Kravchenko and Moin [83] also stated that simulations with dynamic SGS model agree better with experimental data compared to the conventional Smagorinsky model. Some discrepancies are observed for transverse velocities at x/D of 1.06 between the present results and the simulations of [56] with a dynamic SGS model, which agreed well with the measurements of [81]. This is probably due to the use of only 24 cells in the span-wise direction for the current simulations compared to 64 cells used by [56]. Kravchenko and Moin [83] observed that number of cells in the span-wise direction can significantly influence the turbulence statistics close to the cylinder and its effect is seen to be less significant at locations further downstream.

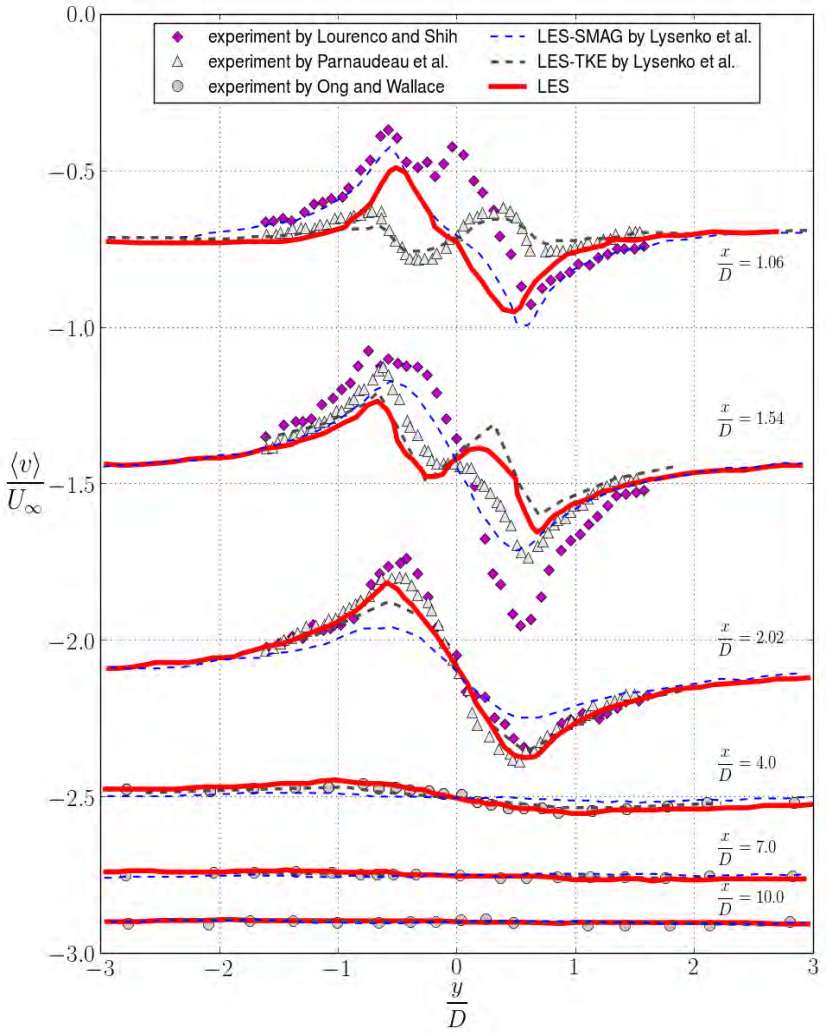

Figure 3-49. Mean transverse velocity at different locations in the wake of a circular cylinder at Re = 3900

The mean stream-wise and transverse velocity fluctuation at different downstream locations is shown in Figure 3-50 and Figure 3-51, respectively. As was seen for transverse velocity, the simulation results did not compare well with the experimental data measured by [81] at x/D of 1.06 and 1.58 (i.e. for locations very close to the cylinder). Even with 64 cells in the span-wise direction, Lysenko et al.'s simulation also showed similar comparison; the simulations generally under-predicted both the stream-wise and transverse velocity fluctuations at x/D locations of 1.06 and 1.58. However, for x/D locations of 2.02, 4.0, 7.0, and 10.0, the LES simulations compared well with experimental data. The Strouhal number (St)

and average drag coefficient (C_D) for the present study was found to be 0.193 and 1.38, respectively, and matched exactly with published results of [83] (refer to Table 3-6) with 24 cells in the span-wise direction.

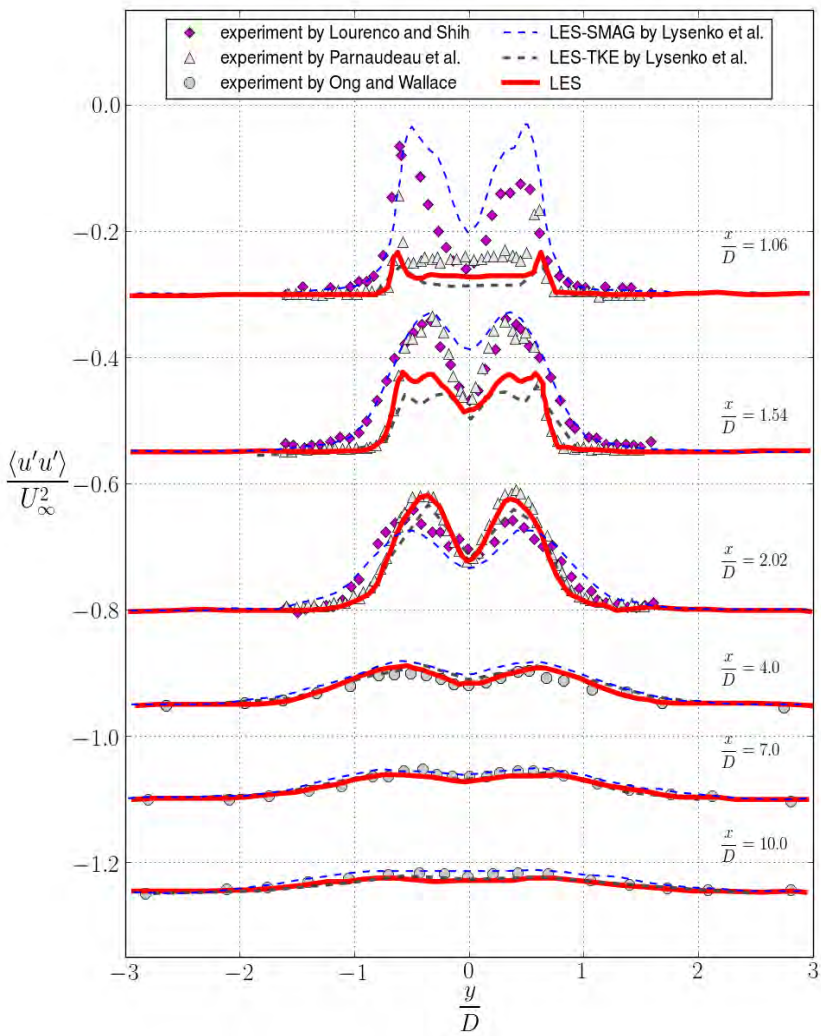

Figure 3-50. Stream-wise velocity fluctuations at different locations in the wake of a circular cylinder at Re = 3900

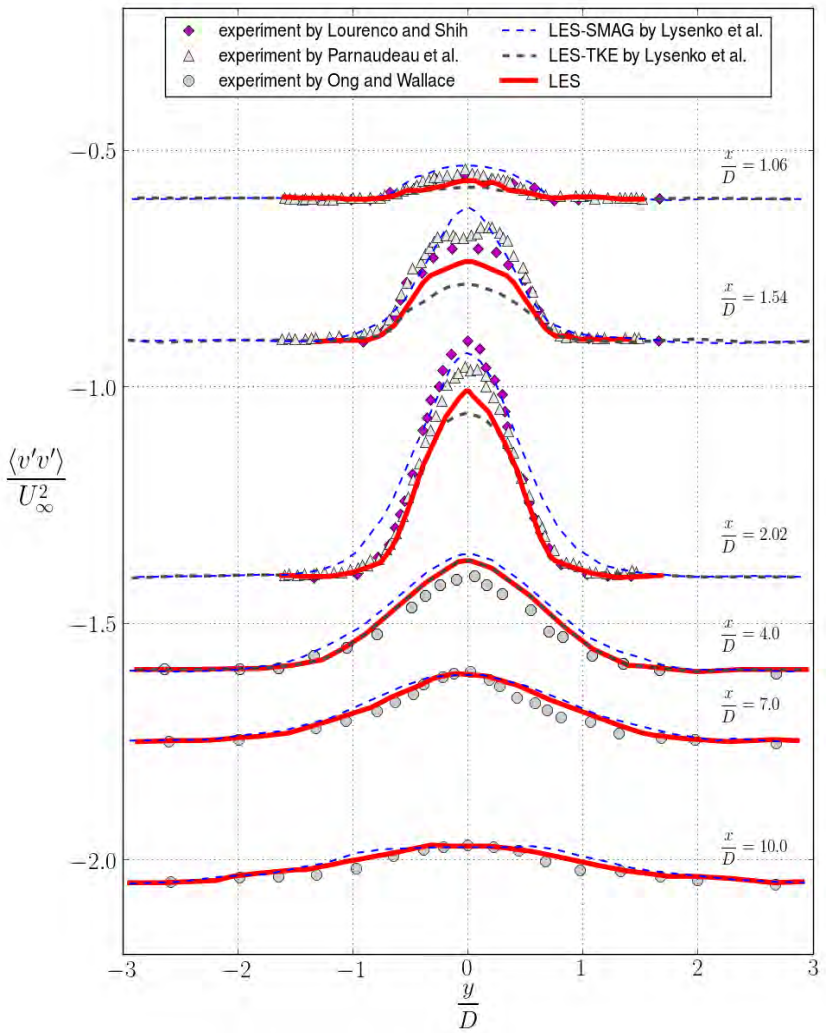

Figure 3-51. Transverse velocity fluctuations at different locations in the wake of a circular cylinder at Re = 3900

In general, CFD results from the open-source computational fluid dynamics package OpenFOAM compared soundly with well-known sets of experimental data and LES simulations for isothermal flow over a cylinder for Re = 3900. Also, isothermal LES jet simulation in the previous section compared remarkably well with benchmark experiment of HCG [51]. Since isothermal simulations compared extremely well with published work, the next effort will focus on exploring and analyzing flow past a non-isothermal cylinder.

3.5.2 Non-Isothermal Flow Over a Cylinder

To evaluate non-isothermal flow over a circular cylinder, the exact same O-type grid, which is shown in Figure 3-45, used for the isothermal flow investigation and by Lysenko et al. [56] is constructed. The computational domain has a radius of $50D$. The domain has a span-wise extension of πD, which was identical to that of [56]. The domain has slightly less than 3M computational cells with 24 cells in the span-wise direction. Grid points are clustered near the surface of the cylinder ($\Delta r/D \approx 10^{-3}$) with a grid expansion factor of 1.025 in the radial direction. Cyclic boundary conditions are used for the front and back faces in the span-wise direction. A non-reflective boundary condition is employed for the outlet condition to prevent numerical waves from coming back inside of the computational domain. Similar to the experimental set up, a constant wall temperature is used for the boundary condition. The temperature difference between the heated surface and incoming flow is fixed to 25 °C.

The SGS model selected for the LES simulation is the dynamic local-averaged Smagorinsky model based on the experience of model selection studies conducted for isothermal and non-isothermal jets. Compressible sets of Navier–Stokes equations are solved via OpenFOAM. Specifically, the PIMPLE version of PISO (Pressure Implicit with Splitting of Operators) algorithm is employed as an efficient method to solve the Navier-Stokes equations in unsteady problems. The PISO algorithm is a pressure-velocity calculation method. The simulation is run for about 300 vortex shedding cycles. Time-averaging of the flow statistics is started after approximately 15 vortex shedding cycles. Turbulence intensity of the incoming flow has also been matched to that reported from the experiment of [85], namely 0.5%.

1.1.1.10. Results and Discussion

Figure 3-52 portrays instantaneous vorticity magnitude contours in the near-wake of the cylinder at the three investigated Reynolds numbers. Even though the difference between Reynolds numbers is not very large, the structural change in the cylinder wake as the Reynolds number increases is visible with comparison of these contours. It can be seen that, as the Reynolds number increases, the location at which the separated shear layer becomes destabilized moves upstream. This is particularly noticeable when

comparing the result for Re = 7400 with those from the two lower Reynolds numbers. Large-scale vortex-shedding is observed at all three Reynolds numbers.

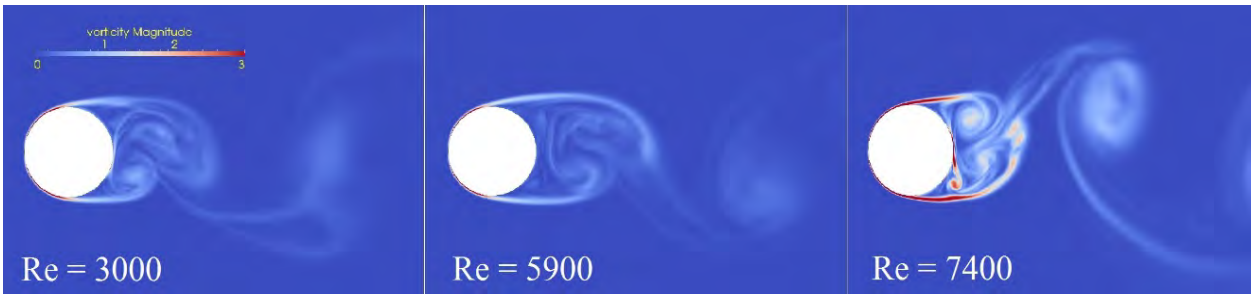

Figure 3-52. Contours of instantaneous vorticity magnitude in the near-wake for different Reynolds numbers

Instantaneous temperature fields are portrayed in Figure 3-53 in the near-wake region of the cylinder. These contour plots and Figure 3-52 exhibit that the instability leads to stronger turbulent mixing of momentum in the near-wake, which causes a drop in the size of the mean recirculation region. It is clear that the shear layer becomes unstable and mixing of momentum leads to the mixing of the scalar quantity (temperature), and as previously discussed, it causes a heat transfer enhancement.

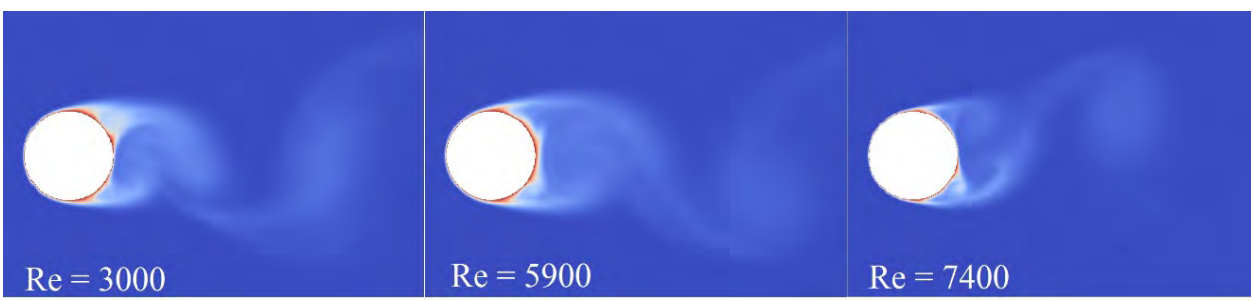

Figure 3-53. Contours of instantaneous temperature in the near-wake for different Reynolds numbers

The distribution of the time-averaged Nusselt number and its RMS value are key metrics to compare with experimental data. Figure 3-54 shows the results of this comparison and reveal excellent agreement for both quantities. The LES data accurately captures the laminar flow region for $\varphi < 80°$, where φ is the angle from the stagnation point of the cylinder. The average Nusselt number is highest at the stagnation point ($\varphi = 0°$) where the thermal boundary layer is thinnest, and then shows a decreasing trend

until φ is between 90 and 100°. The magnitude of the Nusselt number fluctuations up to this point is very small, both experimentally and as suggested by the LES data, further highlighting the fact that this region of flow can be classified as laminar. The increase in both average and fluctuating Nusselt numbers coincides with the flow fluctuations resulting from the separated shear. The magnitude of heat transfer increases and reaches a second peak at the rear stagnation point (φ = 180°). Although the average Nusselt number at the stagnation point is fairly independent of Reynolds number ($\overline{Nu}/Re^{0.5} \approx 1$ at φ = 0° for all three cases), this is clearly not case when considering behavior at the rear stagnation point. For comparison, the average Nusselt number at φ = 180° is approximately 0.2, 0.4, and 0.6 for Re = 3000, 5900, and 7400, respectively. Similarly, for the fluctuating Nusselt number, the stagnation point value is roughly the same for all three Reynolds numbers, and the rear value increases with Re. It is interesting to note that the value at φ = 180° is roughly 60-65% of the time-averaged Nusselt number. In other words, the Reynolds number dependence is the same for both the fluctuating and average Nusselt number trends. For a Re = 7400, the sharp upswing in heat transfer is not continuously monotonic. In other words, there is an intermediate peak reached around φ = 115°, after which a local minimum is reached quickly, followed by a subsequent increase in both the fluctuating and time-averaged Nusselt number profiles. This indicates that an additional reattachment point near the rear of the cylinder is first observed at Reynolds number around 7400. A fluctuating pressure distribution around a circular cylinder is known to have a local maximum at φ = 105°, at which point the reattached reverse flow separates. This maximum disappears below Re = 6000-8000, corresponding to the range for which the reattached flow disappears [85, 86]. Therefore, the LES model is capturing the important physics, not only of the flow, but for the expected thermal behavior as well.

Figure 3-55 shows time traces of the fluctuating Nusselt number at a Reynolds number of 5900 where Nakamura and Iragashi [85] reported similar data at the same Reynolds number. The data is collected at several azimuthal locations at the mid-span of cylinder. As can be seen at φ = 70°, the point is in the laminar region since fluctuations are small enough to be neglected. As φ is increased, both the flow features and heat transfer is affected by the instability of the separated shear layer and vortex shedding. As boundary

layer instability grows (150° < φ < 180°), the fluctuating Nusselt number become much larger. The same observation is made by Nakamura and Iragashi [85].

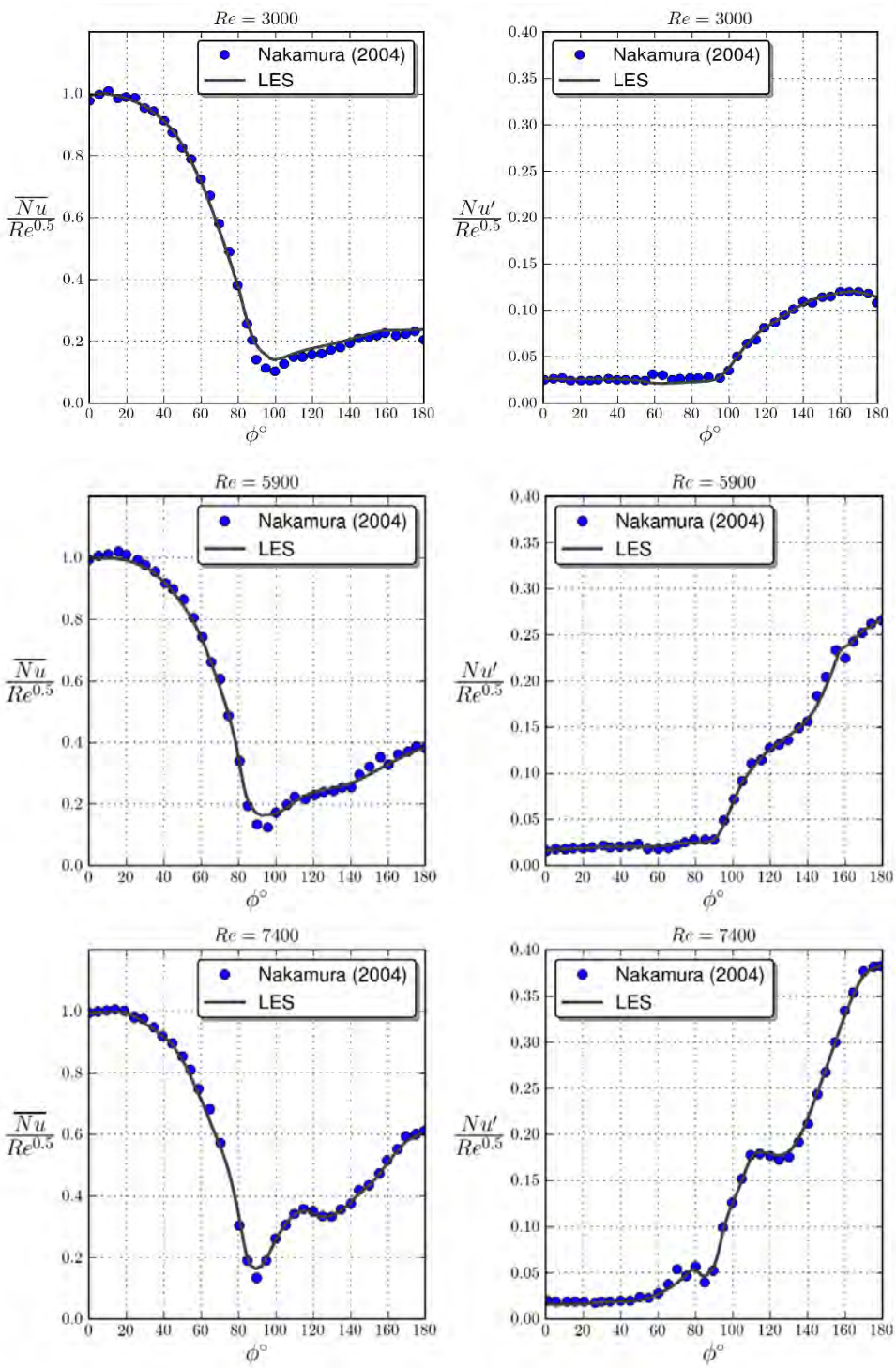

Figure 3-54. Time-averaged and RMS Nusselt number distributions around a circular cylinder for Reynolds number of 3000, 5900, and 7400.

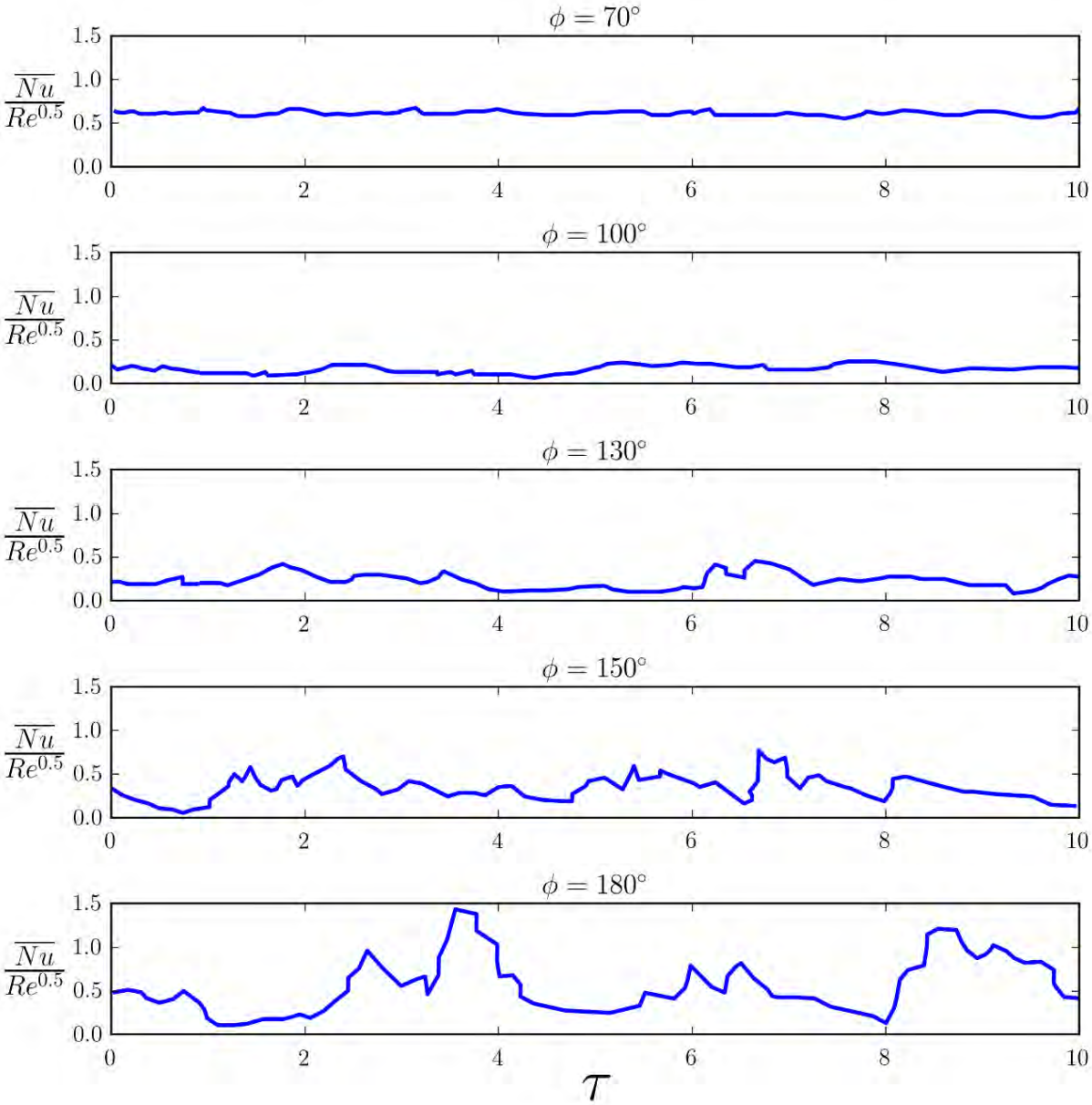

Figure 3-55. Time-histories of the instantaneous RMS Nusselt number for Re = 5900.

The LES of turbulent flow and heat transfer around a circular cylinder was conducted using OpenFOAM at three Reynolds numbers (Re = 3000, 5900, and 7400). From these results, it can be seen that the physics of the heat transfer are captured very faithfully. The heat transfer characteristics of the laminar boundary layer upstream of the separation point as well as the entire region behind the cylinder is accurately modeled. Excellent agreement is seen with the experimental data regarding time-averaged and

RMS Nusselt numbers. The sharp increase both in the mean Nusselt number and the RMS fluctuating Nusselt number is also reproduced with high fidelity. Strong correlation between the heat transfer characteristics and the underlying flow characteristics is also confirmed.

3.6 Large Eddy Simulations of Unit Cell

Before comparing against our experimental data, it is useful to take preliminary steps for a flow as complex as the unit cell. Therefore, a qualitative study is first conducted in this section. The three unit cell configurations are labeled as A, B, and C, corresponding to values initially anticiapated from our experimetnal facility. A one to one comparison of experimental and numerical data is conducted in section 3.7. To remove confusion, these direct comparison will make use of the labels presented in section 2.6, namely unit cell 1, 2, and 3. The current section will provide insight into the flow physics to help motivate experimental replication of the same scenario and identify locations where detailed measurements should be made in addition to providing a valuable understanding of the thermal hydraulics in the lower plenum of VHTR. To computationally mimic the scenario similar to the unit cell experimental facility, a cubic computational domain is chosen identical to the experimental test section. Based on experimental design, the post diameter is 1.25 in, with a plenum height of 8.56 in. The width of the computational domain is selected as 24 in, while all the jet diameters are 0.875 in. The computational domain is shown in Figure 3-56(a) for unit cell A and C and Figure 3-56(b) for unit cell B, a similar domain, but a 30° rotation to accommodate flow across an in-line tube bundle.

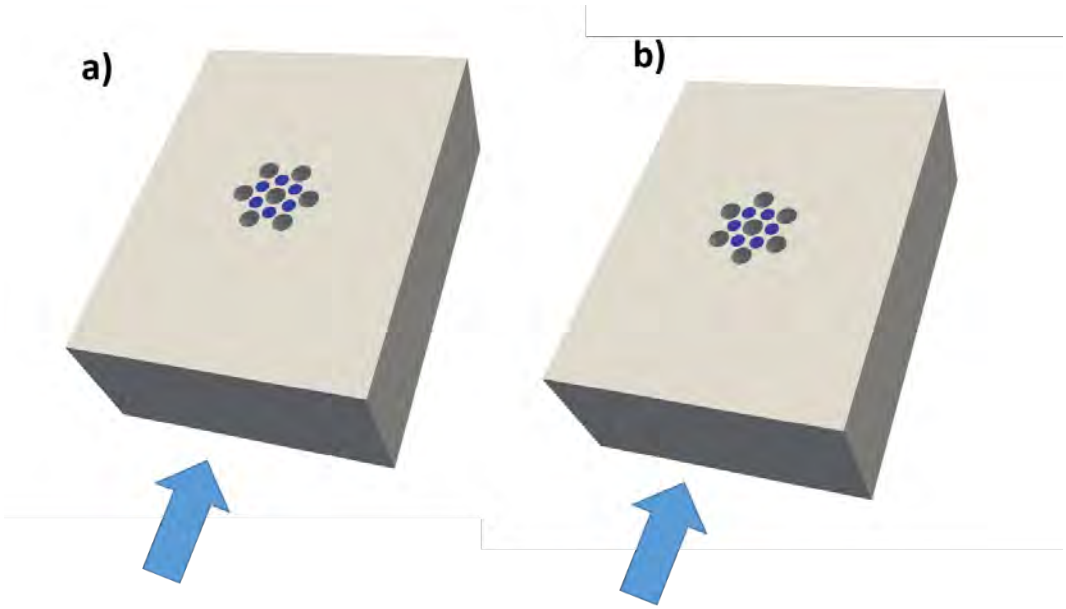

Figure 3-56. Computational unit cell domain for LES studying of lower plenum of the VHTR a) unit cells A and C, and b) unit cell B

3.6.1 Temperature and Velocity Specification

The three cases are illustrated in Figure 3-57 where the posts are identified by their position with respect to the center post. As noted previously for cases A and C, the posts are oriented in a staggered fashion considering the direction of the crossflow (blue arrow pointing upwards). For both of these cases, there is a post directly to the left and one to the right of the center cylinder labeled W and E, respectively. The remaining four posts are located at off normal positions, and therefore labeled with NW, NE, SW, and SE. For case B, the unit cell orientation is an in-line flow configuration, with posts directly downstream and upstream of the center cylinder labeled with N and S, respectively. It should be noted that although case B includes four posts with NW, NE, SW, and SE labels, they are not in the exact same location as those with identical labels in cases A and C. These labels only serve as a reference to the reader for the nominal position of each post with respect to the center of the unit cell. Also shown in Figure 3-57 are the six jets located between the posts. They are similarly labeled (e.g., NW), and the same significance should be interpreted here as was specified for the posts. The actual temperatures of the jets are also included in the figure. For cases A and C, two unique temperatures exist, while case B accommodates three unique temperature values. Notice for case A, the high temperatures are those closest to the approaching crossflow,

while for case C the opposite is true. For these cases as well as case B, the pattern of temperatures is chosen to qualitatively reflect expected conditions in the VHTR, assuming a Gaussian distribution of temperatures within the core. The actual magnitude of the temperatures as well as the velocities (reported in a later section) are selected based on initial experiments run in these same configurations.

The conditions for each case are shown in Figure 3-57 and Table 3-8. These numbers were estimated from a scaling analysis after conducted a full scale RANS of the entire VHTR lower plenum previously discussed (see Section 3.1). Case A, among all three cases, has the highest crossflow of 24.33 m/s, and each of its jets has an identical velocity of one-quarter of the crossflow velocity. As depicted in Figure 3-57, two different temperatures are assigned for the jets. The jets closer to the crossflow have 40 K higher temperature than those far from inlet of the domain. On the other hand, case B shows more thermal variation with three different jet temperatures, where a maximum of 25 K temperature difference exists (intermediate temperature is halfway between minimum and maximum temperatures). All jets in case B have a velocity of 5.88 m/s which is half of the magnitude velocity of the crossflow. Case C has an equal crossflow and jet velocity of 8.82 m/s and a maximum temperature difference of 20 K between jets. As previously noted for case C, the jets are oriented with higher temperatures located closer to the outlet as can be seen in Figure 3-57.

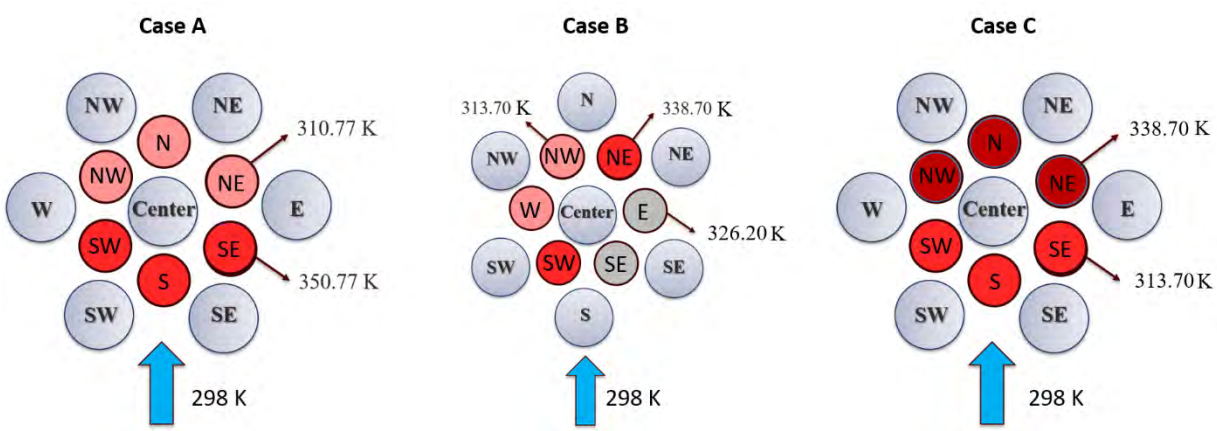

Figure 3-57. Jets and posts identification and jet temperature specifications for each case

Table 3-8. Jets and Crossflow velocity and temperature specification for each case

	Crossflow Velocity (m/s)	Jets Velocity (m/s)	**Jets Temperature (K)** (ambient T= 298 K)					
			SW	**S**	**SE**	**NW**	**N**	**NE**
Case A	24.33	6.083	350.77	350.77	350.77	310.77	310.77	310.77
Case C	8.82	8.82	313.70	313.70	313.70	338.70	338.70	338.70
Case B	11.76	5.88	**SW**	**SE**	**E**	**NE**	**NW**	**W**
			338.70	326.20	326.20	338.70	313.70	313.70

3.6.2 Mesh Configuration

Due to its complex geometry, the most challenging part of the LES study of unit cells is the mesh. Based on our experience of previous studies, it is very crucial for LES to keep the mesh as structural as possible. Also, from jet studies, we learned that LES is very sensitive to mesh expansion in the jet direction and that the size of the mesh particularly near the inlet of the jets is significant. Similarly, mesh around the post and inside of the jets (jet elements) should be fine enough to capture the physic of the problem correctly. Likewise, close to the wall, mesh size should again be fine enough to eliminate any need for wall modeling. Addressing those factors altogether requires a detailed effort to ensure that the number of elements meets the needs of the flow physics, but is also computationally reasonable.

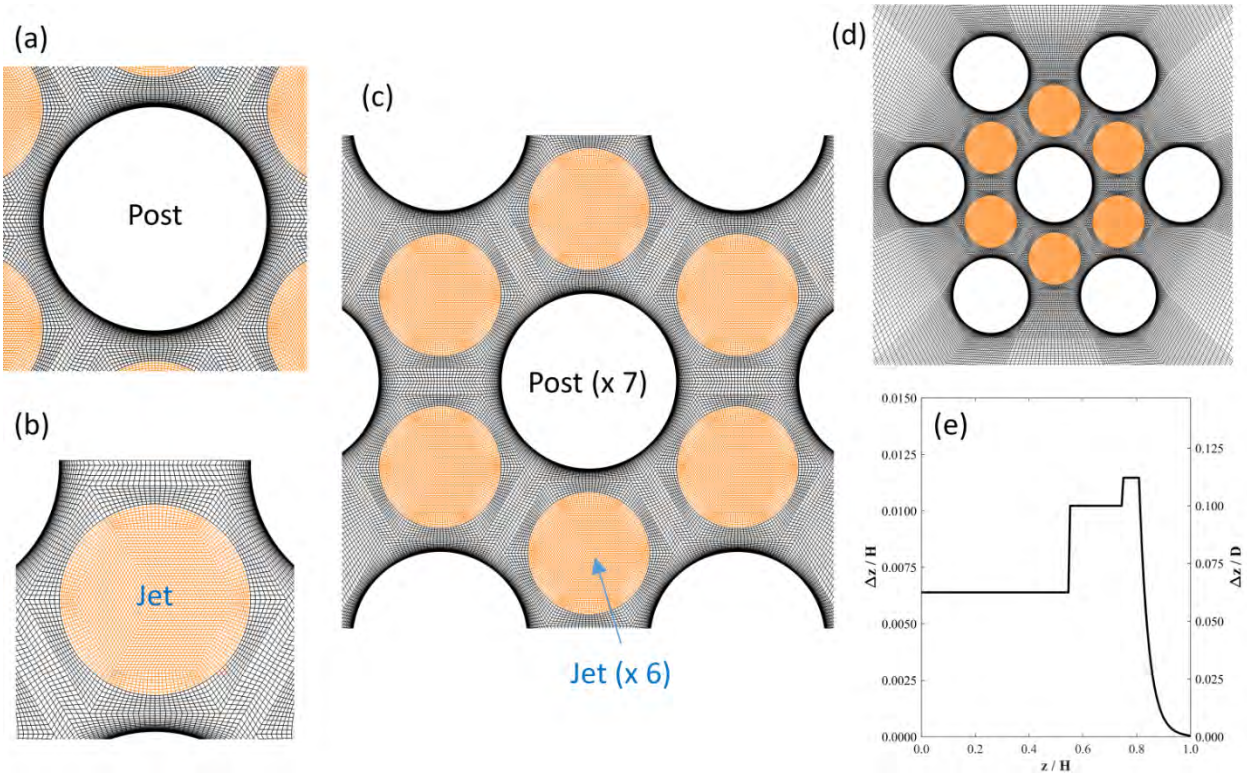

Figure 3-58. Unit cell mesh configuration

The mesh used in these studies is shown in Figure 3-58. The mesh design is initiated with flow around the cylinders in mind (see Figure 3-58(a)), where the azimuthal divisions are determined based on mesh requirements for turbulent flow past a circular cylinder. Well accepted criteria for this type of flow are outlined in a few seminal LES studies on the topic [56, 83] which suggest 200 azimuthal divisions is an adequate in capturing the flow physics for a post Reynolds numbers of 10^4. This number then divides all the jets in the same number of the azimuthal divisions which is a very safe number based on LES studies of jets [52]. Similar to many LES jet studies, a hexagon shape set of uniform grids is located inside of the center of each jet to keep the size of the mesh inside of the jet nearly equal (see Figure 3-58(b)) throughout the jet region. The mesh around each post and inside each jet is then stitched together to define the complete mesh inside the unit cell (see Figure 3-58(c)). This is then extended to domain inlet and outlet, as shown in Figure 3-58(d). For the z-direction (perpendicular to the cross flow), the size is a function of the z-location, the dependence of which is shown in Figure 3-58(e). A uniform mesh is employed from the jet inlet (z/H =

0) to approximately z/H = 0.55 (or approximately 5.5 jet diameters). This enables the energy of the jet flow to be adequately resolved in what would normally be considered the potential core of the jet when no cross flow existed. The size of the cells then are stepped up twice and then become smaller near the bottom wall (z/H = 1.0) of the domain in order to capture the turbulent boundary layer at that bottom surface. This results in a total of 14,817,600 cells.

3.6.3 LES Specification

Based on non-isothermal LES of flow over a cylinder and jet, the compressible solver implemented in OpenFOAM is used for the simulations of the unit cells. This transient compressible solver is suitable for the current study as the flow field was expected to be both density variable due to high thermal variation and highly turbulent because of the high crossflow velocity and jet Reynolds numbers. A flexible pimple (PISO-SIMPLE) algorithm is adopted to solve the coupled equations of velocity and pressure. This solver inherits both the Semi-Implicit Method for Pressure-Linked Equations (SIMPLE) algorithm and the Pressure Implicit Splitting Operator (PISO) algorithm. SIMPLE allows coupling the Navier-Stokes equations with an iterative procedure, while in the PIMPLE algorithm outer correctors are the iterations, and once converged will move on to the next time step until the solution is complete. Better stability is obtained from PIMPLE over PISO for this reason (see [87] or [88] for more details). The solver allows application of a non-reflective boundary condition at the outlet. This is a vital tool to avoid any numerical waves coming into the domain at this boundary, which could be caused by the massive amount of flow transporting through the outlet and also because of the large area of the outlet itself. Similar to two non-isothermal LES studies, the local dynamic Smagorinsky SGS model is applied [89]. Also, all posts are assumed to be perfectly insulated. The wall boundary conditions used for top, bottom and side walls as well as for all the posts. Adjustable time stepping with a maximum Courant number of 0.4 is used for the simulations. Turbulnce intensity for the inlet conditions of the jets as well as the crossflow are 0.001 which is identical to our inilat experminlat study. The time averaging procedure started when the crossflow passed seven times through the computational domain, at which point all the second order statistics including

variance of temperature fluctuations remained constant. The time averaging ends after over fifty times of crossflow passed through the domain

3.6.4 Results and Discussion

Due to the differences in the thermal-fluid character of each case, a broad range of flow features would be expected. The penetration distance of the jets into the computational domain varies between each case as can be seen clearly in Figure 3-59. The bottom row of the figure shows the time-averaged temperature contours which visibly indicates the effect of the jet penetration into the domain. The top row in the figure also displays the instantaneous temperature which helps to visualize the thermal mixing for each case. These results reveal case A having the shortest jet penetration, which is not surprising since it has the highest crossflow velocity. Because three different jet temperatures exist for case B, more thermal variations are observed between the posts when compared with case A and C. On the other hand, for case C, the location of the hotter jets are far from the inlet and the crossflow is slower. Therefore the impact of the jets is more noticeable in downstream locations closer to the outlet. In cases A and B, where shorter jet penetration is observed (less than half of the height of the domain), the crossflow properties are dominant for most of the domain, while for case C, a smaller region of the domain near the bottom is predominantly crossflow influenced.

The mesh quality can be a very sensitive factor in any LES study. To address this concern, the yPlus values for each wall are carefully measured. All side walls and posts have yPlus values less than one, which highlights the quality of the mesh without the need for any wall modeling. Among the wall boundaries, the bottom wall of the domain is the only one that contains yPlus values higher than unity, but the affected area is very small in comparison to the surface area within the entire computational domain. The mesh is considered acceptable since most of the thermal mixing is anticipated away from this bottom surface. As the strength of the crossflow is increased in relation to the jet velocity, the mixing will occur even closer to the jet inlets (further away from the bottom surface). As previously noted, the surfaces in the mixing region all contain the surface elements with yPlus well below unity.

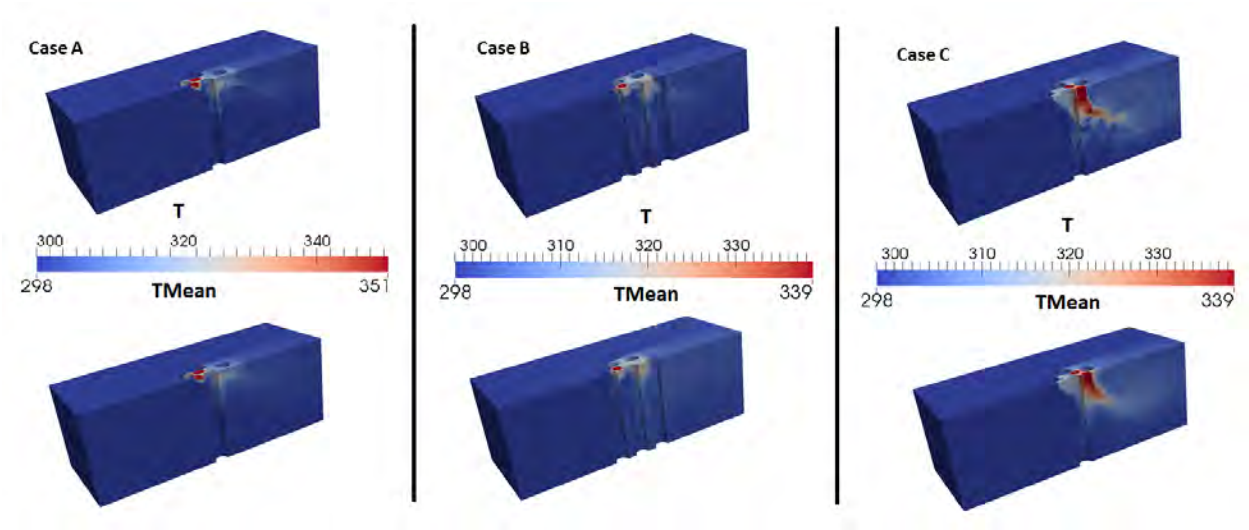

Figure 3-59. Jet penetration for each case

Figure 3-60 shows the time-averaged distribution of surface temperatures for all posts in case A. In the bottom left corner of the figure, a 3D view of these posts is provided, where the blue arrow shows the crossflow direction. The surface temperature distributions are unwrapped circumferentially and provided as well. In the top right of this figure, the azimuthal definition is illustrated where 0° is located in the wake region of each cylindrical post. From these results, some interesting behavior can be seen. As expected, close to the stagnation point of $\theta = 180°$ (two side edges of each plot in Figure 3-60) for Posts W, E, SW, and SE, crossflow property is dominant, and all the temperature values are very close to the ambient temperature of the crossflow along the entire length of the posts. The only posts that get affected by hot jets at their respective stagnation points are NW and NE posts (and to a lesser extent, the center post) at small locations near the jet inlets to the domain (top corners of these plots). However, the location of maximum temperature for each post does not occur at stagnation, but rather in the wake region of the flow. This is not surprising for the SW and SE posts where elevated temperatures are only introduced in their vicinity by jets located in the actual wake region. But this is also true for the center post, despite the fact that higher temperatures are introduced from the jets upstream (350.77 K) versus the downstream (310.77 K) jets. The location of the maximum temperature on each post suggests that because the crossflow velocity

is so high, the flow originating from the jets is immediately transported to the wake region of the posts, where a low pressure zone would allow the high temperature flow to have some residence time near a solid surface before being transported away downstream.

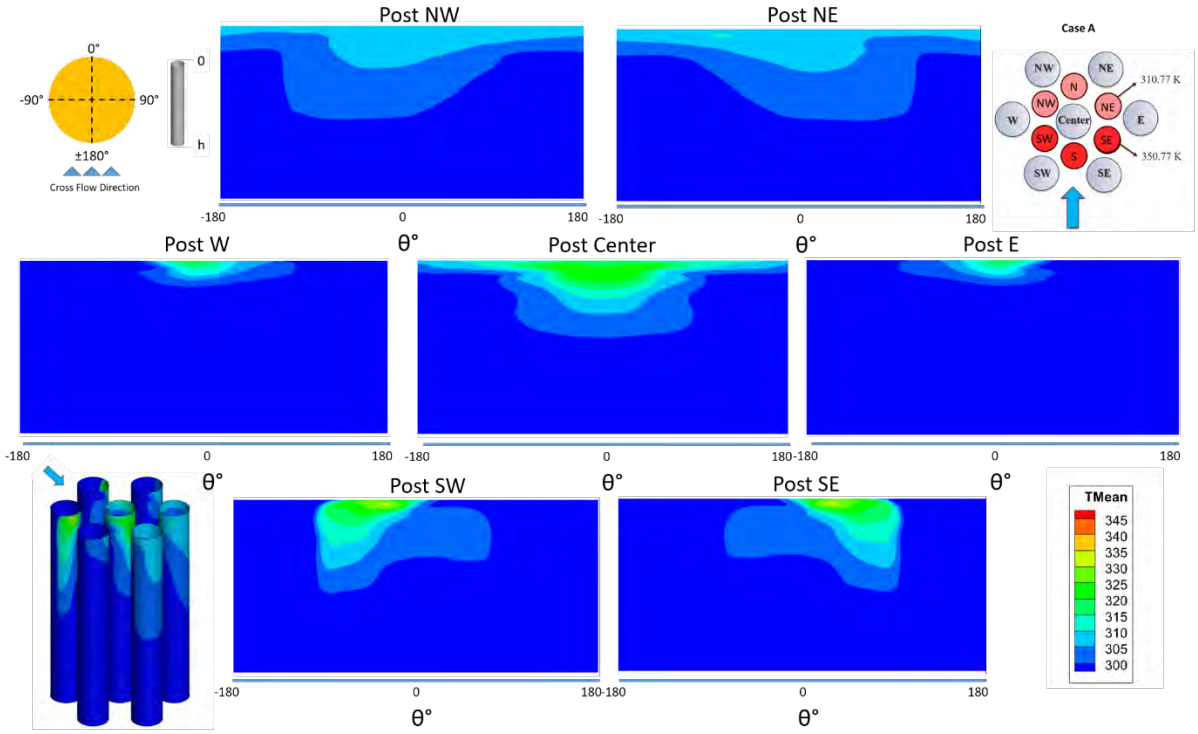

Figure 3-60. Flattened time-averaged temperature distribution on posts for case A. The vertical axis for all plots is the z-direction with z = 0 (jet inlets) at the top.

This behavior can more easily been seen by taking line traces through the contours of Figure 3-60. This is done for three heights of Z = h/4, h/2, and 3h/4 and shown in Figure 3-61 for each of the seven posts. The temperature distribution for Z = h/4 is symmetric for the center post and biased away from the center for each of the six posts around the circumference of the unit cell. This asymmetric skew is heavier for the SW and SE posts, but still very noticeable for NW and NE posts. Due to the strong crossflow, significant temperature signatures are not present for Z = h/2 and 3h/4, and distributions take on the value of the incoming flow from upstream. It is also worth discussing the temperature fluctuations at the surface since they can indicate regions with high potential for thermal stresses. The variance of the temperatures <T'T'>

is shown in Figure 3-62 for the same three line traces. Similar to the patterns for temperature magnitude, the location of the maximum temperature fluctuations is also in the wake region of each cylinder. The strong influence of the crossflow is revealed in the fluctuation signature in the same fashion as the average temperatures, namely that even halfway down the posts, the temperature signal is primarily that of the crossflow temperature, whose variance is zero. Not surprisingly, the posts where the fluctuations are smallest (E and W) are the same posts where the average temperature contours are lowest. The wake region of the center post is the location where mixing is most aggressive with $\langle T'T' \rangle$ as high as 14 K^2 (T_{rms} = 3.7 K), but on this post, there exists two peaks in the distribution for the temperature variance located at $\theta = \pm 40°$, with a local minimum at $\theta = 0°$, as opposed to a single peak for the average profile as seen in Figure 3-61. It is also worth noting that although the center post in Figure 3-62 has the maximum value for variance, the maximum average temperature (see Figure 3-61) is located on both posts SW and SE. For reference, the variance on those posts only reaches 6 K^2 (T_{rms} = 2.4 K). The maximum average temperature on post SW and SE are approximately located at $\theta = -80°$ and +80°, respectively, whereas the peak locations of the variance on the same posts are shifted by almost 30° toward the wake region in each case. The SW and SE posts also reveal a pattern consistent with the two peak behavior of the center post, although their peak locations are closer together when compared to those from the center post. It is worth noting that the region of non-zero variance is nearly identical to that where the average temperatures are still above the crossflow temperature of 298 K. This region is approximately between -100° and 100° for the center post, while it is between -75° and 100° and -100° and 75° for the SE and SW posts, respectively.

For the NW and NE posts (furthest downstream posts), the temperature variance resembles a low, nearly constant signal. Multiple peaks technically exist, but the variance is roughly 2 K^2 (T_{rms} = 1.4 K) for nearly 70% of the circumference. This suggests the thermal mixing has become more uniform at these locations, which is not surprising given the fact that the variance is expected to be well distributed further downstream and eventually tend to zero once the new intermediate, and fully mixed, temperature has been reached.

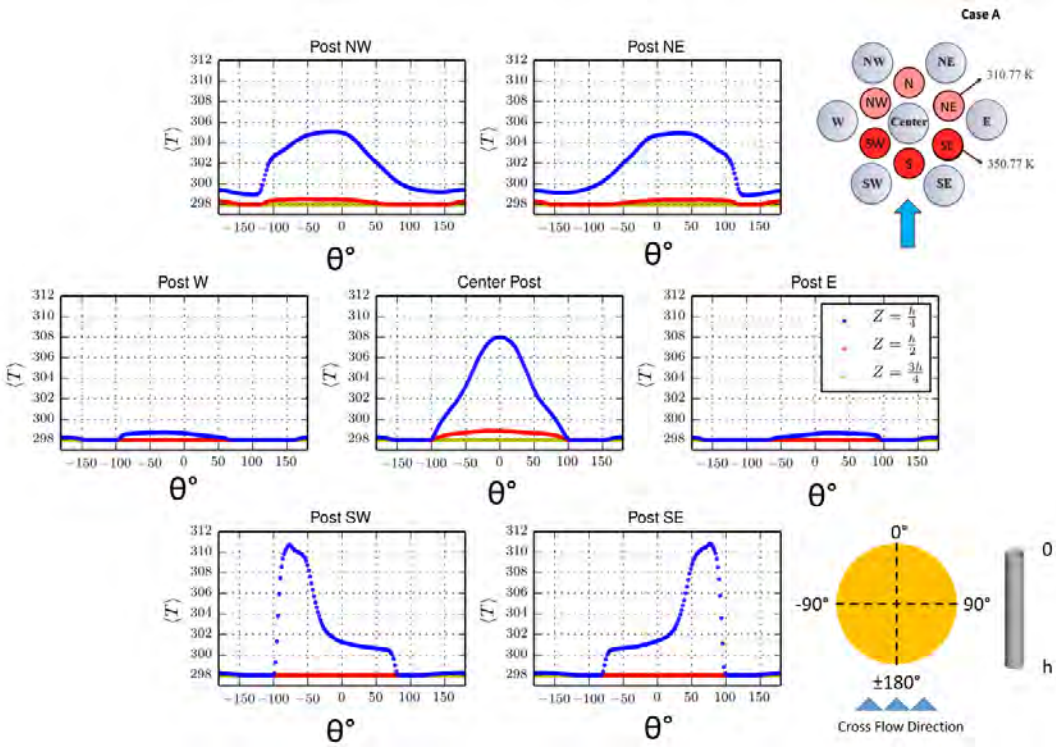

Figure 3-61. The time-averaged temperature of posts for different height locations - case A

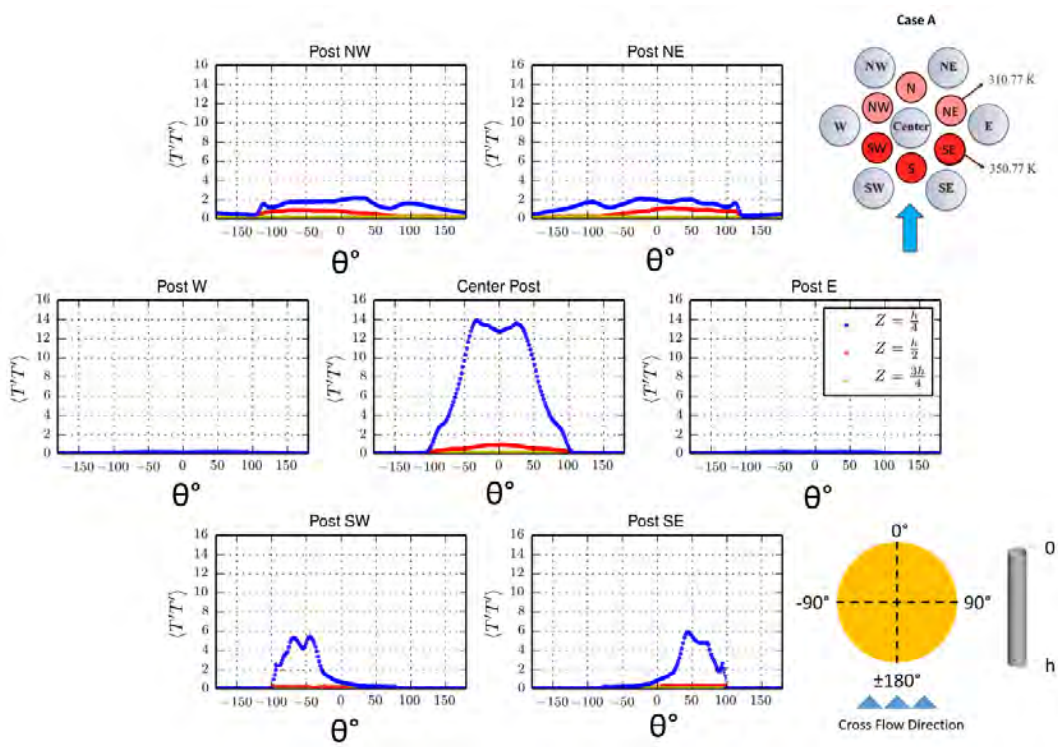

Figure 3-62. The time-averaged square of temperature fluctuations of posts for different height locations - case A

With the purpose of clarifying the effect of the jets, stream tracers of the NW jet are shown in Figure 3-63 from two different views. This jet penetrates downward shortly before being swept away by the high crossflow velocity; then it divides in three directions. The significant part of it travels along the east side of the NW post. Another portion travels backward toward the W post due to the negative velocity in the wake region of that post. And finally, a small part of the jet travels around the post along its west side. This is somewhat surprising based on the result from Figure 3-61 which shows a NW post temperature contour skewed toward the side where only a small portion of the NW jet apparently travels. The reason for this is the fact that the contour is at a location of h/4. The majority of the hot flow from the NW jet does indeed travel along the east side of the NW post, but then continues to wrap around the post as the Z direction is increased. By the time a location of Z = h/4 is reached, the peak temperature is skewed to the west side instead of the east.

Stream tracers for jets SW and S are shown on the right and left side of Figure 3-64, respectively. It should be noted that both of these jets are hotter than the NW jet. For the SW jet, the major portion travels toward the NW post, but as the jet travels in that direction, it has a downward velocity too. This trace can be seen in Figure 3-60 and Figure 3-61 for post NW close to the top wall producing a higher temperature at the stagnation point of this post in comparison to other posts (except post NE which is a twin post of NW with similar physics). Also, Figure 3-64 clearly shows how jet S divides in all direction, and the hot flow issuing from this jet influences almost all the posts around it.

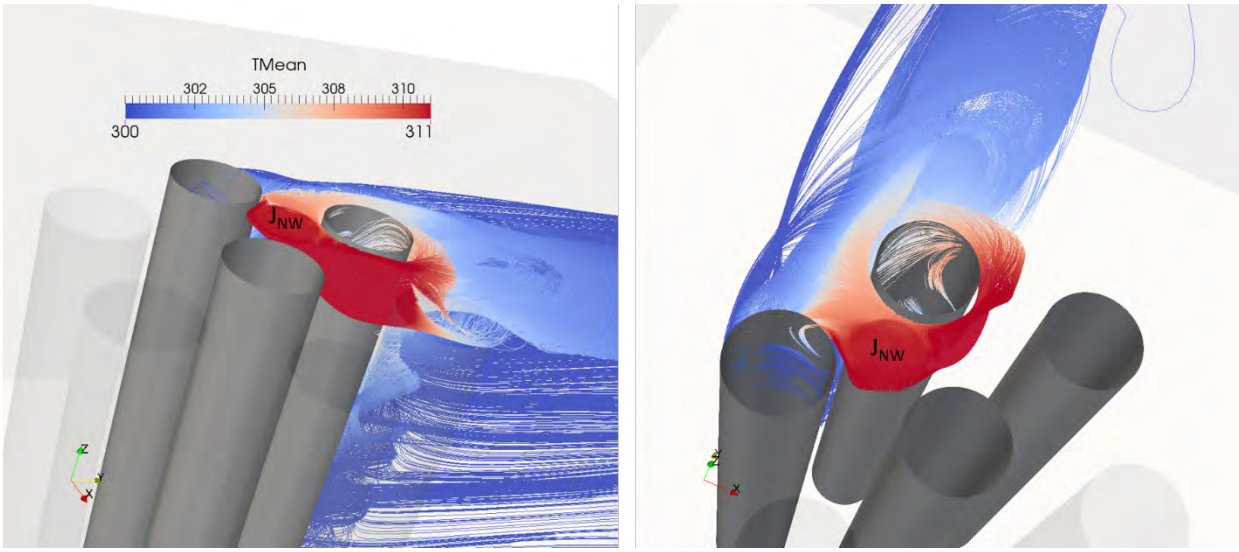

Figure 3-63. Stream tracer of jet NW for case A

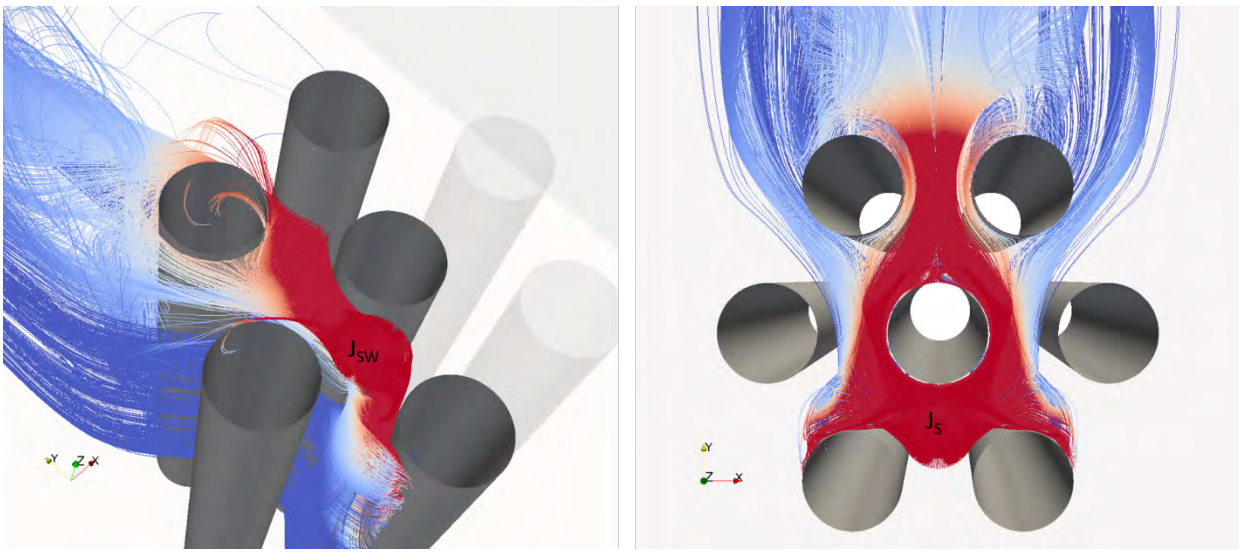

Figure 3-64. Stream tracer of jet SW and S for case A (the colorbar in Figure 3-63 also applied here).

For case B, due to the non-symmetrical jet inlet temperatures, significantly different thermal distributions are realized and shown in Figure 3-65, Figure 3-66, and Figure 3-67 (analogous to Figure 3-60, Figure 3-61, and Figure 3-62). Even though the jet temperatures are not arranged symmetrically as for case A and C, the average temperature on all posts show a near-symmetrical pattern in Figure 3-66. This is coming from the fact that the jet velocities are equal. The center post also shows nearly a symmetrical pattern with a peak leaning toward the east side which is due to the direct effect of the very hot NE jet. Post

NE and NW are qualitatively similar in that the distributions are similar (a nearly mirror image of each other), but the peak temperatures are different. This is most easily seen in the line traces of Figure 3-66. For the NE post, the peak for the h/4 curve is located at 10° and this peak location moves eastward as the line trace of interest is selected closer to the bottom plate. Similar patterns can be seen in Figure 3-66 for the NW post as the peak is found to move westward starting around 10° and finally at 40° for 3h/4. Comparing posts SE and SW, similar quantitative trends are again observed (magnitude of mean temperature is different).

Figure 3-67 displays the temperature variance in all posts, and reveals that at the three heights shown, the fluctuation magnitudes are of the same order. Also, unlike unit cell A, the temperature fluctuations do not quickly transition to zero. The maximum fluctuations for the center post and posts NW, SW and SE are actually on the 3h/4 curve (furthest away from the jet inlets). For the S post, the middle height of h/2 has the highest temperature fluctuations, while the NE post reveal behavior more consistent with case A where its highest fluctuations occur at the h/4 trace. For the N post, the fluctuation profile remains more or less unchanged between the h/4 and 3h/4 curves. Since the crossflow velocity is lower for case B compared to case A, the thermal mixing region is extended not only in terms of the jet penetration as previously noted, but also with respect to the temperature fluctuations themselves. Not only do they remain non-zero across more surface area of the posts, the magnitude is also higher for case B (peaks shown for each post in Figure 3-67 are between 15 and 20 K^2).

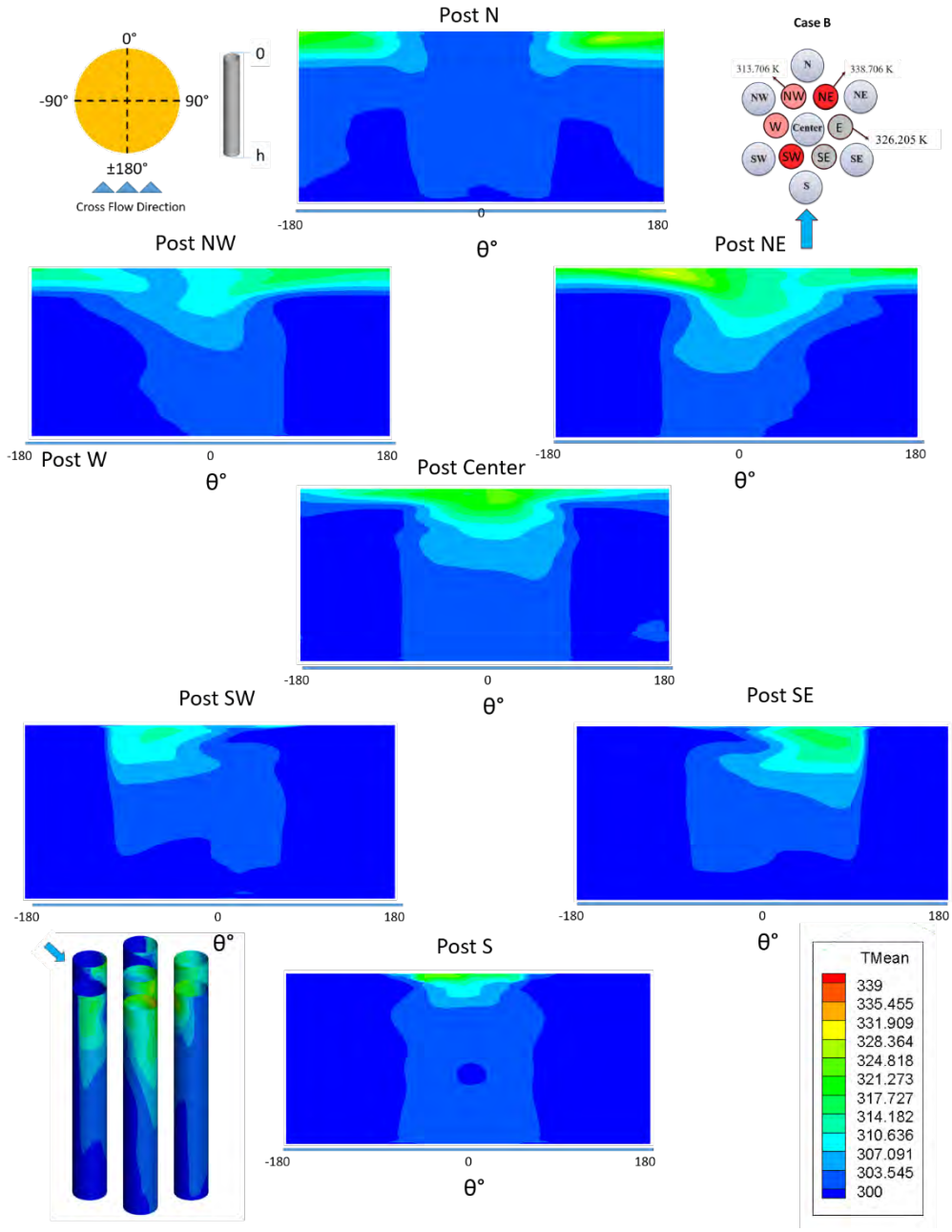

Figure 3-65. Flattened posts temperature distributions for case B. The vertical axis for all plots is the z-direction with z = 0 (jet inlets) at the top.

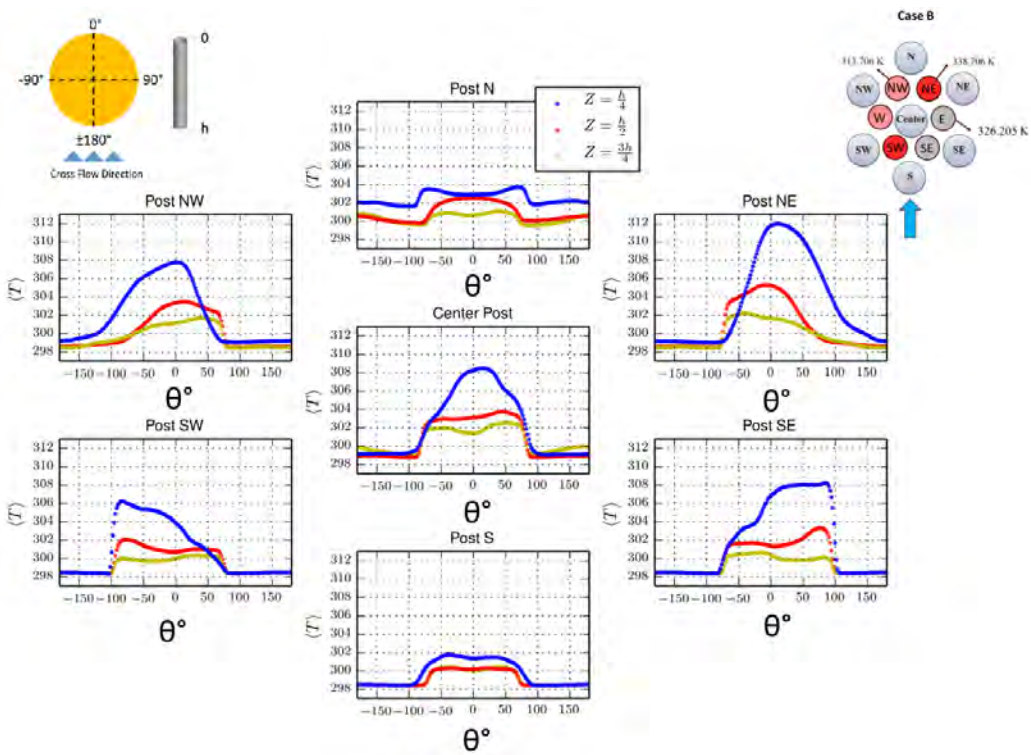

Figure 3-66. The time-averaged temperature of posts for different height locations - case B

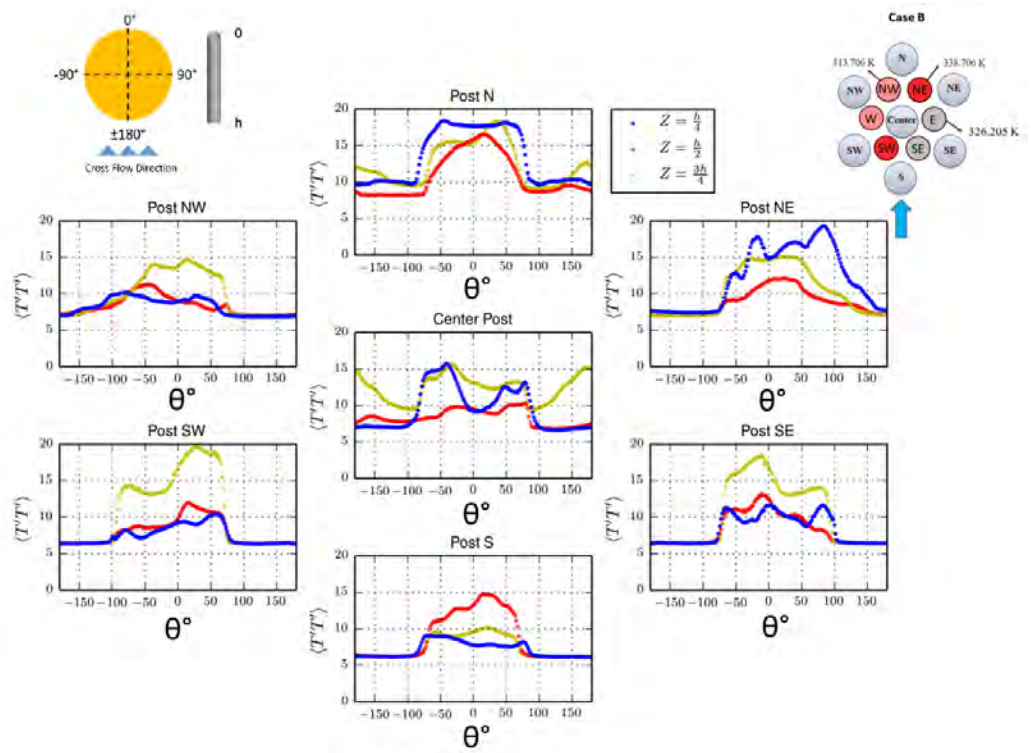

Figure 3-67. The time-averaged square of temperature fluctuations of posts for different height locations - case B

In case C, since the velocity ratio of crossflow to the jet is smaller compared to cases A and B, all the jets penetrate further into the domain and also have a chance to hit directly into the posts in some regions. As can be seen in Figure 3-68, the thermal signatures for some posts are non-trivial even past the halfway point of the domain, which is not seen in cases A and B where these thermal signatures are limited to the upper half of the posts. For the center post, there even appears to be a band near the top of the domain starting at the stagnation point and wrapping around the post, where the temperatures are higher than the crossflow temperature. There are many features in common between case A and case C. First, the center post reveals a symmetrical temperature distribution, and the remaining posts around the circumference of the unit cell show symmetry about the center post (i.e., post E is a mirror image of post W, NE is a mirror image of NW, and SE is a mirror image of SW). It is also worth noting that peak temperatures are again found in the wake region of the cylinders. But as this was consistent for all posts in case A, there are two exceptions for case C, namely the NE and NW posts. In these two instances, the maximum temperature is found in the stagnation region, while the wake region experiences only slightly elevated temperatures. This suggests that the reduction in crossflow velocity significantly affects the temperatures on the post surfaces, and for the furthest downstream posts, the hot jets are not pulled around to the wake region as is seen for all posts in case A and for the other five posts in case C. This is likely dictated by a combination of increased jet penetration as well as different approaching flow conditions (i.e., incoming flow to the NE and NW jets is significantly different compared to that seen in case A.

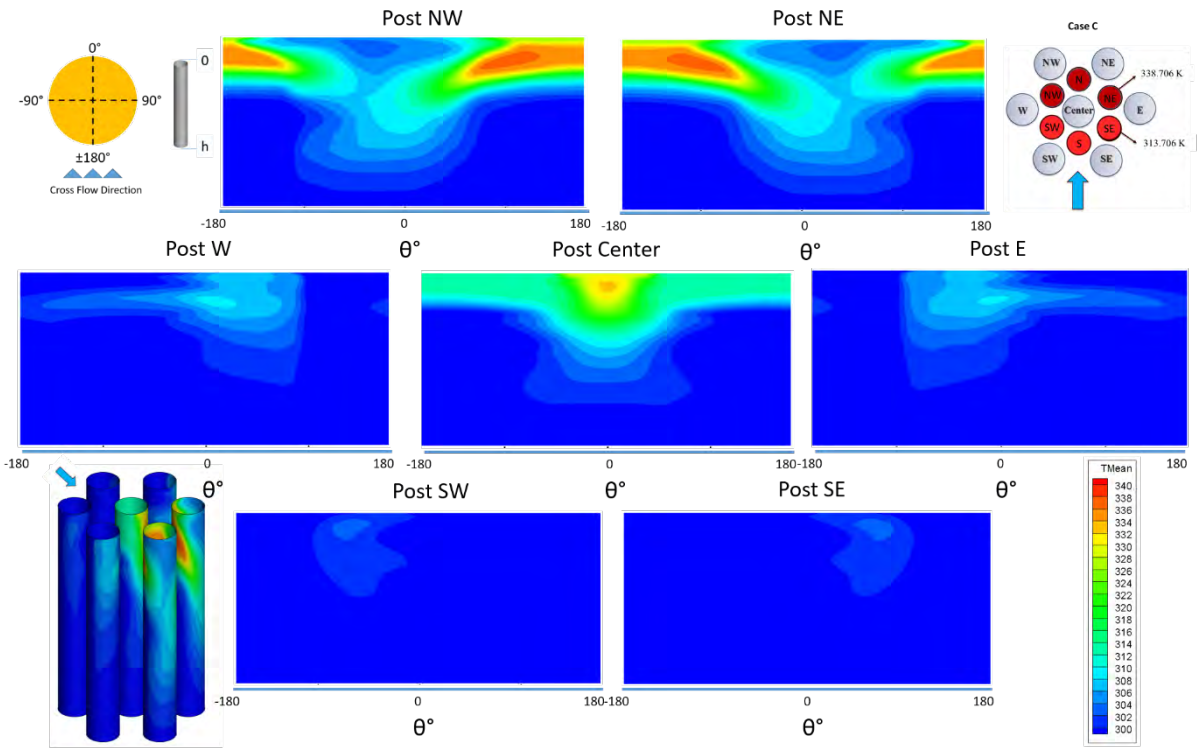

Figure 3-68. Flattened posts temperature distributions for case C. The vertical axis for all plots is the z-direction with z = 0 (jet inlets) at the top.

The line traces are provided in Figure 3-69 and reveal the same symmetry patterns previously noted. These behaviors are of course expected since case C is perfectly symmetric in its jet inlet temperature conditions. For the h/4 curve on the NE and NW posts, there are two distinct peak temperatures. One peak is near the location between of the N jet, and has a higher temperature due to the direct influence of the N jet, and the second peak is almost 180 opposite of that, a location facing the side walls of the unit cell domain. It is important to note that this double peak feature vanishes when considering locations closer to the bottom plate. The profiles for h/2 and 3h/4 have merged to a single peak that leans slightly toward the center. In other words, even when the crossflow is reduced, the peak temperature moves toward the wake region if one is far enough away from the jet inlets. The distance at which this behavior is observed will be different, depending on the magnitude of the crossflow with respect to the jets. Although significantly attenuated, this is also seen for the NW and NE post in case B (Figure 3-66), where multiple peaks exist for

the h/4 curve while only a single maximum point is found for the other two curves. It is also worth noting that the temperature range for the case C curves in Figure 3-69 (as high as 20-25 K) is greater than the corresponding ranges for case A or B in Figure 3-61 and Figure 3-66, respectively. The same can be said of the temperature signal variance provided in Figure 3-70. Just as with case A and B, the scales for all seven subplots are the same here, but it should be noted that the scales are different between Figure 3-70 compared to those in Figure 3-61 and Figure 3-67. For case C, the variance is highest for the NW and NE posts, reaching values slightly higher than 100 K^2 (T_{rms} = 10 K), much higher than anything seen in case A or B. The center post reveals two peaks for h/4 which transitions to only one local maximum at h/2. In cases E, W, SE, and SW, the temperature fluctuations are negligible in comparison to the NE and NW posts. This is primarily due to the location of the hotter jets and their relatively low impact on the upstream posts. Therefore, any fluctuations in the upstream half of the unit cell would stem from the roughly 15 K temperature difference between the three southern jets (313.706 K) and the freestream temperature (298 K).

Since the temperature distributions on the NW and NE posts are unique (especially for the h/4 trace), the flow approaching these posts is now analyzed in more detail. This jet penetrates the domain and begins to be swept away by the crossflow. It then directly impinges into post NW which explains the much higher than freestream temperature in the stagnation region for the h/4 trace of Figure 3-69, something not seen for other cases or posts. The flow then wraps around the NW post in a similar fashion as discussed for previous cases, and leaves its signature on the sides of the post. The physics that dictate this behavior are only active when the crossflow to jet velocity ratio is low enough. As previously noted, the behavior for case C begins to qualitatively mimic that of case A for the h/2 and 3h/4 traces in Figure 3-69.

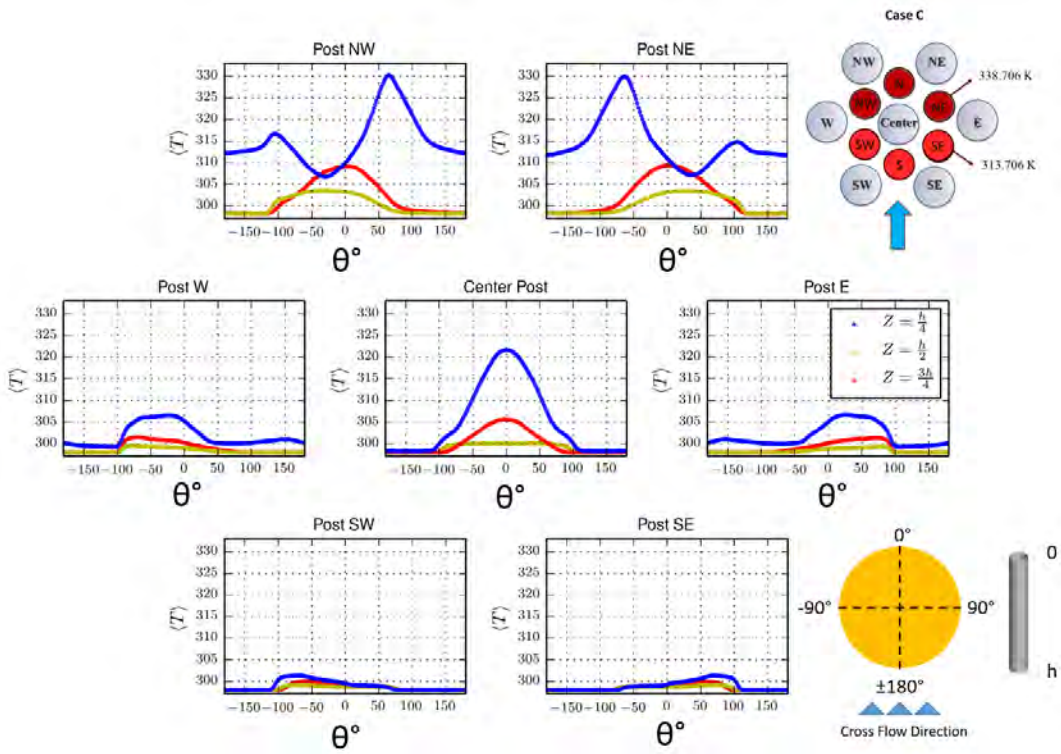

Figure 3-69. The time-averaged temperature of posts for different height locations - case C.

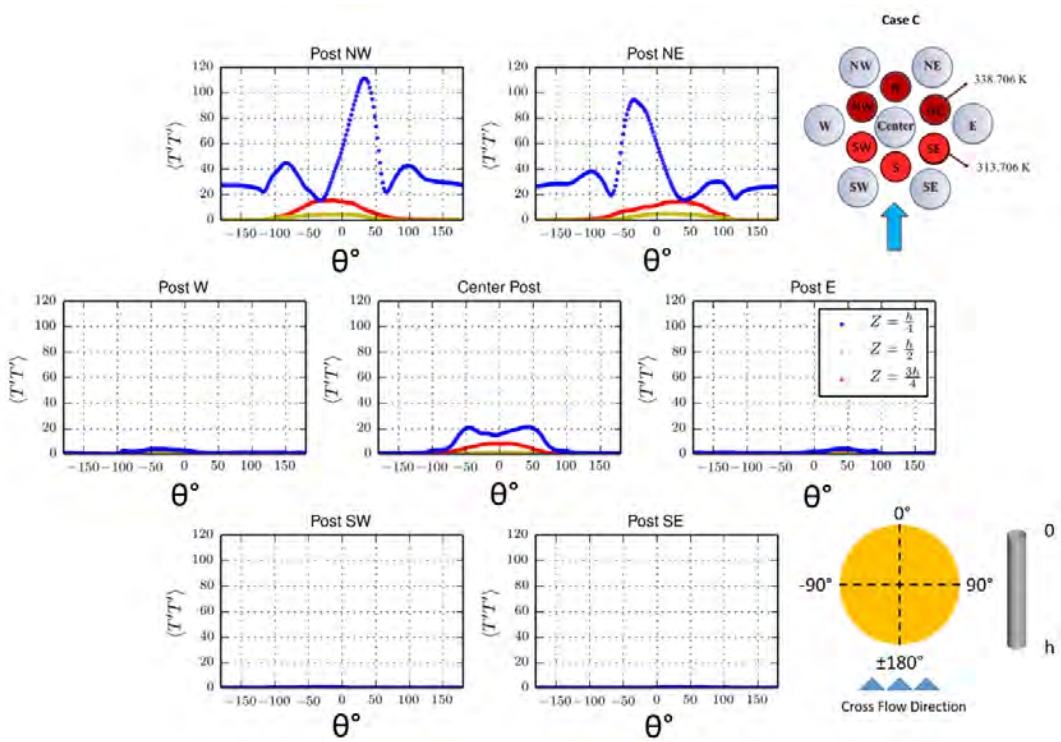

Figure 3-70. The time-averaged square of temperature fluctuations of posts for different height locations - Case C

In order to investigate the effect of the jets on flow fields of case A in greater detail, time-averaged velocity contours at different heights are shown in Figure 3-71 for the x (crossflow) and y (transverse) directions. For the transverse velocity (v), all three heights are nearly identical, where each post has a large negative traverse velocity on its east side and a similarly large positive transverse velocity on its west side. These regions are located closer the stagnation point than the wake area, and seem to grow in size the further downstream a post happens to be located. With the exception of the center post, the larger of the two high/low velocity regions near each post is always that furthest from the center of the unit cell. In any case, the flow is hitting the stagnation point of each post and being redirected away in a transverse direction towards to east and west sides of the post. This is the behavior expected from flow across a bank of cylinders, and therefore consistent with other conclusions previously noted for case A (e.g., jet penetration is minimal and therefore flow physics mimic the bank of cylinders configuration). For the crossflow direction, results are also quite similar for all three heights shown, although definite differences exist in the area considered to be the wake of the entire unit cell, which is located some distance downstream of the NE and NW posts. The size of this wake region becomes slightly larger as the interrogation plane approaches the bottom surface of the domain (i.e., the width of the unit cell wake is largest for the 3h/4 plane). The velocities closer to each post appear almost identical and reveal a negative velocity region in the wake area of each post. It is no surprise that locations of peak temperatures seem to coincide with these regions of high negative velocity. In other words, these regions serve to wrap the hot flow around the post and direct the flow toward the post surface in the wake area behind each post.

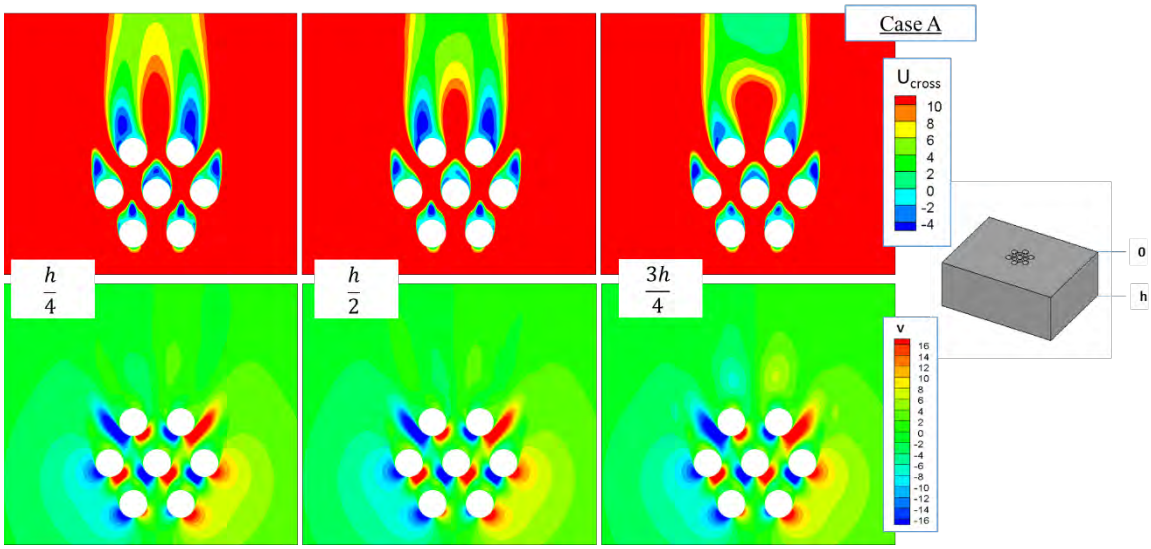

Figure 3-71. The time-averaged velocities (m/s) near posts at different heights for case A: crossflow direction (top row) and transverse direction (bottom row)

Figure 3-72 shows crossflow and transverse direction of the velocities at three different heights for case B. This case, due to the different alignment of the posts and also different crossflow to jet velocity ratio, has a different trend in comparison to case A. For this inline flow configuration, near the first posts that the crossflow approaches (SE, S, and SW), there is a pattern in the transervse velocity contours consistent with that shown for case A, namely the regions near the stagnation point with high negative and positive transvers velocities. This is not the case for the other posts however. This is primarily due to the fact that the other posts are positioned directly behind the leading posts, even within what could be considered the wake region of those leading posts. This is readily apparent for the contours around the NW post, where only a negative transverse velocity region exists, directing flow westward. The opposite is true for the NE post. In terms of the crossflow direction of the velocity, there still exists strong negative components in the wake region of each post, especially when considered the plane closest to the inlet of the jets. The strength of this negative velocity region close to each post generally decreases with increasing distance from the jets, yielding a condition which is again similar to flow past a bank of cylinders oriented in an inline fashion. For the h/4 plane, there is a large region of negative velocity in the wake of the unit

cell, and disappears for the h/2 plane. This attribute is further explored for all three cases by considering the current data compared with the scenario where no jets exist (purely flow past a bank of cylinders). This comparison aids in identifying the source of this large negative velocity region and helps to determine whether it is due to the case geometry or the jets themselves.

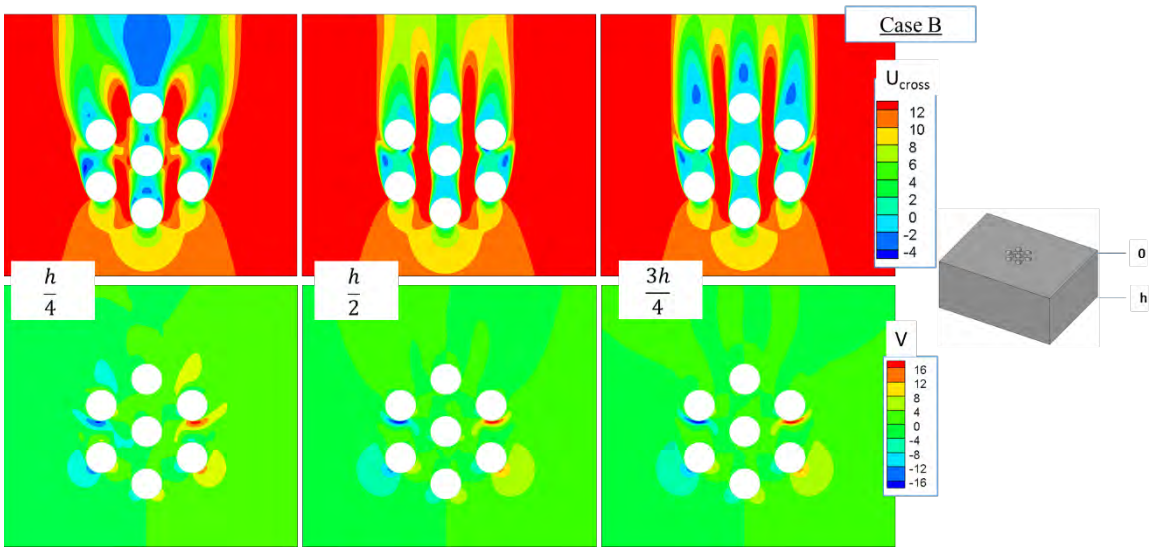

Figure 3-72. The time-averaged velocities (m/s) near posts at different heights for case B: crossflow direction (top row) and transverse direction (bottom row)

Figure 3-73 and Figure 3-74 display the crossflow direction of velocity for case B and case B without jets at the halfway downstream location from the center of the computational domain. As can be seen in Figure 3-73, the negative region of the velocity extends from top wall to a location of roughly Z = 3h/8. There is no evidence of the negative velocity in case B without the jets in Figure 3-74. Although case A did not reveal this downstream region of negative velocity, a similar analysis in Figure 3-75 and Figure 3-76 for case A shows that this is simply because this region has disappeared before h/4 (first plane provide in Figure 3-71). This is further evidence that the existence of a negative velocity region is a consequence of the jets.

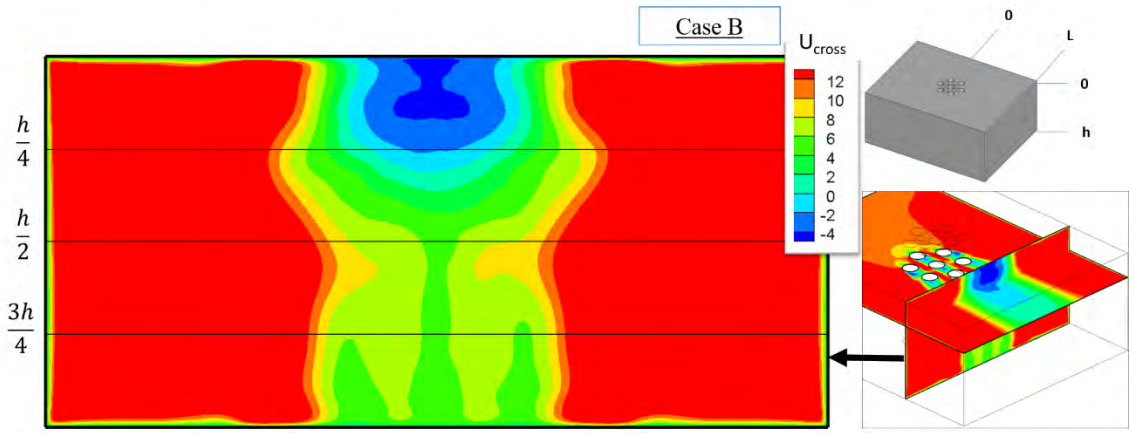

Figure 3-73. Time-averaged crossflow direction of velocity (m/s) at *L/2* for case B.

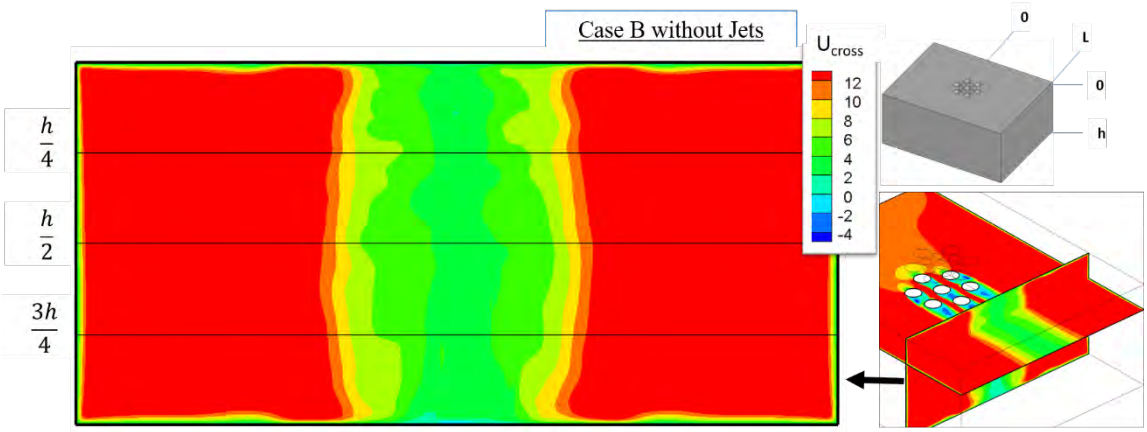

Figure 3-74. Time-averaged crossflow direction of velocity (m/s) at *L/2* for case B without Jets.

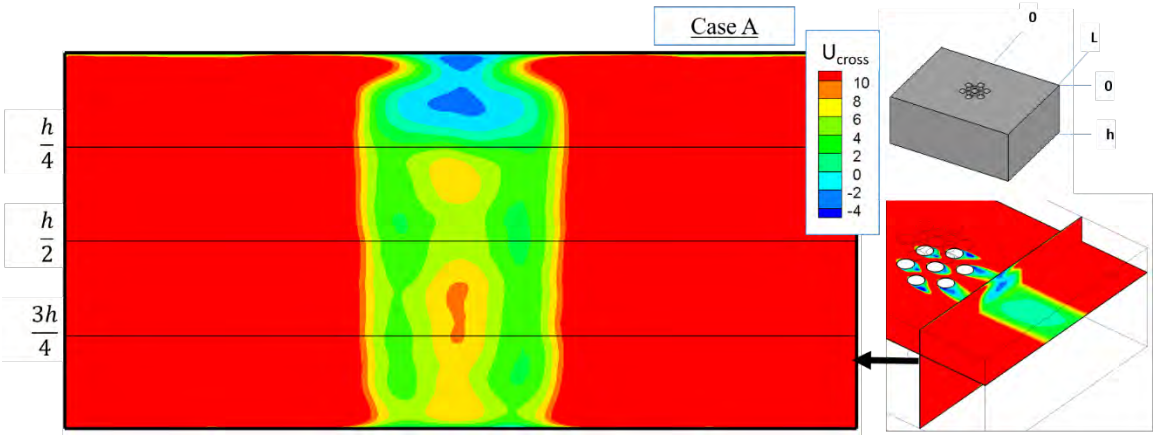

Figure 3-75. Time averaged crossflow direction of velocity (m/s) at *L/2* for case A.

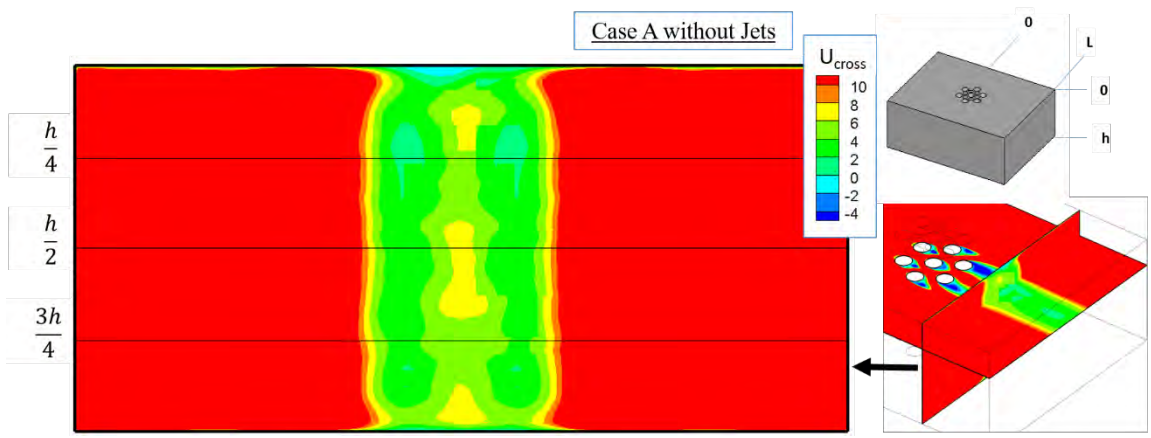

Figure 3-76. Time-averaged crossflow direction of velocity (m/s) at *L/2* for case A without Jets.

The time-averaged velocity contours of crossflow direction and transverse direction at three different heights for case C are displayed in Figure 3-77, and show qualitatively similar results at case A, as expected. However, since the strength of the crossflow is reduced, the large region of negative velocity is observed even at h/4. Further plots of the crossflow velocity in Figure 3-78 and Figure 3-79 show the tight coupling between the crossflowjet penetration and the size of this downstream negative velocity region.

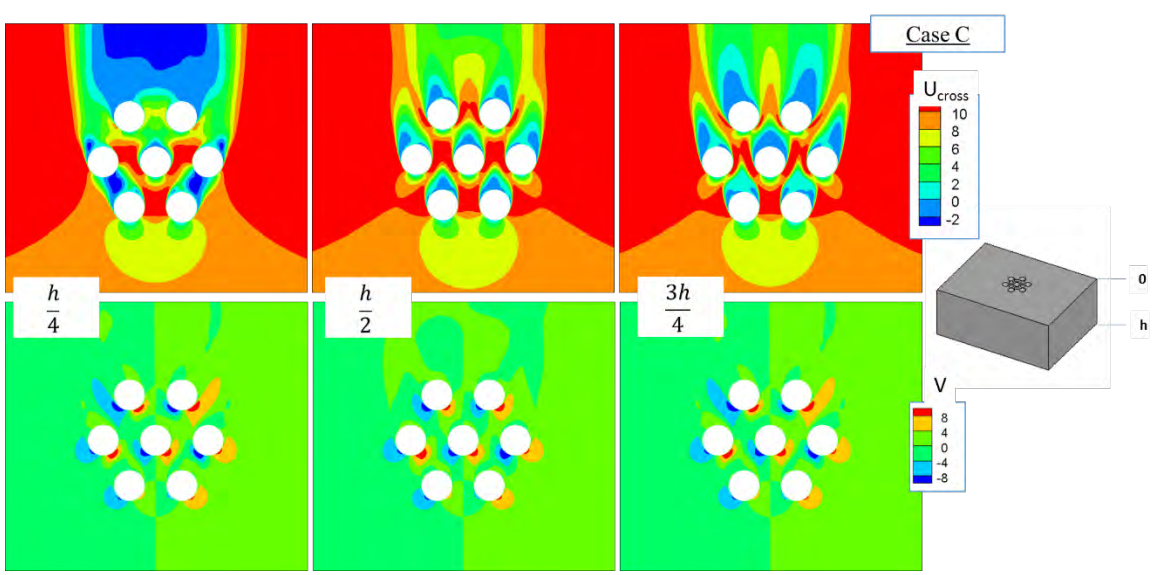

Figure 3-77. Time-averaged velocities (m/s) near posts at different heights for case C: crossflow direction (top row) and transverse direction (bottom row)

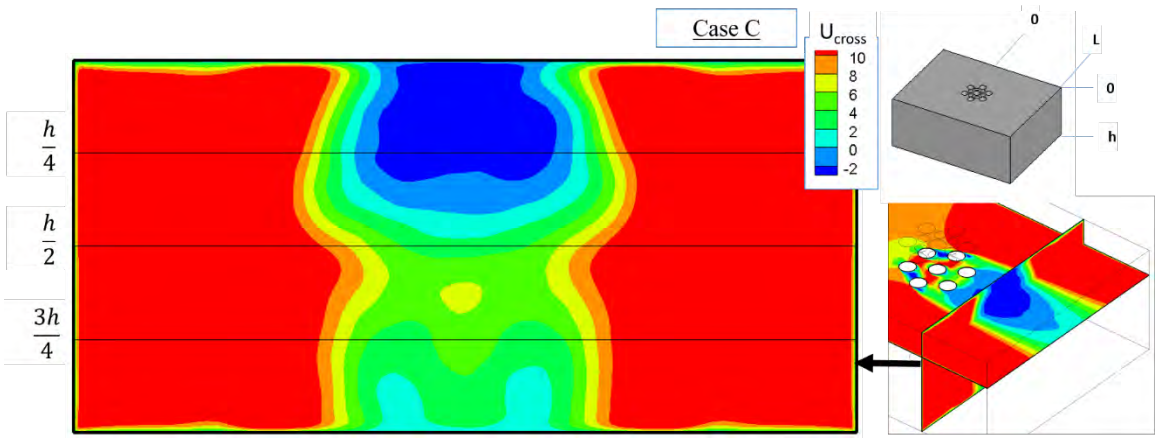

Figure 3-78. Time-averaged crossflow direction of velocity (m/s) at *L/2* for case C.

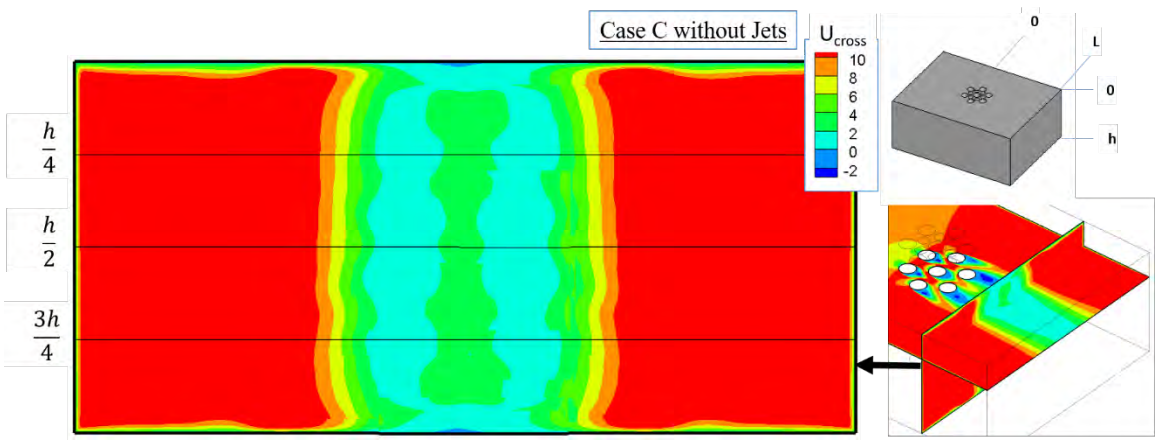

Figure 3-79. Time-averaged crossflow direction of velocity (m/s) at *L/2* for case C without Jets.

From the above analysis, it is clear that the region of flow traveling in a direction opposite of the crossflow is a result of the jets issuing into the domain. Further insight into explaining the physics behind this result can be achieved by looking to studies of confined submerged jet impingement. Confined submerged single and multiple jet impingement due to its various thermal fluid applications has a rich history in literature [90 -94]. In this flow configuration, a jet issues into the domain and immediately adjusts its direction right after colliding into the solid surface and creates a wall jet, afterwards forming a recirculation region due to the top and bottom confinement planes. Similarly, in unit cell configuration, each jet slightly changes its direction toward the post surface and creates a scenario similar to the confined submerged impinging jet situation. To better demonstrate the recirculation zone, a schematic diagram for

case C is shown in Figure 3-80. The size of this zone varies for each case as jet penetration and jet to crossflow ratio play important role for the dimension of this recirculation region. The greater the jet penetration, the more prominent this region becomes. Although difficult to quantify exactly, the jet penetration height in the current cases is analogous to the channel width (i.e., distance from bottom wall to top wall) in confined submerged jets. As the channel width decreases, the recirculation zone becomes smaller and smaller. The same is true when the jet penetration in the current study is low (e.g., case A).

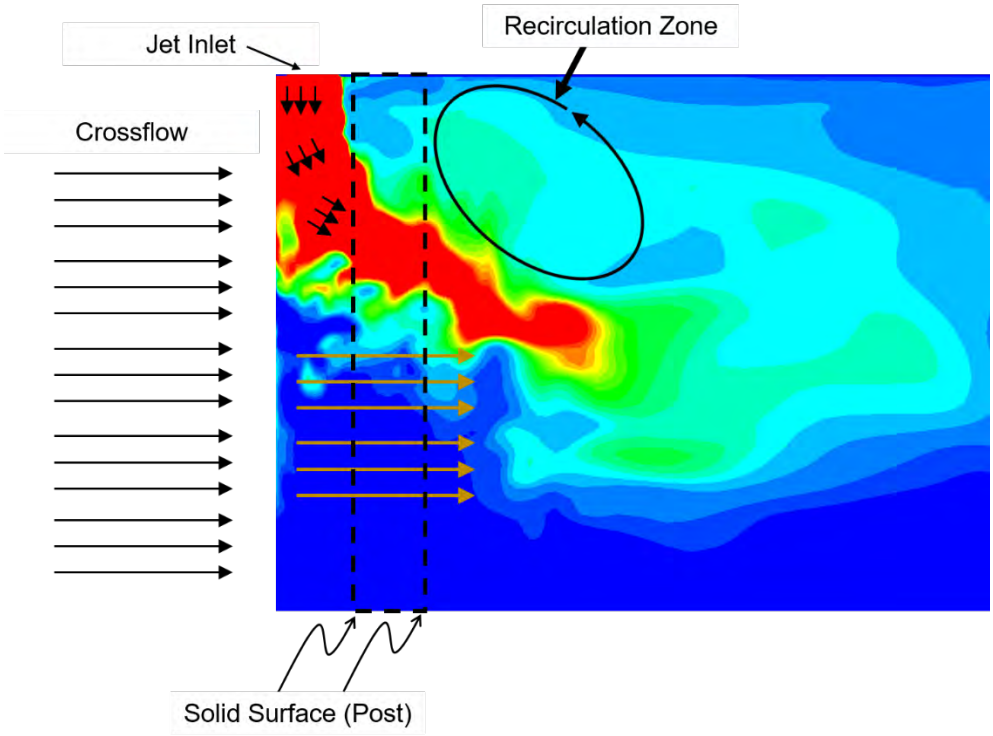

Figure 3-80. Schematic representation of flow recirculation in case C (background contour is instantaneous temperature).

For a better understanding of thermal fluid features of the lower plenum of an HTGR, a unit cell test section is proposed. The unit cell represents a portion of the lower plenum and consists of six jets and seven posts combined with a crossflow. In order to reproduce a flow field similar to the lower plenum, three different scenarios are considerd based on the post configuration and crossflow to jet velocity ratios. A preliminary Large Eddy Simulation of the three unit cells is conducted to investigate the primary flow

features. Nonisothermal compressible Large Eddy Simulation implemented in OpenFOAM combined with a structural mesh design are employed.

The results show that the maximum temperature and also temperature fluctuations do not occur on the spots where the jets are impinging into the posts since the crossflow conveys the hot jets around the posts and positions the hot spot on opposite locations in the wake region of each post. Also, it has been noted that both the post configuration and jet to crossflow velocity ratio play an essential role in the temperature distribution on the posts. Also as expected, the flow feature is very sensitive to the magnitude of crossflow velocity, which if small enough for a given domain size and jet velocity, will yield results similar to flow over a bank of cylinders and consequently the effects of the jets can vanish due to a high crossflow or can be limited to a small region close to the top wall. The combination of the jets and crossflow creates a condition similar to submerged confined impinging jets where a recirculation region exists and increases in size when the penetration depth becomes larger.

In general, the current qualitative LES analysis discloses that due to the complex conditions in the lower plenum, careful consideration needs to be taken to fully understand the flow physics of the problem. Accordingly, the LES shows that the location of the posts in the lower plenum can entirely change the thermal fluid quantities of the adjacent posts and walls. Current LES provides many valuable insights regarding the area where more detailed experimentally and computationally analysis need to be done. The concept of the unit cell itself is also of great value due to the fact that there are many canonical problems like impinging jets, jets in crossflow, and flow past a bank of cylinders that are closely related to the lower plenum, and can be used as a motivation to help guide more effective designs that could mitigate or at least reduce thermal striping. The unit cell can also be considered as a valuable source to enhance and validate new approaches in turbulence modeling and further CFD development. In the next section, the LES models are updated to reflect the boundary conditions given in 2.6.3 and direct comparisons are made, which help to give the discussion points in this section some level of validity.

3.7 Unit Cell Simulations vs. Experimental Data

This section focuses on direct comparison between experiments and LES modeling of unit cell I, II, and III. The temperature and velocity boundary conditions are applied based on results presented in section 2.6. A full validation analysis would also require input uncertainty to be accounted for in the simulations. Although this was not done, the results nonetheless show promise in being able to capture the flow physics of this complex thermal fluid phenomenon. It should be noted that in order to save computation time, a conjugate heat transfer model was not undertaken. The non-isothermal aspects were accounted for in the simulation, but since only the fluid was modeled and the post surfaces were taken as adiabatic, direct temperature comparison is not of value, even though future modelers could account for aluminum posts properties and compare to data in Table 2-18 through Table 2-21. Results for velocity and planar Reynolds stresses are now discussed for each unit cell.

3.7.1 Case I

Three line traces were chosen for in depth analysis, the illustration of which is provided in Figure 3-81. The first two lines are chosen to be halfway between the centers of neighboring posts. With the center post (post A) as the origin, this places line G at x = – 0.0233 m and line Ein at x = 0.0233 m. The final line (Eout) is placed such that it too would be halfway between post E and the next neighbor if the array continued downstream. This places line Eout at x = 0.0699 m. All three line traces are analyzed at two different heights (x-y planes) equal to 50% and 75% of the distance from jet inlet to the bottom surface of the test section. Also shown in the figure are the six jets colored by nominal temperatures (hot or cold). Initially, the planar PIV approach was attempted for a third plane closer to the jet inlets, but the out of plane velocity for those measurements proved to be too high compared to the in plane velocities, making useful data extraction difficult.

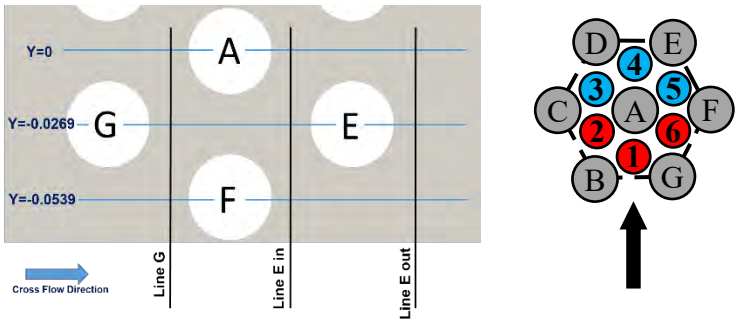

Figure 3-81. Unit cell I showing the three line traces of interest for further analysis. Dimensions shown in the figure are meters. The z direction is into the page.

The velocities along line G are shown in Figure 3-82 for U and V components at the z/H = 0.50 plane. The experiments and simulations both reveal a negative U velocity directly in the wake of post G, as expected. The peak velocities are approximately 20% higher than the approaching cross flow magnitude. This is also expected since the flow area through the unit cell is reduced, and the flow should therefore accelerate according to mass conservation principles. The velocity in the transverse direction also reveals anticipated behavior of positive values on one side of post G and negative values on the other. This can qualitatively be compared to the bottom row of Figure 3-71. The z/H = 0.75 plane provided in Figure 3-83 reveals nearly identical results compared to those shown in Figure 3-82. This suggests that for such a high crossflow, the jets are swept away before they are able to penetrate too far in the z direction. Therefore, planes for z/H = 0.5 and z/H = 0.75 mostly mimic flow past a bank of cylinders, and could be considered nearly two-dimensional.

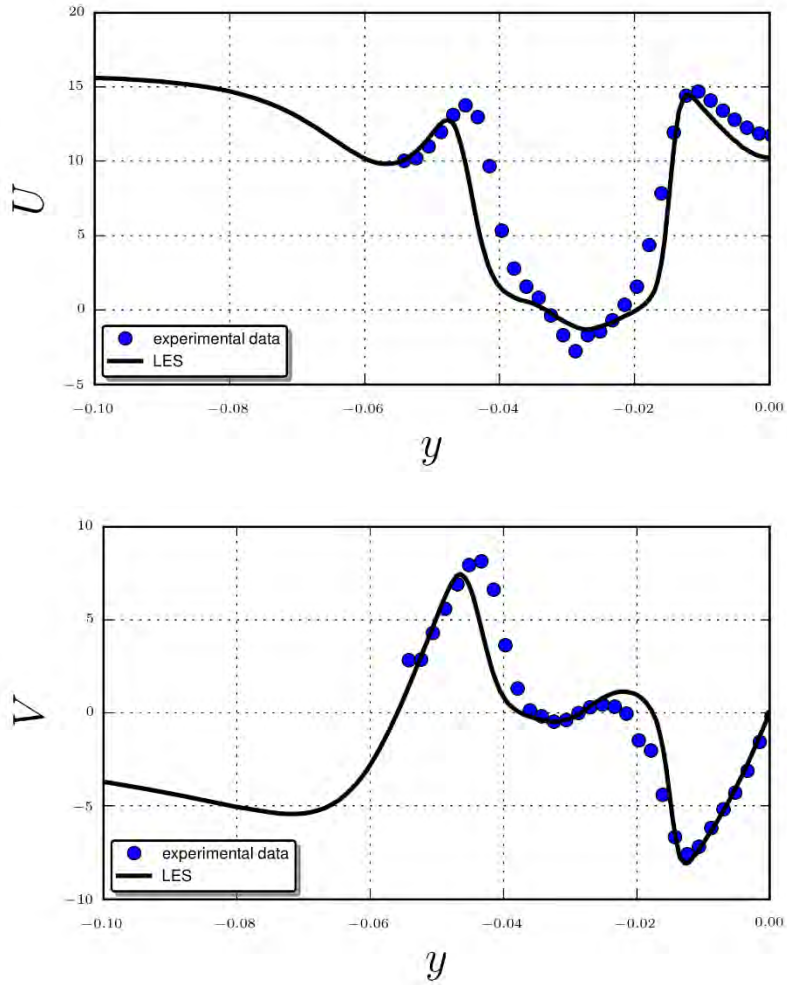

Figure 3-82. Velocities (m/s) along line G at z/H = 0.50 for unit cell I. Unit for y is meters. For reference, the crossflow velocity is 12.53 m/s.

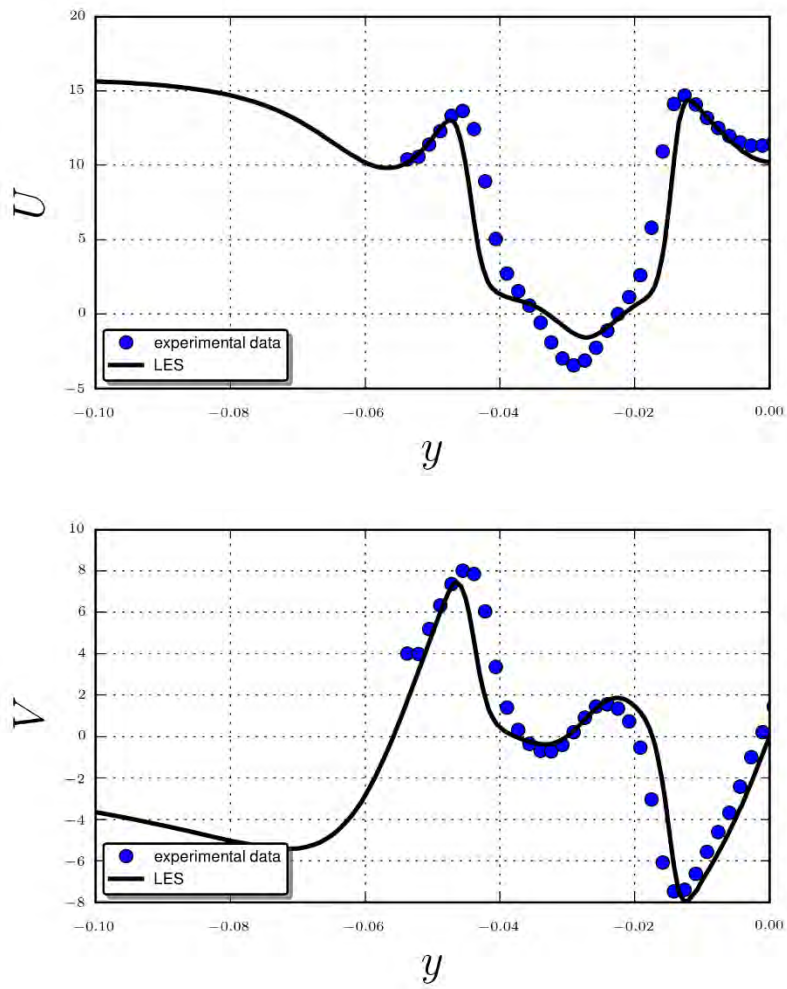

Figure 3-83. Velocities (m/s) along line G at z/H = 0.75 for unit cell I. Unit for y is meters. For reference, the crossflow velocity is 12.53 m/s.

The normal and shear stresses for line G at z/H = 0.50 are provided in Figure 3-84 and reveal the highest stresses are those in the transverse direction, $< vv >$. The computational and experimental data do not agree quite as well compared to those from the first order velocities, but nonetheless contain similar physics and overall magnitudes. The agreement is closer for the z/H = 0.75 plane, which is shown in Figure 3-85. It should be noted that although the velocities might suggest a 2D condition has been reached by z/H = 0.5, that message is not quite as clear when considering the higher order moments, which reveal slight differences in magnitude and even shape between the two planes.

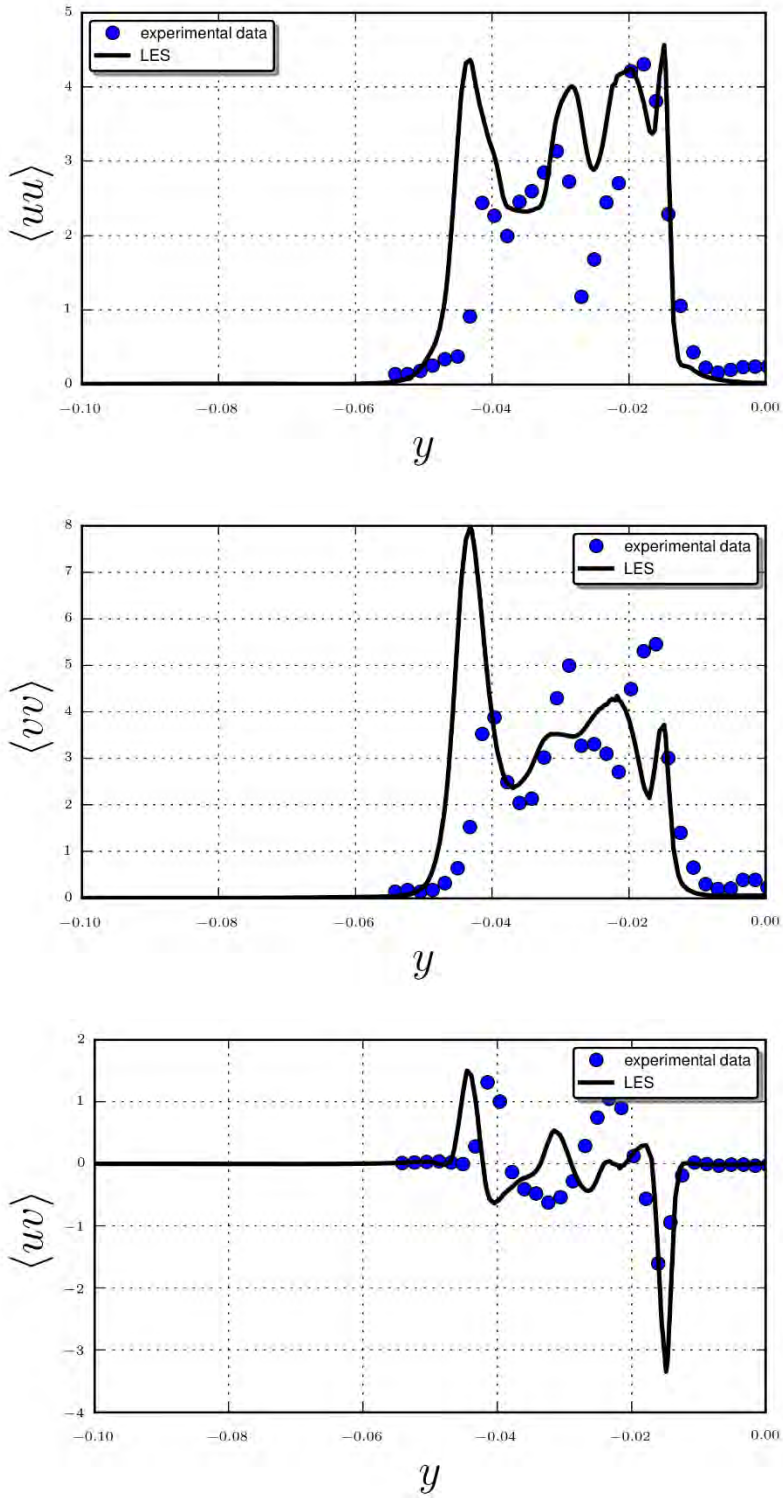

Figure 3-84. Reynold stresses (m^2/s^2) along line G at z/H = 0.50 for unit cell I. Unit for y is meters. For reference, the crossflow velocity is 12.53 m/s.

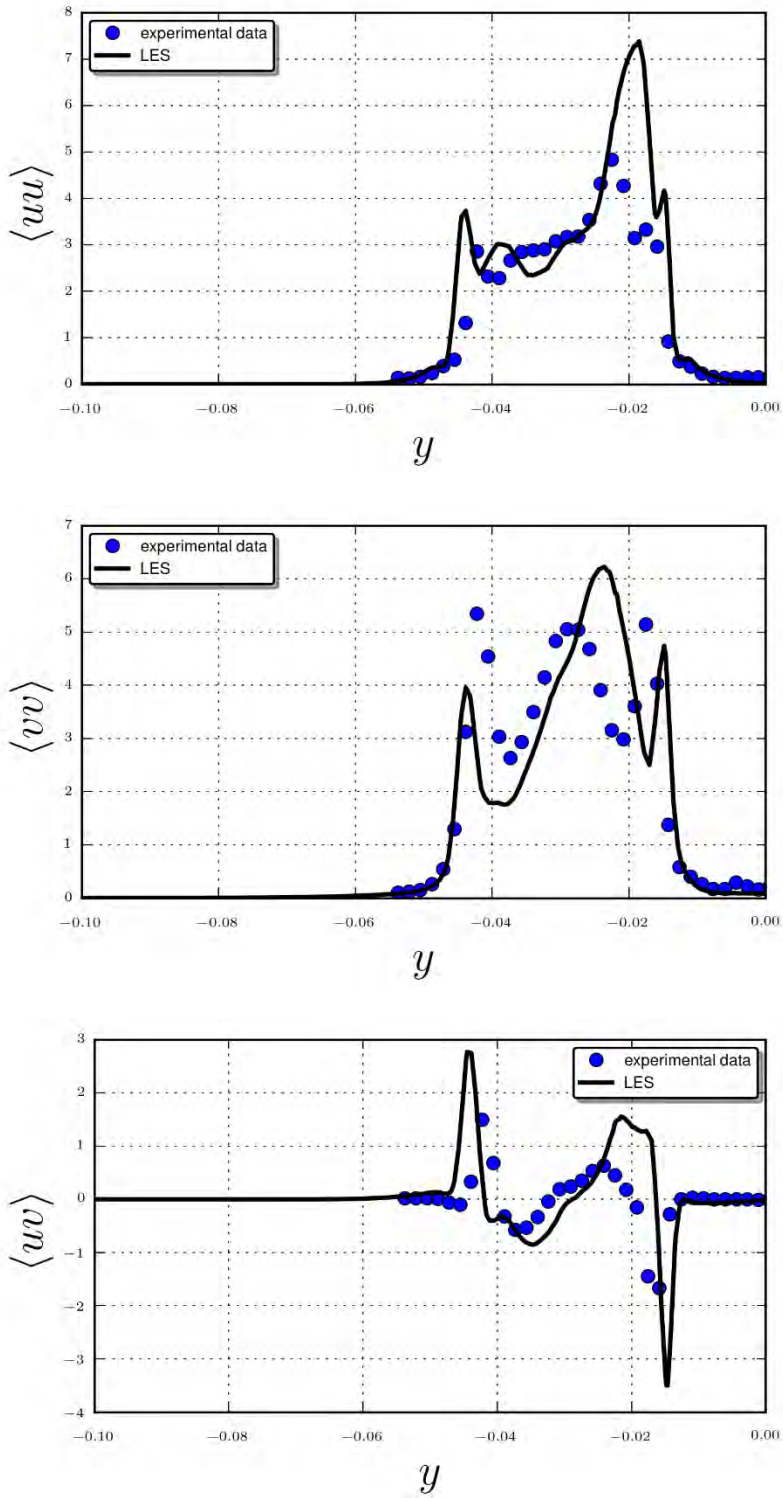

Figure 3-85. Reynold stresses (m^2/s^2) along line G at z/H = 0.75 for unit cell I. Unit for y is meters. For reference, the crossflow velocity is 12.53 m/s.

For the Ein line for this unit cell, velocities are shown in Figure 3-86 for the z/H = 0.5 plane, and show excellent agreement. Note that the z/H = 0.75 is not provided since it reveled nearly identical values as the z/H = 0.5 plane. Figure 3-87 provides stress profiles in the same plane, and once again reveals the magnitude and trends are captured by the current modeling approach.

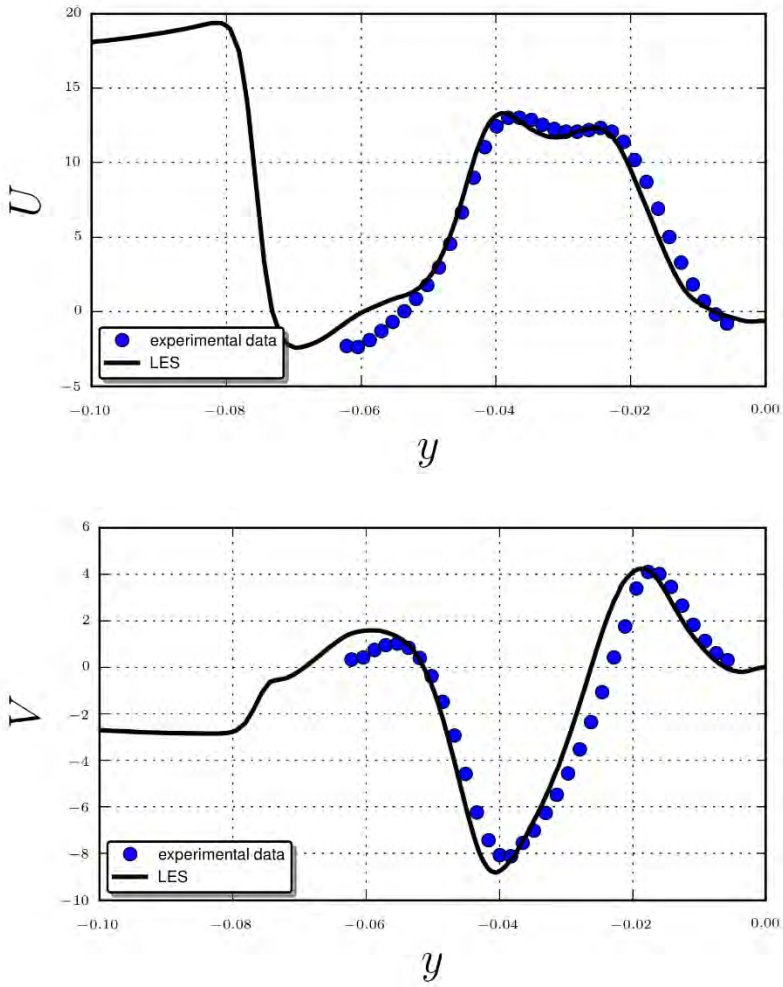

Figure 3-86. Velocities (m/s) along line Ein at z/H = 0.50 for unit cell I. Unit for y is meters. For reference, the crossflow velocity is 12.53 m/s.

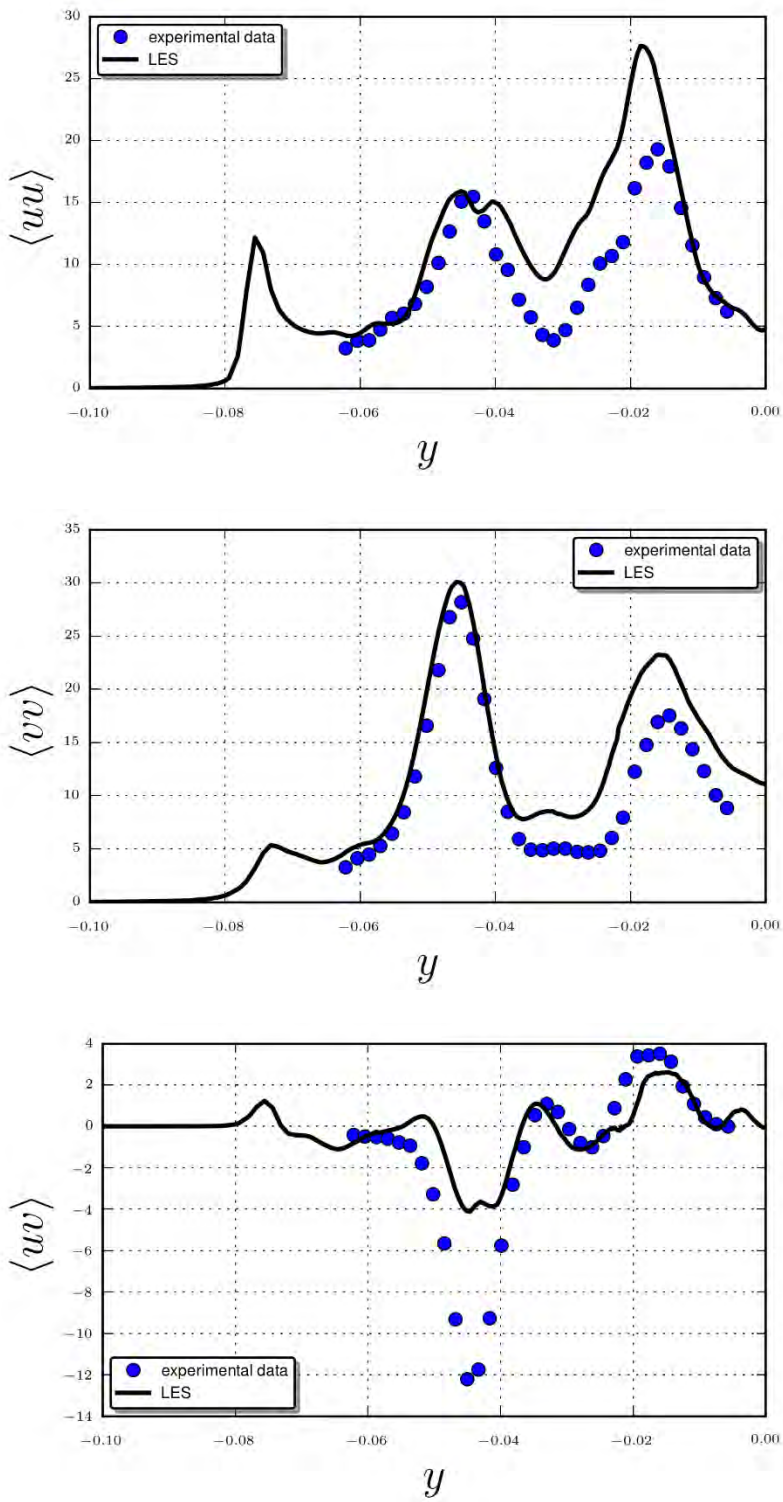

Figure 3-87. Reynold stresses (m^2/s^2) along line Ein at z/H = 0.50 for unit cell I. Unit for y is meters. For reference, the crossflow velocity is 12.53 m/s

For the Eout line shown in Figure 3-88 and Figure 3-89 for the velocities and stresses, respectively, the agreement is not as good. For some metrics (e.g. U velocity), it appears as if a simple offset exists in the y direction. This theory becomes less grounded when considering different measurements along this line trace. For example, the local valley for the $< uu >$ plot is similar for both experiments and simulations (approximately y = – 0.025 m), but the gradients of the profiles to either side do not agree well between the two. This line trace should arguably contain the most complicated degree of flow physics since the influence is felt from all jets, but the flow has not become fully mixed yet. Further, more in depth validation efforts are required to gain a deeper appreciation for this mismatch.

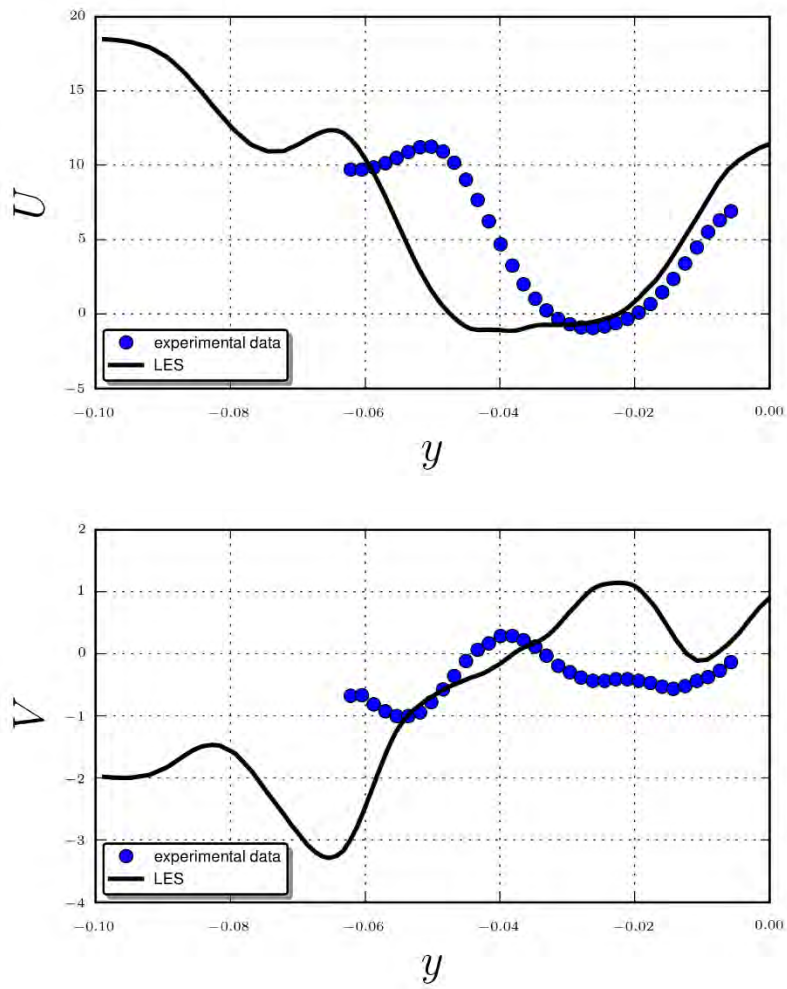

Figure 3-88. Velocities (m/s) along line Eout at z/H = 0.50 for unit cell I. Unit for y is meters. For reference, the crossflow velocity is 12.53 m/s.

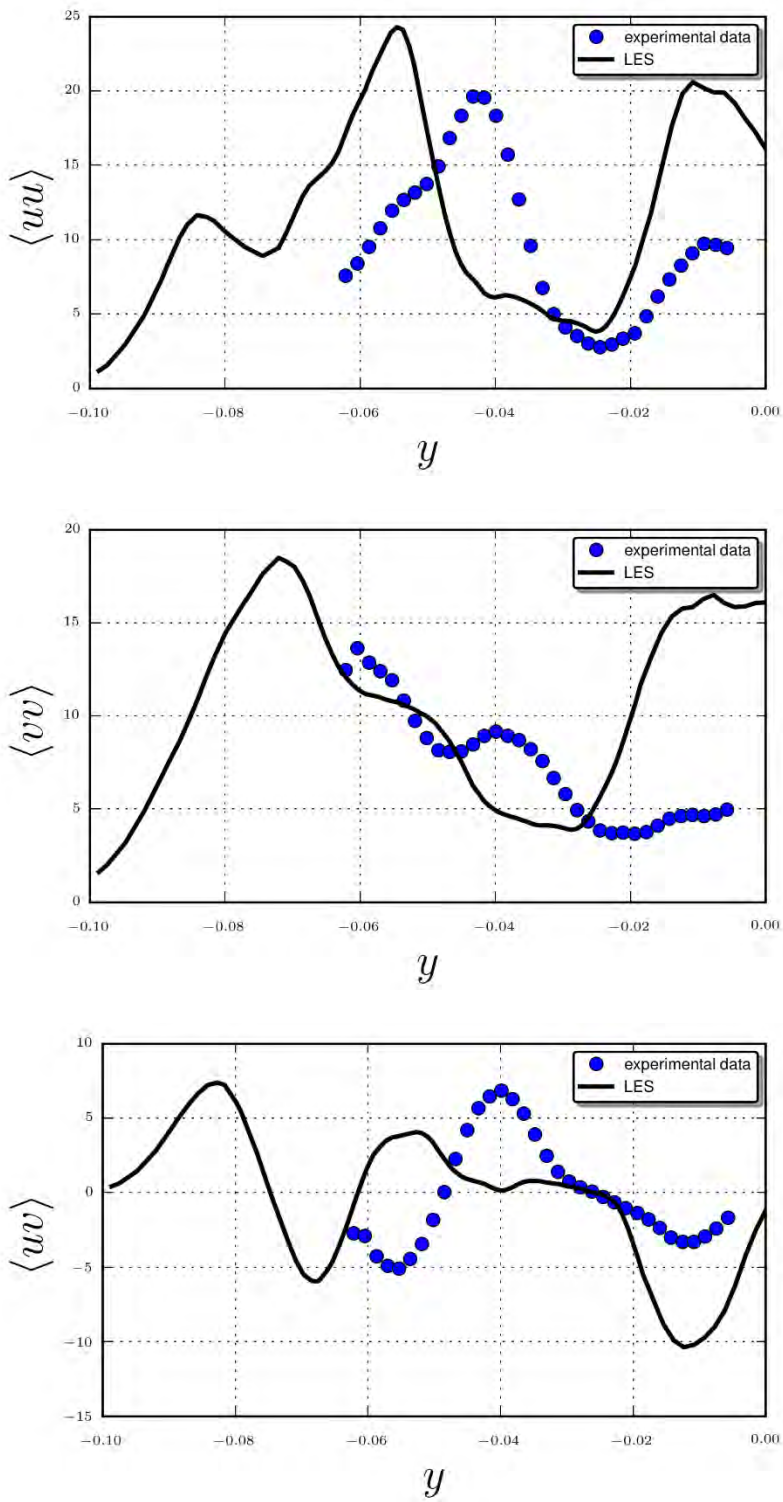

Figure 3-89. Reynold stresses (m^2/s^2) along line Eout at z/H = 0.50 for unit cell I. Unit for y is meters. For reference, the crossflow velocity is 12.53 m/s.

3.7.2 *Case II*

For this case, which is rotated by 30°, only two lines are chosen for analysis. The first is along the direct center of the unit cell, and the second is a full post diameter downstream of post E. The geometry and orientation are illustrated in Figure 3-90, along with the jet and post labels.

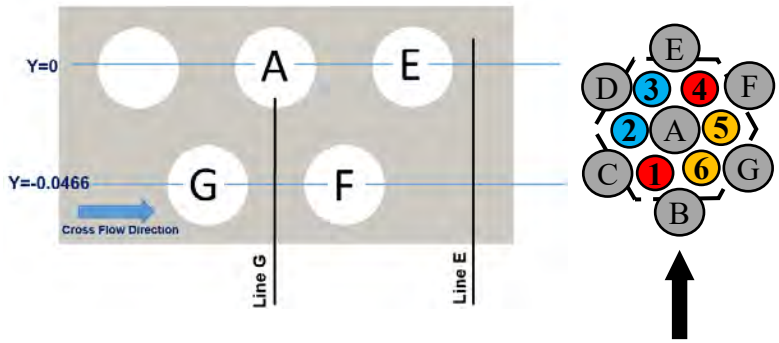

Figure 3-90. Unit cell II showing the two line traces of interest for further analysis. Dimensions shown in the figure are meters. The z direction is into the page.

Velocities and stresses for line G at z/H = 0.5 are shown in Figure 3-91 and Figure 3-92, respectively. These profiles are not provided for z/H = 0.75 since they were nearly identical to those shown for z/H = 0.5. The U velocity shows excellent agreement, and reveals trends expected for flow past an array of in line cylinders. Specifically, the flow between the cylinders (– 0.03 m < y < – 0.02 m) is nearly uniform since the path through array is much more streamlined compared to the staggered arrangement from case I. The magnitude of this flow is approximately 50% higher than the approaching crossflow, which again is an expected attribute when considering the reduction in cross sectional area through which the flow travels. The agreement in the V component is not as good, showing an overestimation in both the positive and negative sense at the extremes. This overestimation in roughly 100% (double the experimental value). Although line G and line Ein from case I are not in the same position as line G from case II, it is worth noting that the velocities show better agreement in both directions (see Figure 3-82 and Figure 3-86).

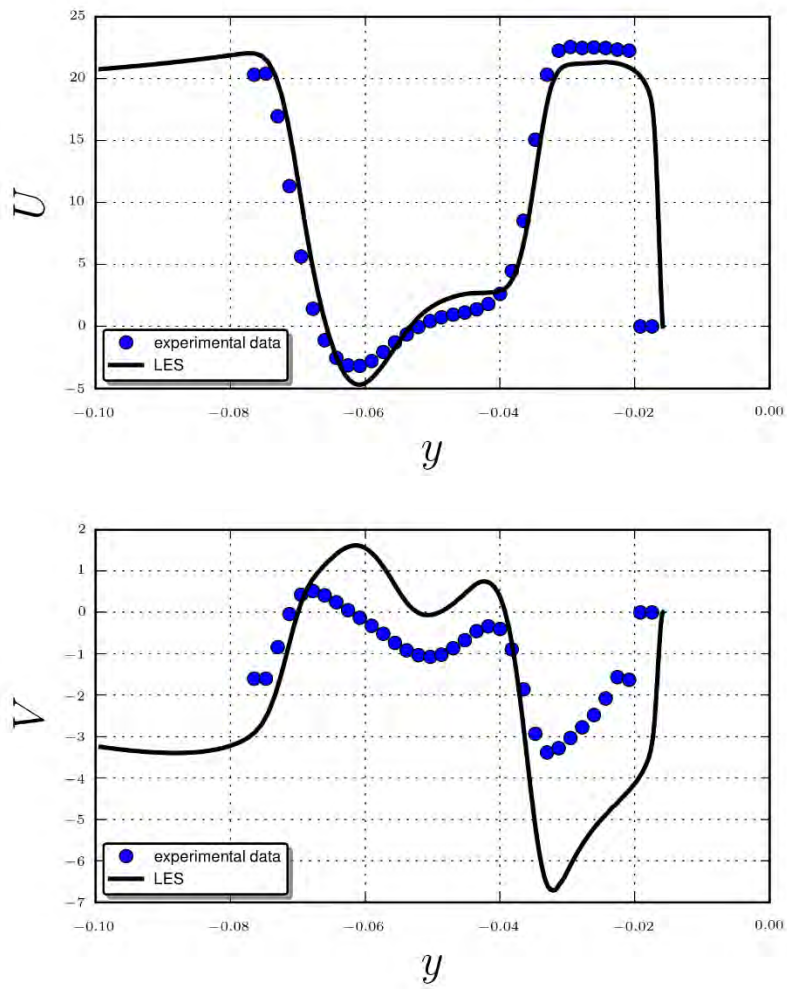

Figure 3-91. Velocities (m/s) along line G at z/H = 0.50 for unit cell II. Unit for y is meters. For reference, the crossflow velocity is 14.72 m/s.

The stresses (Figure 3-92), although by and large suggest the trends of the experimental data are captured, there are considerable differences between the two, especially in magnitude. In most instances, the computational data is over-predicting the stresses. This can be as large as 450% (see peak near y = –0.035 m on $< vv >$ plot). The velocities for line E reveal similar conclusions when considering line G for case II, namely that the U component is captured quite well, but some discrepancies exist for the V component. This is true for the z/H = 0.50 plane (Figure 3-93) and the z/H = 0.75 plane (Figure 3-94).

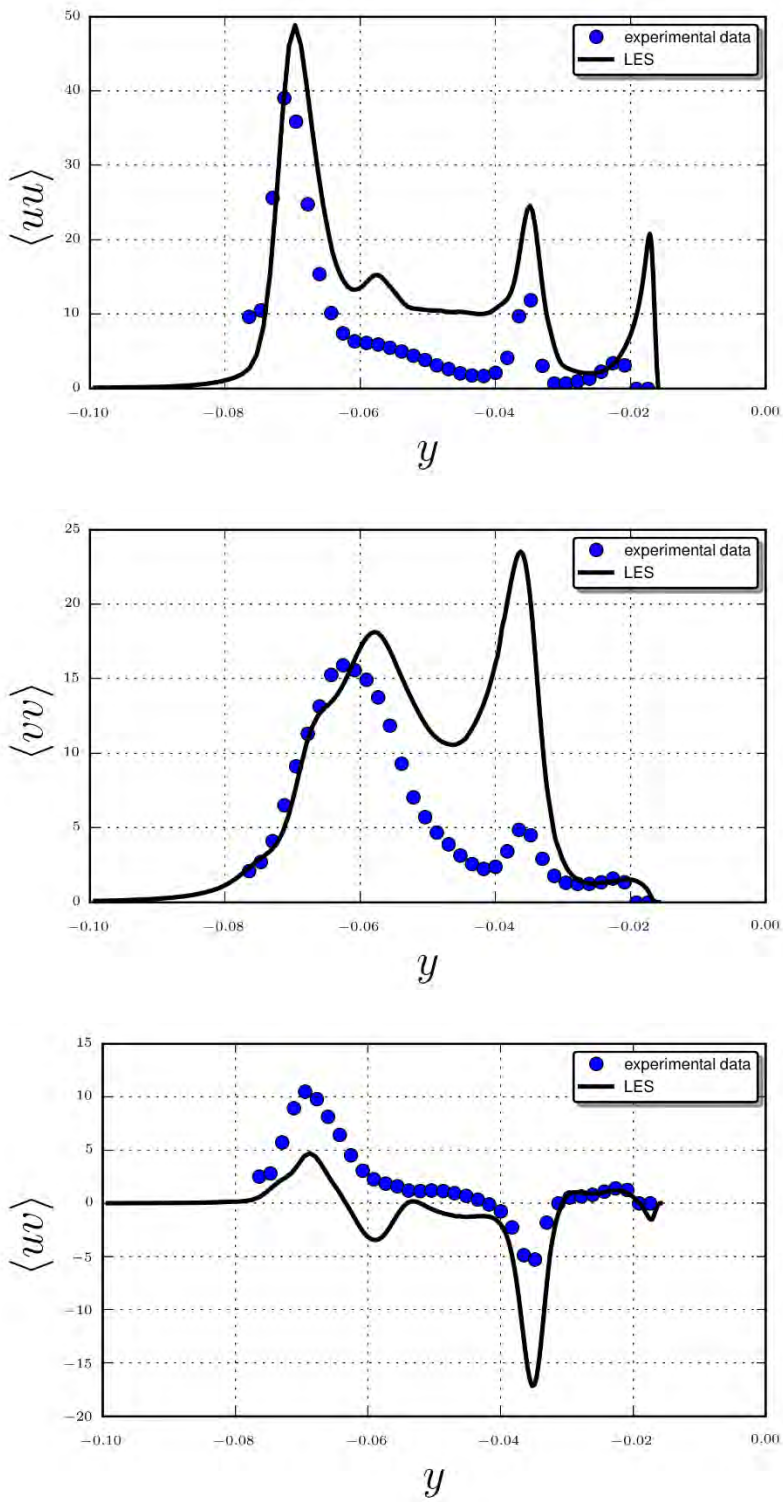

Figure 3-92. Reynold stresses (m^2/s^2) along line G at z/H = 0.50 for unit cell II. Unit for y is meters. For reference, the crossflow velocity is 14.72 m/s.

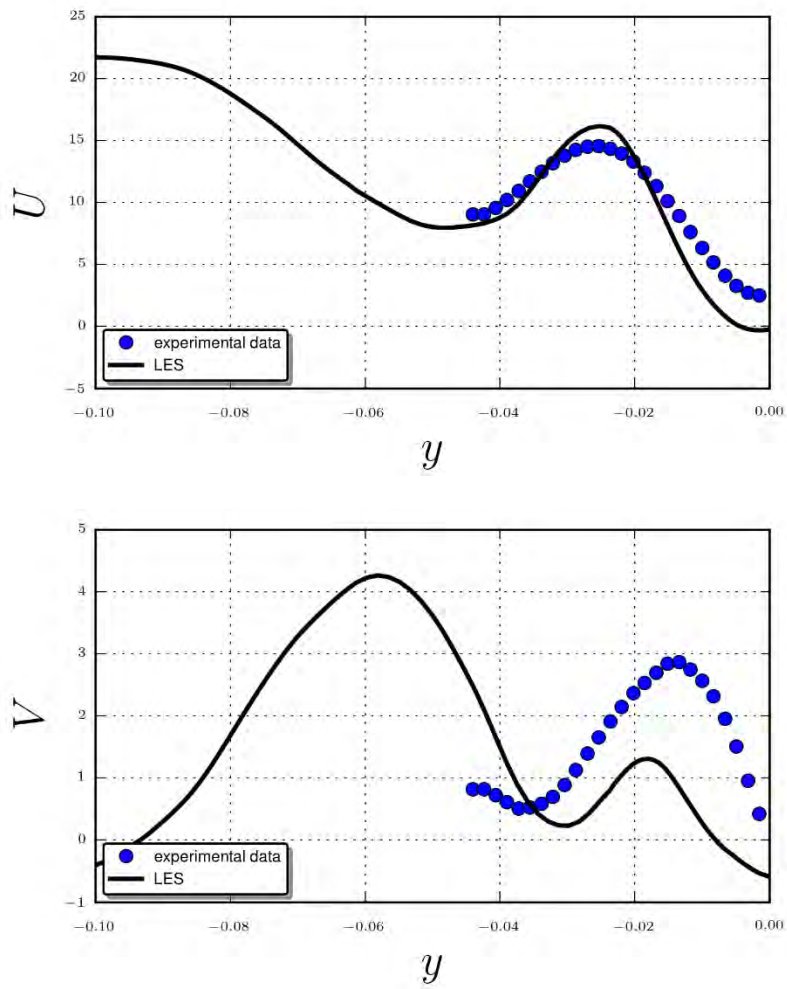

Figure 3-93. Velocities (m/s) along line E at z/H = 0.50 for unit cell II. Unit for y is meters. For reference, the crossflow velocity is 14.72 m/s.

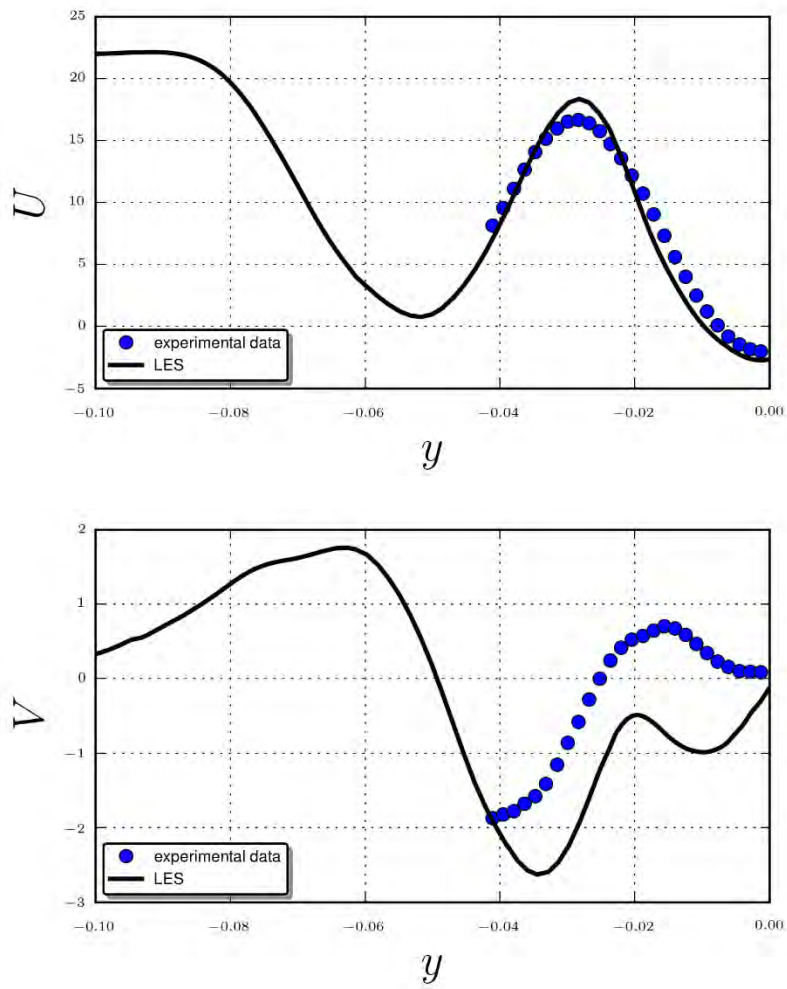

Figure 3-94. Velocities (m/s) along line E at z/H = 0.75 for unit cell II. Unit for y is meters. For reference, the crossflow velocity is 14.72 m/s.

The Reynolds stresses for line E of case II are shown in Figure 3-95 and Figure 3-96 for z/H = 0.5 and 0.75, respectively. Compared to the most downstream line trace of case I, that for case II seems to capture the physics more reliably. The gradient of stresses, and in many situations the magnitudes as well, show good agreement between experiments and simulations. It should also be noted that the trends seen in each plane are different from each other. This suggests that for the inline flow case, the wake of the unit cell is more heavily dependent on the z location of interest. For $< uu >$ a second, non-negligible peak appears at z/H = 0.75, and the profile for $< vv >$ is markedly different between the two planes. Attributes of these differences are seen both experimentally and computationally.

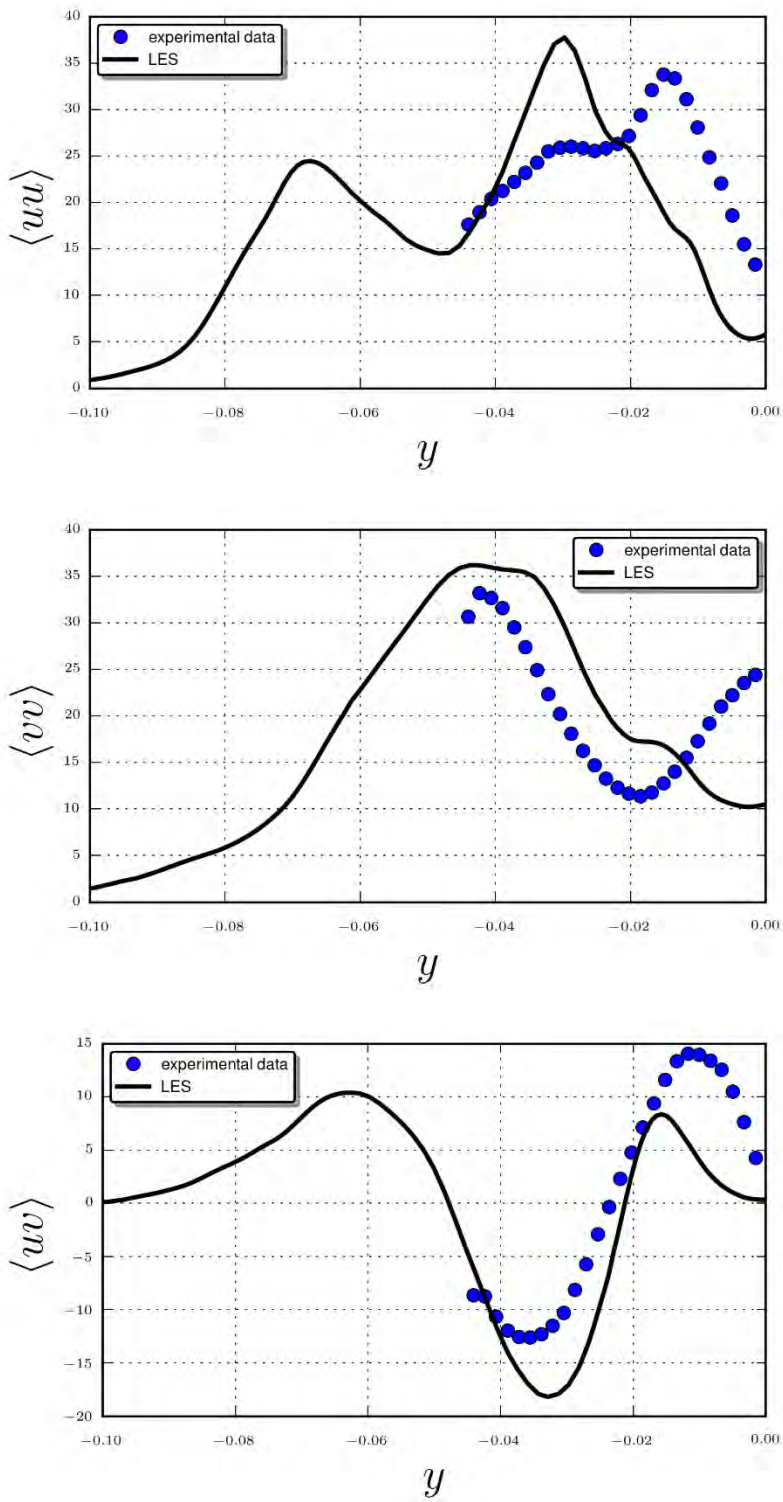

Figure 3-95. Reynold stresses (m^2/s^2) along line E at z/H = 0.50 for unit cell II. Unit for y is meters. For reference, the crossflow velocity is 14.72 m/s.

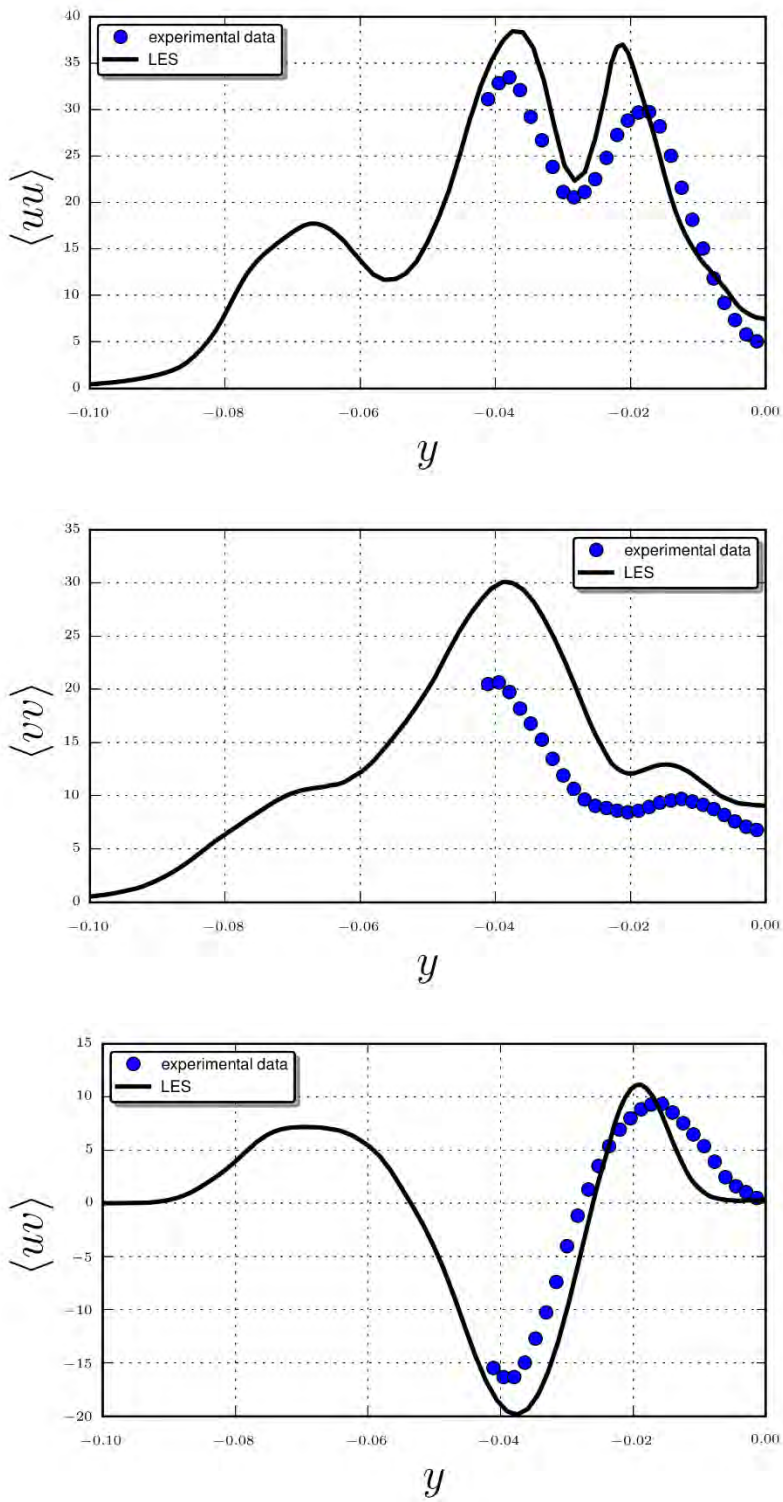

Figure 3-96. Reynold stresses (m^2/s^2) along line E at z/H = 0.75 for unit cell II. Unit for y is meters. For reference, the crossflow velocity is 14.72 m/s.

3.7.3 *Case III*

Case III is similar to case I, except the crossflow velocity has been reduced and the jet velocities have been increased. Because of this, the jet penetration in the z direction is expected to increase for this case compared to the others. This then affects the two-dimensional nature of the flow previous observed in case I and case II where the z/H = 0.5 and 0.75 planes were nearly identical. More specifically, the flow becomes highly three-dimensional, showing considerable differences between the two planes of analysis. The flow configuration and labeling conventions are shown in Figure 3-97. The line traces are exactly the same as described for case I.

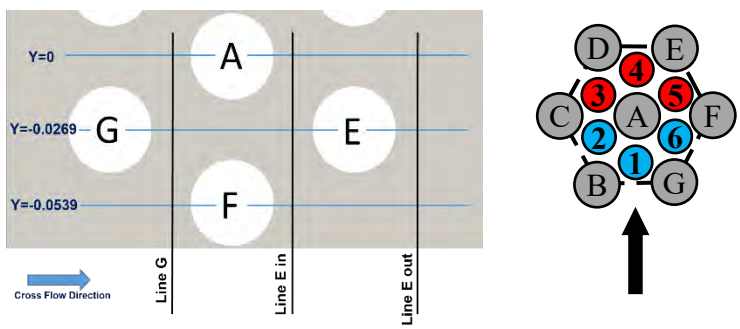

Figure 3-97. Unit cell III showing the three line traces of interest for further analysis. Dimensions shown in the figure are meters. The z direction is into the page.

The velocities are shown for line G in Figure 3-98 and Figure 3-99 for z/H = 0.5 and 0.75, respectively. The accuracy seen from these line traces in case I is beginning to reduce due to the three-dimensional nature of the flow. Although there is still decent agreement for both U and V, the computational model is beginning to explain less of the data attributes. The stresses at z/H = 0.5 and 0.75 are shown in Figure 3-100 and Figure 3-101, respectively and reveal the largest discrepancies observed thus far, at least when considering $< uu >$ and $< vv >$. The experimental data between the two figures suggests a several fold increase exists in the magnitude of the stresses. Although the magnitude also changes between these two planes for the computational results, the difference is not nearly as drastic. One possible culprit for explaining this inconsistency between experimental data and computational predictions is the inability to

fully capture the jet penetration. With the current data, it is difficult to test this theory, and more data with appropriate data analysis would be required. Needless to say, if significant errors exist in the jet penetration prediction, then the planar analysis currently conducted would be offset by some amount. The fact that case I and case II show similar magnitudes and trends from a computational and experimental standpoint for both the z/H = 0.5 and 0.75 planes suggests additional planes of data should be acquired. In addition, planes orthogonal to the current acquisition planes should be attempted in order to better capture the jet flow, thereby gaining additional insight into the jet penetration metrics.

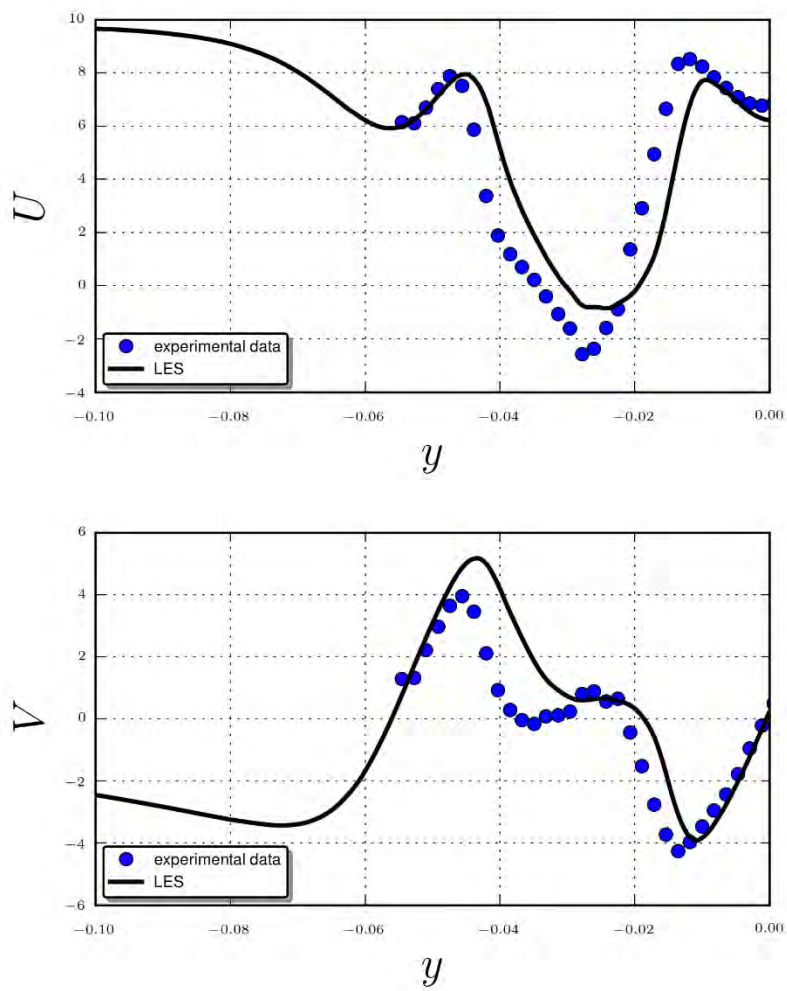

Figure 3-98. Velocities (m/s) along line G at z/H = 0.50 for unit cell III. Unit for y is meters. For reference, the crossflow velocity is 7.68 m/s.

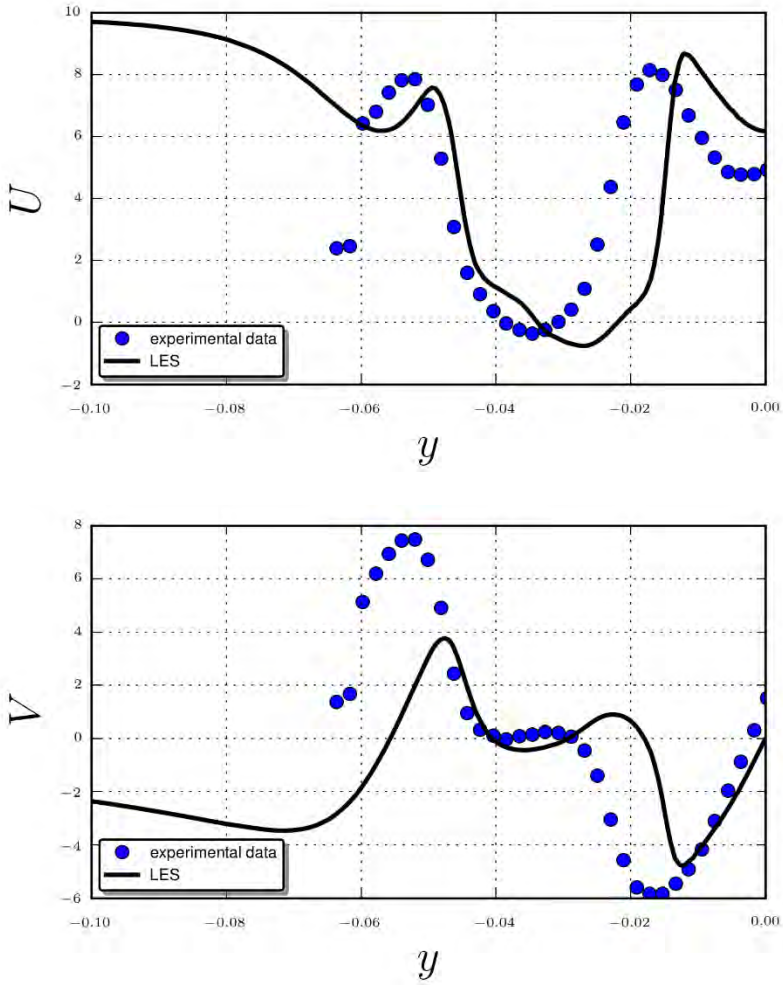

Figure 3-99. Velocities (m/s) along line G at z/H = 0.75 for unit cell III. Unit for y is meters. For reference, the crossflow velocity is 7.68 m/s.

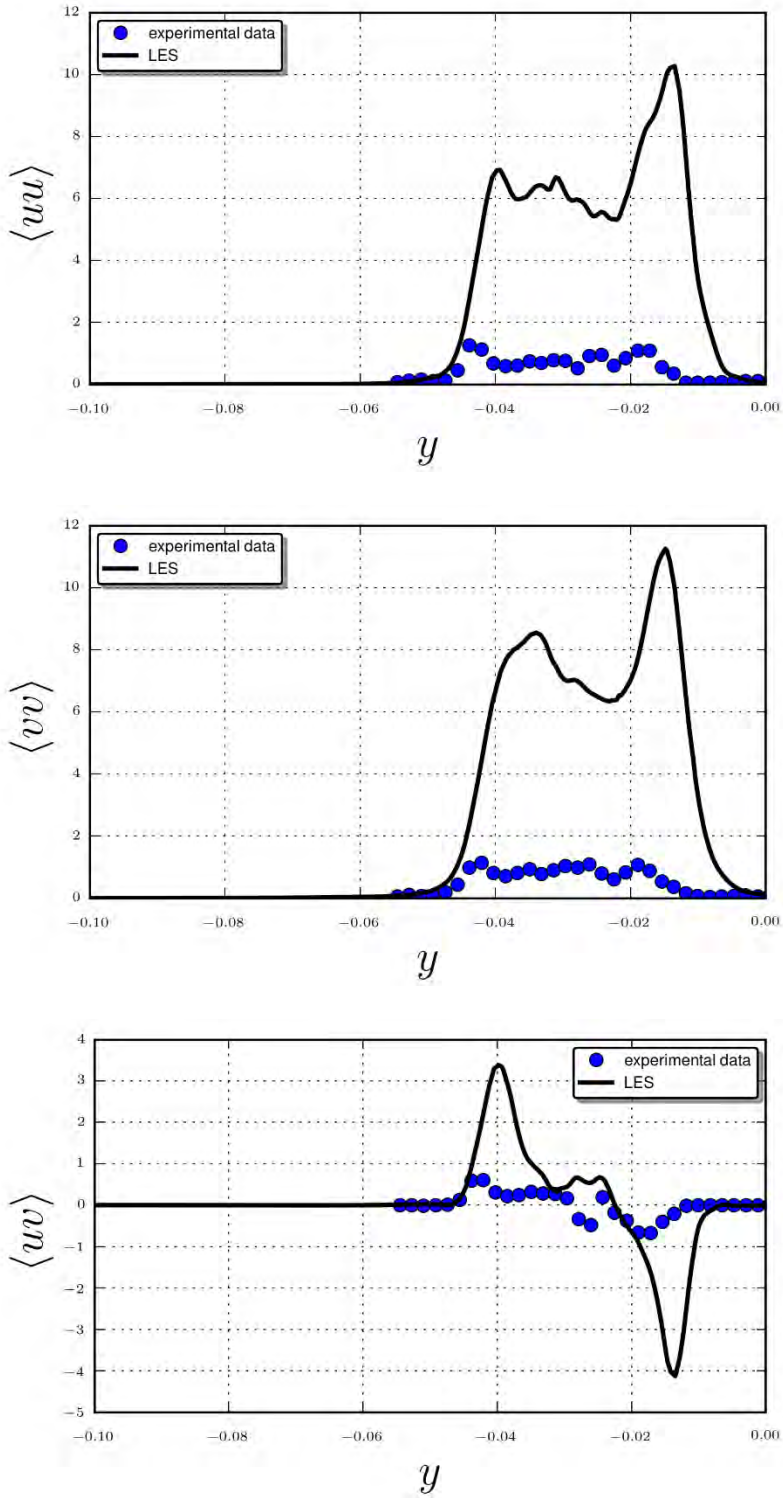

Figure 3-100. Reynold stresses (m^2/s^2) along line G at z/H = 0.50 for unit cell III. Unit for y is meters. For reference, the crossflow velocity is 7.68 m/s.

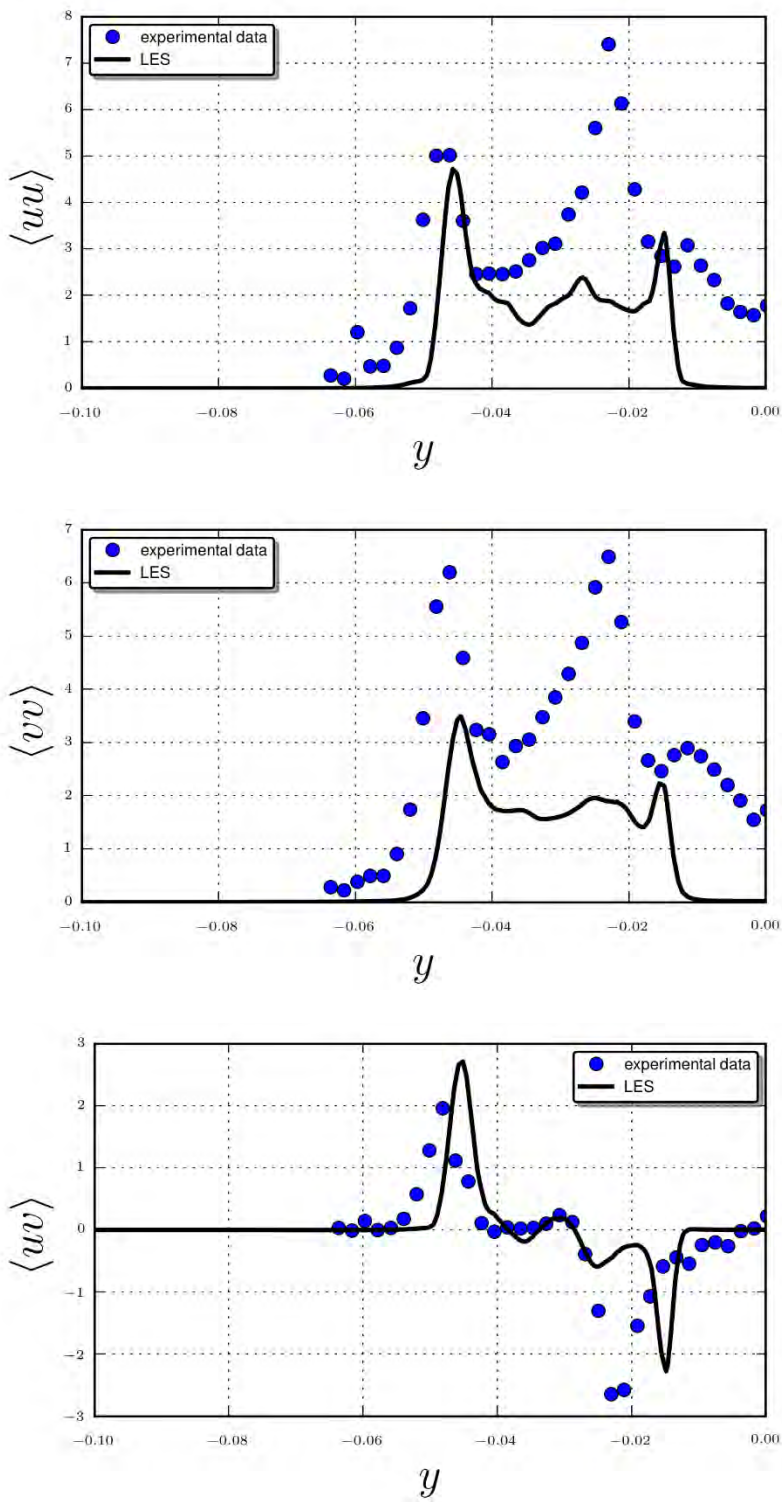

Figure 3-101. Reynold stresses (m^2/s^2) along line G at z/H = 0.75 for unit cell III. Unit for y is meters. For reference, the crossflow velocity is 7.68 m/s.

Results from line Ein showed the same level of difficulty in capturing the full three-dimensional nature of the flow as previously discussed for line G, and are not presented here. However, for line Eout, which is the wake of the unit cell, the accuracy of the modeling approach has increased, and mimics the degree of agreement seen in case I and case II, suggesting the flow has become better mixed, although still not as two-dimensional as certain line traces in case I. Results for velocity are shown in Figure 3-102 and Figure 3-103 for z/H = 0.5 and 0.75, respectively, and the stresses are shown in Figure 3-104 and Figure 3-105 for those same planes.

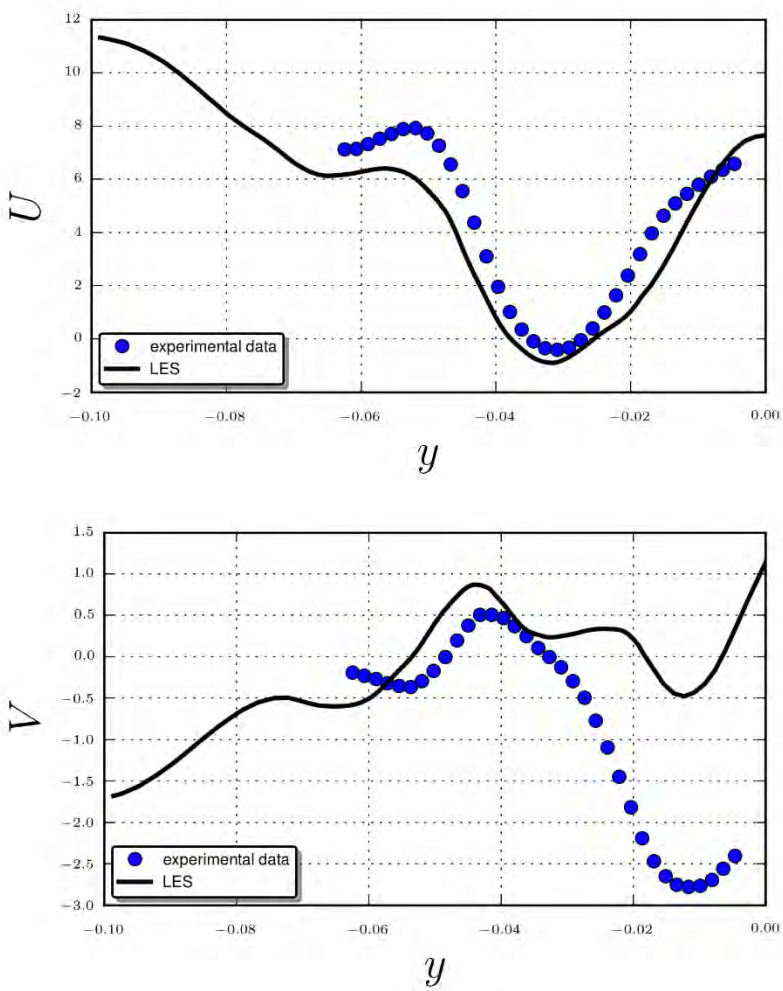

Figure 3-102. Velocities (m/s) along line Eout at z/H = 0.50 for unit cell III. Unit for y is meters. For reference, the crossflow velocity is 7.68 m/s.

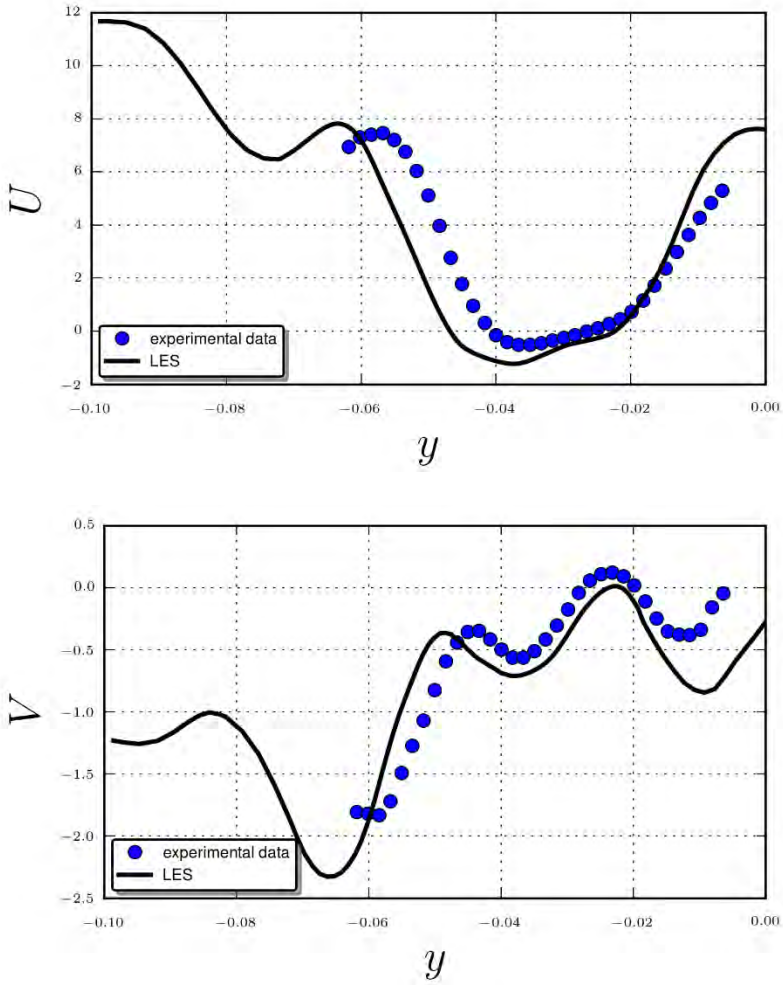

Figure 3-103. Velocities (m/s) along line Eout at z/H = 0.75 for unit cell III. Unit for y is meters. For reference, the crossflow velocity is 7.68 m/s.

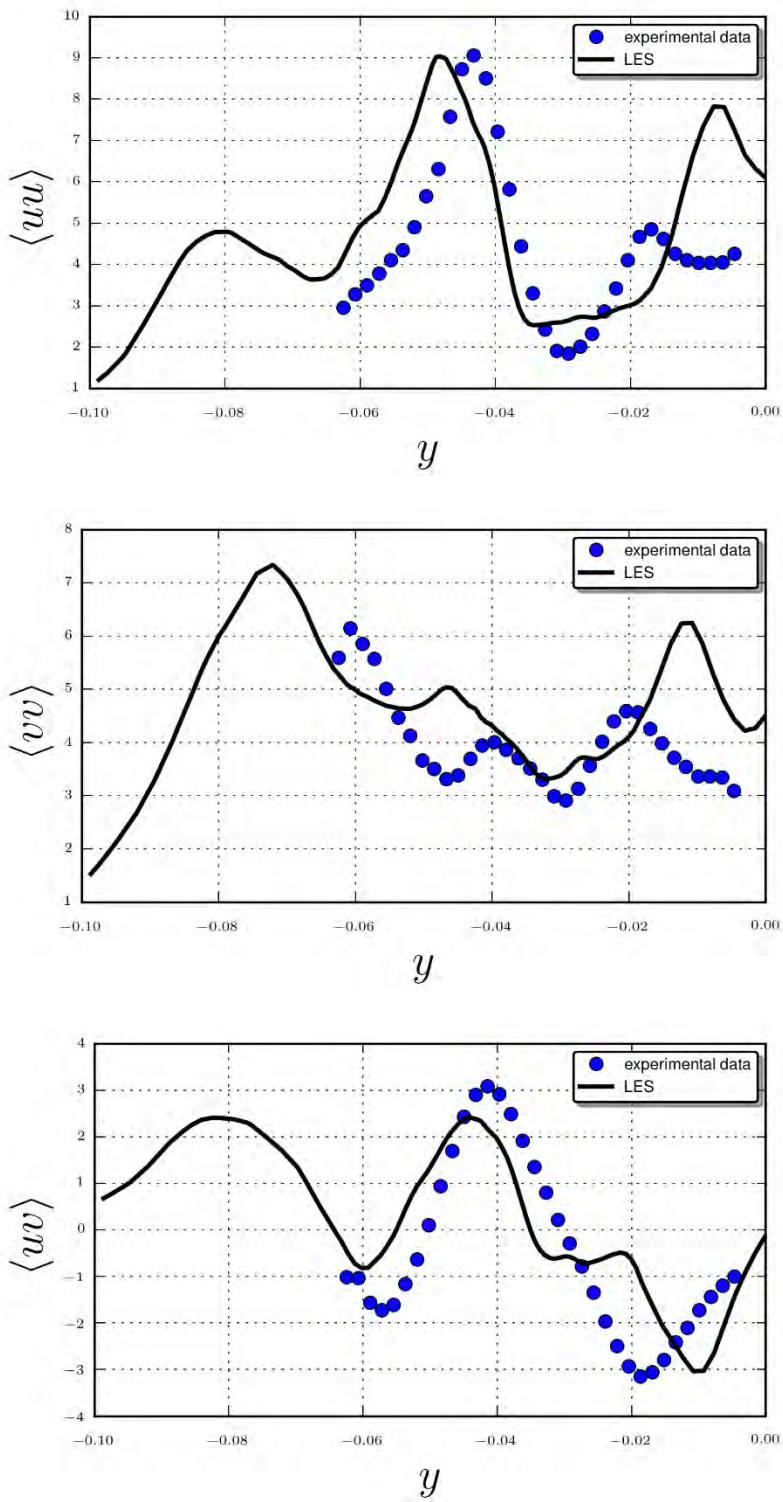

Figure 3-104. Reynold stresses (m^2/s^2) along line Eout at z/H = 0.50 for unit cell III. Unit for y is meters. For reference, the crossflow velocity is 7.68 m/s.

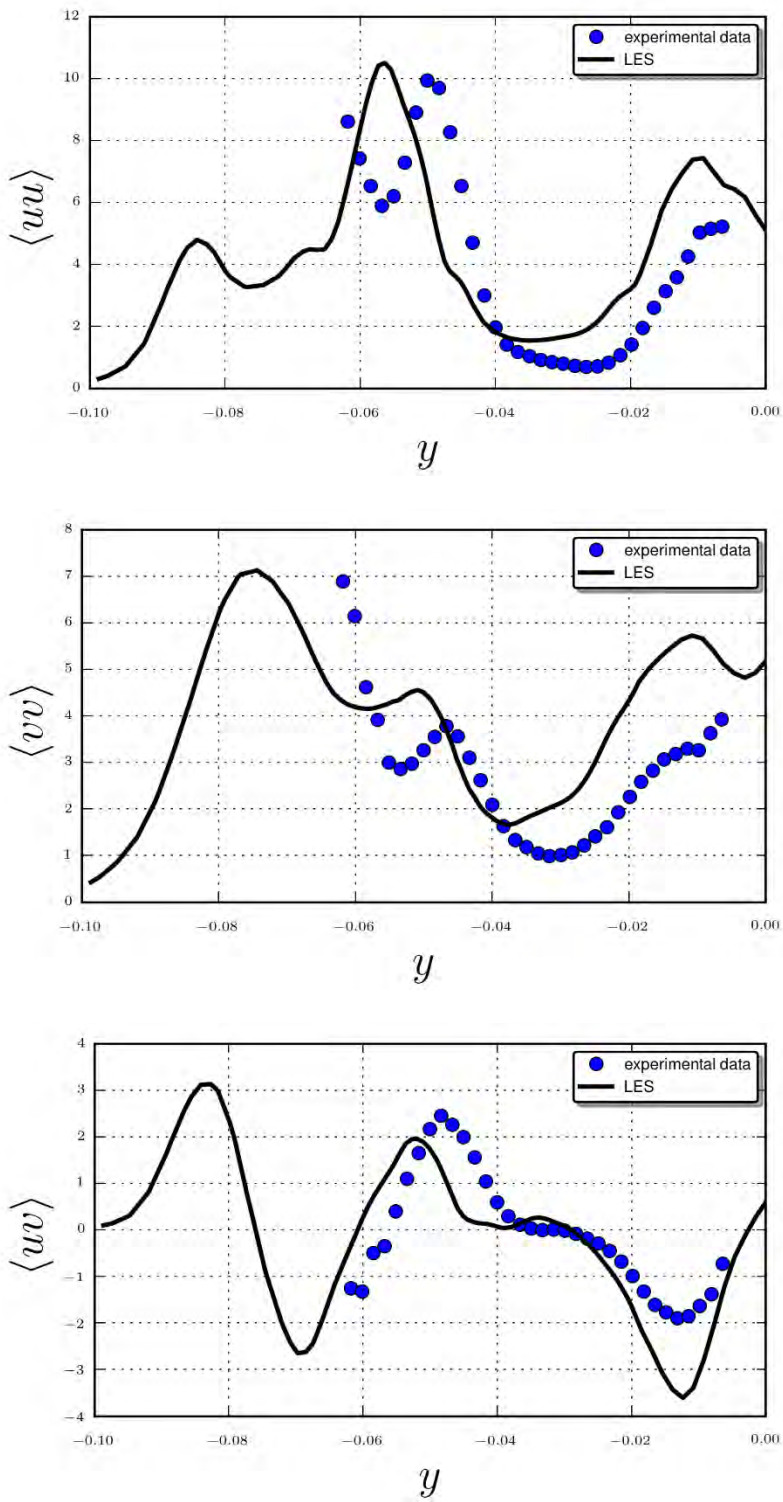

Figure 3-105. Reynold stresses (m^2/s^2) along line Eout at z/H = 0.75 for unit cell III. Unit for y is meters. For reference, the crossflow velocity is 7.68 m/s.

This very preliminary data comparison has provided promise in ultimately capturing the flow physics of this complex thermal-fluid condition. Although the current data set can prove useful for modeling efforts, further experimental work is recommended to establish metrics for the jet penetration behavior. This will aid in determining whether observed discrepancies are due to the inability to capture the mixing behavior or the physics related to the jet penetration. Further computational work is also recommended in order to evaluate turbulence models and determine the usefulness of RANS based approaches (recall only LES was conducted here).

4 Reduced-Order Modeling

4.1.1 Proper Orthogonal Decomposition

The main idea in proper orthogonal decomposition (POD) is finding a subspace V_{POD} such that the average L_2-norm of the difference between solution fields and the projection of solution fields onto V_{POD} is minimized. The POD subspace, V_{POD}, can be formed by a set of basis functions, $\{\phi_i(\vec{x})_{i=1}^m\}$ ($V_{POD} = span\{(\phi_i(\vec{x})_{i=1}^m\} \subset L_2(\Omega)\big)$. In other words, if $\hat{u}_k(\vec{x})$ represents the projection of a solution field, $u_k(\vec{x})$, onto V_{POD}, POD problem can be formulated as follows:

$$<\| u_k(\vec{x}) - \hat{u}_k(\vec{x}) \|_{L^2(\Omega)}> \tag{4-1}$$

where $<\cdot>$ represents the averaging operator, and $L^2(\Omega)$ is the Hilbert space of square-integrable functions with the following properties:

$$\big(f(\vec{x}), g(\vec{x})\big) = \int_\Omega f(\vec{x}) g^*(\vec{x})\, d\vec{x} \quad \forall f(\vec{x}), g(\vec{x}) \in \Omega \tag{4-2}$$

$$\| f(\vec{x}) \|_{L^2(\Omega)} = \big(f(\vec{x}), f^*(\vec{x})\big)^{\frac{1}{2}} \quad \forall f(\vec{x}) \in \Omega \tag{4-3}$$

where $f^*(\vec{x})$ is the complex conjugate of function $f(\vec{x})$.

A computationally efficient method of calculating the POD modes is by the method of snapshots. This process is summarized as follows. Applying variational calculus to the maximization problem of Eq. (4-1) provides the following equation (Euler-Lagrange integral):

$$\int_{\Omega_x} < u(x) \cdot u(x') > \varphi(x') dx' = \lambda \varphi(x) \tag{4-4}$$

Writing the ensemble average (i.e., the terms inside the angled brackets) as a time average of the N_T snapshots and interchanging the sum and integral provide:

$$\frac{1}{N_T} \sum_{k=1}^{N_T} u_{(k)}(x) \int_{\Omega_x} u_{(k)}(x') \varphi(x') dx' = \lambda \varphi(x) \tag{4-5}$$

This equatuion could be solved as an eigenvalue problem. However, that is computationally expensive because $u(x)$ is the size of the number of data points (i.e., grid points in a mesh). The method of

snapshots offers a computationally efficient way of solving for these modes. To do so, Eq. (4-5) can be concisely expressed as:

$$\sum_{j=1}^{N_T} c_j \int_{\Omega_x} u_{(i)}(x) u_{(j)}(x) dx = \lambda \int_{\Omega_x} u_{(i)} \varphi(x) dx \tag{4-6}$$

Letting $a_{ij} = \int_{\Omega_x} u_{(i)}(x) u_{(j)}(x) dx$, this problem may be solved as an $N_T \times N_T$ eigenvalue problem. Each snapshot can be represented as a linear combination of the POD modes, where N is the number of retained modes.

$$U_j = \sum_{i=1}^{N} a_{ij} \varphi_i \tag{4-7}$$

where U_j is the jth velocity field, a_{ij} is the reconstruction coefficient for the jth velocity field with the ith mode, and φ_i is the ith mode. Each row of the coefficient matrix represents the projection of the jth mode onto the ith snapshot:

$$a_{ij} = \left(\varphi_j, U_i\right) \tag{4-8}$$

To quantify the error associated with reconstructing the velocity field like this, the following L_2 error formulation is utilized.

$$L_{2,Error} = \frac{\int_{\Omega} \left(\left|U_j\right|^2 - \left|\sum_{i=1}^{N} a_{ij} \varphi_i\right|^2 \right) d\Omega}{\int_{\Omega} \left(\left|U_j\right|^2 \right) d\Omega} \tag{4-9}$$

For the treatment of the surrogate modeling, a radial basis function interpolation is utilized. A regression approach may be employed to construct a surrogate model of a velocity field within the bounds of the time-based snapshots. That is,

$$U_j = \sum_{i=1}^{N} a_{ij}(t) \varphi_i \tag{4-10}$$

Given a plot of POD mode amplitude from the correlation matrix, y, versus time, t:

$$f(\vec{t}) = \sum_{i=1}^{N} \alpha_i g_i(\vec{t}) \tag{4-11}$$

where α_i are the coefficients of this linear combination and g_i are the selected radial basis functions (RBF). The forms of radial basis function, g_i, that are used in the present study include:

- linear spline, $\| t - t_j \|$
- cubic spline, $\| t - t_j \|^3$
- Gaussian, $e^{-\frac{\|t-t_j\|}{c_j^2}}$

Then, applying a specific radial basis function to the general equation:

$$f(\vec{t}_j) = y_i = \sum_{i=1}^{N} \alpha_i g_i(t_j), \quad j = 1,2,\dots,N \tag{4-12}$$

In matrix form, the coefficients can be calculated via:

$$\{\alpha\} = [G]^{-1}\{y\} \tag{4-13}$$

Given the RBF interpolation coefficients, α, the new velocity field may be interpolated for a given time, t:

$$u^{new}(\vec{x}, t) = \sum_{i=1}^{N} \alpha^{new} \varphi_i(\vec{x}) \tag{4-14}$$

4.1.2 Galerkin-Projection for Incompressible Navier-Stokes

For Newtonian fluids, the Navier-Stokes equations can be written as:

$$\rho \dot{\vec{u}}(\vec{x}, t) = 0, \quad \forall \vec{x} \in \Omega, t \in [0, t_{max}] \tag{4-15}$$

$$\rho \dot{\vec{u}}(\vec{x}, t) + \vec{u}(\vec{x}, t) \cdot \nabla \vec{u}(\vec{x}, t) = -\nabla p(\vec{x}, t) + \mu \nabla^2 \vec{u}(\vec{x}, t), \quad \forall \vec{x} \in \Omega, t \in [0, t_{max}] \tag{4-16}$$

or in indicial (i.e., Einstein or summation) notation (and dropping the functional dependencies for brevity) as:

$$\rho \dot{u}_i = 0 \tag{4-17}$$

$$\rho \dot{u}_i + u_k u_{i,k} = -p_{,i} + \mu u_{i,jj} \tag{4-18}$$

where $\vec{u}$ is the velocity vector, ρ is the fluid density, and μ is the fluid viscosity. Additionally, the overdot in the first term of each of the four previous equations symbolizes a temporal derivative. The weak form of Eqs. (4-17) and (4-18) can be derived by taking the inner product of the equation with a test function (vector-valued function) which satisfies the following condition:

$$\vec{v} \in L^2(\Omega) \tag{4-19}$$

where $L^2(\Omega)$ is a set of functions that are square-integrable along with their first derivative in the domain of Ω. Then, integrating over the domain, the weighted residual equations can be written as:

$$\int_\Omega \rho v_i \dot{u}_i d\vec{x} + \int_\Omega v_i u_k u_{i,k} d\vec{x} - \int_\Omega p v_{i,i} d\vec{x} + \int_\Omega \mu v_{i,j} u_{i,j} d\vec{x} = 0 \tag{4-20}$$

To implement the POD modes into the above weak form to create a ROM, all that is then necessary is to apply the m previously obtained vector modes, $\{\phi_{ji}\}_{j=1}^{m}$, as the test and trial functions such that:

$$v_i(\vec{x}) = \phi_{qi}(\vec{x}), \quad for\ q = 1,2,\dots,m \tag{4-21}$$

$$u_i(\vec{x},t) = \bar{u}_i(\vec{x}) + \sum_{r=1}^{m} a_r(t)\phi_{ri}(\vec{x}) \tag{4-22}$$

where $\bar{u}_i$ is the average velocity field calculated from the ensemble used to generate the modes and a_r is the modal coefficient corresponding to the rth POD mode (i.e., the coefficients to be solved for in the ROM velocity numerical approximation). Noting that if the modes are generated from an ensemble that assumes incompressibility, then the modes will naturally have zero divergence. Substituting Eq. (4-22) into (4-20), and using product rule and divergence theorem results in the following relationship:

$$\int_\Omega \rho \phi_{qi} \left(\dot{u}_i + u_k u_{i,k}\right) + \mu \phi_{qi,j} u_{i,j} d\vec{x} - \int_\Gamma p \phi_{qi,i} n_i d\vec{x} = 0 \tag{4-23}$$

where n_i represents the normal vector of each boundary. The second integral in Eq. (4-23), which is over the boundaries of the domain, requires careful consideration.

4.1.3 Application to Flow Around a Circular Cylinder

To test the formulated POD-based ROM, a fundamental test case of flow around an isothermal cylinder is investigated, the schematic and boundaries of which can be seen in Figure 4-1 and Figure 4-2, respectively.

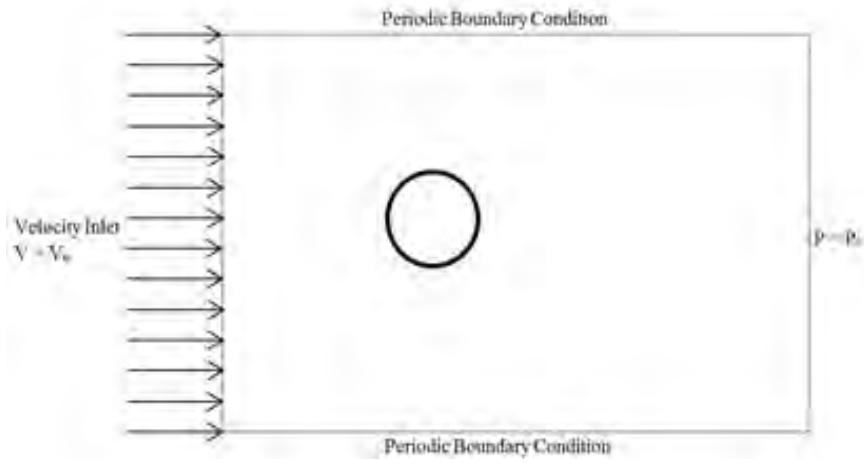

Figure 4-1: Schematic of flow around a circular cylinder

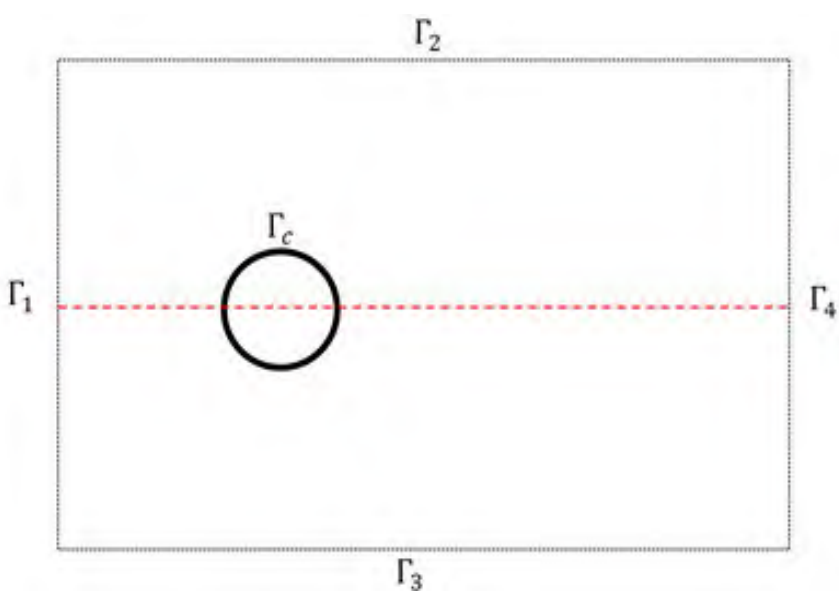

Figure 4-2: Boundary designations for POD test case

Utilizing the boundaries preset in Figure 4-2, the second integral in Eq. (4-23) can be divided into five components, each corresponding to one of the boundaries. On Γ_1, all of the POD modes are zero since:

$$u_i(\vec{x},t)|_{\Gamma_1} = \bar{u}_i(\vec{x})|_{\Gamma_1} + \sum_{r=1}^{m} a_r(t)\phi_{ri}(\vec{x}) \tag{4-24}$$

$$u_i(\vec{x},t)|_{\Gamma_1} = V_i^{in}(\vec{x}), \bar{u}_i(\vec{x})|_{\Gamma_1} = V_i^{in}(\vec{x}) \Longrightarrow \phi_{ri}(\vec{x})|_{\Gamma_1} = 0 \tag{4-25}$$

The POD modes also satisfy the periodic boundary condition on Γ_2 and Γ_3. Since the normal vectors of Γ_2 and Γ_3 are in opposite directions, $\int_{\Gamma_3} p\phi_{qi,i}n_i d\vec{x} + \int_{\Gamma_4} p\phi_{qi,i}n_i d\vec{x} = 0$. The POD modes are skew symmetric with respect to the dotted line in Figure 4-2 and this means that:

$$\int_{\Gamma_3} p\phi_{qi,i}n_i d\vec{x} = \int_{\Gamma_4} p\phi_{qi,i}n_i d\vec{x} = 0 \tag{4-26}$$

Now, Eq. (4-23) reduces to:

$$\int_{\Omega} \rho\phi_{qi}\left(\dot{u}_i + u_k u_{i,k}\right) + \mu\phi_{qi,j}u_{i,j}d\vec{x} = 0 \tag{4-27}$$

Substituting the solution expansion (Eq. (4-22)) into Eq. (4-27), a non-linear evolution equation for the coefficients can be obtained as:

$$\rho\dot{a}_q + A_{qrs}a_r a_s + B_{qr}a_r + C_q = 0, \quad for\ q = 1,2,\dots,m \tag{4-28}$$

where:

$$A_{qrs} = \int_{\Omega} \phi_{qi}\phi_{rk}\phi_{si,k}d\vec{x} \tag{4-29}$$

$$B_{qr} = \int_{\Omega} \phi_{qi}\phi_{rk}\bar{u}_{i,k}d\vec{x} + \int_{\Omega} \phi_{qi}\phi_{ri,k}\bar{u}_k d\vec{x} + \int_{\Omega} \phi_{qi,j}\phi_{ri,j}d\vec{x} \tag{4-30}$$

$$C_q = \int_{\Omega} \phi_{qi}\bar{u}_k\bar{u}_{i,j}\, d\vec{x} + \int_{\Omega} \phi_{qi,j}\bar{u}_{i,j}d\vec{x} \tag{4-31}$$

Eq. (4-27) can then be solved with any standard nonlinear ordinary differential equation solution method to determine the values of each modal coefficient over the time domain of the problem considered, $a_q(t)$, and thereby approximate the flow field through a ROM.

4.1.4 Accuracy of Reduced Order Model

To compare the accuracy of ROMs constructed from URANS and LES data, two case studies were considered here: (1) a 2D model of a cylinder in a channel was created to obtain turbulent fields akin to what is present in a small part of the lower plenum. The model was built and meshed using the commercial software package ANSYS and subsequently pre-processed and analyzed using the FLUENT CFD software. The URANS solver was used in conjunction with a κ-ϵ turbulence model was employed. A LES simulation of a 2D flow past a cylinder was performed in OpenFOAM. The schematic of the LES model is shown in Figure 4-3. The diameter of the cylinder is 1 m and the diameter of the domain is 100 m. The inlet velocity and viscosity is set such that the Reynolds number of the turbulent flow was fixed at 3900. LES requires a relatively fine mesh which will make the post-processing computationally expensive. Therefore, once the LES simulation was completed, a coarse mesh was built on the domain and the flow fields was interpolated to be compatible with the new coarse mesh.

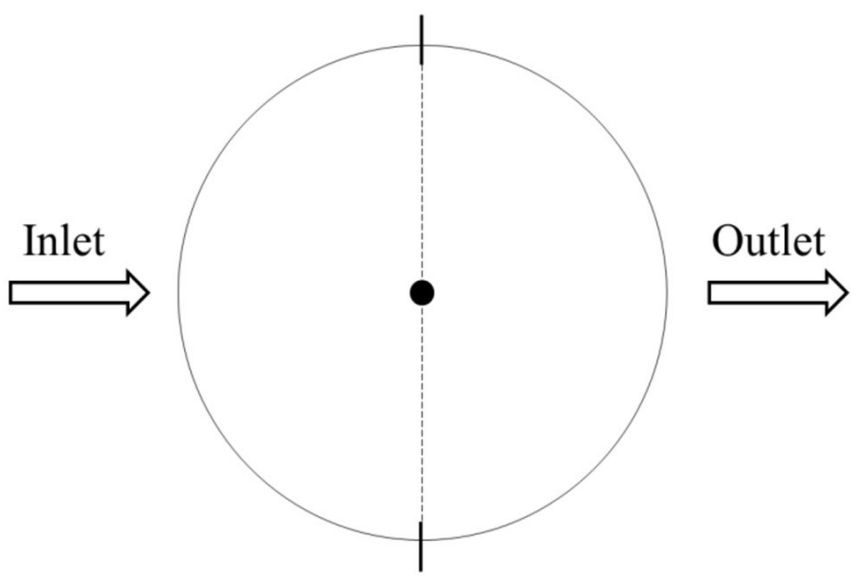

Figure 4-3: Schematic of LES computational domain

Sixteen snapshots of the fluid velocity within on period of the vortex shedding were extracted for both simulations. POD was then applied to the snapshot fluid fields to extract a set of fluid velocity modes that are both orthogonal and optimal in an L_2-average sense for the representation of the original set of fluid fields. The x-component of the first two POD modes (i.e., coherent structures) for each simulation are shown in Figure 4-4. In addition, Table 4-1 and Table 4-2 show the eigenvalues corresponding to the first four POD modes for each simulation.

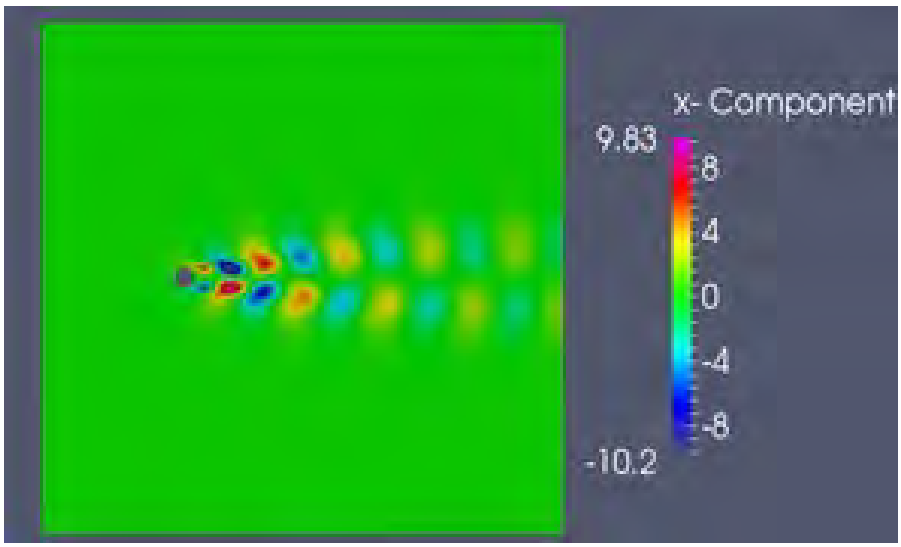

Figure 4-4: x-component of the first POD mode obtained from URANS

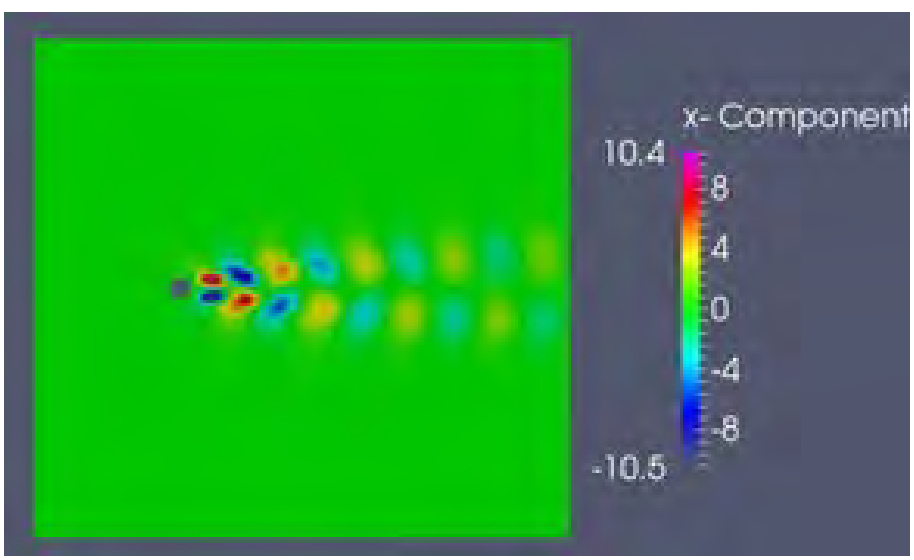

Figure 4-5: x-component of the second POD mode obtained from URANS

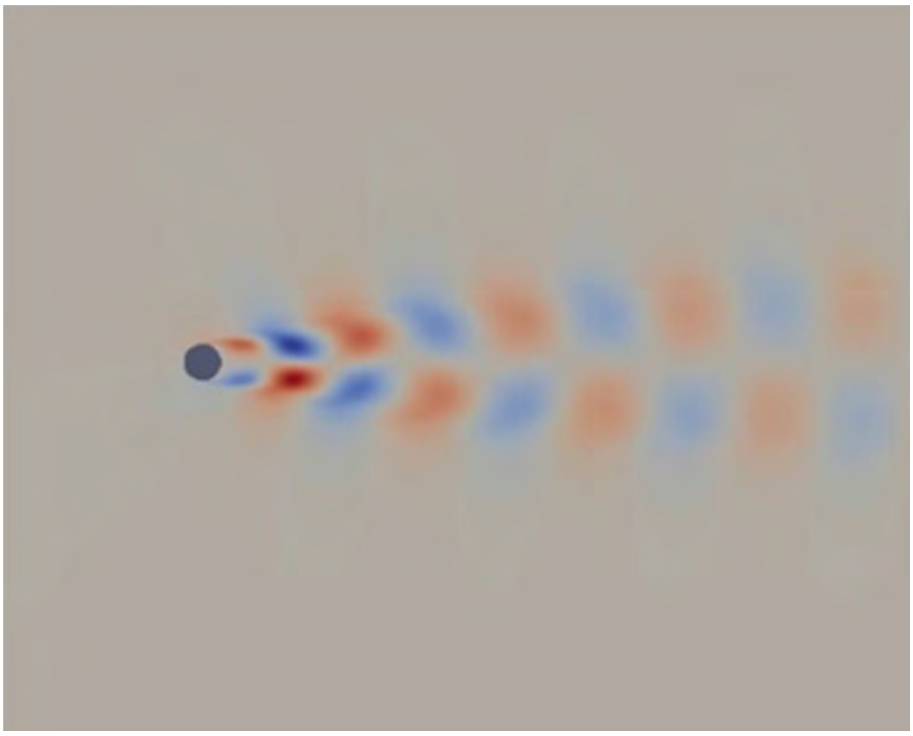

Figure 4-6: *x*-component of the first POD mode obtained from LES

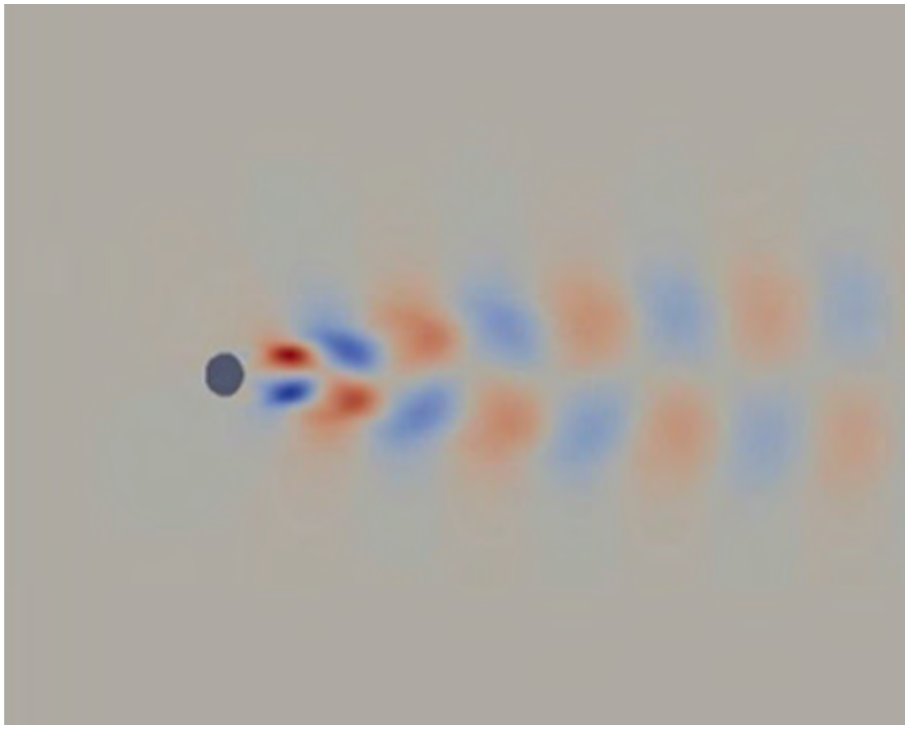

Figure 4-7: *x*-component of the second POD mode obtained from LES

Solving Eqs. (4-28)-(4-31) gives the modal coefficients of the POD approximation (Eq. (4-27)). Figure 4-8-Figure 4-10 show the variation of the first two modal coefficients obtained Galerkin projection approach for both URANS and LES data.

Table 4-1: POD Modes and Corresponding Eigenvalues Obtained from URANS

Mode	Eigenvalue	Cumulative Energy (%)
1st	2.29×10^{-3}	37.04
2nd	2.19×10^{-3}	72.53
3rd	1.54×10^{-3}	97.44
4th	6.45×10^{-5}	99.73

Table 4-2: POD Modes and Corresponding Eigenvalues Obtained from LES

Mode	Eigenvalue	Cumulative Energy (%)
1st	2.29×10^{-3}	50.90
2nd	2.19×10^{-3}	98.28
3rd	1.54×10^{-3}	99.17
4th	7.71×10^{-5}	99.96

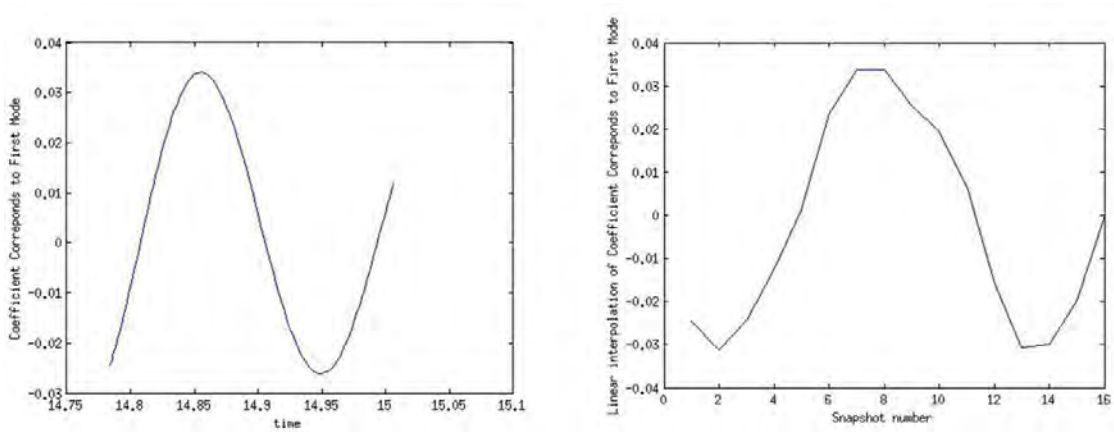

Figure 4-8: Comparison between the first modal coefficient results of the Galerkin projection approach (LHS figure) and the linear interpolation (regression-based approach) (RHS figure)

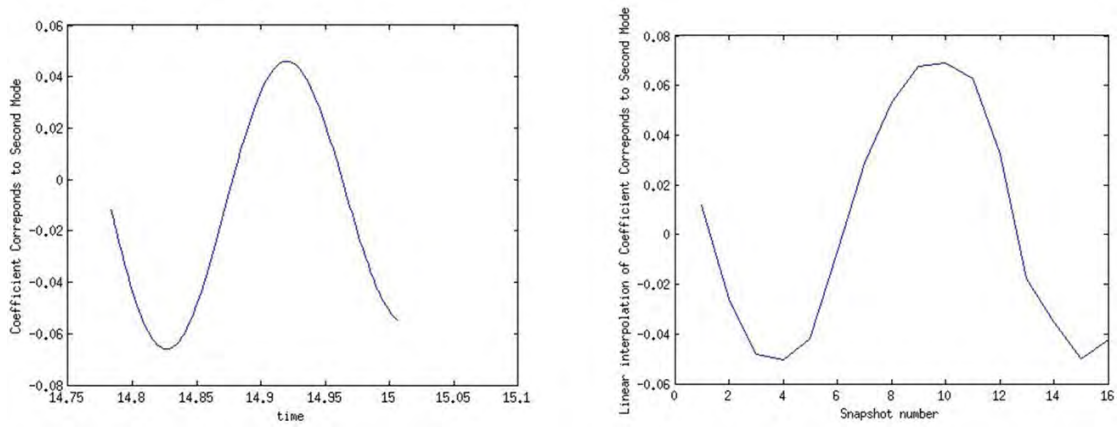

Figure 4-9: Comparison between the second modal coefficient results of the Galerkin projection approach (LHS figure) and the linear interpolation (regression-based approach) (RHS figure)

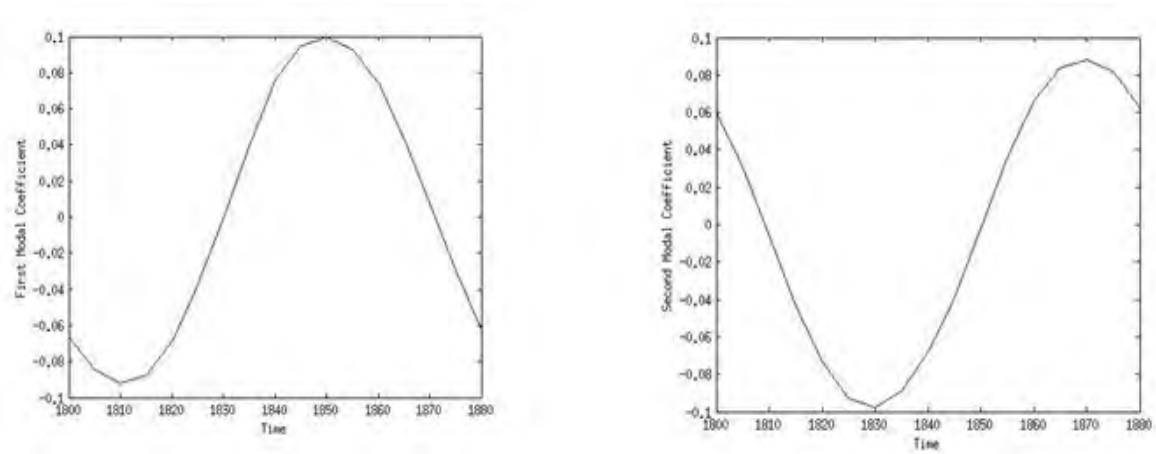

Figure 4-10: Variation of first two model coefficients of the ROM constructed from LES data

Clearly the Galerkin projection provides a smoother representation of the entire transient response, which is expected since the Galerkin projection is solving a transient differential equation. In addition, although there is clear similarity between the Galerkin projection, there is also significant differences at some time points, with the Galerkin projection providing a more accurate representation overall.

To test the accuracy of the Galerkin projection approach, randomly-selected flow field was predicted (note that these flow fields were not in the original set of snapshots) using ROM constructed from

both LES data and URANS data. The results for predictions of these new flow fields using Galerkin projection approach is summarized in Table 4-3 and Table 4-4.

Table 4-3: Prediction of velocity fields using ROM constructed from URANS data

Time	14.84	14.90	14.95
1st Modal Coefficient	0.031	0.055	-0.026
2nd Modal Coefficient	0.055	0.033	0.023
3rd Modal Coefficient	0.021	0.038	-0.036
4th Modal Coefficient	-0.002	0.012	0.008
L_2 Error (%)	1.86	1.93	1.34

Table 4-4: Prediction of velocity fields using ROM constructed from LES data

Time	1810	1860
1st Modal Coefficient	-0.092	0.074
2nd Modal Coefficient	0.012	0.067
3rd Modal Coefficient	0.005	0.008
4th Modal Coefficient	0.002	-0.012
L_2 Error (%)	3.11	2.74

A comparison between ROMs constructed from URANS data and LES data was presented. Through a URANS simulation of a flow past a cylinder, the Galerkin projection approach was applied and compared to a computationally inexpensive regression-based reduced-order modeling approach. A flow past a cylinder in an open domain was selected to show the capability of ROM constructed from LES data in prediction of velocity fields. The accuracy of the predication of velocity fields for both ROM are in the same order and there is no significant difference in the L_2 error listed in Table 4-3 and Table 4-4.

4.2 Reduced-Order Modeling of Compressible Turbulent Flows

For incompressible flows, velocity is the only flow variable that is dynamically important since pressure acts only to enforce the incompressibility constraint. In some cases (e.g., confined flow past a cylinder), pressure may be eliminated completely from the equations. However for compressible flows, the thermodynamic variables are dynamically important and must be included in the actual dynamics, not merely as a constraint. Therefore, a Galerkin projection basis that can be incorporated into the compressible

Navier-Stokes equations can be obtained from velocity and thermodynamic variables field. The following outlines the details of the POD Galerkin projection for the ROM of the compressible Navier-Stokes equations.

4.2.1 POD Galerkin Projection ROM for Compressible Navier-Stokes

Fully-compressible Navier-Stokes equations can be written as follows:

$$\frac{\partial \rho}{\partial t} + \frac{\partial}{\partial x_i}(\rho u_i) = 0 \tag{4-32}$$

$$\rho \frac{Du_i}{Dt} = -\frac{\partial p}{\partial x} + \frac{1}{\mathrm{Re}} \frac{\partial}{\partial x_j}\left[2S_{ij} - \frac{2}{3}\delta_{ij}\frac{\partial u_k}{\partial x_k}\right] = 0 \tag{4-33}$$

$$\rho \frac{DT}{dt} + (\gamma - 1)\rho T \frac{\partial u_k}{\partial x_k} = \frac{\gamma}{\mathrm{Re}}\left(2S_{ij}S_{ij} - \frac{2}{3}\left(\frac{\partial u_k}{\partial x_k}\right)^2\right) + \frac{\gamma}{\mathrm{RePr}}\frac{\partial^2 T}{\partial x_k^2} \tag{4-34}$$

And the following constitutive model can be used, assuming that the fluid is an ideal gas:

$$p = (\gamma - 1)\rho T \tag{4-35}$$

where ρ is the density, $\vec{u}$ is the velocity vector field, p is the pressure field, μ is the viscosity, and δ_{ij} is the Kronecker delta function. The rate of strain tensor, S_{ij}, can be obtained from the following equation:

$$S_{ij} = \frac{1}{2}\left(\frac{\partial u_i}{\partial x_j} + \frac{\partial u_j}{\partial x_i}\right) \tag{4-36}$$

To combine the first three equations of Navier-Stokes (Eqs. (4-32), (4-33), and (4-34)), a vector $\vec{q}$ is defined as: $\vec{q} = f(\rho, u_1, u_2, u_3, T)$. With the definition of $\vec{q}$, each equation can be re-written as follows:

$$\frac{\partial \rho}{\partial t} = R(\vec{q}) \tag{4-37}$$

$$\rho \frac{\partial u_i}{\partial t} = U_i(\vec{q}) \tag{4-38}$$

$$\rho \frac{\partial T}{\partial t} = \Theta(\vec{q}) \tag{4-39}$$

where

$$R(\vec{q}) = -(\vec{u} \cdot \nabla)p - \frac{\partial u_k}{\partial x_k} \tag{4-40}$$

$$U_i(\vec{q}) = -\rho(\vec{u} \cdot \nabla)u_i - \frac{\partial p}{\partial x_i} + \frac{1}{\mathrm{Re}}\frac{\partial}{\partial x_j}\left(2S_{ij} - \frac{2}{3}\delta_{ij}\frac{\partial u_k}{\partial x_k}\right) \tag{4-41}$$

$$\Theta(\vec{q}) = -(\gamma - 1)\rho T\frac{\partial u_k}{\partial x_k} + \frac{\gamma}{\mathrm{Re}}\left(2S_{ij}S_{ij} - \frac{2}{3}\left(\frac{\partial u_k}{\partial x_k}\right)^2 + \frac{\gamma}{\mathrm{RePr}}\nabla^2 T\right) \tag{4-42}$$

Now, the compressible Navier-Stokes equations can be presented in the following compact form:

$$A(\vec{q})\dot{\vec{q}} = \vec{f}(\vec{q}) \tag{4-43}$$

where

$$A(\vec{q}) = B + L(\vec{q}) = \begin{bmatrix} 1 & 0 & 0 \\ 0 & \rho & 0 \\ 0 & 0 & \rho \end{bmatrix} \tag{4-44}$$

$$\vec{f}(\vec{q}) = \left(R(\vec{q}), U_i(\vec{q}), \Theta(\vec{q})\right) \tag{4-45}$$

Now, the POD algorithm can be applied to snapshots of vector $\vec{q}$. Let $\{\phi_k\}$ be a basis for the space containing $\vec{q}$, then any possible solution of $\vec{q}$ can be expressed as a linear combination of bases:

$$\vec{q}(\vec{x}, \mathrm{t}) = \sum_k a_k(t)\vec{\varphi}_k(\vec{x}) \tag{4-46}$$

Inserting the solution expansion into Eq. (4-45) gives:

$$\left[B + L\left(\sum_t a_l(t)\vec{\varphi}_l(\vec{x})\right)\right]\sum_k \dot{a}_k\,(t)\vec{\varphi}_k(\vec{x}) = \vec{f}(\vec{q}) \tag{4-47}$$

By taking an inner product of Eq. (4-47) with the basis, the following equation can be obtained:

$$\sum_k \dot{a}_k\left(\left(\vec{\varphi}_j, B\vec{\varphi}_k\right) + \sum_l a_l\left(\vec{\varphi}_j, L(\vec{\varphi}_l)\vec{\varphi}_k\right)\right) = \left(\vec{\varphi}_j, \vec{f}(\vec{q})\right) \tag{4-48}$$

Then Eq. (4-48) can be written in matrix form:

$$M(a)\dot{a} = \check{f}(a) \tag{4-49}$$

where

$$M_{jk} = \left(\vec{\varphi}_j, B\vec{\varphi}_k\right) + \sum_l a_l\left(\vec{\varphi}_j, L(\vec{\varphi}_l)\vec{\varphi}_k\right)\check{f}_j = \sum_l a_l\left(\vec{\varphi}_j, f_1(\vec{\varphi}_l)\right)$$
$$+ \sum_{l,m} a_l a_m \left(\vec{\varphi}_j, \left(f_2(\vec{\varphi}_l, \vec{\varphi}_m)\right)\right) + \sum_{l,m,n} a_l a_m a_n \left(\vec{\varphi}_j, f_3(\vec{\varphi}_l, \vec{\varphi}_m, \vec{\varphi}_n)\right) \tag{4-50}$$

4.2.2 Application to Flow Around a Circular Cylinder

An example set was considered to verify the capability of the POD Galerkin projection approach presented and examine a simple comparison between this Galerkin projection approach and the regression-based approach. A LES simulation of 3D flow past a cylinder was performed in OpenFOAM to obtain turbulent fields. The schematic of the model of flow past a cylinder is shown in Figure 4-3. The diameter of the cylinder is 1 m and the diameter of the domain is 100 m, with thickness of π in the axial direction. The Reynolds number of the turbulent flow was set to 7190. LES requires a relatively fine mesh which will make the post-processing computationally expensive. Therefore, once the LES simulation was completed, a coarse mesh was built on the domain and the flow fields were interpolated to be compatible with the new coarse mesh. Twelve snapshots were chosen within the interval of 1640 – 1780 s to build a reduced-order model. As it was stated earlier, for compressible flows, the thermodynamic variables are dynamically important and must be included in the actual dynamics, not merely as a constraint. Therefore, the solution fields that were extracted from the simulation (snapshots) has the following format:

$$\left(u_x, u_y, u_z, T, \frac{P}{\rho}\right) \tag{4-51}$$

where u_x, u_y, and u_z are velocity components in the x, y, and z direction respectively, T is the temperature field, P is the pressure field, and ρ is the density field. To study the effects of considering thermodynamic variables in creating reduced-order models, POD was first applied to the snapshots of velocity fields only. Figure 4-11 shows the x-component and y-component of the first two highest-energy velocity modes obtained from POD. In addition, Table 4-5 shows the eigenvalues corresponding to each of these five modes and also the corresponding cumulative energy and Figure 4-12 shows how the cumulative energy converges.

Table 4-5: Eigenvalues corresponding to each of the first five velocity POD modes

	1st Mode	2nd Mode	3rd Mode	4th Mode	5th Mode
Eigenvalue	3.5541	2.4458	0.7267	0.6225	0.4927
Cumulative Energy	38.71	62.51	73.27	80.05	85.43

A similar approach was pursued for temperature and P/ρ snapshots, but no meaningful basis was obtained for each of the dynamic variables. It appears that temperature and P/ρ snapshots do not change significantly during the interval of interest. To measure the change of each dynamic variable in the ensemble of snapshots, the variance of each field was computed:

$$var(P/\rho) = 7.84 \times 10^{-8} \tag{4-52}$$

$$var(T) = 2.20 \times 10^{-5} \tag{4-53}$$

$$var(u) = 0.133 \tag{4-54}$$

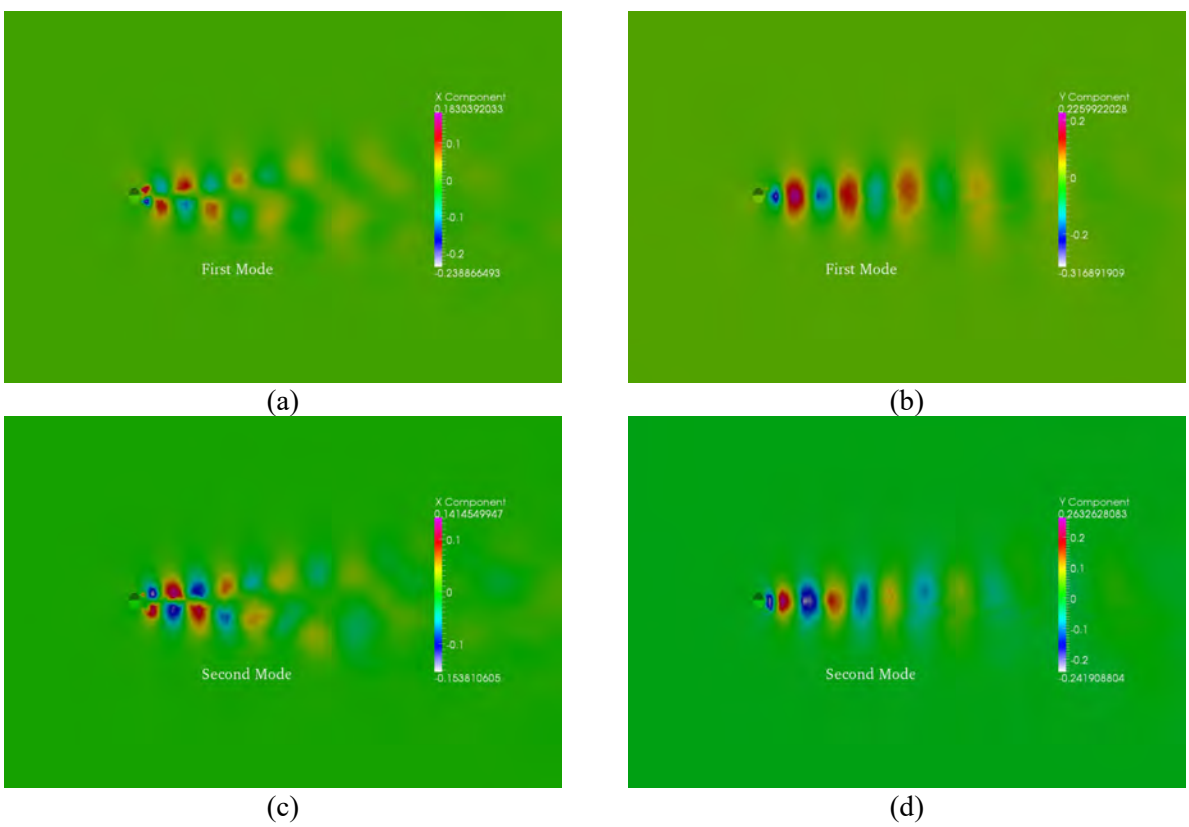

Figure 4-11: (a) x-component of the first velocity POD mode; (b) y-component of the first velocity POD mode; (c) x-component of the second velocity POD mode; (d) y-component of the second velocity POD mode

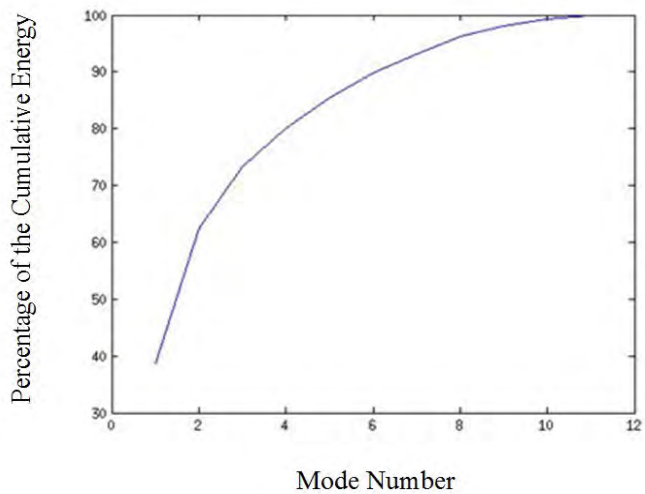

Figure 4-12: Convergence of the cumulative energy of velocity modes vs. mode number

Note that all the variances were normalized by the Eulerian norm of the corresponding vector. From the computed variance, it can be concluded that for temperature and the $\frac{P}{\rho}$ field, the mean of the ensemble is the dominant mode and by subtracting the snapshots from the mean of the ensemble, the modified snapshots are almost the same and no meaningful modes can be obtained. The next step is to consider all the dynamical variables together and apply POD on the various snapshots. Table 4-6 shows the eigenvalues corresponding to each of these five modes and the corresponding cumulative energy while Figure 4-13 shows how the cumulative energy converges.

Table 4-6: Eigenvalues corresponding to each of the first five velocity POD modes

	1st Mode	2nd Mode	3rd Mode	4th Mode	5th Mode
Eigenvalue	3.860	2.585	0.802	0.763	0.622
Cumulative Energy	36.87	61.56	69.22	76.51	82.45

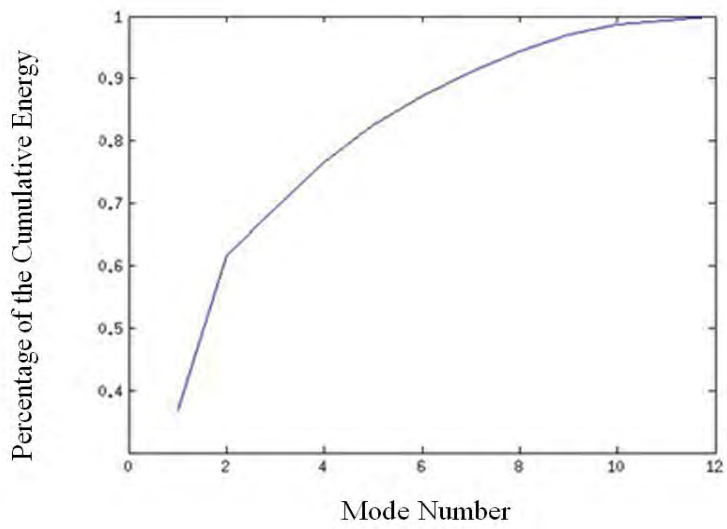

Figure 4-13: Convergence of the cumulative energy of modes vs. mode number

4.2.3 Regression-Based Reduced-Order Modeling

First, a series of regression-based approaches (akin to those previously described in the previous section) were implemented and tested to study the capability of this approach for predicting new flow fields (i.e., fields not included in the snapshot ensemble) in a simple way that utilizes the POD modes. Regression-based approaches are straightforward and computationally inexpensive in comparison to a reduced-order modeling approach that incorporates the modes in a numerical solution to the original differential equations (such as the Galerkin projection). For the series of regression-based approaches, the assumption is again made that any flow fields corresponding to a similar system (e.g., but at different time steps than that used for the snapshot ensemble) can be approximated by the five most dominant modes shown above. However, the regression-based approach assumes that the general relationship between the modal coefficients and the dependent variable, time, can be determined by choosing some functional form for each coefficient and using regression with the modal coefficients found for the snapshots to identify the parameters of these chosen modal coefficient functions. The present analysis chose a linear-combination, radial-basis function form for the modal coefficients, such that:

$$a_i(t) = \sum_{j=1}^{N} c_{ij} g_j(t) \tag{4-55}$$

where c_{ij} are the parameters of the linear combination of RBFs, g_j are the selected RBFs, and N is the number of RBFs selected, which is set equal to the number of snapshots utilized herein for simplicity. A linear regression-based approach is considered:

$$\text{Linear Spline:} \quad g_j(t) = \| t - t_j \| \tag{4-56}$$

where $t_j$are the snapshot sampling times as specified in Table 4-7. Two sets of linear regression-based approach was studied for the example of compressible flow past a cylinder: (1) based on POD modes that are obtained from the velocity modes (results for this regression-based approach are summarized in Table 4-7); (2) based on POD modes that are obtained from all dynamical variables together (results for this regression-based approach are summarized in Table 4-8).

Table 4-7: Prediction of new velocity fields based on a regression-based approach for velocity POD modes (M.C. stands for modal coefficient)

Time Level	1st MC	2nd MC	3rd MC	4th MC	5th MC	$\boldsymbol{L_2}$ Error (%)
1650	0.1604	0.7898	-0.3765	0.8701	-0.7480	14.31
1690	-0.0389	0.6603	-0.0958	0.3864	0.8453	11.79
1740	0.0555	0.3038	-0.0046	-0.0516	-0.9421	13.01
1800 (Extrapol.)	-0.4815	0.6984	0.8914	1.0893	-0.6907	15.22

Table 4-8: Prediction of all dynamical variables based on a regression-based approach (M.C. stands for modal coefficient)

Time Level	1st MC	2nd MC	3rd MC	4th MC	5th MC	$\boldsymbol{L_2}$ Error (%)
1650	-0.0146	0.1311	-0.0234	0.0194	-0.0180	10.24
1690	0.0648	0.0707	0.0100	-0.0540	-0.0312	10.88
1740	0.0932	-0.01755	0.0829	0.0219	0.0012	9.37
1800 (Extrapol.)	-0.0087	-0.0677	0.0214	-0.0530	-0.0248	10.49

Regarding the mathematical formulation of Galerkin projection for compressible flows, it is important to note that the inner product of two snapshots is defined as:

$$(\overrightarrow{q_1}, \overrightarrow{q_2}) = \int_{\Omega} \left(u_{x1}u_{x2} + u_{y1}u_{y2} + u_{z1}u_{z2} + T_1T_2 + \rho_1\rho_2\right)d\Omega \tag{4-57}$$

It is obvious that this inner product does not make dimensional sense. Therefore, one could simply non-dimensionalize the variables, but then the sense in which projections are optimal is rather arbitrary and depends on the choice of coordinates.

The reason that the L_2-errors listen in Table 4-8 are smaller than the ones listed in Table 4-7 is that when all the dynamical variables are considered, temperature and the $\frac{P}{\rho}$ field can be approximated with their corresponding mean within a vortex shedding period and the error associated with the regression-based approach will not be effective in prediction of these two fields. However, in calculating the L_2-error, the denominator will increase and therefore one period of vortex shedding applying the Galerkin projection approach for creating reduced-order model does not seem to be useful. To obtain a set of meaningful modes, accurate temperature gradients through the domain are needed (e.g., flow over a cylinder with a constant surface heat flux).

5 Bibliography

[1] McEligot, D., Condie, K., Foust, T., McCreery, G., Pink, R., Stacey, D., Shenoy, A., Baccaglini, G., Pletcher, R., Wallace, J., 2002, "Fundamental Thermal Fluid Physics of High Temperature Flows in Advanced Reactor Systems-Nuclear Energy Research Initiative Program Interoffice Work Order (IWO) MSF99-0254 Final Report for Period 1 August 1999 to 31 December 2002," INEEL/EXT-02-01613, doi:10.2172/822187.

[2] Anderson, N., Hassan, Y., and Schultz, R., 2008, "Analysis of the hot gas flow in the outlet plenum of the very high temperature reactor using coupled RELAP5-3D system code and a CFD code," *Nuclear Engineering and Design*, 238, pp. 274-279.

[3] S.B. Rodriguez and M.S. El-Genk, "On Enhancing VHTR Lower Plenum Heat Transfer and Mixing via Swirling Jet." Procs. of ICAPP 10, Paper 10160, 2010.

[4] Bayless. "RELAP5/ATHENA calculations of VHTR conduction-cooldown. Private communication." 2006.

[5] P. Chellapandi, S. C. Chetal, and B. Raj, "Thermal striping limits for components of sodium cooled fast spectrum reactors," *Nuclear Engineering and Design*, vol. 239, 2009, pp. 2754-2765.

[6] J. H. Kim, R. M. Roidt, and A. F. Deardorff, "Thermal stratification and reactor piping integrity," *Nuclear Engineering and Design*, vol. 139, 1993, pp. 83-85.

[7] N. Kimura, H. Ogawa, and H. Kamide, "Experimental study on fluid mixing phenomena in a T-pipe junction with upstream elbow," *Nuclear Engineering and Design*, vol. 240, 2010, pp. 3055-3066.

[8] H. Kamide, M. Igarashi, S. Kawashima, N. Kimura, and K. Hayashi, "Study on mixing behavior in a tee piping and numerical analyses for evaluation of thermal striping," *Nuclear Engineering and Design*, vol. 239, 2009, pp. 58-67.

[9] A. Nakamura, T. Oumaya, and N. Takenaka, "Numerical investigation of thermal striping at a mixing tee using detached eddy simulation," Proceedings NURETH-13, Kanazawa City, Ishikawa Prefecture, Japan, 2009.

[10] A. Tokuhiro and N. Kimura, "An experimental investigation on thermal striping mixing phenomena of a vertical non-buoyant jet with two adjacent buoyant jets as measured by ultrasound doppler Velocimetry," *Nuclear Engineering and Design*, vol 188, 1999, pp. 49-73.

[11] N. Kimura, M. Nishimura, and H. Kamide, "Study on convective mixing for thermal striping phenomena (experimental analyses on mixing process in parallel triple-jet and comparisons between numerical methods)," *JSME International Journal, Series B*, vol. 45, 2002, pp. 592-599.

[12] N. Kimura, H. Miyakoshi, and H. Kamide, "Experimental investigation on transfer characteristics of temperature fluctuation from liquid sodium to wall in parallel triple-jet," *International Journal of Heat and Mass Transfer*, vol. 50, 2007, 2024-2036.

[13] S. Choi and S. Kim, "Evaluation of turbulence models for thermal striping in a triple-jet," *Journal of Pressure Vessel Technology*, vol. 129, 2009, pp. 583-592.

[14] R. Knystautas, "The turbulent jet from a series of holes in a line." The Aeronautical Quarterly, Vol 15, February 1964.

[15] B. Pani, and R. Dash, "Three-dimensional single and multiple free jets," *Journal of hydraulic engineering*, Vol. 109, 1983, pp 254-269.

[16] T. Harima, S. Fujita, and H. Osaka, "Mixing and diffusion processes of the twin circular free jets with various nozzle spacings," *Experimental Heat Transfer, Fluid Mechanics, and Thermodynamics*, 2001

[17] K. Svensson, "Experimental and Numerical Investigations of Confluent Round Jets," PhD Thesis, Kinkping University, Sweden, 2015.

[18] Johnson, R. W., 2007, "Modeling strategies for unsteady turbulent flows in the lower plenum of the VHTR," Nuclear Engineering and Design, 238, pp. 482-491.

[19] Guillen, D. P., and McIllroy, H. M., 2007, "Preliminary study of turbulent flow in the lower plenum of a gas-cooled reactor," 12th International Topical Meeting on Nuclear Reactor Thermal Hydraulics, NURETH-12, Pittsburgh, PA.

[20] Guillen, D. P., 2006, "Computational flow predictions for the lower plenum of a high-temperature, gas-cooled reactor," Transactions of the American Nuclear Society, 95, pp. 827-828

[21] Condie, K. G., McCreery, G. E., McIllroy, H. M., and McEligot, D. M., 2005, "Development of an experiment for measuring flow phenomena occurring in a lower plenum for VHTR CFD Assessment," Idaho National Laboratory, Idaho Falls, ID.

[22] McEligot, D. M., and McCreery, G. E., 2004, "Scaling studies and conceptual experiment designs for NGNP CFD Assessment," Idaho National Laboratory, Idaho Falls, ID

[23] Cengel, Y. A., and Cimbala, J. M., Fluid Mechanics: Fundamentals and Applications, McGraw-Hill.

[24] Bean, H. S., 1971, "Fluid meters: Their theory and application," American Society of Mechanical Engineers, 2

[25] K. G. Condie, G. E. McCreery, H. M. McIllroy, D. M. McEligot, “Development of an experiment for measuring flow phenomena occurring in a lower plenum for VHTR CFD Assessment,” INL/EXT-05-00603, September 2005

[26] G.E. McCreery and K.G. Condie, “Experimental Modeling of VHTR Plenum Flows During Normal Operation and Pressurized Conduction Cooldown,” INL/EXT-06-11760, September 2006

[27] M.A. Van Horn, “Scaling of the Thermal Mixing Processes within the Lower Plenums of VHTR Designs,” Master Thesis, Oregon State University, June 2, 2005

[28] H. M. McIllroy, D. M. McEligot, and R. J. Pink “Measurement of turbulent flow phenomena for the lower plenum of a prismatic gas-cooled reactor,” Nuclear Engineering and Design, vol 240, 2010, pp. 416-428

[29] Mazumdar, S., Landfried, D. T., Jana, A., and Kimber, M., 2013, "Initial computation study of the thermal mixing in a VHTR lower plenum," 15th International Topical Meeting on Nuclear Reactor Thermal Hydraulics, NURETH-15, Pisa, IT.

[30] Panton, R. L., 2006, Incompressible Flows, John Wiley & Sons

[31] Mehta, R. D., 1985, "Turbulent Boundary Layer Perturbed by Screen," American Institute of Aeronautics and Astronautics Journl, 23(9), pp. 1335-1342

[32] Scheiman, J., 1958, "Comparison of Experimental and Theoretical Turbulence Reduction Characteristics for Screens, Honeycomb, and Honeycomb-Screen Combinations," NASA Technical Paper.

[33] Mehta, R. D., and Bradshaw, P., 1970, "Design rules for small low speed wind tunnels," Journal of Royal Aeronautical Society, 73.

[34] Bell, J. H., and Mehta, R. D., 1988, "Contraction design for small low-speed wind tunnels," NASA-CR-177488, NASA Contractor Report.

[35] HEXCEL Composites, 1999, "HexWeb^{TM} Honeycomb Attributes and Properties: A comprehensive guide to standard Hexcel honeycomb materials, configurations, and mechanical properties."

[36] H.H. Bruun, “Hot Wire Anemometry: Principles and Signal Analysis,” Oxford university Press, USA 1995.

[37] F.E. Jorgensen “How to measure turbulence with hot-wire anemometers – a practical guide,” Dantec Dynamics, 2002.

[38] H. Schlichting, “Boundary-Layer Theory 7th Edition,” McGraw Hill Press, USA, 1979

[39] J. Mi, D.S. Nobes, and G.J. Nathans, “Influence of jet exit conditions on the passive scalar field of an axisymmetric free jet,” *Journal of Fluid Mechanics*, Vol. 432, 2001, pp. 91-125

[40] Pope, S. B., 2000, Turbulent flows, Cambridge university press.

[41] NASA jet Propulsion Laboratory Web Site, http://masterweb.jpl.nasa.gov/reference/ paints.htm (1997)

[42] Cao, Q., Lu, D., and Lv, J., "Numerical investigation on temperature fluctuation of the parallel triple-jet", Nuclear Engineering and Design, 249, pp. 82-89 (2012).

[43] Tenchine, D., Vandroux, S., Barthel, V., Cioni, O., "Experimental and numerical studies on mixing jets for sodium cooled fast reactors", Nuclear Engineering and Design, 263, pp. 263-272, (2013)

[44] L. GmbH, Product-Manual DaVis 8.3 Software, Gottingen, Germany, 2016.

[45] Sagaut, P., 2002, Large eddy simulation for incompressible flows, Springer.

[46] NIST. 2012. Thermophysical Properties of Fluid Systems. http://webbook.nist.gov/chemistry/fluid/

[47] Shih, T-H, Liou, W.W., Shabbir, A., Yang, Z. and Zhu, J. 1995. A New k-e eddy viscosity model for high reynolds number turbulent flows. Computers Fluids. 24(3), 227-238.

[48] Saxena, A. 2012. Guidelines for Specification of Turbulence at Inflow Boundaries: http://support.esi-cfd.com/esi-users/turb_parameters/

[49] Panchapakesan, N., and Lumley, J., 1993, "Turbulence measurements in axisymmetric jets of air and helium. Part 1. Air jet," Journal of Fluid Mechanics, 246, pp. 197-223.

[50] Wygnanski, I., and Fiedler, H., 1968, Some measurements in the self preserving jet, Cambridge Univ Press

[51] Hussein, H. J., Capp, S. P., and George, W. K., 1994, "Velocity measurements in a high-Reynolds-number, momentum-conserving, axisymmetric, turbulent jet," Journal of Fluid Mechanics, 258, pp. 31-75.

[52] Kim, J., and Choi, H., 2009, "Large eddy simulation of a circular jet: effect of inflow conditions on the near field," Journal of Fluid Mechanics, 620, p. 383

[53] Bogey, C., and Bailly, C., 2009, "Turbulence and energy budget in a self-preserving round jet: direct evaluation using large eddy simulation," Journal of Fluid Mechanics, 627, p. 129.

[54] Kandakure, M.T., Patkar, V.C. and Patwardhan, A.W. 2008. Characteristics of turbulent confined jets. Chemical Engineering and Processing. 47, 1234–1245.

[55] Clément, A., 1996, "Coupling of two absorbing boundary conditions for 2D time-domain simulations of free surface gravity waves," J Comput Phys, 126(1), pp. 139-151.

[56] Lysenko, D. A., Ertesvåg, I. S., and Rian, K. E., 2012, "Large-eddy simulation of the flow over a circular cylinder at Reynolds number 3900 using the OpenFOAM toolbox," Flow, turbulence and combustion, 89(4), pp. 491-518.

[57] Lysenko, D. A., Ertesvåg, I. S., and Rian, K. E., "Large-Eddy Simulation of the Flow Over a Circular Cylinder at Reynolds Number 2×10^4," Flow, Turbulence and Combustion, pp. 1-26.

[58] Smagorinsky, J., 1963, "General circulation experiments with the primitive equations: I. The basic experiment*," Monthly weather review, 91(3), pp. 99-164.

[59] Lilly, D., 1992, "A proposed modification of the Germano subgrid-scale closure method," Physics of Fluids A: Fluid Dynamics (1989-1993), 4(3), pp. 633-635.

[60] Kim, S.-E., "Large eddy simulation using an unstructured mesh based finite-volume solver," Proc. 34th AIAA fluid dynamics conference and exhibit, Portland, pp. 1-7.

[61] Fureby, C., Tabor, G., Weller, H., and Gosman, A., 1997, "A comparative study of subgrid scale models in homogeneous isotropic turbulence," Physics of Fluids (1994-present), 9(5), pp. 1416-1429.

[62] Chai, X., and Mahesh, K., 2012, "Dynamic-equation model for large-eddy simulation of compressible flows," Journal of Fluid Mechanics, 699, pp. 385-413

[63] Bogey, C., and Bailly, C., 2006, "Large eddy simulations of round free jets using explicit filtering with/without dynamic Smagorinsky model," Int J Heat Fluid Fl, 27(4), pp. 603-610

[64] Han, Y. O., George, W. K., and Hjarne, J., 2005, "Effect of a contraction on turbulence. Part 1: Experiment," Spectrum, 1, p. 11.

[65] Spalart, P. R., 2009, "Detached-eddy simulation," Annual Review of Fluid Mechanics, 41, pp. 181-202.

[66] Lipari, G., and Stansby, P. K., 2011, "Review of experimental data on incompressible turbulent round jets," Flow, turbulence and combustion, 87(1), pp. 79-114.

[67] Taub, G., Lee, H., Balachandar, S., and Sherif, S., 2013, "A direct numerical simulation study of higher order statistics in a turbulent round jet," Physics of Fluids (1994-present), 25(11), p. 115102

[68] Corrsin, S., and Kistler, A. L., 1955, Free-stream boundaries of turbulent flows, NACA Washington, DC.

[69] Chevray, R., and Tutu, N., 1978, "Intermittency and preferential transport of heat in a round jet," Journal of Fluid Mechanics, 88(01), pp. 133-160

[70] Chua, L., and Antonia, R., 1990, "Turbulent Prandtl number in a circular jet," International Journal of Heat and Mass Transfer, 33(2), pp. 331-339

[71] Antonia, R., and Mi, J., 1993, "Temperature dissipation in a turbulent round jet," Journal of Fluid Mechanics, 250, pp. 531-551

[72] Mi, J., Nobes, D. S., and Nathan, G., 2001, "Influence of jet exit conditions on the passive scalar field of an axisymmetric free jet," Journal of Fluid Mechanics, 432, pp. 91-125

[73] Mi, J., and Nathan, G., 2010, "Statistical properties of turbulent free jets issuing from nine differently-shaped nozzles," Flow, turbulence and combustion, 84(4), pp. 583-606

[74] Smith, E., Mi, J., Nathan, G., and Dally, B., 2004, "The" Round Jet Inflow-Condition Anomaly" for the k-ε Turbulence Model," School of Mechanical Engineering, University of Adelaide (Australia).

[75] Suto, H., Matsubara, K., Kobayashi, M., and Kaneko, Y., 2004, "Large eddy simulation of flow and scalar transport in a round jet," Heat Transfer—Asian Research, 33(3), pp. 175-188

[76] Colombo, E., Inzoli, F., Muzzio, A., and Teatini, J., "modelling for free, incompressible and non-isothermal round jets’’," Proc. 5th European Thermal-Science Conference

[77] So, R., Zhu, J., Ötügen, M., and Hwang, B., 1990, "Some measurements in a binary gas jet," Experiments in Fluids, 9(5), pp. 273-284

[78] Lockwood, F., and Moneib, H., 1980, "Fluctuating temperature measurements in a heated round free jet," Combustion Science and Technology, 22(1-2), pp. 63-81

[79] Dowling, D. R., and Dimotakis, P. E., 1990, "Similarity of the concentration field of gas-phase turbulent jets," Journal of Fluid Mechanics, 218, pp. 109-141

[80] Lourenco, L., and Shih, C., 1993, "Characteristics of the plane turbulent near wake of a circular cylinder, a particle image velocimetry study," private communication

[81] Parnaudeau, P., Carlier, J., Heitz, D., and Lamballais, E., 2008, "Experimental and numerical studies of the flow over a circular cylinder at Reynolds number 3900," Physics of Fluids (1994-present), 20(8), p. 085101

[82] Ong, L., and Wallace, J., 1996, "The velocity field of the turbulent very near wake of a circular cylinder," Experiments in fluids, 20(6), pp. 441-453

[83] Kravchenko, A. G., and Moin, P., 2000, "Numerical studies of flow over a circular cylinder at ReD= 3900," Physics of Fluids (1994-present), 12(2), pp. 403-417

[84] Franke, J., and Frank, W., 2002, "Large eddy simulation of the flow past a circular cylinder at Re D= 3900," Journal of wind engineering and industrial aerodynamics, 90(10), pp. 1191-1206

[85] Nakamura, H., and Igarashi, T., 2004, "Unsteady heat transfer from a circular cylinder for Reynolds numbers from 3000 to 15,000," Int J Heat Fluid Fl, 25(5), pp. 741-748

[86] Norberg, C., 2003, "Fluctuating lift on a circular cylinder: review and new measurements," J Fluid Struct 17(1), pp. 57-96

[87] Ferziger, J.H., 1997, Computational methods for fluid dynamics, AIP

[88] Issa, R.I., Gosman, A., Watkins, A., 1986, “The computation of compressible and incompressible recirculating flows by a non-iterative implicit scheme,”J Comput. Phys. 62, pp. 66-82.

[89] Ghosal, S., Lund, T.S., Moin, P., Akselvoll, K., 1995, “A dynamic localization model for large-eddy simulation of turbulent flows,” Journal of Fluid Mechanics 286, pp. 229-255.

[90] Garimella, S.V., 2000, “Heat transfer and flow fields in confined jet impingement,” Annual Review of Heat Transfer 11 (11).

[91] Fitzgerald, J.A., Garimella, S.V., 1998, “A study of the flow field of a confined and submerged impinging jet,” International Journal of Heat and Mass Transfer, 41, pp. 1025-1034.

[92] Garimella, S.V., Rice, R., 1995, “Confined and submerged liquid jet impingement heat transfer,” Journal of Heat Transfer 117, pp. 871-877.

[93] Guo, T., Rau, M.J., Vlachos, P.P. Garimella, S.V., 2017, “Axisymmetric wall jet development in confined jet impingement,” Physics of Fluids 29, 025102.

[94] Jeffers, N. Stafford, H., Conway, C., Punch, J., Walsh, E., 2016, “The influence of the stagnation zone on the fluid dynamics at the nozzle exit of a confined and submerged impinging jet,” Experiments in Fluids 57, pp. 1-15.